Structural, Compositional and Mechanical Characterization of Bovine Dental Enamel

Vom Promotionsausschuss der

Technischen Universität Hamburg

zur Erlangung des akademischen Grades

Doktor-Ingenieurin (Dr.-Ing.)

genehmigte Dissertation

von

Jasmin Koldehoff

aus

Hamburg, Deutschland

2022

The printed thesis is available under the ISBN 978-3-8439-5081-7.

Erstgutachter: Prof. Dr. rer. nat. Gerold A. Schneider

Zweitgutachter: Prof. Dr. habil. Michael M. Morlock

Vorsitz der Prüfungskomission: Prof. Dr. rer. nat. Patrick Huber

Tag der mündlichen Prüfung: 22. April 2022

“In biology, nothing is clear, everything is too complicated, everything is a mess, and just when you think you understand something, you peel off a layer and find deeper complications beneath. Nature is anything but simple.”

- Richard Preston

Thank you!

From the bottom of my heart, I want to thank everyone who supported me during my PhD journey!

I would like to thank my doctoral supervisor, Prof. Dr. Gerold A. Schneider, for supervising my thesis. I thank Prof. Dr. Michael M. Morlock filing the role of the second examiner and Prof. Patrick Huber being the chair of the examination committee. Prof. Michael V. Swain, I want to thank for many helpful technical discussions and the possibility to do a part of my work in Sydney. I would also like to thank the BeEM and in particular Dr. Tobias Krekeler, for their support in all my microscopy projects (which were many hours spent at the microscopes in the basement).

I would like to thank all my colleagues for the wonderful time at the institute (even if you are not quite rid of me yet). The coffee and tea breaks and of course the "random beers" were indispensable to having a good time together or to vent your frustration. Especially I want to thank the strong ladies, I learned a lot from you. Berta and Büsra who shared an office with me for a long time and cheered up the day with our "Wall of Happiness" and Catalan curses. My students, who contributed to the success of this work in their theses and as HiWis. Manfred and Anja, who always had an open ear for technical and other problems. Without you the institute would not be the same!

I thank my family and friends for accompanying me through all the ups and downs. I thank my parents for financing my studies and especially my father for many intensive conversations at the kitchen table, which helped to awaken my interest in math and physics. Without all of you I would not have made it this far!

Last, but definitely not least: Paul. Thanks for being my love and partner in crime for more than 10 years.

Content

Nomenclature

BSE	Backscattered Electron	HPLC	High Performance Liquid Chromatography
CLH	Constant Load Hold	KOH	Potassium Hydroxide
CSM	Continuous Stiffness Measurement	NMR	Nuclear Magnetic Resonance Spectroscopy
FIB	Focused Ion Beam	SE	Secondary Electrons
FFT	Fast Fourier Transform	SEM	Scanning Electron Microscopy
FTIR	Fourier Transform Infrared Spectroscopy	SRS	Strain Rate Sensitivity
HAADF	High Angle Annular Dark Field	TEM	Transmission Electron Microscopy
HAP	Hydroxyapatite	TGA	Thermogravimetric Analysis
HBSS	Hank's Balanced Salt Solution	TOC	Total Organic Carbon

α	Geometric factor for a defect	σ	Stress
β	correction factor for indenter tips	σ_{max}	Maximum stress
γ	Surface energy	τ_p	Shear stress in the protein
ε	Strain	τ_i	Time constant of the material due to damping
ε_c	Creep	φ_n	Mineral volume fraction of the n^{th} hierarchal level
η	Constant describing a dashpot element	Φ	Porosity
θ	Half angle of a cone	v_{HAP}	Volume fraction of HAP bridges
ν	Poisson ratio	ω	Frequency of the CSM method
ρ	Aspect ratio		

a	Radius of projected contact area	K_{hyd}	Hydraulic conductivity
a_{crit}	Critical crack length	K_{IC}	Fracture toughness (mode I)
A_c	Projected area of Contact	K_m	Material constant for creep
C_f	Instrument frame compliance	l_n	Particle length on nth level
C_i	Constant	m	Exponent
c_i	Constant describing a dashpot element	m_s	Strain/ creep rate sensitivity
d	Thickness of the material ligaments	P_i	Load
E_i	Elastic modulus	R	Indenter radius
G_i	Shear modulus	R_{eff}	Effective indenter radius
h	Indentation depth	R_r	Radius of the residual impression
h_a	Distance from the edge of contact to the specimen surface at full load	RCF	Ramp correction factor
h_{amp}	Displacement amplitude of the CSM method	S	Contact stiffness
h_c	Contact depth	t_i	time
h_d	Displacement due to thermal drift	t_R	Ramp rise time
h_e	Elastic displacement	w_n	Particle width on nth level
h_{max}	Indentation depth at full load		
h_s	Depth of partial unloading		
h_r	Depth of residual impression after plastic deformation		
H_I	Indentation Hardness		
k	Constant factor		

Summary

In this work a thorough structural and mechanical characterization of untreated and deproteinized bovine dental enamel was carried out. Enamel was deproteinized by chemical treatment with KOH-solution and H_2O_2 containing bleaching agents, and by heat treatment. Advanced microscopy techniques such as FIB and TEM revealed that the interfaces between single HAP crystallites likely cannot accommodate organic structures due to their narrow gap size of often <1 nm. Furthermore, the boundaries between enamel rods are discontinuous, porous structures and there is no complete organic layer engulfing the rods. In untreated enamel frequent bridging filaments could be found that might be of organic origin and were not present in the deproteinized enamel. While chemical treatment did not affect the crystal structure and arrangement, heating enamel leads to decomposition of inorganic components and sintering of the HAP crystallites. Additionally, at high temperatures large cracks are formed in the sample which lead to a largely reduced elastic modulus and hardness. Chemical treatment on the other hand did not affect the modulus and hardness, showing that the protein content is not the decisive factor for those properties. Nanoindentation creep studies confirmed that the protein content does not have a large influence on the mechanical behavior of dental enamel, as virtually no differences could be observed between deproteinized and untreated enamel. However, a pseudo-elastic behavior of enamel and a noticeable influence of water on the mechanical properties of enamel could be observed. Wet enamel, both deproteinized and untreated, had a lower elastic modulus and showed considerably more creep (~10% of the complete deformation) and recovery than dry enamel on both the first and second hierarchical level. It is proposed that the predominant creep mechanism in dental enamel is frictional sliding of the HAP crystallites which is facilitated by the water that is present in the pores and interfaces.

1. Introduction

Natural materials succeed in combining the, usually mutually exclusive, properties of a high toughness while being stiff and strong. On top of that, nature produces these materials at low temperatures and from components that, on their own, do not provide exceptionally high strength and stiffness. This has attracted the interest of the Materials Science community and lead to a new branch studying biological materials and how to apply this knowledge to engineering problems, thus creating bio-inspired materials. Biological materials achieve their exceptional mechanical behavior by combining a hard mineral and a soft organic phase in a self-similar structure on several length scales, a so-called hierarchical structure. While the mineral phase provides strength, stiffness and hardness, the organic phase provides compliance, toughness and even viscous behavior. Prominent examples for such materials are nacre and bone [1–4].

Another example for a hierarchal biological material is dental enamel, which describes the outer layer of the tooth. Due to its high mineral content (~96 w%) [5] it is considered a bio-ceramic [6]. Although the mineral content is among the highest found in natural materials, dental enamel has proven to be highly damage resistant. During its lifetime, cracks accumulate in dental enamel, but the tooth retains its function. Cracks usually are stopped form progressing through the tooth thus protecting the underlying dentin and vascular structures [7–9]. To incorporate this highly damage resistant behavior into synthetic ceramics a better understanding of the structure property relationship in enamel on all hierarchical levels is needed. Although the structural characterization of dental enamel has been undertaken since as early as the 1960s, a lot is still unknown. Characterization of the geometry of the interfaces in dental enamel, i.e. the size of the gap or the amount of it that is occupied by organic material, are rare. On top of that, there is a lack of studies that systematically quantify the effect of the organic component on the mechanical properties.

The work in this thesis aims to close some of these gaps in the knowledge about dental enamel by providing a detailed structural description of the interfaces in dental enamel. Additionally, dental enamel will be subjected to several deproteinization treatments and a systematic analysis of the structure and mechanical behavior will be carried out. The results of this analysis will be discussed regarding the influence of the protein content compared to other structural features.

2. State of Research

The following chapters will discuss the current state of the art in dental enamel research. The development of structural descriptions in the last decades, chemical and mechanical characterization of dental enamel will be highlighted.

2.1 Hierarchical Biological Materials

Due to their exceptional mechanical properties that often combine high strength, stiffness and fracture resistance biological materials have been the focus of research as well as a source of inspiration for many scientists. Typically, biological materials consist of a hard, mineral phase and a soft, organic phase. These two components are then arranged in repeating patterns over several length scales which are then called hierarchical structures. Among the best investigated materials in nature are nacre and bone [1–3,10–12].

The best-known analytical model for an estimation of elastic modulus of hierarchical biological materials, is the model established by Huajian Gao [13] based on the hierarchical structure of bone. Here, on the first level, nanometer-sized hard, mineral particles are enveloped by a soft, organic matrix. The composite building block serves as the hard phase on the next higher level and this structure is repeated on several length scales, yielding a self-similar structure (Figure 1a). The mineral particles provide stiffness and strength in tension while the organic phase is responsible for load transfer in between the mineral particles [10,13].

Due to this self-similarity, the maximum stress the structure is able to withstand, can be calculated on each hierarchical level. It is assumed that the structure is loaded in tension. The mineral phase is assumed to carry the tensile stress completely while the sole purpose of the soft phase is load transfer in between the hard particles which is realized by shear stresses. The load transfer path can thus be simplified by a one-dimensional serial spring system consisting of protein elements (shear) connecting mineral elements (tension) [10]. This concept of load transfer in biological materials was originally developed by Jäger and Fratzl [14] and resulted in the so-called tension-shear chain model (Figure 1b) [10].

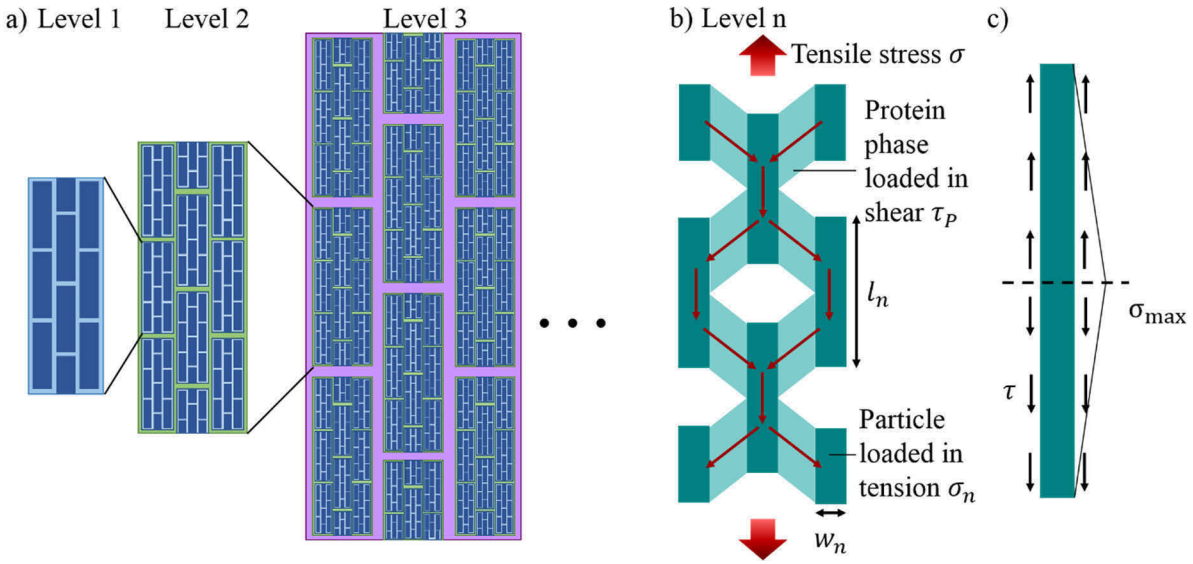

Figure 1: a) The building block consisting of hard mineral phase surrounded by soft organic phase (level 1) serves as the hard phase in the next higher hierarchical level (level 2), which is again surrounded by a soft organic phase. This is repeated for each hierarchical level, resulting in a self-similar structure. b) Assuming a remote tensile stress σ acting on the structure (level n) the soft protein phase can transfers the load between the hard particles. The proteins are therefore loaded in shear whereas the particles (with length l_n and width w_n) are only loaded in tension. c) Considering a single particle, the maximum stress σ_{max} resulting from the shear acting along the particle occurs in the middle of the particle. Adapted with permission from [10,15]

In order to only transfer a small load across each protein ligament, the aspect ratio of the mineral particles needs to be large. Assuming a linear stress distribution along the length of the mineral particles, the maximum σ_{max} (Figure 1c) and average tensile stress σ can be calculated by:

$$\sigma_{max} = \rho\tau_p \tag{1}$$

$$\sigma = \frac{\rho\tau_p}{2} \tag{2}$$

With $\rho = l_n/w_n$ as the aspect ratio of the mineral particles with length l_n and width w_n, and τ_p as shear stress in the protein. From the equations it can be seen that the shear stress of the protein is amplified ρ times, meaning small shear stresses in the proteins result in high tensile stresses in the mineral. The elastic modulus of the composite can be estimated by:

$$\frac{1}{E} = \frac{4(1-\varphi)}{G\varphi^2\rho^2} + \frac{1}{\varphi E_m} \quad (3)$$

With the mineral volume fraction φ, the protein shear modulus G_p and the elastic modulus of the mineral E_m. To ensure the load transfer between the protein and the mineral it is essential that a strong interface exists between the mineral and protein [10].

This model can be adapted to include further hierarchical levels by assuming the composite building block from the first level serves as the hard phase on the next higher level. Repeating this for several hierarchical levels results in a self-similar structure that can be described analytically [15,16]. The average stress within the composite at level *n+1*, σ_{n+1}, can be calculated with

$$\sigma_{n+1} = \frac{\sigma_n \varphi_n}{2} = \frac{\rho_n \tau_p \varphi_n}{2} \quad (4)$$

With the mineral volume fraction φ_n, the mineral aspect ratio ρ_n and τ_p shear stress in the protein at level *n*. For the elastic modulus at level *n+1* equation (3) can be written as:

$$\frac{1}{E_{n+1}} = \frac{4(1-\varphi_n)}{G_n \varphi_n^2 \rho_n^2} + \frac{1}{\varphi_n E_n} \quad (5)$$

With the protein shear modulus G_p and the elastic modulus E_n of level *n* [15,16]. This elegant model has been used to calculate the mechanical properties of several biological materials such as nacre, bone and dental enamel [15].

2.2 Hierarchical Structure of Dental Enamel

Dental enamel describes the outermost layer (ca. 1-2 mm thickness) of the tooth. It is a highly mineralized structure that protects the underlying dentin layer and the tooth against environmental influences. It must withstand high forces during mastication cycles for the whole lifespan of the individuum and therefore has adapted to be hard, stiff and damage resistant. Like many biological materials dental enamel has a hierarchical structure. The structure is characterized in five hierarchical levels according to a widely accepted description by Koenigswald and Clemens [17] (Figure 2).

The lowest level, level 0, is made up by a single hydroxyapatite (HAP) crystallite. One crystallite is approximately hexagonal in cross-section with a width of 40-150 nm and a thickness of 15-50 nm while its length is at least several microns but is considered to can reach up to several mm thus spanning the entire enamel layer [5,18]. Level 1 is comprised of several of said crystallites together. Several of the crystallites can be arranged in diverging orientations, forming enamel rods (also often referred to as enamel prisms or prismatic enamel) with a diameter of about 5 µm and interrod enamel (also known as interprismatic enamel or interprismatic matrix) at level 2 in enamel structure. The difference in orientation between these features is founded in the way enamel is formed and will be discussed in more detail in chapter 2.4. The arrangement of rod and interrod enamel results in level 3 of the hierarchical structure, the so-called enamel types. These types can vary between species. In bovine enamel radial enamel with a parallel arrangement of rods and decussation enamel the so-called Hunter-Schreger bands predominate. The last level, level 4, is called schmelzmuster and describes the spatial distribution of enamel types. In bovine enamel there are three distinctions: innermost enamel (modified decussating enamel), inner enamel (decussating enamel) and outer enamel (radial enamel) [5,17,18].

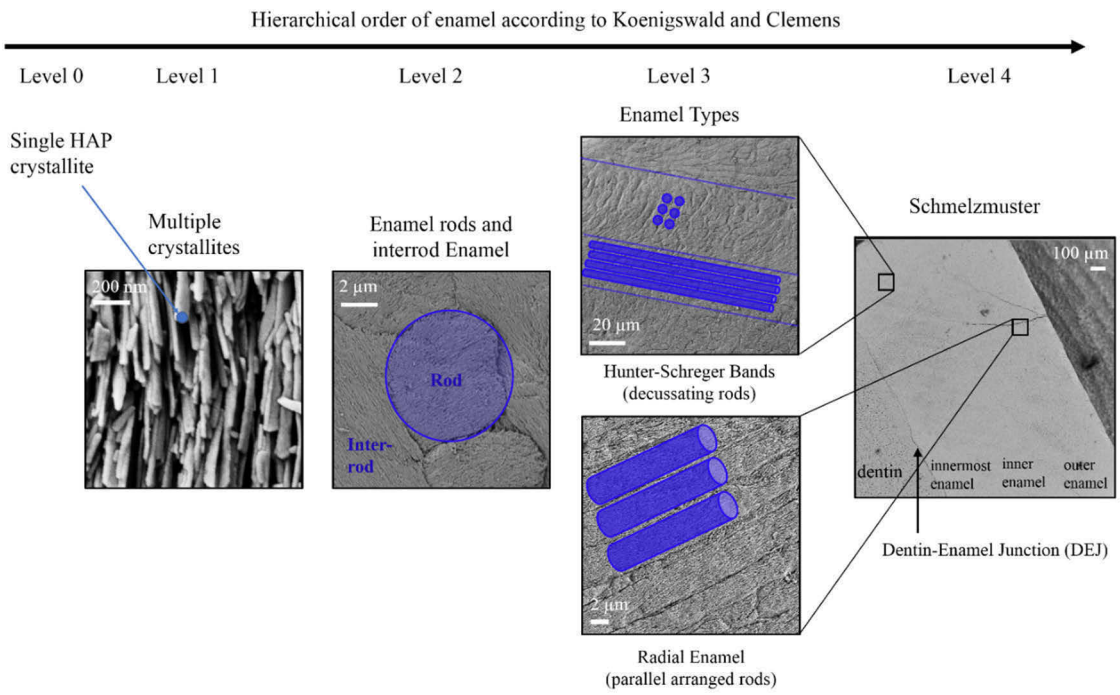

Figure 2: Hierarchical structure of dental enamel. Multiple HAP crystallites (level 1) are bundled together and form rod and interrod enamel (level 2). Spatial arrangement of the rods, decussating or parallel, makes up level 3 and is called enamel type. The schmelzmuster (level 4) describes the distribution of the enamel type across the enamel thickness.

2.3 Composition of Dental Enamel

The composition of dental enamel has been investigated by various researchers employing various techniques, such as TGA, FTIR and NMR. Generally, enamel is described as highly mineralized with up to 96 w% HAP and the remaining 4% consisting of water and organic matter [5]. However, due to the variety of methods used, a wide range of values for the organic and water content (0.3-11 w%, for human and bovine enamel [5,19–22] and 0.22-3.5 w% [19,20,23–27], respectively) can be found in literature. In the following subchapters the nature of the components will be discussed in further detail.

2.3.1 Hydroxyapatite Crystals

The mineral component of dental enamel consists of hydroxyapatite (HAP), a form of calcium phosphate. Calcium phosphate is abundant in nature and thus its chemistry has been of interest to researchers already centuries ago. The research interest spanned a variety of fields, ranging from geology, chemistry, biology and medicine [28]. In living organisms HAP is the most common variant of calcium phosphates and has the chemical formula $Ca_{10}(PO_4)_6(OH)_2$. However, this structure is not perfect, as a variety of ion substitutions are possible and occur readily in biological materials [29].

The unit cell of HAP is described as a hexagonal structure with the lattice parameters a = b = 9.432 Å and c = 6.881 Å, Z = 1 in the space group $P6_3/m$ [30]. Figure 3 shows the structure of the unit cell. The ten Ca^{2+} ions are located in two crystallographically different symmetry sites (4*f* and 6*h*), where four Ca ions occupy the 4*f* sites. As they are arranged in columns along the three-fold axes at 1/3, 2/3, 0 and 2/3, 1/3, 0 they are also commonly referred to as column Ca (or Ca1). These ions are separated by approximately half of the c-axis. Ca1 is coordinated to nine O atoms, whereby six shorter bonds define an approximate trigonal prism and three longer bonds are capping the prism faces. The Ca-O_9 polyhedra form chains parallel to the c-axis by sharing the trigonal faces. The remaining six Ca^{2+} ions are located at the 6*h* sites and are commonly called Ca2 or triangular Ca. They form two triangular sets at z = 1/4 and 3/4 on the mirror planes and are seven-coordinated, with six O atoms and one OH^- ion. The six PO_4^{3-} ions are in expanded triangular positions occupying 6*h* positions similar to the Ca2 ions. The adjacent Ca1 and Ca2 polyhedra are linked through the O atoms of the PO_4^{3-} tetrahedra. Due to the crystallographic symmetry that is imposed by the $P6_3/m$ space group each OH^- ion must be considered at statistically disordered positions (4*e*) above and below the mirror planes [30].

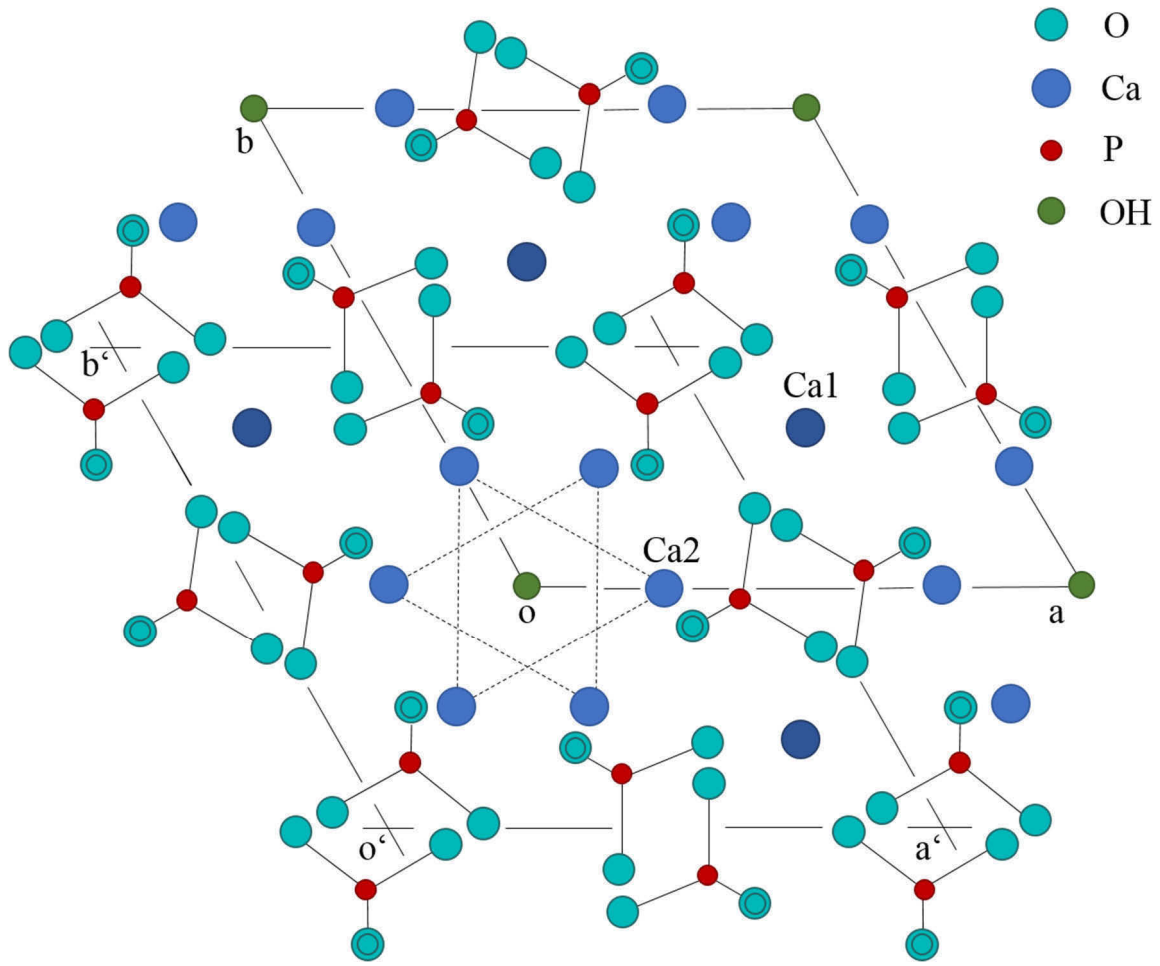

*Figure 3: Crystal structure of HAP projected down the c-axis. The OH ions (green) mark the corners of the unit cell. An alternative of unit cell is denoted by a' and b'. 4 Ca ions (blue) occupy the 4*f *sites and are arranged in columns along the three-fold axes (Ca1). Ca1 is coordinated to 9 O atoms, whereby 6 shorter bonds define an approximate trigonal prism and three longer bonds are capping the prism faces. The Ca-O_9 polyhedra form chains parallel to the c-axis by sharing the trigonal faces. The remaining 6 Ca^{2+} ions are located at the 6*h *sites (Ca2). They form two triangular sets at z = 1/4 and 3/4 on the mirror planes and are seven-coordinated, with six O atoms and one OH^- ion. The six PO_4^{3-} ions (red and cyan) are in expanded triangular positions occupying 6*h *positions similar to the Ca2 ions. The adjacent Ca1 and Ca2 polyhedra are linked through the O atoms of the PO_4^{3-} tetrahedra. Reprinted with alteration from [30].*

A further source of disorder are the various substitutions that are possible in HAP. The HAP in bone and teeth is non-stochiometric, calcium deficient and partially carbonated. It can be represented by the chemical formula $(Ca, Z)_{10}(PO_4,Y)_6(OH,X)_2$ with $Z = Na^+, Mg^{2+}, K^+, Sr^{2+}$, etc., $Y = CO_3^{2-}$, HPO_4^{2-}, and $X = Cl^-, F^-$ [31]. However, the carbonate ions can not only substitute the phosphate group, a substitution that is also commonly referred to as carbonate

type B substitution but can also be accommodated in the structural channel formed by the Ca2 ions, thus replacing the OH^- ions. The latter is known as carbonate type A substitution [29].

The ability of HAP to incorporate these various substitutions results in an astounding flexibility of the crystal lattice. In biological HAP approximately 20% of the Ca^{2+} are substituted by cationic impurities. The substitutions distort the crystal lattice and affect the crystallinity, thermal stability, morphology, solubility and other physicochemical and biological properties of the material. For example, substitution of Ca^{2+} with Mg^{2+} reduces the lattice constant *c* by 0.33% and increases the lattice constant *a* by 0.1% which causes significant lattice disturbances and increase the solubility of the HAP. Considering the frequent incorporation of CO_3^{2-} ions in either the A-site or the B-site, the former leads to an increased lattice parameter *a* with a lesser decrease in *c*-direction while the latter has the opposite effect [31]. While not the most common, substitution of OH^- ions by F^- ions is another important substitution in HAP. It is generally more favorable, as the F^- bind more strongly to the Ca ions. In dental enamel fluoride substitution is an important mechanism for caries prevention due to the lower solubility of the fluorinated HAP. Fluoride incorporation in teeth is limited to the surface [29,32]. As can be seen from the chemical formula, various substitutions are possible in biological HAP. Table 1 shows the typical composition of the mineral fraction in dental enamel [33].

Table 1: Typical composition (w%) of dental enamel's mineral fraction [33]

Component	Ca	P	CO_2	Na	K	Mg	Sr	Cl	F	**Ca/P molar**
w%	37.6	18.3	3.0	0.7	0.05	0.2	0.03	0.4	0.01	**1.59**

Another alteration to the crystal structure is caused by structurally incorporated water. In the past many diverging opinions on the water content in biological apatite have been postulated and are largely dependent on the methods that were used for the sample analysis. More recent studies using NMR have shown that water is structurally incorporated into the HAP crystal. Vacancies in the OH^- and Ca2 sites leave wide open channels, that readily accommodate water molecules. The similarity in size of OH^- ions and H_2O molecules further supports their structural incorporation into the crystal lattice. With 6.6 w% CO_3, as typically present in bone apatite, and assuming the Ca2 vacancies are 3-times more abundant than the Ca1 vacancies, half of the OH ions and more than 12% of the Ca2 would be missing, leaving ample space for incorporation of the water molecules [34].

2.3.2 Organic Matter

The wide range of organic content given in literature of 0.3-11 w%, for human and bovine enamel [5,19–22] results from mostly thermogravimetric analyses (TGA). However, during heating enamel not only organic matter but also carbonate is decomposed, and water is removed. Therefore, mass losses determined by TGA are usually not equal to the amount of organic in the sample. Analyses that used solvent to remove the proteins from the mineral coupled with electrophoresis or chromatography methods are generally more accurate and can be used to determine the size of the proteins or even their amino acid composition.

The organic matter plays a major role in enamel formation and has therefore been studied thoroughly. During enamel formation, ameloblast cells secrete proteins that are organized into a matrix structure. These proteins provide the scaffold for the hydroxyapatites to grow and regulate crystal growth but are mostly removed during the enamel maturation process. Enamel formation and maturation will be discussed in more detail in chapter 2.4. While many studies were carried out in developing enamel due to the increased amount of proteins present and the interest in the role of the proteins on crystal growth, mature enamel has also been studied. It has been found that in mature enamel three main proteins are present: amelogenin, ameloblastin and enamelin.

Amelogenin is the most abundant protein in dental enamel and constitutes around 90% of the organic content. Its molecular weight is about 22-30 kDa and it has hydrophobic properties. Amelogenin has been shown to assembles into nanospheres, ranging in size from 5-100 nm, during enamel crystal formation and plays a major role by modulating crystal morphology and promoting parallel crystal organization [6,35,36].

Ameloblastin, also known as amelin, is the second most abundant protein in dental enamel and makes up about 5% of the total protein content [6,37]. It is secreted at the same time as amelogenin during enamel formation and has been shown to interact with amelogenin although the functional significance of these interactions is still unclear [6]. In developing enamel, ameloblastin is found in organic sheaths that guide enamel rod growth [38,39]. It is believed that, in mature enamel, remnants of ameloblastin are retained primarily in the space between enamel rods (also called sheath space), although a recent study has placed both amelogenin and ameloblastin more closely related to the HAP crystallites [40]. Instead the organic found in the

rod spaces has been associated with keratins, which are fibrous structural proteins that are highly cross-linked and give a unique strength to epithelial tissues such as skin and hair [40,41].

Enamelin is the largest known glycoprotein in dental enamel and, like amelogenin, belongs to the secretory calcium-binding gene family. It is therefore believed to also regulate crystal growth by binding to the calcium sites. In contrast to amelogenin however, it is much less abundant and has a hydrophilic nature [6]. In developing enamel, enamelin was restricted to the rod and interrod enamel and absent in the sheath space between enamel rods, further indicating its binding to the HAP crystallites [36].

Due to the small amount of protein in mature dental enamel, visualization of the proteins is challenging. One research group reported a fibrillar proteinaceous network near the dentin-enamel junction [42], but in later studies by this research group it was found that this network was not made up of enamel proteins but consisted of collagen. Therefore, it was concluded that there is a collagenous network that extends from the dentin-enamel junction into the innermost enamel layer [43,44].

Although the organic content in mature dental enamel is low, many researchers have reported the proteins' influence on the mechanical properties. Depending on the method of protein removal, either a reduction in elastic modulus and hardness when using chemical agents [45,46] or an increase when heating the sample [47,48] has been observed. However, a lower fracture toughness [45,46,48,49] and lower ability to creep [45–47] in deproteinized samples have been reported consistently.

2.3.3 Water

Little and Casciani differentiated three types of water in dental enamel depending on the temperature that was required to remove the water. Water removable below 100°C was called loosely bound or free water. The other types were both named caged water and was separated into water that is removable by temperatures below 900°C and water that is only removable above 900°C, where the latter cannot be hydrated by normal means. Caged water can still move freely but is trapped among the crystal structure [23].

In recent years and with new, advanced techniques the water in biological apatite could be further investigated and the definition provided by Little and Casciani has been disproved.

There is evidence, provided by several research groups, that water molecules are incorporated into the crystal structure of the HAP crystal. As described in chapter 2.3.1, vacancies in the OH^- and Ca2 sites leave wide open channels, that readily could accommodate water molecules. Thus nowadays, water in hydroxyapatite is differentiated between adsorbed water and structurally incorporated water [34,50,51].

Due to the differences in sample preparation, and measurement techniques and parameters the water content reported in literature also shows a wide range of values. Generally, the adsorbed water, that can be removed by drying at temperatures <100-200°C, makes up roughly 1 w% of dental enamel (0.22-1.9 w%) [19,20,23–26]. Determination of the amount of structurally incorporated water by TGA is hindered by the overlap in decomposition of organic and carbonate at temperatures >200°C and needs to be coupled with further techniques such as IR [52]. Literature gives values for structurally incorporated water in HAP as 1.5-3.5 w% [23,27].

2.4 Enamel Formation

Enamel formation, or amelogenesis, is a two-step process. It is divided into enamel formation, where partial mineralization to about 30% already occurs, and mineralization, where mineralization to the final mineral content of enamel, up to 96%, occurs. Generally, three stages of amelogenesis are described:

1) Presecretory stage
2) Secretory (formative) stage
3) Maturation stage

These three main stages can again be described by several sub-stages, resulting in as many as six described stages. Amelogenesis is a time extensive process, that can take up to five years in humans, of which 2/3 fall into the maturation stage [5]. The description in this work will concentrate on the events occurring in the main stages that are important to understand the origin of enamels exceptional microstructure.

In the presecretory stage the special cells, called ameloblasts, acquire their phenotype, meaning, among others, they assume their morphology and biochemical and physiological properties. The ameloblasts develop the extensive protein synthetic apparatus and prepare to secrete the organic matrix of enamel [5].

In the secretory, or formative, stage the ameloblasts lay down the *organic matrix*, elaborating and organizing the entire thickness of the enamel layer. This process starts at the dentin surface and continues to the outer layer of enamel, resulting in a highly ordered structure. In order to do so, the ameloblasts secrete proteins that immediately participate in formatting an initial layer of enamel that does not contain any rods [5]. Throughout the secretory stage, at least five enamel proteins are expressed and secreted into the enamel matrix, namely amelogenin, ameloblastin, enamelin, enamelysin (MMP-20) and enamel matrix serine proteinase I (EMSPI) [37]. The ameloblasts move away from the dentin surface and develop the so-called *Tomes' process*, an 'extension' of the cell where the matrix proteins are excreted. The secreted proteins self-assemble and form a supramolecular structural framework, the *organic matrix*. The Tomes' process contains a distal and proximal part. The excretion of matrix proteins from the proximal portion results in enamel partitions that delimit a pit. The enamel partitions are not distinct units but form a continuum throughout enamel that is known as *interrod enamel*. The distal part of the Tomes' process resides inside the pit that is delimited by the interrod enamel and secretes what is known as *enamel rods*. As both enamel rods and interrod enamel are secreted by the same ameloblast, they are identical in composition and only differ in crystallite orientation. The orientation of the crystallites is determined by the angle of the Tomes' process. As the enamel layer thickens, the distal part of the Tomes' process elongates and is eventually squeezed out of existence, creating a narrow space between rod and interrod enamel. This small space is known as *rod sheath* and filled with organic. Due to the orientation of the secretory surface on the distal part of the Tomes' process, there is a small area where rod and interrod enamel are confluent, known as *tail* in some structural descriptions. As the ameloblasts reach the end of the enamel layer and thus are nearing the end of this stage, they become shorter again and the Tomes' process retracts. As the rod and interrod structure is formed in relation to the Tomes' process, the last enamel layer again does not contain any rods, also known as *prismless enamel* [5,36].

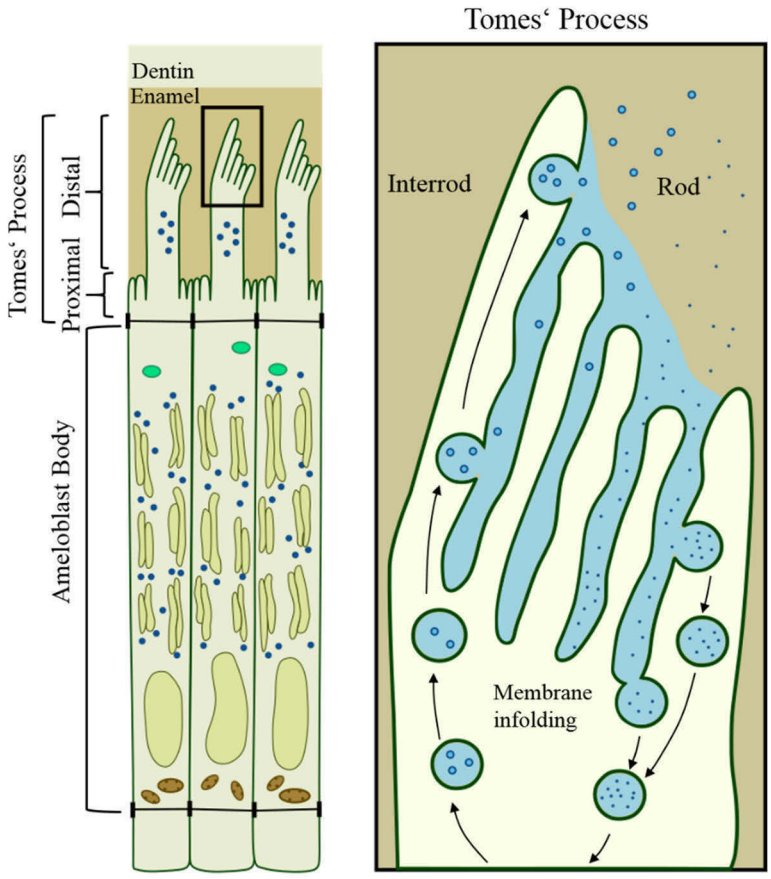

Figure 4: Schematic of an ameloblast. The Tomes' process consists of a proximal portion and a distal portion. The proximal portion is associated with formation of interrod enamel, the distal portion with enamel rod formation. Adapted from [53], available via license: CC BY 4.0

The organic matrix plays a major role in guiding the crystal growth. It has been shown that the organic matrix is structured by amelogenin molecules that self-assemble into nanospheres of ~20 nm. These nanospheres then form long nanoribbons that act as a template for the crystallites [54,55]. The first and partial mineralization of dental enamel occurs already during the secretory stage, shortly after the organic matrix has been laid down by the ameloblasts. FTIR studies during this phase have shown a poorly crystalline and highly carbonated mineral phase [56–58]. This mineral phase has been identified as an amorphous calcium phosphate (ACP) precursor formed along the protein nanoribbons that is subsequently gradually transformed into oriented apatite fibers [55]. The shape of this mineral phase is determined by the geometric arrangement of the organic molecules delimiting the space in which the mineral forms [59].

During the maturation stage the main function of the ameloblasts are to modulate and transport the ions that are needed for the crystal growth and to secrete the proteinases that regulate crystal

growth. After the formation stage is complete the ameloblasts change their morphology again, by shortening and restructuring into maturation cells. In this stage ameloblasts exist in two configurations, the ruffle-ended ameloblasts and smooth-ended ameloblast. Each ameloblast undergoes modulation and change from one configuration to the other frequently, in rats as often as every eight hours. Whereas the ruffle-ended ameloblasts release numerous calcium binding proteins, the smooth-ended ameloblasts allow the exit of protein fragments and water. Additionally, bicarbonate ions are released that aid in optimizing the pH value to prevent demineralization and control the activity of the enzymes that degrade the organic matrix. During maturation, the crystals that were seeded in the formation stage will only grow in width and thickness, at the expense of proteins and water [5,59]. The proteins are largely removed with only about 1 w% remaining in mature enamel [57,60]. The maturation stage is also the stage where most of the mineral deposition occurs. It has been shown that no crystal growth happens until the organic matrix is partially broken down, suggesting that the maturation is driven by the proteinases that remove the crystal growth inhibiting proteins [37]. The enamel crystallites will continue to grow in thickness until they touch each other. This results in irregular cross-sections, interlocking and fusion of neighboring crystallites in fully mature enamel [5,54,59,61]. The boundaries between enamel rods, referred to as sheaths during the secretory stage, is the only region where a more imperfect packing of the crystallites occurs. It is thus hypothesized that here an accumulation of organic material in mature dental enamel may occur due to the sole fact that this space is available [62].

2.5 Existing Structural Descriptions of Dental Enamel

In the past decades a great number of studies have investigated the structure of dental enamel. A special interest has been dental enamel formation and the role of the proteins in this process. Therefore, the amount of studies investigating fully developed dental enamel is limited. In immature enamel the concentration of organic matter (proteins) is much higher than in the later, fully matured stage. Due this difference in composition structural descriptions of immature enamel cannot be directly applied to mature enamel. The lack of detailed descriptions of the structure of the organic matrix in fully mature enamel, and possibly a lack of knowledge of the complicated biological process of enamel mineralization, has led to discrepancies in the structural descriptions between the biological and materials science community. A summary of structural descriptions of dental enamel in literature similar to the one given in this chapter has

also been published in *Acta Biomaterialia* with the title 'The geometrical structure of interfaces in dental enamel: A FIB-STEM investigation' [63].

During the formation, as described in the previous chapter 2.4, the mineral crystallites are engulfed by an organic matrix to guide their growth. Often the term *organic sheath* is used to describe this structure. On the one hand, this term has been used to describe the protein layer covering the mineral crystallites during enamel formation [58,61,64,65]. On the other hand, it is also used to describe organic interacting with the larger enamel rods [6,35,62,64,66–69]. While 'organic sheath' or 'protein sheath' is used interchangeably in literature to describe either proteins interacting with crystallites or associated with the rod boundaries the terms 'prism sheath' and 'rod sheath' are solely used for the latter.

However, in some early studies the term organic sheath has also been used to refer to the enamel between the rods [64,70,71], that now is better known as *interprismatic enamel*, *interprismatic matrix* or *interrod enamel*. It has been shown that the only difference between these two types of enamel is solely their orientation, as evident from their simultaneous formation by the same ameloblast (see chapter 2.4) [5,70,71]. Nowadays, the term *rod sheath* or its equivalents are mainly used to denote the small space delineating enamel rods. It is described as a mineral free space where a greater volume of organic and fluid is present or where crystallites abruptly change their orientation [5,64,72–75]. They are clearly visible in developing enamel, but as maturation progresses the organic matrix is progressively broken down and removed and the space gets filled by the growing crystallites. Thus, in mature enamel the sheaths are barely visible and their existence as a distinct organic structure has been doubted [68,71,76–79], nevertheless some accumulation of organic material in that space could be observed [74].

Studies that show clearly visible sheaths in fully mature enamel are undertaken on strongly etched samples [70,80,81]. As the resistance to acid between the sheaths and rods differs, this greatly improves visibility of the sheaths. In human enamel the shape of the sheaths is described as an arcade or horseshoe, meaning that on one side there is a clearly defined boundary between rod and interrod enamel. Opposite this region however, there is an area – or more precisely – an interface volume where there is continuity between rod and interrod enamel [5,69,82–85]: This results from the formation of both rod and interrod enamel from one ameloblast, as described in chapter 2.4. Depending on the species and location in dental enamel the circumference of the boundary varies and rods can by classified in patterns according to Boyde, where in the case of the so-called closed boundary, the boundary or sheath actually encloses an

enamel rod completely [80]. The term ‘rod sheath’ implies complete coverage of one rod with an organic layer. This may be accurate for the case of the closed boundaries. In the case of the ‘open boundary’, where continuity between rod and interrod enamel is achieved and which is the predominant motif in human and bovine enamel, however, this term is misleading.

The aforementioned studies describing organic sheaths were mostly carried out by groups with a strong biological background and focused on the components present during enamel formation and the changes in their structure during maturation [35,36,61,64,65,69,71,76,78,83,85–87]. Unfortunately, these studies usually only briefly mention the structure of the interfaces in mature enamel as part of the structural changes during maturation. The structure of the interfaces in mature enamel has rarely been investigated [61,72,77,81,87] and studies investigating the interfaces mostly focus on a comparison between healthy enamel and enamel that is afflicted by caries [68] or hypomineralization [88–90]. Therefore, especially literature showing the morphology of the organic matrix in fully mature enamel is rare and lacking in detail [40,48,91,92].

In the last 20 years materials scientists have investigated the mechanical properties of mature dental enamel in numerous studies. Here the structural description usually is the following: HAP crystallites are covered and/ or glued together by organic material [80,92–101], they then form bundles that are called prisms or rods and are separated from each other by an organic sheath [72,95,102–104]. Different arrangements of these rods make up the different enamel types whose spatial distribution is called Schmelzmuster. Mechanical models are then created according to this assumption: Mineral particles are embedded in an organic matrix, on the next hierarchy level these building blocks are then again covered by organic material [97,105,106]. This structural description might have its origin in a publication by Spears where the structure of enamel was modelled as rods separated by organic layers [107] and is analogous to the model of bone developed by Gao et al. (see chapter 2.1) [13,108].

While a protein coating of the HAP crystallites has been demonstrated in developing enamel [65], the degradation of this coating during maturation is well known. Already several decades ago, it has been described that in mature enamel an organic sheath on the crystallites is no longer visible [61]. Recent investigations of the composition and structure of mature human and rodent enamel use atom probe tomography (APT), a technique where a thin needle of material (around 100 nm in diameter) is evaporated atom by atom by an electric field and laser pulses. From the time of flight to a detector with high spatial resolution the elemental

composition of the evaporated atom and its position in the sample can be determined. This technique is thereby able to analyze composition and structure down to the atomic scale. These studies confirmed the absence of an organic layer covering the HAP crystals on mature enamel. Instead, some organic clusters could only be found in locations where a boundary between three crystals existed. Interestingly, the interface between crystals showed a higher concentration of magnesium [109,110].

The advance of characterization technology has spawned new investigations of biominerals. Using polarization-dependent imaging contrast and x-rays, Beniash et al. recently revealed that enamel crystallites are misoriented with respect to each other. Frequently, directly neighboring crystallites are misoriented up to 30° while their long axes are perfectly aligned. Across a rod, where crystallites run parallel to each other, crystallite orientation can vary up to 90°, meaning that the elongation direction of the crystallites can be perpendicular to their c-axis [111].

In order to correctly interpret the mechanical behavior of dental enamel, understanding its structure is essential. The implications of the here described features of enamel structure on the mechanical properties will be discussed at a later point (ch. 6.3).

2.6 Characterization of Dental Enamel's Mechanical Properties on Multiple Length Scales

Enamel as a strong and stiff biological material has been of interest for materials scientists for some time. With more recent developments in measurement techniques that allow to probe small sized samples, already a decent number of studies investigating the mechanical behavior of dental enamel have been undertaken.

2.6.1 Stiffness, Hardness and Strength

The strength and stiffness of the first hierarchical level in dental enamel, namely a single HAP crystallite, has not been investigated experimentally due to its small size and the accompanying constraints for isolating a single crystal in the tissue. According to the model postulated by Gao et al. (see ch. 2.1) the nanometer sized scale of these crystallites has evolved to achieve optimum fracture strength. Opposed to ductile materials where dislocation propagation is the main mechanisms occurring under stress concentrations, brittle materials are sensitive to flaws like cracks and break before reaching their theoretical strength. Griffith's theory postulates that the fracture stress σ_{crit} is dependent on material parameters such as elastic modulus E, surface

energy γ and on the size of the flaw a. If the size of the brittle material is below a certain critical level, the material becomes insensitive against flaws and the theoretical strength is reached [108]. The critical length scale a_{crit} can be estimated with equation (6) [112,113]

$$a_{crit} \approx \alpha \frac{\gamma E}{\sigma_{th}^2} \qquad (6)$$

with α being dependent on the flaw geometry and approximated as $\sqrt{\pi}$ for a half-cracked platelet [108]. Taking $\gamma_{HAP} = 1\,Jm^{-2}$ [42], $E_{HAP} = 125\,GPa$ [43] and $\sigma_{th} = E/30$ [30] as values for the parameters, a_{crit} is estimated to be approximately 36 nm. The actual dimensions of the HAP crystallites fall in this range and strengthen the hypothesis that minerals in biological tissues are optimized regarding their fracture strength. As the mechanical properties of a single HAP crystal in dental enamel could not yet be evaluated experimentally due to its small size, only theoretical calculations with experimental results from a higher hierarchical level and analytical results for hierarchical biological materials. Such the strength of a single HAP crystallite was estimated as 2 GPa [114] which is the order of magnitude one obtains from the estimation of the theoretical strength (4 GPa) by $\sigma_{th} = E/30$, as the denominator of 30 is a very rough estimate.

In recent years nanoindentation has become a popular tool to determine elastic modulus and hardness in small sized structures. Several studies have employed nanoindentation on dental enamel to determine its elastic modulus and hardness. The elastic modulus has been found to be in the range of roughly 60 to 105 GPa and hardness ranges from 2.5 to 4.6 GPa with a decrease in elastic modulus from outer enamel to inner enamel [115–118]. The wide range of values found in literature may be related to natural variations in the teeth, as well as the difference in indentation depths that were used in the studies. Zhou and Hsiung reported a 30% decrease in hardness when changing the indentation depth from 300 nm to 2000 nm [96]. On top of that, a gradient exists in enamel that will be discussed later (ch. 2.6.3).

3-point bending on bulk samples and bending with micro-cantilevers fabricated by focused ion beam to test the lower hierarchical levels have been carried out in several studies. Chan et al. have found the flexural strength of multiple HAP crystallites in enamel (level 1) to be 0.85 ± 0.20 GPa. In this study the elastic modulus however was only determined by nanoindentation and reported as 95 ± 15 GPa [119]. The elastic modulus and fracture strength

was found to decrease by about 50% from the first to second hierarchical level, with values given as 36 ± 8 GPa and 478 ± 93 MPa, respectively [114]. In the bulk sample (level 4) a further decrease of fracture strength and elastic modulus was found. Here also a direction dependency was noted with fracture strength and elastic modulus of samples tested with load perpendicular to the enamel rod orientation being 95 ± 7 MPa and 56 ± 7 GPa, respectively. Meanwhile the samples loaded parallel to rod orientation showed a significantly lower fracture strength and elastic modulus of 69 ± 20 MPa and 35 ± 6 GPa, respectively. This was explained by the fact, that for the perpendicularly loaded enamel the inner enamel, which has a higher resistance against crack propagation, is involved in the fracture process from the beginning and over the complete loading process, whereas in the parallel loaded sample the crack may easily propagate once it reaches the outer enamel with its parallel arrangement of rods [113,120].

Similar to the bending experiments, compression tests have been carried out on bulk samples and micrometer-sized pillars (fabricated by focused ion beam). On bulk samples the fracture strength and elastic modulus are reported as 864 ± 78 MPa and 40 ± 7 GPa for multiple HAP crystallites loaded in fiber direction (longitudinal) [121]. Furthermore, in the micro-level compression tests an elastic modulus that is independent of the direction of loading on the HAP fibers has been observed and the values are reported as 70 ± 8 GPa, 72 ± 6 GPa and 74 GPa in transverse, longitudinal and oblique direction, respectively. However, fracture strength differed and was highest in transverse direction, were the fibers were positioned perpendicular to the applied load (failure strengths for transverse, longitudinal and oblique loading directions are 1362 ± 333 MPa, 790 ± 112 MPa and 848 MPa. respectively) [122]. Based on the isotropic elastic modulus in the compression tests, an adapted sandwich model with mineral to mineral contact has been proposed [122]. Larger sized pillars, representing the second hierarchical level have also shown an orientation independent elastic modulus of 61 ± 11 GPa. Compressive strength was again dependent on the orientation of the HAP fibers, and hence enamel rod orientation, with values from 700 MPa for parallel orientation and 1500 MPa in transverse direction. The high value for the transverse direction, which is in the order of magnitude of the theoretical strength, was attributed to mineral failure as the main failure mechanism. In contrast, in the other loading directions, fiber buckling and interface debonding likely reduced the overall strength [123].

In macroscopic compression test, first a linear elastic stress-strain response was observed with the modulus determined as 30 GPa. The elastic limit was reached at a stress of 400 MPa, the

enamel then deformed inelastically with decreased stiffness and reached a maximum stress of 700 MPa without failing catastrophically. Instead the sample retained integrity and could be reloaded to similar stresses as in the first loading [124].

The decrease in strength and elastic modulus with increase in hierarchical level that has been observed by the aforementioned various studies is inherent with increase in protein content. According to the analytical model of Gao [16] the mineral content of the composite can be calculated by:

$$\varphi_{total} = \varphi_1 \varphi_2 \dots \varphi_n \qquad (7)$$

with φ_n as the mineral volume fraction of the nth hierarchal level. If we assume the mineral volume fraction on all hierarchical levels as equal ($\varphi_1 = \varphi_2 = \varphi_n$) the mineral volume fraction decreases with increasing hierarchical level. Thus, the overall organic content increases with each additional hierarchical level and consequently the composite's strength and stiffness are reduced [113].

2.6.2 Fracture Behavior

The fracture toughness on several hierarchical levels has been investigated by nanoindentation, 3-point bending on macroscopic samples and bending experiments on micro-cantilevers which were fabricated via focused ion beam milling. Samples from level 1 and 2 of the hierarchical structure showed a brittle fracture behavior. Assessment of the first hierarchical level by bending notched cantilevers showed K_{IC} values of 0.44 to 0.91 MPam$^{0.5}$ which is in the range of values determined for synthetic HAP. Cantilevers consisting of several parallel rods (level 2) and decussating rods (which in this study was interpreted as level 3) had a fracture toughness of ~0.86 MPam$^{0.5}$ and ~0.42 MPam$^{0.5}$, respectively. However, the authors explained that level 3 could not be accurately represented as multiple Hunter-Schreger bands due to size constrictions for the FIB assisted preparation. On top of that, the weaker interfaces were oriented perpendicular to the direction of tensile stress which is more favorable for fracture [125]. Due to the large scatter on level 1, it is assumed that level 1 and 2 have a relatively similar fracture toughness that is < 1.0 MPa m$^{0.5}$ [113]. In contrast, Ang et al. determined the fracture toughness in enamel by measuring the crack openings after Vickers indentation. Mode I K_{I0} and mode III K_{III0} were both determined by applying the cohesive zone solution of the Dugdale–Muskhelishvili crack model and Irwin's 'near-field' solution. The values for K_{I0} and K_{III0} ranged between 0.52 and 1.62 MPam$^{0.5}$ and between 0.05 and 0.15 MPam$^{0.5}$, respectively.

Cracks were observed to propagate within the enamel rods but propagated preferably along the rod boundaries, thereby spanning level 1 and 2. Crack bridging and micro-cracking occurred on several length scales with bridge lengths from ~85 nm to ~3 µm and the microcracks from 100–500 nm up to ~6 µm [113,126].

3-point bending with notched bars made from bulk enamel showed quasi-ductile behavior. Even though cracks propagated through the sample, material bridging the cracks was present and keeping the sample together and transferring load. Fracture toughness (K_{IC}) values at the beginning of crack propagation were determined as 0.8 – 1.5 $MPam^{0.5}$ and are in the range of the first two hierarchical levels. With increasing crack length however, fracture toughness increased (rising R-curve behavior). Finally, a maximum fracture toughness of 4.4 $MPam^{0.5}$ was reached [112]. While a rise in fracture toughness was apparent irrespective of sample orientation (rods parallel or perpendicular to the applied load), crack growth from inner to outer enamel was less stable and the increase in fracture toughness was more pronounced than the other way around. This is owed to the microstructure, where decussating arrangement of enamel rods in the inner enamel hinder crack propagation, whereas cracks can propagate more easily in the parallel arrangement of enamel rods in outer enamel [91,127–129]. The ability of dental enamel to deform quasi-plastically without complete failure was also observed in compression experiments. Tests on macroscopic samples (level 4) showed microcracking but did not fracture completely [124]. Lower hierarchical levels (1 and 2) however, showed sudden and complete failure, so that it was not possible to observe damage progression. Here either fiber fracture or sliding of fiber bundles along the interfaces occurred, depending on the hierarchical level and the orientation in which samples were loaded [121,122].

Yahyazadehfar et al. observed a significant influence of the proteins on the fracture behavior of enamel. In samples that were treated with a KOH solution to remove proteins (validated by measuring the increase of proteins in solution), K_0 was reduced by 25% for cracks growing parallel to the HAP fibers. For cracks perpendicular to the fibers no significant difference was found. For both directions an increase in toughness with increasing crack length could be observed, but the increase was notably lower than for untreated enamel. They found that protein removal reduced the overall fracture toughness K_C of enamel by about 40% in both testing directions [49]. Similar results of a reduced fracture toughness in deproteinized enamel (treated with H_2O_2 containing bleaching agents and by O_2 plasma ashing, respectively) have been found in indentation studies by Elfallah et al. and Baldassari et al. [45,48]. In the latter study, it was

also found that the presence of water affected the toughness. If proteins were also present in the sample, wet samples had a higher toughness than dried. The opposite was true if the proteins were removed [48].

While the strength and stiffness are reduced with increasing hierarchical level, as has been discussed in the previous chapter (ch. 2.6.1), the main advantage of increased hierarchical structuring appears to be an increased damage tolerance. This could be seen from the transition from a brittle fracture in the lower hierarchical levels to inelastic deformation without catastrophic failure as demonstrated in the bulk material. Even though initiation fracture toughness stayed relatively constant across all hierarchical levels, crack propagation is hindered by mechanisms like microcracking, crack bridging and crack deviation. This results in an increasing fracture toughness with increasing crack length, as demonstrated by several researchers [112,127,128], which leads to the exceptional damage tolerance in a highly mineralized material.

2.6.3 Mechanical Gradient Outer to Inner Enamel

Due to the higher organic content in dentin, its mechanical behavior differs from the enamel layer. Several researchers have reported a decrease in hardness and elastic modulus from outer enamel to inner enamel [115–118]. This is accompanied by an increase in organic content [116] and a decrease in density [130] from outer to inner layers in enamel. In contrast, a study by Eimar et al. found no linear correlation between organic content and hardness in enamel. Instead they observed a correlation between hardness and crystallite size, i.e. hardness increases with increasing crystallite size. They found that hardness could be well predicted by the Hall-Patch model for polycrystalline materials. While hardness and organic content did not appear to be directly correlated, they saw some evidence that crystallite size was inversely correlated to relative organic content. As proteins have been shown to act as inhibitors for crystal growth, a higher protein concentration may lead to a smaller crystal size along both the a-axis and c-axis in fully mature teeth [131]. The increase in hardness from outer to inner enamel that was observed in the aforementioned studies may therefore result from an increase in crystallite size from inner to outer enamel. Recently it has been revealed that inside a rod, enamel's HAP crystallites are slightly misaligned with respect to each other and their c-axis is not necessarily parallel to the long axis of the rod. Surprisingly, the degree of misalignment between the crystallites was higher in outer enamel layers with parallel rod patterns. In inner enamel, with decussating rods however the crystallites c-axes where revealed to be more parallel to each

other. The degree of misalignment correlated positively with elastic modulus and hardness, i.e. the higher the degree of misalignment, the harder and stiffer the enamel. Additionally, simulations with molecular dynamics demonstrated that a slight misalignment between the c-axis of neighboring crystallites acts as a toughening mechanism [111,132]. This feature of the enamel structure could be another reason for the observed gradient in mechanical properties from outer to inner enamel. On top of that, one research group has reported collagen fibers reaching from the dentin into the enamel layer [42,43] which further increase the organic content and could lead to crack inhibition and reduced elastic modulus and hardness.

As has been described in chapter 2.6.2, the resistance to fracture increases from outer to inner enamel. Cracks in the outer enamel region could easily propagate through the enamel layer and were only arrested when reaching the inner enamel region. On the one hand this was attributed to the increased organic content in this region, on the other hand, the direction of enamel rods played a role. While in outer enamel rods are parallel to each other, decussating patterns dominate the inner enamel. Cracks will propagate preferably in the weaker interfaces between rods, which were orientated in the direction of crack propagation. Therefore, cracks could easily propagate until they reached the decussating patterns where cracks were diverted and arrested, leading to increased toughness. Additionally, crack branching and micro-cracking in front of the crack tip acted as crack arrest mechanisms. The role of orientation is further supported by experiments on the micro-scale, where fracture toughness micro-beams loaded perpendicular to the rod orientation was lower than in parallel orientation [15,113,133,134]. As a result of these gradient properties of dental enamel, special care must be taken when choosing the testing site in dental enamel, especially if the tested volume is small.

3. Research Objectives and Strategy

As described in the previous chapter, there are still some gaps in the knowledge of the structure-property relationship in dental enamel. In the past, researchers observed a higher fracture toughness, lower elastic modulus and hardness and an increased ability to creep in untreated dental enamel compared to deproteinized enamel leading to the widely accepted understanding, that these properties are due to the proteins contained in enamel. Organic layers between the crystallites (or rods) would allow more (visco)elastic and -plastic deformation, reducing the stress in the material, thus rendering the overall material more pliant, enable creep and increasing the fracture resistance. However, such protein layers have to date not been observed in mature enamel and recent TEM observations raise doubts towards this model. Specifically, there is a lack of knowledge on the geometry of the interfaces in mature dental enamel and a systematic analysis on the influence of the organic component on mechanical properties on several length scales is missing. Assuming the protein content influences the mechanical behavior, untreated and deproteinized dental enamel should behave differently during mechanical testing.

The main objectives of this work are therefore twofold:

1) provide an in-depth description of the interfaces in enamel
2) quantify the influence of the organic component on the mechanical properties by comparing untreated and deproteinized samples.

To this end, several deproteinization methods, as described in literature were carried out, namely chemical treatment with KOH solution, peroxide (H_2O_2) containing tooth bleaching agents and heat treatment (details on the methods see ch. 4.2). The removal of the proteins by these deproteinization methods was validated by TGA, FTIR and determination of amino acid concentration and TOC. In order to separate the influence of the proteins from the influence eventual changes in the crystal structure on the mechanical properties, a method that leaves the mineral phase unchanged while removing the organic was required. Thus, the morphology of the treated and untreated enamel and enamel crystallites were investigated by SEM and TEM. High resolution TEM was used to investigate the geometry of interfaces between enamel rods and enamel crystallites.

The elastic modulus and hardness as basic mechanical properties of untreated and treated enamel were determined by nanoindentation. Additionally, nanoindentation creep tests were carried out to determine the viscoelastic and -plastic properties. To decouple the influence of the proteins from the water that is contained in enamel, creep tests were both carried out on dry and wet samples.

4. Theoretical Basis & Experimental Set Up

In this chapter the theoretical basis for the characterization methods is briefly explained and the configuration and parameters of the experiments are described. Part of these descriptions have already been published in in *Acta Biomaterialia* with the title 'The geometrical structure of interfaces in dental enamel: A FIB-STEM investigation' [63] and *Materialia* with the title 'Effect of deproteinization treatments on the structure and mechanical properties of dental enamel' [135].

4.1 Sample Preparation

Bovine incisors were used due to their larger size, easier acquisition and less expected variation between specimen than in human samples, as the age, nutrition and living circumstances of the cattle are similar. Bovine teeth have been shown to be very similar to human in structure and composition [136–138]. The teeth were acquired at a local slaughterhouse (HF Fleisch, Hamburg, Germany), cleaned, the root cut off and the pulp removed. As a larger number of teeth became necessary, bovine teeth were sourced from a local supplier of tooth samples (Rocholl GmbH, Eschelbronn, Germany; officially registered with the veterinary authority for the preparation of bovine teeth DE08 2 25 0001 14). These teeth came already prepared (cleaned, root cut off and pulp removed). All teeth were stored in Hank's Balanced Salt Solution (HBSS, Invitrogen, USA) at 4°C until further preparation.

For nanoindentation creep experiments synthetic HAP samples were prepared as a reference. HAP samples were prepared by uniaxial pressing hydroxyapatite powder (Sigma-Aldrich Chemie GmbH, Taubingen, Germany) with 65 MPa for 10 s (one-sided) followed by a second densification step (two-sided) with 130 MPa for 30 s. Further densification was achieved by cold-isostatic pressing at 500 MPa for 2 min. The obtained green body was then sintered with the following parameters: heating with 4 K/min to 1100°C, 3 h isothermal sintering at 1100°C, cooling to room temperature with 4 K/min, all steps carried out in air atmosphere. The sintered HAP samples were cut into bars of similar size to the enamel samples with a saw (Mecatome T210, Presi GmbH, Hagen, Germany).

4.2 Deproteinization Treatments

Before treatment for deproteinization were applied, the teeth were cut into bars (~2 mm wide) using a saw with constant water irrigation (Buehler Isomet 4000, Buehler, Esslingen, Germany and Presi Mecatome T210, Presi GmbH, Hagen, Germany). Dentin was removed using a multifunction rotary tool with a grinding applicator (Dremel, Conrad Electronic, Hirschau, Germany) and grinding paper (SiC 500 grid) and its removal was controlled using an optical light microscope (Jenavert, Carl Zeiss Jena GmbH, Jena, Germany).

In the past two general methods to remove proteins from enamel samples have been used: heat treatment or a chemical treatment. Chemical treatment with potassium hydroxide (KOH), hydrogen peroxide (H_2O_2) or hydrazine (N_2H_4) has been established in the literature. In this work, KOH-treatment consisted of placing an enamel bar into a potassium hydroxide (KOH, 85%, Chemsolute, Th. Geyer, Renningen, Germany) solution of 0.004 mol/L for nine days, according to the protocol described by Yahyazadehfar and Arola [49]. Additionally, deproteinization with hydrogen peroxide (H_2O_2) containing tooth bleaching agent (Polaoffice+, SDI Germany, Cologne, Germany) was carried out by applying the agent according to the manufacturer's instructions. It has been shown by Elfallah et al. [45] that this treatment removes enamel proteins. Due to the high toxicity and environmental damage of hydrazine, it was not used as a deproteinization agent in this work. Deproteinization by heat treatment has been amply described in literature, but there is a large variation in the reported experimental parameters i.e. application times, temperatures and atmosphere. Therefore, heat treatments at various temperatures and holding times in nitrogen or synthetic air atmosphere have been carried out in this work. An overview of the applied deproteinization treatments in this work can be found in Table 2.

Table 2: Deproteinization treatments

Short name	Procedure	Literature
Heat Treatment	Heating the sample (enamel powder or enamel bars) to final temperature (200, 250, 300, 350, 400, 450 and 600°C) with 1°C/min ramp; holding period at final temperature for 15 min or 24h and cooling down to RT. Procedure carried out in either air or nitrogen atmosphere with a TGA device (TGA/DSC 1, Mettler Toledo, Gießen, Germany).	[19,21,25,26,47]
KOH-Treatment	Placing an enamel bar into a KOH solution of 0.004 mol/L (pH=11) for 9 days	[49]
H_2O_2-Treatment	Application of bleaching gel (35 w% H_2O_2) to dental enamel bars, removal after 8 min (according to supplier's instructions)	[45]

4.3 Electron Microscopy Techniques

Electron microscopy uses the interaction of a high energy electron beam with matter to produce an image. The electron beam is produced by applying large electric fields to a cathode material (typically tungsten or lanthanum hexaboride) so that the energy is high enough for electrons to be emitted. The emitted electrons are accelerated and focused to a beam that interacts with the sample [139]. Depending on sample morphology and electron beam energy, different types of electron microscopy can be distinguished.

4.3.1 SEM

Scanning Electron Microscopy (SEM) can be used to image bulk samples. There are two ways the electrons interact with the material. The incident electron beam can be 'reflected' (backscattered). However, the incoming electrons (primary electrons that are emitted by the electron source) can also interact with the atoms in the material and increase their energy. This leads energy release by emission of secondary electrons. These secondary electrons (SE) have a range of energies, which makes it harder to detect and focus them into an image. In scanning electron microscopes this problem is solved by focusing the incident beam into a small probe that scans a rectangular area, known as a raster, of the sample. SE from each point are collected and an image is formed. The depth of the interaction volume between primary electrons and

atoms of the sample depends on the energy of the primary electrons (hence accelerating voltage used) and the atomic number of the sample atoms, e.g. a 1 keV electron penetrates only about 50 nm into carbon and less than 10 nm into gold. It should be noted that as the SE travel through the sample, further inelastic scattering occurs. As a result, most SE are stopped within the interaction volume. SE that were created close to the surface, however, may escape the sample, especially if they are initially traveling toward the surface. This usually only occurs in a limited distance from the surface, called the escape depth, which is typically < 2 nm. As only the SE that escape the sample can be detected, the SE derived image is a property of the surface structure (topography) of the sample. On the other hand, due to elastic scattering with a small energy loss, backscattered electrons (BSE) escape from the sample surface with high energies, close to the primary-beam energy. As the fraction of primary electrons that escape as BSE increases with atomic number, BSE images can show contrast due to variations in chemical composition of a specimen [139].

In this work, a Zeiss Supra 55 VP (Carl Zeiss AG, Oberkochen, Germany) scanning electron microscope was used. The samples designated for electron microscopy were glued to a SEM sample holder using conductive silver and then ground with 1200 and 4000 grit SiC paper and further polished with 1 µm diamond suspensions (ATM GmbH, Mammelzen, Germany) for 1 min. Etching with hydrochloric acid (0.05 mol/L) for 10 s was carried out in order to increase the visibility of the rod boundaries in the SEM. To reduce charging effects the samples were then sputter-coated with a thin gold layer (a few nm).

4.3.2 FIB

Focused Ion Beam (FIB) systems are similar to SEMs, but ions instead of electrons, are emitted from the source and focused on the sample. In fact, often a set-up with both an ion-beam and electron-beam (dual-beam systems) are used. Due to their larger size, ions are much heavier than electrons and the interaction between them and the atoms in the sample can be used to remove material (milling). It is also possible to deposit material onto the sample surface by a targeted interaction between the ion beam and a pre-cursor gas, typically $C_9H_{16}Pt$, for a deposition of platinum. The spatial resolution of both processes is high and intricate structures can be fabricated. Depending on the interaction of atoms in the sample and the ions, however several artefacts, such as redeposition of atoms and amorphization, can occur, and FIB parameters have to be optimized [140]. Employing several steps with decreasing beam currents can reduce these artifacts and lead to a higher accuracy in the structures.

The samples for FIB were prepared as the SEM samples but polished with 1 µm, 0.25 µm and 0.05 µm diamond suspensions (ATM GmbH, Mammelzen, Germany) for 1 min, 2 min and 3 min respectively. Afterwards, the samples were etched with hydrochloric acid (0.05 mol/L) for 1 s to increase visibility of the enamel rod boundaries in order to set the FIB milling location correctly. This procedure differed from the SEM sample preparation procedure, as the sample surface needed to be more finely finished in order to achieve a good TEM sample. Etching time was minimized to just be able to recognize the rod boundaries and minimize the damage to the surface due to the etching. Finally, both the SEM and FIB the samples, were vacuum-dried and sputter-coated with a thin gold layer (a few nm). In this work a dual-beam FIB-SEM system (FEI Helios NanoLab G3, FEI Deutschland GmbH, Frankfurt/ Main, Germany) with a Ga ion source was used to fabricate thin lamellae for TEM investigation. The sample was oriented in a way that the enamel rods would be cut perpendicular to the lamella (see Supplementary Information B.1). For more information on FIB assisted sample preparation the reader is referred to [141]. In this work, lamellae cut from three regions of enamel (innermost, inner and outer enamel) were investigated. In total seven lamellae from the untreated and four lamellae from the KOH-treated enamel were investigated. The sample preparation procedure was similar to the one employed by Xie et al. [88]. After the deposition of a Pt protection layer to prevent damage to the underlying structure, two trenches were milled with a current of 21 nA followed by cleaning steps with currents of 0.79 nA and 0.43 nA to remove milling artifacts and to guarantee a smooth surface. Then the lamella was cut free on two sides, attached to the nanomanipulator and completely cut free. With the help of the nanomanipulator, the lamella was attached onto the copper lift-out grid. Subsequently several thinning steps with currents of 0.79 nA, 0.23 nA, 80 pA and finally 40 pA followed to achieve electron transparency (thickness of ~100 nm).

4.3.3 TEM

Transmission Electron Microscopy (TEM) uses electrons that are transmitted through a sample. As electrons can only penetrate small depths into solids, sample for TEM need to have a small thickness (~100 nm or smaller). To achieve these small thicknesses often particles are dispersed onto a carbon grid, but with the emergence of FIB technology thin lamellae can be fabricated directly from bulk samples as described in chapter 4.3.2. TEM can also be used to scan a sample area (STEM), similar to the principle of SEM. When the emitted electrons are transmitted through the sample they are scattered, which results in many variants and processes that need to be taken into account when interpreting TEM images [139,142]. To explain all the intricacies

of TEM imaging is beyond the scope of this work, but the main effects will be briefly mentioned. For more information, the reader is referred to the extensive literature on this topic, e.g. [139,142].

Incoming electrons can be elastically scattered, with little to no energy loss or inelastically scattered, where the transmitted electron loses some of its energy. Electrons can be scattered by the nucleus of the atoms in the sample, or even by the atomic electrons if they pass closely. The elastic scattering is highly dependent on the atomic number of the atoms in the sample (Z-contrast). However, thicker regions of the sample also scatter a higher fraction of the incident electrons, so that the corresponding regions in the image appear dark, giving rise to thickness contrast in the image. Together, these two effects are often described as mass-thickness contrast. In crystalline materials, elastic scattering leads to diffraction. Due to the regular spacing of the atomic nuclei, scattering of incoming electrons creates constructive and destructive interference patterns. Or expressed differently, electrons are not scattered in a continuous angular distribution but in preferred orientations. These diffraction patterns can be used to investigate the crystal structure of a material or even the lattice parameters of a single crystal [139,142]. It is important to note that electrons are a type of ionizing radiation, which can damage the sample severely, particularly if the sample consists of polymers and some ceramics. This poses a limit to the application of the TEM, particularly at high voltages [142].

In this work, the acquisition of the STEM and TEM pictures was carried out with a FEI Talos F200X (FEI Deutschland GmbH, Frankfurt/ Main, Germany). The lamellae were fabricated with FIB as described in the previous chapter. For imaging an accelerating voltage of 200 kV and a current of 50 pA for STEM and 10 nA for TEM was used. All STEM images were recorded with a high-angle annular dark-field (HAADF) detector. This imaging technique collects elastically and inelastically scattered electrons. As elastic scattering gives a Z-contrast, the image contains information about the distribution of light (often organic) and heavy elements in the sample. In addition, Bragg scattered electrons are detected by the HAADF detector (diffraction contrast). The intensity of the signal depends on the number of electrons detected, which is dependent on the orientation of the crystal planes to the incident electron beam [143]. For the TEM, bright field images were recorded.

4.4 Compositional Analyses

Several analyses have been used to determine the composition of dental enamel and will be described in the following chapter.

4.4.1 Thermogravimetric Analysis

Thermogravimetric analysis (TGA) measures the mass loss of a sample during an applied temperature program. To determine the organic content, untreated and chemically treated enamel bars (dentin was removed) were ground with mortar and pestle until a fine powder was obtained. The powdered samples were heated to a temperature of 900°C with a ramp of 1 K/min in nitrogen atmosphere in a TGA/DSC 1 device (Mettler-Toledo GmbH, Gießen, Germany) and mass loss was measured. An isothermal period of 30 min in air atmosphere followed to clean the system, which was not considered in the analyses of the mass loss.

Measurements to determine water content were carried out with enamel bars (dentin was removed). Treated and untreated enamel bars were either stored in air (ambient conditions) or distilled water for ≥ 24h, before the TGA measurement. Samples stored at ambient conditions underwent an additional drying treatment for 60 min in a desiccator with applied vacuum directly before TGA measurement. Wet samples were taken out of the water directly before the TGA measurement and briefly dabbed dry with a tissue to remove surface water. TGA was carried out with a STA 449 F5 Jupiter TGA device (NETZSCH Holding, Selb, Germany), by heating the samples from 25 to 200°C (1 K/min), followed by a 15 min isothermal segment under N_2-atmosphere.

All TGA curves were smoothed (FFT filter with 100 points window and cutoff frequency of 0.3) and derived. A peak fitting was carried out and the areas of the peaks were used to calculate the mass loss in different temperature ranges.

4.4.2 Elemental Analyses

The determination of total organic carbon (TOC) by NCHS elemental analysis [144] and amino acid content by high-performance liquid chromatography with fluorescence detection (HPLC-FLD) after derivatization [145] were carried out by the central lab for chemical analysis at the Hamburg University of Technology. NCHS elemental analysis is based on combustion analysis. A powdered sample is heated and weight changes are detected. The combustion products are separated and quantified with the aid of an internal thermal conductivity detector. By dissolving

the inorganic carbon with hydrochloric acid, the amount of organic carbon in the sample can be determined [144]. The amino acid content is determined by dissolving the free amino acids from the sample. To separate the single amino acids bound in proteins and peptides, a first step of hydrolysis using hydrochloric acid is carried out. Analysis of the amino acids is carried out with reversed-phase chromatography after precolumn derivatization with OPA (o-phthalaldehyde) in the presence of borate buffer and injection solution. Proline and hydroxyproline do not react with OPA and can instead be derivatized with FMOC (fluorenylmethyloxycarbonyl chloride). After separation, the sample is measured with the fluorescence detector (FLD) [145].

The analyses were carried out for untreated, chemically treated and heat-treated enamel. Because of the labor-intensive sample preparation due to the needed high sample mass (>120 mg for NCHS analysis and >50mg for HPLC, resulting in ca. 16 h preparation time for one sample for TOC determination and 8 h for one sample for amino acid analysis), only samples treated at selected temperatures (200°C, 250°C, 300°C and 900°C) were prepared (n=3). The 900°C sample was selected to control the effectiveness of heat treatment in general, as it was expected that after treatment at such high temperatures all organic matter should be removed from the enamel sample. The lower temperatures were selected, as here the mass change observed in TGA was the greatest. For all samples, dentin was removed, the sample was ground to a fine powder by mortar and pestle and heat treatment was carried out in a tube furnace in air atmosphere (1 K/min ramp, 15 min isothermal hold at max. temperature; same as the TGA procedure).

4.4.3 Infrared Spectroscopy

Infrared (IR) or Fourier transform infrared (FTIR) spectroscopy can be used to analyze the composition of matter by probing the molecular vibrations. Functional groups have fundamental vibrations and thus can be associated with specific infrared absorption bands. When a sample is irradiated with IR-radiation several vibration modes can occur. A mode of vibration is considered infrared active if it absorbs the infrared light, which occurs if there is a change in the dipole moment of the molecule during the vibration. When a molecule is symmetric, all vibrations that are symmetric with respect to the center of symmetry are not infrared active and therefore cannot be detected in IR. In contrast, the asymmetric vibrations of all molecules are detected which allows probing the properties of almost all chemical groups in one sample. Groups with permanent dipoles have a strong IR absorption and such the carbonyl

groups of the polypeptide backbone in proteins contribute largely to their infrared absorption spectra. In the mid-infrared region (4,000–1,000 cm^{-1}), two main types of vibrations are observed: vibrations along chemical bonds, called stretching vibrations, which involve bond-length changes; and vibrations involving changes in bond angles, and notably bending vibrations [146].

To conduct FTIR analyses, bars of dental enamel were cut, dentin was removed mechanically, and some bars underwent chemical deproteinization treatment. Afterwards the bars were ground to a fine powder by mortar and pestle. In contrast, the heat-treated enamel samples were ground into a powder before undergoing heat treatment. The such obtained powders were mixed with KBr (Carl Roth GmbH + Co. KG, Karlsruhe, Germany) such that a concentration of 1 w% of the sample was reached, desiccated and pressed into pellets. During pressing (1 min at 237 MPa and 5 min at 1657 MPa) a vacuum was applied to prevent water absorption. FTIR was carried out with a Tensor II system (Bruker Optik GmbH, Ettlingen Germany) in transmission mode (MIR range 400-4000 cm^{-1} with 2 cm^{-1} resolution).

4.5 Nanoindentation

Nanoindentation uses a tip with a known geometry and high stiffness to make an imprint into the surface of the testing material. In this work the commonly used nomenclature and associated indices as used by Oliver and Pharr and Fischer-Cripps will be employed [147,148].

The contact mechanics of a loading situation as given in nanoindentation are based on Hertz' theory for elastic contact between a flat surface and a rigid sphere (equation (8)). The radius of the circle of contact a (see also Figure 5 and Figure 6) depends on the indenter radius R, the indentation load P and the elastic properties of the contact. The latter combines the elastic modulus of indenter and the surface and is referred to as reduced elastic modulus E_r [148]. E_r is given by the elastic moduli of the respective bodies E_1 and E_2 and their Poisson's ratios ν_1 and ν_1 (equation (9)) [147,149].

$$a^3 = \frac{3}{4}\frac{PR}{E_r} \tag{8}$$

$$\frac{1}{E_r} = \frac{(1-\nu_1^2)}{E_1} + \frac{(1-\nu_2^2)}{E_2} \tag{9}$$

The stiffness *S* for an elastic contact (contact stiffness) is described by the derivative of the contact force *P* with respect to indentation depth *h* (10). For the contact of a rigid indenter and a flat surface E_r can be expressed dependent on the projected area of contact A_c, which is related to *a*, and S (11) [148].

$$S = \frac{dP}{dh} \tag{10}$$

$$E_r = \left(\frac{\sqrt{\pi}}{2}\right)\left(\frac{S}{\sqrt{A_c}}\right) \tag{11}$$

It has been shown that the Hertz' theory (8) and the related equations (9)-(11) also hold for other shapes, like cones or pyramids, on a flat surface. Thus, Oliver and Pharr developed a standard procedure for nanoindentation with conical indenters where *S* and A_c are determined in order to calculate E_r. They noted that, instead of approximating the contact stiffness in the initial unload by a linear function, a fit with a power law is more accurate (more details in Supplementary Information A.3) [147]. With the known quantities E_2 and υ_2 for the indenter tip ($E_2 = 1140\ GPa$ and $\upsilon_2 = 0.07$ for diamond tips) the elastic modulus of the sample E_1 can be calculated, if its Poisson's ratio is known (9) [149]. The projected area of contact can be obtained from the known tip geometry and the contact depth h_c (Figure 5). For any pyramidical indenter A_c is given by:

$$A_c = 3\sqrt{3}h_c^2 \cdot \tan^2\theta \tag{12}$$

[148]. The contact depth is dependent on, but not equal to, the measured indentation depth *h*. When indenting a surface deformation at the edge of the contact will occur. In order to obtain the correct contact depth, the distance from the edge of contact to the specimen surface at full load h_a needs to be considered.

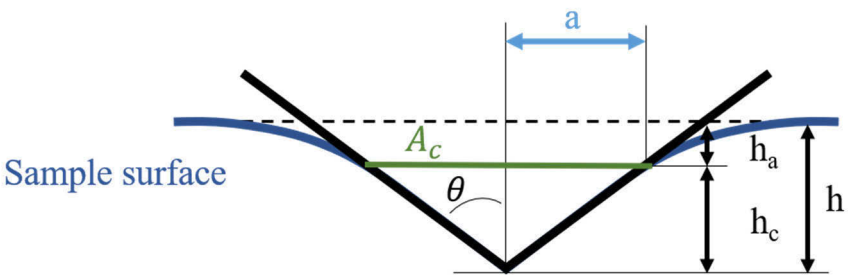

Figure 5: Contact of a conical indenter into a sample surface. The contact radius a of the projected contact area A_c can be determined from the contact depth h_c which is dependent on, but not equal to, the measured indentation depth h. h_a describes the distance from the edge of contact to the specimen surface at full load. Adapted with permission from [148].

From the projected area of contact A_c and the load P, the so-called nano-hardness or indentation hardness H_I can be calculated (13) and is equal to the mean contact pressure.

$$H_I = \frac{P}{A_c} \tag{13}$$

4.5.1 Berkovich Indenter

A Berkovich indenter is a three-sided pyramid with the contact angle $\theta = 65.27°$. For a perfect Berkovich tip the contact area function (12) is thus given as $A_c \approx 24.5\, h_c^2$. As the tip gets blunted with use, Oliver and Pharr found a that A_c is best approximated by:

$$A_c = 24.5\, h_c^2 + C_1 h_c^1 + C_2 h_c^{1/2} + C_3 h_c^{1/4} + \cdots + C_8 h_c^{1/128} \tag{14}$$

where C_i are constants [147]. To obtain this function the tip is calibrated with a material of which properties are known, (typically fused silica). The tip area function is then saved to the nanoindenter system and used to calculate the sample properties elastic modulus and hardness in situ.

4.5.2 Spherical Indenter

Spherical indenter tips are better described as sphero-conical, meaning there is an indentation depth, h_{sphere}, above which the shape of the tip is described as a cone. Below this depth, the

tip can be described as a sphere with radius R (Figure 6). The projected area of contact for a spherical tip can be calculated as:

$$A_c = \pi a^2 = \pi(2Rh_c - h_c^2) \quad (15)$$

Thus, the radius of the spherical tip needs to be known precisely to analyze indentation data from a spherical tip. The radius is measured from light microscopy images by the manufacturer but can also be determined by a series of indentations on a material with known elastic modulus to account for deviations from a perfect sphere. If the contact is purely elastic, the Hertz equation can be rewritten as:

$$P = \frac{4}{3} E_r R^{1/2} h^{3/2} \quad (16)$$

with the displacement $h = h_e$. This relationship can be used to fit the recorded load displacement curves in order to obtain the radius of the spherical tip [148].

From Figure 6 it can be seen that for an elastic-plastic contact the total indentation depth h is the sum of the contact depth h_c and the distance to the projected area of contact h_a. From the Hertz equations it has been found that h_a is half the elastic displacement h_e. Therefore, for a purely elastic contact at full load the following equations hold true, where h_{max} is the indentation depth at full load:

$$h_a = h_c = h_{max}/2 \quad (17)$$

$$h_{max} = h_c + h_a \quad (18)$$

$$h_c = h_{max} - \frac{h_e}{2} \quad (19)$$

[148].

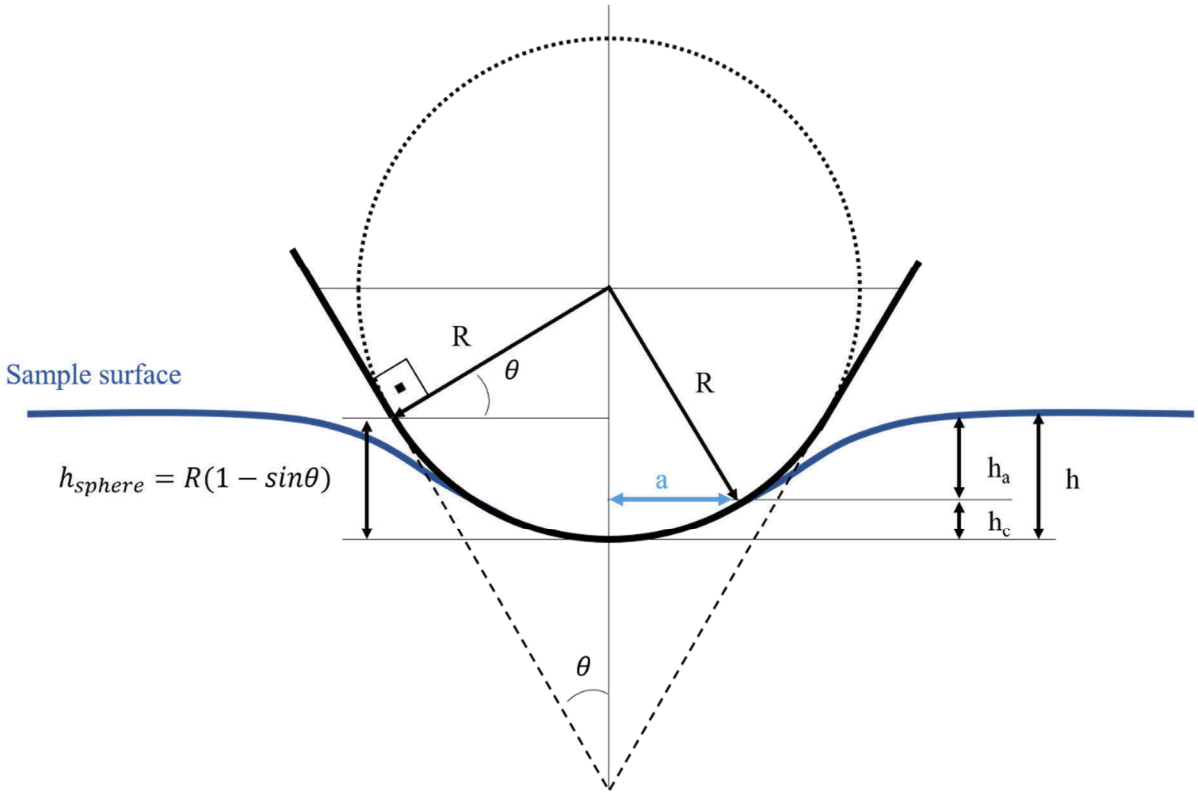

Figure 6: Displacement of a sphero-conical indenter into a sample surface. Until a depth h_{sphere} is reached, the indenter can be described as a sphere with radius R. Afterwards, the indenter is equivalent to a conical indenter with angle θ. The contact radius a can be determined from the contact depth h_c which is dependent on, but not equal to, the measured indentation depth h. h_a describes the distance from the edge of contact to the specimen surface at full load. Adapted with permission from [148].

4.5.3 Elastic Plastic Transition

During indentation with large loads or sharp tips the stresses underneath the tip are usually high so that not only elastic but also plastic deformation in the sample occurs. This leaves a residual impression in the sample surface (compare Figure 7). When analyzing nanoindentation data, this deformation must be accounted for. In the following, calculations will be presented for a spherical tip but can be analogously carried out for other tip shapes.

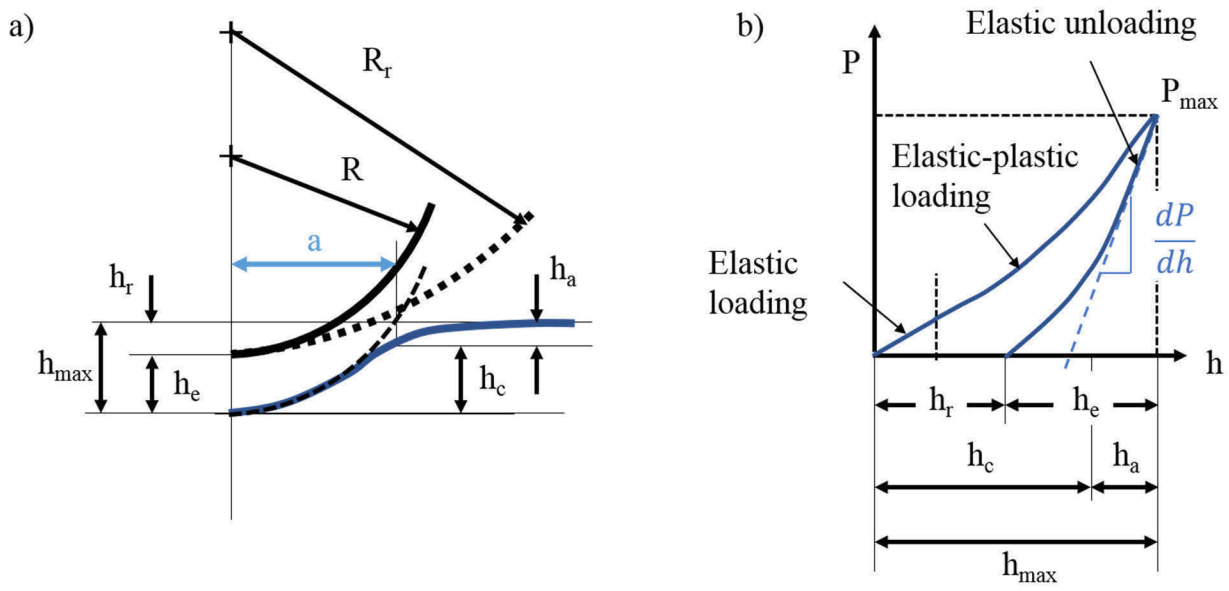

Figure 7: a) Loading of a preformed impression with radius R_r with a rigid indenter of radius R. b) Load displacement curve for an elastic-plastic behavior. After an initial purely elastic loading in the beginning an elastic-plastic loading follows. Unloading occurs elastically. After unloading completely, a residual impression with depth h_r remains. Adapted with permission from [148].

When loading a surface with a spherical indenter, initially elastic deformation occurs followed by plastic-elastic behavior at higher loads. At full load P_{max} the indentation depth is h_{max}. When removing the load, the sample behavior is considered elastic under the assumption that no reverse plasticity occurs. A residual impression with depth h_r remains. When reloading the sample with P_{max} the reloading is elastic through a distance $h_e = h_{max} - h_r$ and the Hertz equation (16) is rewritten as:

$$P = \frac{4}{3} E_r R^{1/2} h_e^{3/2} \tag{20}$$

The contact depth h_c can be determined from the relationship between h_{max} and h_a (equations (18) and (19)) and is needed to determine the hardness of the sample. The elastic depth can be found by the multiple-point unloading or single-point unload method. The first method loads and fully unloads the sample at multiple points to determine the contact stiffness $S = \frac{dP}{dh}$ from the initial slope of the unloading and determine h_e from rearranging

$$P = \frac{2}{3}\frac{dP}{dh}h_e \tag{21}$$

[148]. The single-point unload method applies the Hertz equations directly to the unloading and is also known as the 'Field and Swain method' [150]. Here, the sample is partially unloaded to a lower load P_s (and respectively depth h_s) and h_r can be calculated by forming the ratio of both loads (22).

$$\frac{h_{max} - h_r}{h_s - h_r} = \left(\frac{P_{max}}{P_s}\right)^{2/3} \tag{22}$$

h_c can be calculated by

$$h_c = h_{max} - \frac{h_e}{2} = h_{max} - \frac{h_{max} - h_r}{2} = \frac{h_{max} + h_r}{2} \tag{23}$$

[148].

4.5.4 CSM

The continuous stiffness measurement (CSM) imposes a small, sinusoidal signal on the DC signal driving the indenter movement. By analyzing the system's response with means of a frequency specific amplifier the contact stiffness can be obtained. Instead of only one value of stiffness at the unloading, with this method, the contact stiffness at any point along the loading curve can be measured. Thus, the mechanical properties of a sample can be measured depending on the indentation depth and changes, as for example in multi-layered materials, can be identified [151].

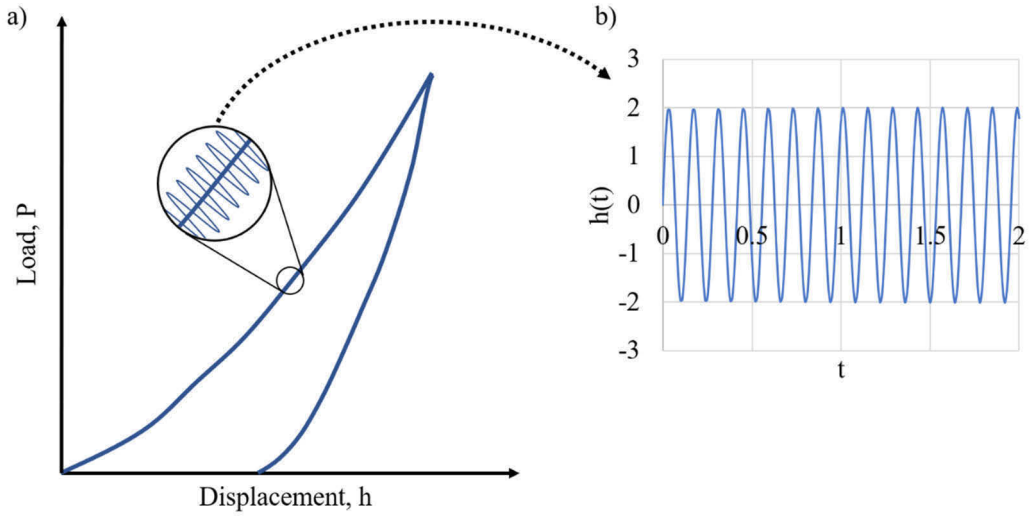

Figure 8: Load displacement curve for CSM (a) where a sinusoidal signal $h(t) = h_{amp} \cdot sin(\omega t)$ *(Exemplary signal shown in b) is superimposed onto the loading. Adapted with permission from [151].*

The CSM method can also be used to correct indentation data, as the contact stiffness is less sensitive to thermal drift. By applying the CSM to a hold segment used to measure creep, the corrected indentation depth can be calculated. Using equation (11), the contact area can be expressed as a function of E_r, S and a correction factor $\beta = 1.034$ for a Berkovich indenter (equation (24)). Solving (14) with the known contact area to find h_c results in the corrected contact depth, which can be used to find the corrected indentation depth [152].

$$A_c = \frac{\pi}{4\beta^2}\frac{S^2}{E_r^2} \tag{24}$$

4.5.5 Experiments

For the determination of the elastic modulus and hardness, the samples as prepared for SEM were used. Nanoindentation was carried out with a G200 nanoindenter (formerly Agilent, now KLA Tencor, CA, USA), employing a Berkovich tip (Synton MDP, Port, Switzerland) and a CSM (frequency of 45 Hz and 2 nm amplitude). An indent depth of 2000 nm was set as maximum indentation depth and the mean values were calculated from 800-1800 nm indentation depth. For each sample a set of 36 indents was performed and to minimize the influence of the indent location, care was taken to select areas with similarly oriented enamel rods.

4.6 Creep behavior

If a deformation in a time-dependent manner occurs, that behavior is referred to as creep. In ceramic materials this usually only occurs at high temperatures. In a polycrystalline material inelastic deformation occurs either at the grain boundaries or within the grains. The latter refers to lattice effects like motion of dislocations or diffusion of vacancies (Nabarro Herring creep). The grain boundary effects can be:

- Viscous flow of an amorphous grain boundary phase,
- Diffusion of vacancies along grain boundaries (Coble creep),
- Formation and extension of cavities at grain boundaries, especially at triple points,
- Dissolution and reprecipitation of material through the glassy phase.

Creep is defined as a change in strain ε within the time t of a volume element and the creep rate is given as the derivative of strain with respect to time t (49).

$$\dot{\varepsilon_c} = \frac{d\varepsilon_c}{dt} \tag{25}$$

Creep can be separated into three stages: primary, secondary and tertiary creep or stage (Figure 9). During the secondary stage the creep rate is constant. To simplify numerical analysis, it is common practice to let the secondary creep start directly after load application. The strain is hence given as:

$$\varepsilon_c = \varepsilon_I + \varepsilon_{II} \tag{26}$$

[153].

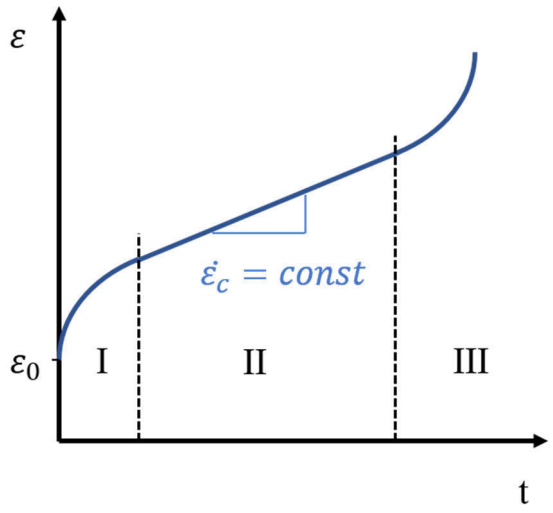

Figure 9: Typical shape of a creep curve. Adapted with permission from [153].

4.6.1 Creep Measurements with Nanoindentation

Nanoindentation can be used to determine the viscoelastic properties of a material and usually an approach to model data with spring and dashpot models is sufficient to obtain meaningful data for a wide range of materials [148]. For materials that exhibit a nonlinear mechanical response the stress depends on the strain rate $\dot{\varepsilon}$, the strain (or creep) rate sensitivity (SRS) m_s and a factor K_m (27). Both parameters m_s and K_m are material constants [154].

$$\sigma = K_m \dot{\varepsilon}^{m_s} \tag{27}$$

For a Berkovich indenter a constant effective strain value can be given as $\varepsilon_r \approx 0.2\ tan\theta$. Thus, the strain rate can be calculated from the relationship between contact depth and time by dividing the displacement velocity by the plastic depth of penetration (28) [154].

$$\dot{\varepsilon} = \frac{\dot{h_c}}{h_c} \tag{28}$$

With $\dot{h_c} = dh_c/dt$.

Spherical tips cause a non-self-similar stress field and therefore the representative strain increases with indentation depth [155]. For a spherical tip the strain rate can be calculated with the change in area function over time as:

$$\dot{\varepsilon} = \frac{1}{\sqrt{A_c}} \frac{d\sqrt{A_c}}{dt} \tag{29}$$

[156].

The function that describes the time-dependent indentation depth is typically based on spring and dashpot models. As the yield response of a material is mainly due to shear and usually the mechanical constants are expressed in terms of the bulk modulus *K* and the shear modulus *G*. In order to transform them into an elastic modulus *E* with the Poisson's ratio ν, for an isotropic material holds:

$$K = \frac{E}{3(1-2\nu)} \tag{30}$$

$$G = \frac{E}{2(1+\nu)} \tag{31}$$

The elastic response of such spring and dashpot models is quantified by the elastic storage modulus and the fluid-like response by the loss modulus. Usually, the storage modulus is associated with the shear modulus *G* of the material. As the nature of loading during an indentation test is a complex mixture of hydrostatic compression, tension, and shear the storage modulus is likely due to all types of materials response. Therefore, for the sake of simplicity, it is assumed that the bulk of elastic response can be described by the conventional elastic modulus and the fluid-like response can be described by the dynamic viscosity. In practice however, viscosity is frequency and temperature dependent and cannot be described by a single value [148].

It has been found that the indentation depth can be described by the parameters of spring and dashpot models (Figure 10) for a constant load P_0. For a spherical indenter and a three element Voigt model the relationship between the indentation depth and time is the following:

$$h^{3/2}(t) = \frac{3}{4} \frac{P_0}{\sqrt{R}} \left[\frac{1}{c_1} + \frac{1}{c_2} \left(1 - e^{-t\frac{c_1}{\eta}} \right) \right] \tag{32}$$

With the term in square brackets describing the time response of the spring and dashpot model with constants c_i and η. $1/c_1$ thereby describes the initial elastic response to a step load,

whereas the second term describes the delayed response. The displacement increases to a maximum value as $t \rightarrow \infty$. For a conical indenter a similar relationship can be found by:

$$h^2(t) = \frac{\pi}{2} P_0 cot\theta \left[\frac{1}{c_1} + \frac{1}{c_2}\left(1 - e^{-t\frac{c_1}{\eta}}\right)\right] \tag{33}$$

Similarly, equations describing the h-t relationship can be found for different combinations of springs and dashpots, e.g. the Maxwell model. Although the above equations are for a step load, analysis of an arbitrary load history can be done with methods of superposition [148].

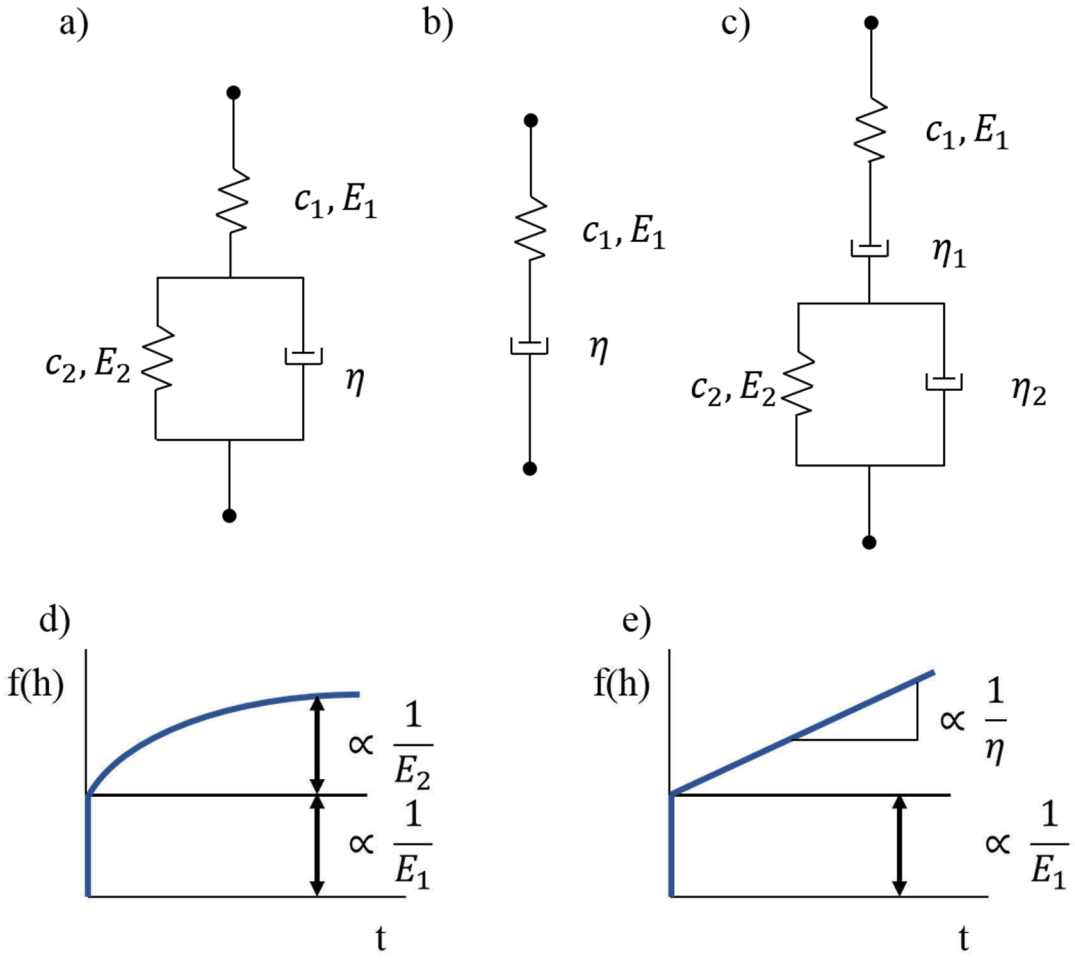

Figure 10: The behavior of the indentation depth over time can be described by spring and dashpot models. This can be a combination of a spring and dashpot in parallel or serial arrangements. a) shows a spring in series with a Kelvin-Vogt model, b) the Maxwell model and c) a combination of both. Arbitrary combinations of the elements are possible. The displacement response can take the shape of d) for a step increase in a spring in series with a Kelvin-Vogt model or e) in a Maxwell model. $f(h) = h^2$ *for a conical and* $f(h) = h^{3/2}$ *for a spherical indenter. Adapted from [148].*

The analytical models describe the response of the material to a step load. Experimentally, a step load cannot be realized, and the accuracy of the results depends on the speed of the applied load and the materials response to it. In elastic-plastic materials plastic deformation can occur rapidly and the initial step response in displacement may be greater than is expected, especially when a sharp indenter is used. Thus, the elastic modulus of the material can be underestimated, and it is likely that the viscous component is associated with viscoplasticity. Using a blunt indenter, such as a spherical indenter is more appropriate to measure the viscoelastic response of a material. To account for the time that is needed to apply the load on the sample, a dimensionless ramp correction factor *RCF*, depending on the time constant of the material τ_i and ramp rise time t_R can be included. This factor is then applied by multiplying every exponential decay term in the creep function with *RCF*.

$$RCF = \frac{\tau_i}{t_R}\left(e^{t_R/\tau_i} - 1\right) \tag{34}$$

The ramp time must be less than one-tenth the dominant material time constant to avoid numerical errors associated with the use of a finite experimental ramp [148].

The elastic modulus of the material can be obtained from conventional analysis of the unloading in creep experiments under the condition that the hold period is long enough so that the creep rate has decayed below a value where the depth increase in 1 min is less than 1% of the indentation depth. Otherwise the obtained modulus is not reliable [148].

4.6.2 Constant Load Hold

During the constant load hold (CLH) protocol a five-step loading protocol (Figure 11) is employed. To avoid creep during the loading period, the load is applied quickly, in an almost stepwise manner and then held constant for an extended time period. The load is then reduced to 95-98% and held constant at that level for another extended time period, before the load is removed completely. The second time period of constant load is used to determine the back-creep behavior of the sample (Figure 11). As the load is held constant during the hold period(s) the indentation depth and plastic zone only vary slightly with time. Inside the sample mainly relaxation occurs and the tip sinks slightly further into the sample. Therefore, indentation hardness and mean contact pressure will decrease until further displacement into the surface can no longer be detected. This means that the material is in a transient condition and no steady state can be reached [157].

During a nanoindentation test the displacement of the tip is recorded constantly. However, due to thermal fluctuations the recorded indentation depth h_I is the sum of the actual indentation depth h and the thermal drift h_d (equation (35)). Especially in the CLH tests, this can lead to large deviations between the recorded indentation depth $h(t)$ and the true indentation depth $h_I(t)$.

$$h_I = h + h_d \tag{35}$$

Therefore, a correction of the data needs to be undertaken. If the test employs the CSM method this can be done via the stiffness S that is recorded by the system, as this parameter is more robust against thermal drift than the displacement [152].

4.6.3 Methods used in this work

In this work, several methods based on a single load-unload protocol according to He and Swain [154] were used. Method 1 (Figure 11) was a five-step CLH method as employed by He and Swain [154]. This method contained the following steps: the sample was loaded to 250 mN in $t_1 - t_0 = 25\ s$, the load was then held constant for $t_2 - t_1 = 900\ s$ and the displacement was recorded. The load was then reduced to 5 mN (98% of the maximum load) in $t_3 - t_2 = 25\ s$ and again held constant for $t_4 - t_3 = 900\ s$ to measure the backcreep (recovery), before the tip was completely removed from the surface. For the whole loading protocol, the displacement was measured as a function of time. The 'load hold' at 250 mN is used to measure the creep whereas the 'load hold' at 5 mN is used to measure the backcreep.

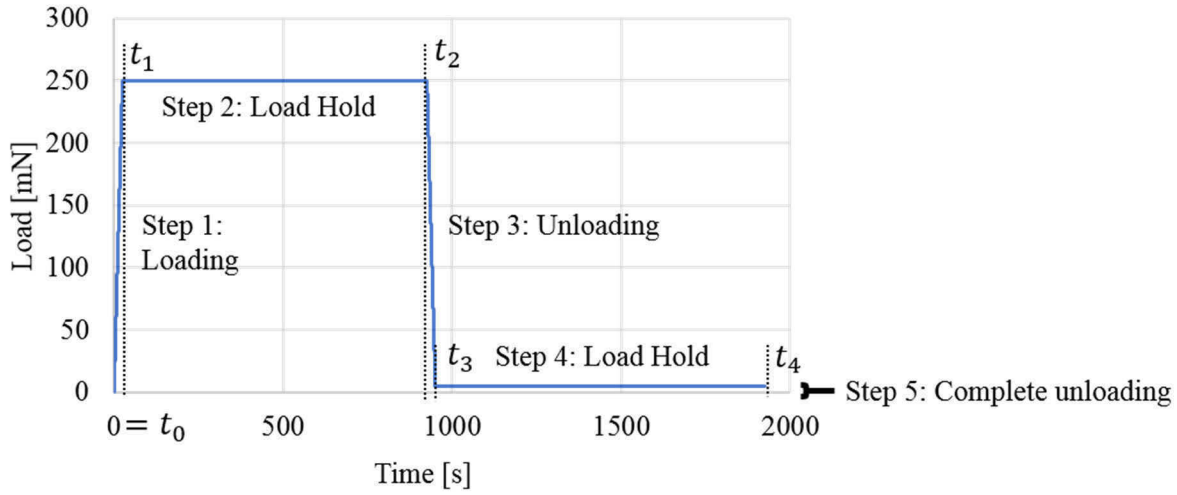

Figure 11: Method 1 consisting of a five-step CLH method after He and Swain [154]

To account for thermal drift and to achieve a good contact between indenter and surface, in later experiments an additional hold segment at low load was implemented before loading to the maximum load for the creep segment. Furthermore, due to large amount of damage, e.g. cracking, in the sample when a Berkovich tip and high maximum loads (e.g. 250 mN as in method 1) were used, tests based on the CLH method were carried out with cono-spherical diamond indenter tips (Synton MDP) with nominal radii of 5 µm and 50 µm and the with comparatively low loads (max. 5 mN for the 5 µm tip and 150 mN for the 50 µm tip). Similarly, trials with a Berkovich tip and a CSM based method to perform a drift correction based on the continuous stiffness measurement, as proposed by Maier at al. [152], could not be employed due to cracking on the enamel surface.

The adapted CLH loading regime, method 2, can be seen in Figure 12. It consists of a loading ramp from t_0 to t_1, with a subsequent hold segment with a load of 1 mN for $t_2 - t_1 = 50\ s$. This is followed by another loading ramp (t_2 to t_3) until the maximum load is reached. The maximum load of 5 mN or 150 mN is then held for $t_4 - t_3 = 900\ s$ (2nd hold segment). Afterwards the sample was unloaded (t_4 to t_5) to 98% of the maximum load (= the minimum load; 0.1 mN or 3 mN) and this load was again held for 900 s (t_5 to t_6). Afterwards the tip is completely removed from the sample surface ($t_7 - t_6$) The time to load to maximum load ($t_3 - (t_2 - t_1)$) and unload ($t_7 - t_4 - (t_6 - t_5)$) was set to 10 s for a maximum load of 5 mN and 25 s for a maximum load of 150 mN, resulting in constant load rates of 0.5 and 6 mN/s, respectively.

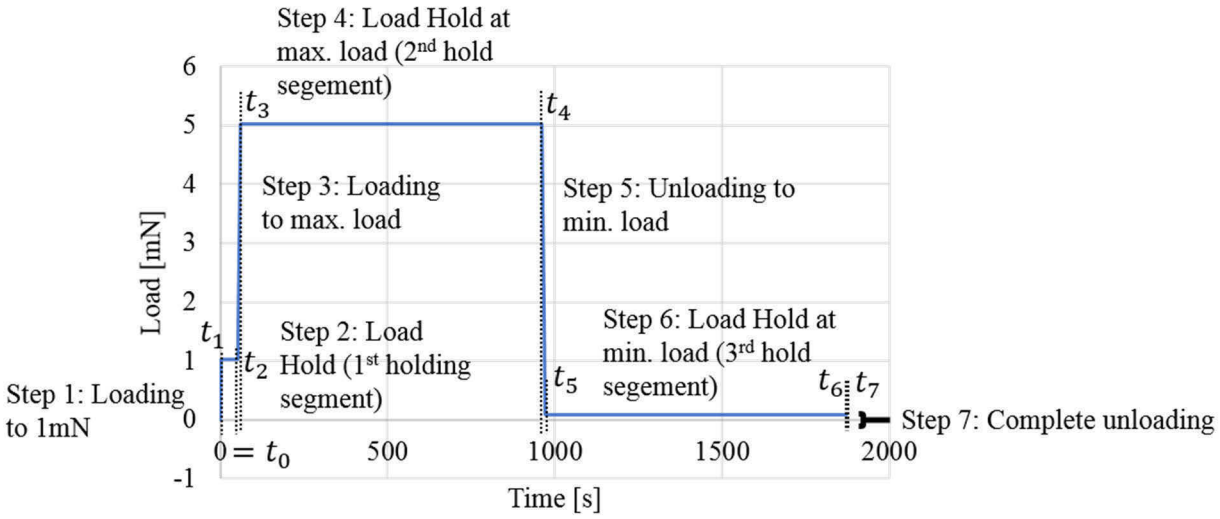

Figure 12: Method 2, adapted CLH method with 3 load hold segments

The five step CLH method as described by He and Swain was again adapted to conduct experiments with varied load rates (method 3, Figure 13). The sample was loaded (t_0 to t_1) with a constant load rate of 0.05, 0.5, 1.5, 5 or 10 mN/s to a maximum load of 5 mN which was held constant for $t_2 - t_1 = 100\ s$. The sample was then unloaded to 90% of the maximum load at an unload rate equal to the load rate (t_2 to t_3). The load was held constant for $t_4 - t_3 = 75\ s$ for the determination of the drift (including a settling time of 25 s), before the sample was unloaded completely.

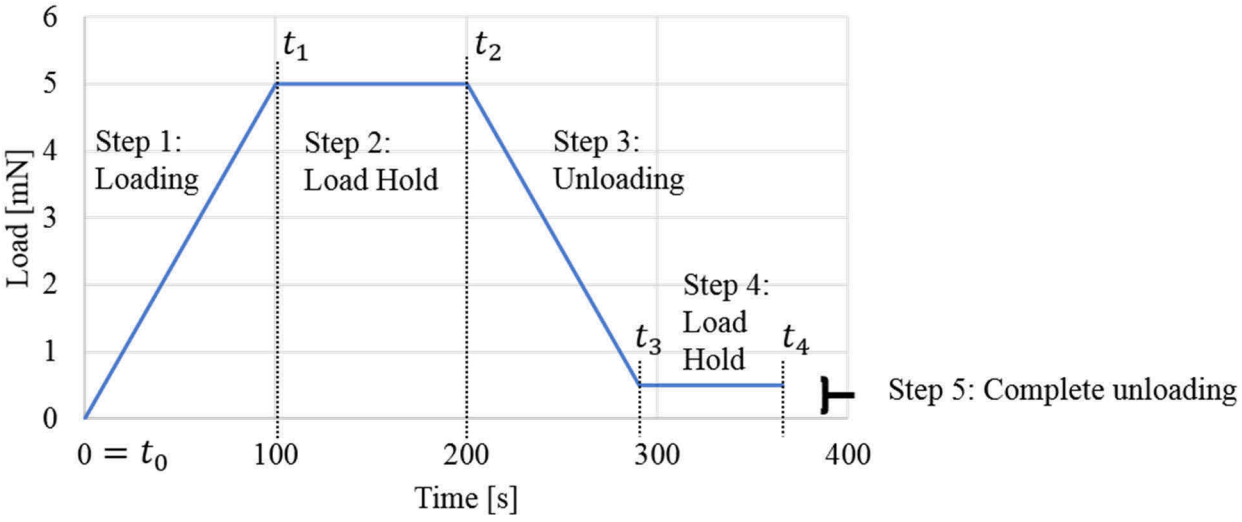

Figure 13:Method 3, adapted five-step CLH method after He and Swain [154]. Above graph shown for an exemplary load rate of 0.05 mN/s.

Enamel samples used for nanoindentation were prepared as for FIB investigations: glued to SEM stubs, grinded and polished with a final polishing step of 0.05 µm diamond polishing agent and a very short etching time to visualize rod boundaries. Untreated and deproteinized samples, as well as commercial HAP were compared. Indents were placed in inner enamel in two directions: load parallel or perpendicular to the main orientation of enamel rods. To verify the drift correction procedure, tests on alumina and silica crystal substrates (CrysTec GmbH, Berlin, Germany) were also conducted.

Samples for dry measurements were stored at ambient conditions for at least 24 h before the measurement. Samples for wet measurements were kept in distilled water for at least 24 h before the measurement. They were taken out of the water briefly to choose the indent locations and were kept submerged in distilled water for the entire duration of the measurement. This was realized by a custom-built sample holder.

5. Results

In the following chapter the results from the structural and compositional analyses will be described. Part of the results of the structural investigation has been published in *Acta Biomaterialia* with the title 'The geometrical structure of interfaces in dental enamel: A FIB-STEM investigation' [63]. The results of the structural investigation after deproteination treatment and the compositional analyses has been published in *Materialia* with the title 'Effect of deproteinization treatments on the structure and mechanical properties of dental enamel' [135]. Additionally, the results from the mechanical characterization via nanoindentation and nanoindentation creep tests will be presented. Part of these results have been published in *Materialia* with the title 'Effect of deproteinization treatments on the structure and mechanical properties of dental enamel' [135].

5.1 Morphological Characterization

The morphology of untreated dental enamel and enamel after deproteinization treatments was characterized by SEM and TEM. In the following chapter the focus are the interfaces in dental enamel. Two length scales will be analyzed, namely the boundaries between rod and interrod enamel (or between two rods) and the interfaces between crystallites.

5.1.1 Interfaces at the Rod Level

Figure 14 shows the rod boundary in the region of inner enamel. The rod boundaries appear not as mineral free gaps or thin organic sheaths as often described in the literature [5,8,45,96,103,115,158]. Instead, there are frequent areas of contact between the rod and interrod enamel or between two rods, where crystallites are bridging the boundary. In these areas of contact, the boundary is poorly defined and a distinction between the features (rod and interrod enamel) can only be made by the variation in crystallite orientation or by extrapolation of the surrounding discontinuities. Especially, in the region between the rods it is not clear if there is a boundary that separates the rods directly or if there are thin layers of interrod enamel in between. Additionally, thin filaments with a width of a couple of nanometers, are bridging the boundary. They will be called 'bridging filaments' in the following and could be detected in all enamel areas.

Figure 15 shows another interface region between interrod and rod enamel. Here, it can be clearly seen that the crystallites of the interrod enamel follow the curvature of the rod boundary,

bifurcate and curve into the space between the rods. Crystallites from rod and interrod enamel touch each other across the boundary and are separated by gaps. However, solely from the STEM images it cannot be determined whether these gaps are filled by some organic material that is postulated to be present in the zone surrounding the rods or whether they are empty pores. Whichever the case, there is a substantial pore space in the boundary region shows compared to the denser area inside the rod. The ratio of pore space to contact across the interface was determined to be 57 ± 15 area% on average (15 interfaces were analyzed; for more details see Supplementary Information B.3). Compared to Figure 14, there are less bridging filaments in Figure 15, but some are still apparent [63].

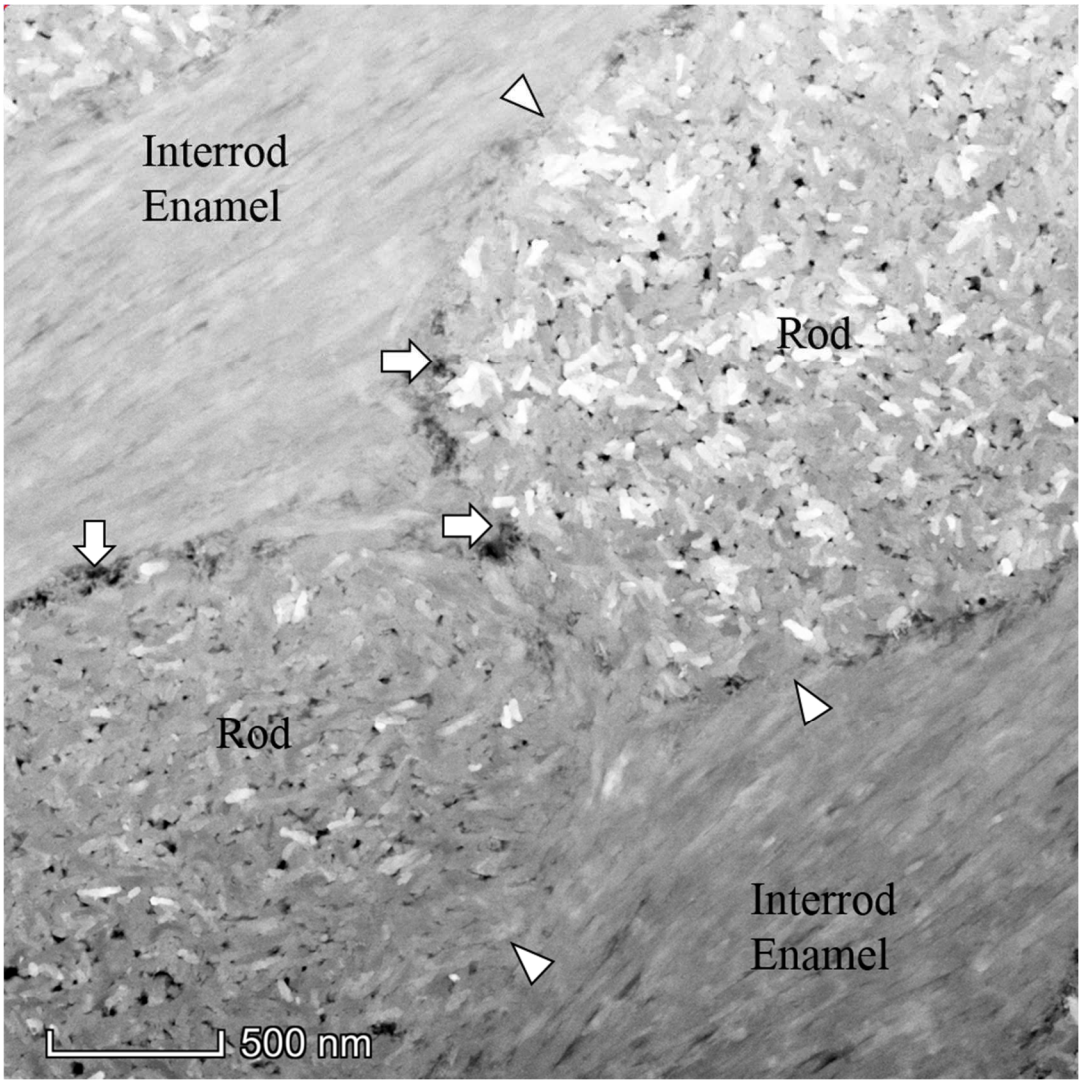

Figure 14: STEM image with a resolution of 2048x2048 px, resulting in approximately 0.6 px per nm showing rod boundaries. There appears to be direct mineral on mineral contact where the crystallites from the interrod enamel curve or fuse into the rod (arrowheads). In areas where there are gaps between the crystallites of the rod and interrod enamel bridging filaments are present (arrows).

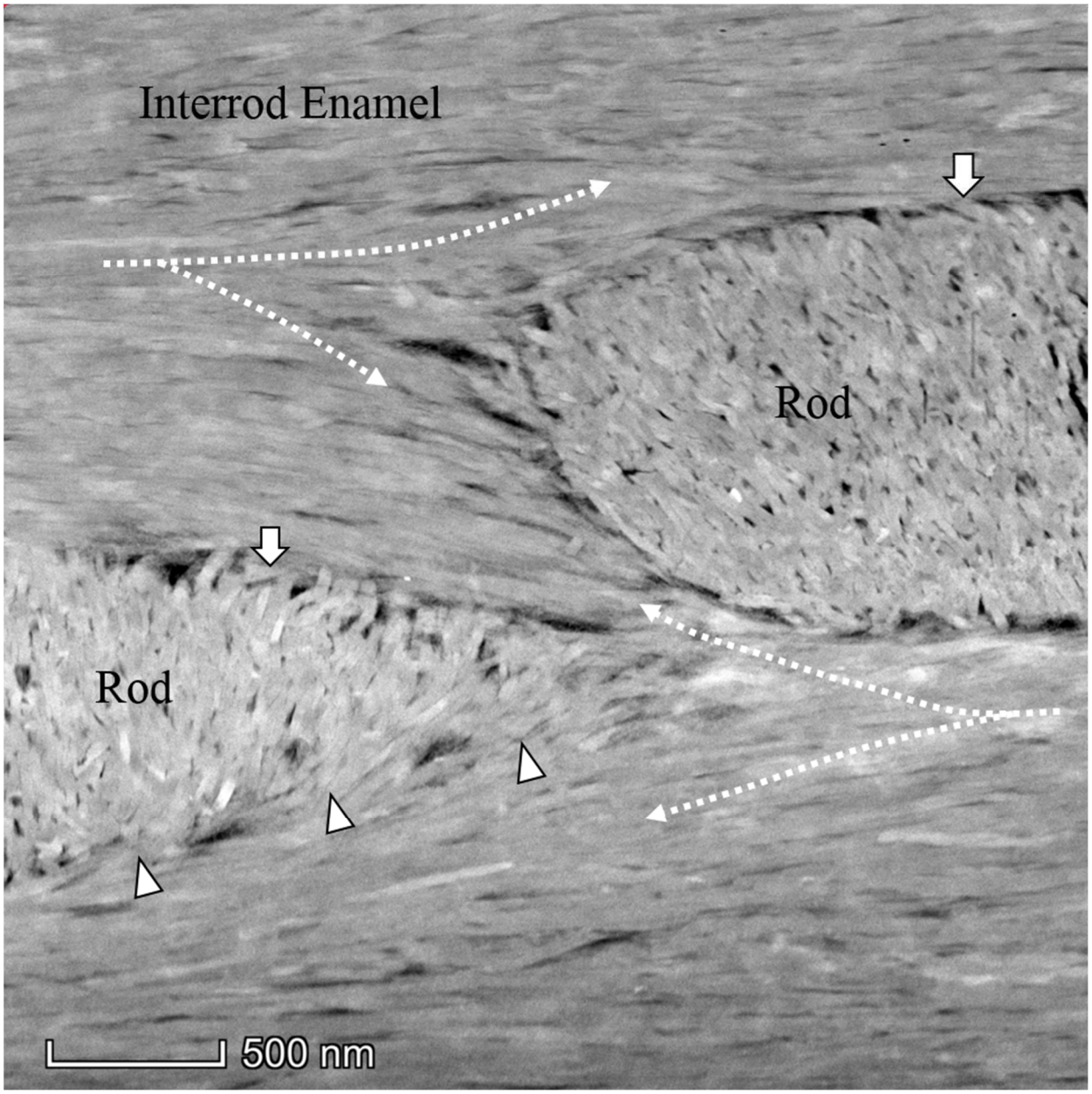

Figure 15: STEM image with a resolution of 2048 x 2048 px, resulting in approximately 0.6 px per nm showing rod boundaries. There are two kinds of mineral on mineral contact. Crystallites from the interrod enamel can curve into the rod (arrowheads) or crystallites bridge the boundary between rod and interrod enamel (arrows). Some bifurcations of the interrod enamel around rods (crystallite orientation indicated by dotted lines) can be seen.

5.1.2 Interfaces at the Crystallite Level

Figure 16 shows a STEM image of the cross-section of crystallites in a layer of rod and interrod enamel and the boundary between both. In cross-section the crystallites appear mostly as elongated hexagonal shapes, whereas some adopt a more undefined polygonal shape, with a width of around 50 nm in the wider axis and around 25 nm in the short axis. Many crystallites appear to be in direct contact with each other, fitting together like interlocking puzzle-pieces, while in other cases, the crystallites are separated by larger gaps. The gaps are evenly distributed throughout the whole cross-section and their size is slightly smaller than the crystallites. In the STEM micrographs the gaps appear as black color, which does not allow to conclude whether they are filled by organic material or not, as both low density material and empty space can result in this contrast. This image covers the cross-section of a single enamel rod almost completely, hence it was used to determine the porosity inside an enamel rod exemplary. The porosity was determined to be about 2.5 area% by using the image processing software Fiji [159] (more details in Supplementary B.4). Figure 17 and Figure 18 show TEM images of the crystallites at a high magnification which were used to analyze their interfaces. In these bright field images, the interfaces between the crystallites appear as white lines and span a distance from a few Å up to about 2 nm. In both figures it is again evident that some crystallites have slightly irregular shapes and fit together like puzzle pieces. Additionally, in these high magnification images, the crystal lattice of some of the crystallites can be seen as small dots, representing the atoms. Some crystallites appear to be in direct contact, although this impression might be the result of crystallites overlapping in the third dimension, rendering the analysis of the interfaces more difficult.

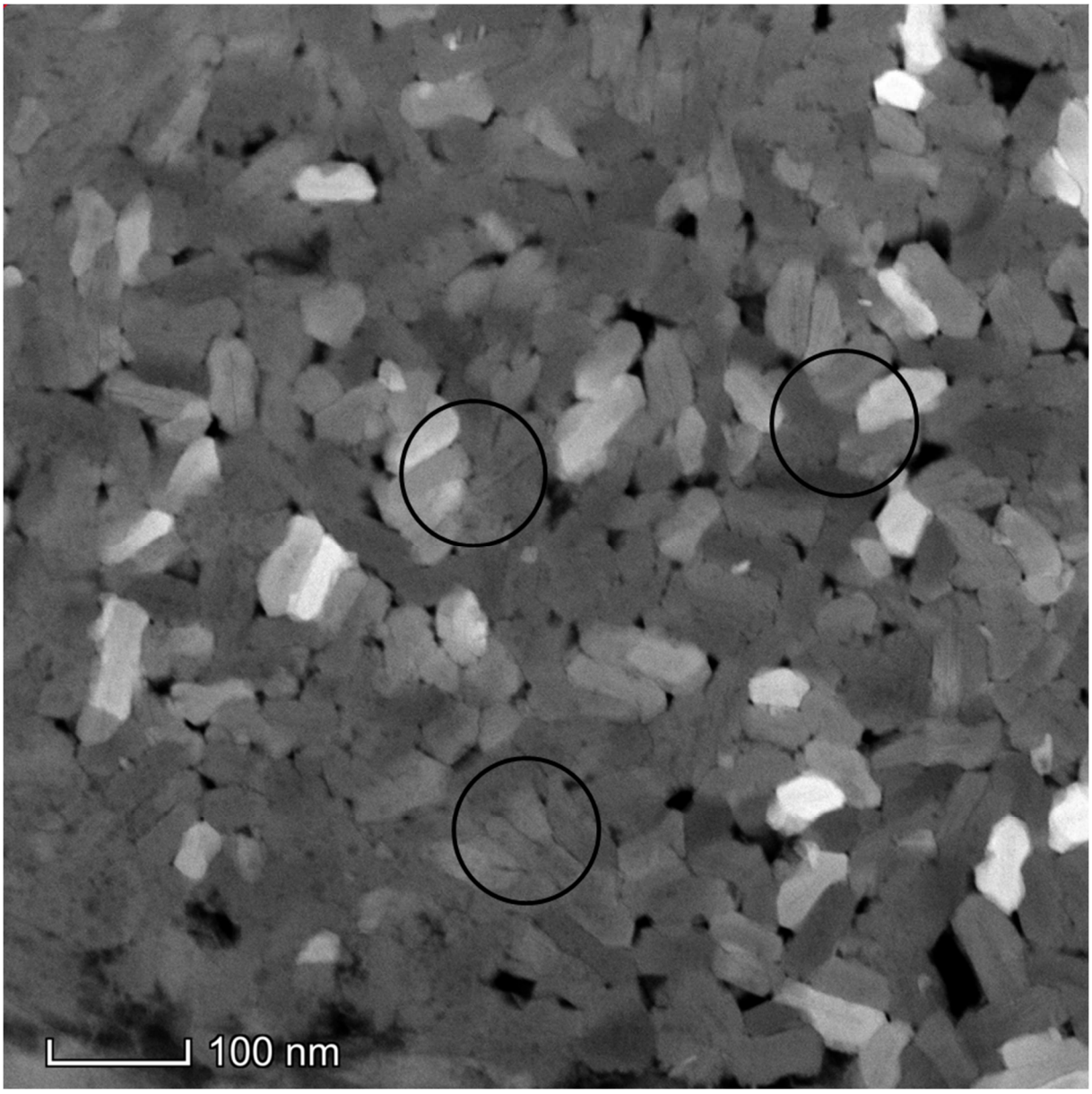

Figure 16: STEM image with a resolution of 2048x2048 px, resulting in approximately 2.6 px per nm showing the crystallites in an enamel rod. The crystallite boundaries appear as a black line. Brighter appearing crystallites do not have a different Z-value but are simply in the right orientation for Bragg scattering to occur which gives an additional signal to the detector. Some HAP crystallites exhibit an elongated hexagonal shape or a polygonal shape in cross-section whereas others do not exhibit a clearly defined shape at all. The shapes of the crystallites often fit together like puzzle-pieces and seem to be interlocking (circled areas) but in some cases there are larger gaps present between the crystallites. Whether these gaps are pores or filled by protein remains unclear.

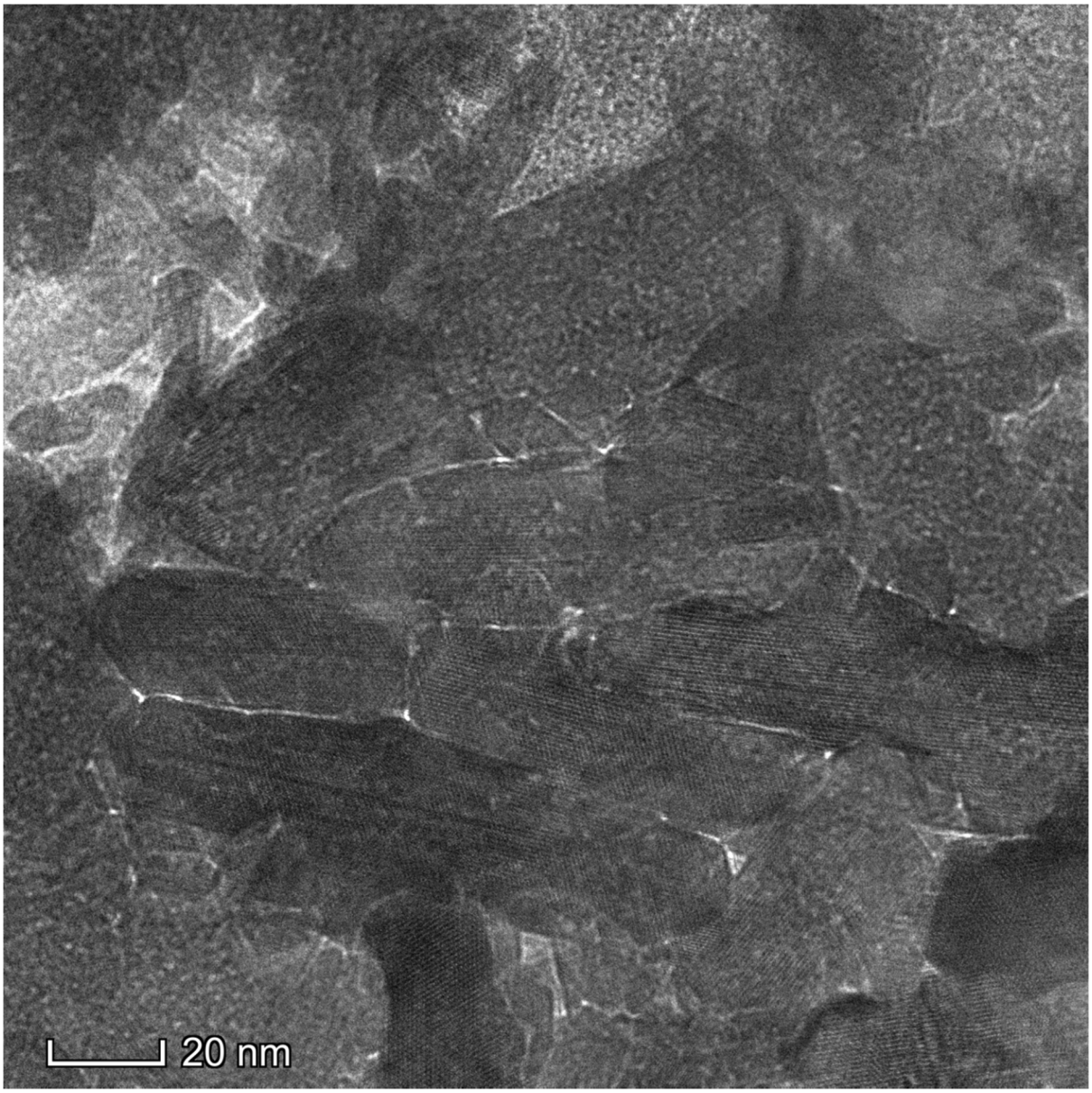

Figure 17: TEM image with a resolution of 4096x4096 px, resulting in approximately 21.2 px per nm showing the HAP crystallites in perpendicular orientation to the image plane. The lattice planes of the crystallites are visible. Crystallite boundaries manifest either as a thin white line or can be distinguished by the different orientations of the lattices the crystallites. Crystallites are overlapping and, in some cases, seem to be in contact with each other. The darker spots appearing all over the picture are artifacts due to the fabrication of the lamella or onset of beam damage.

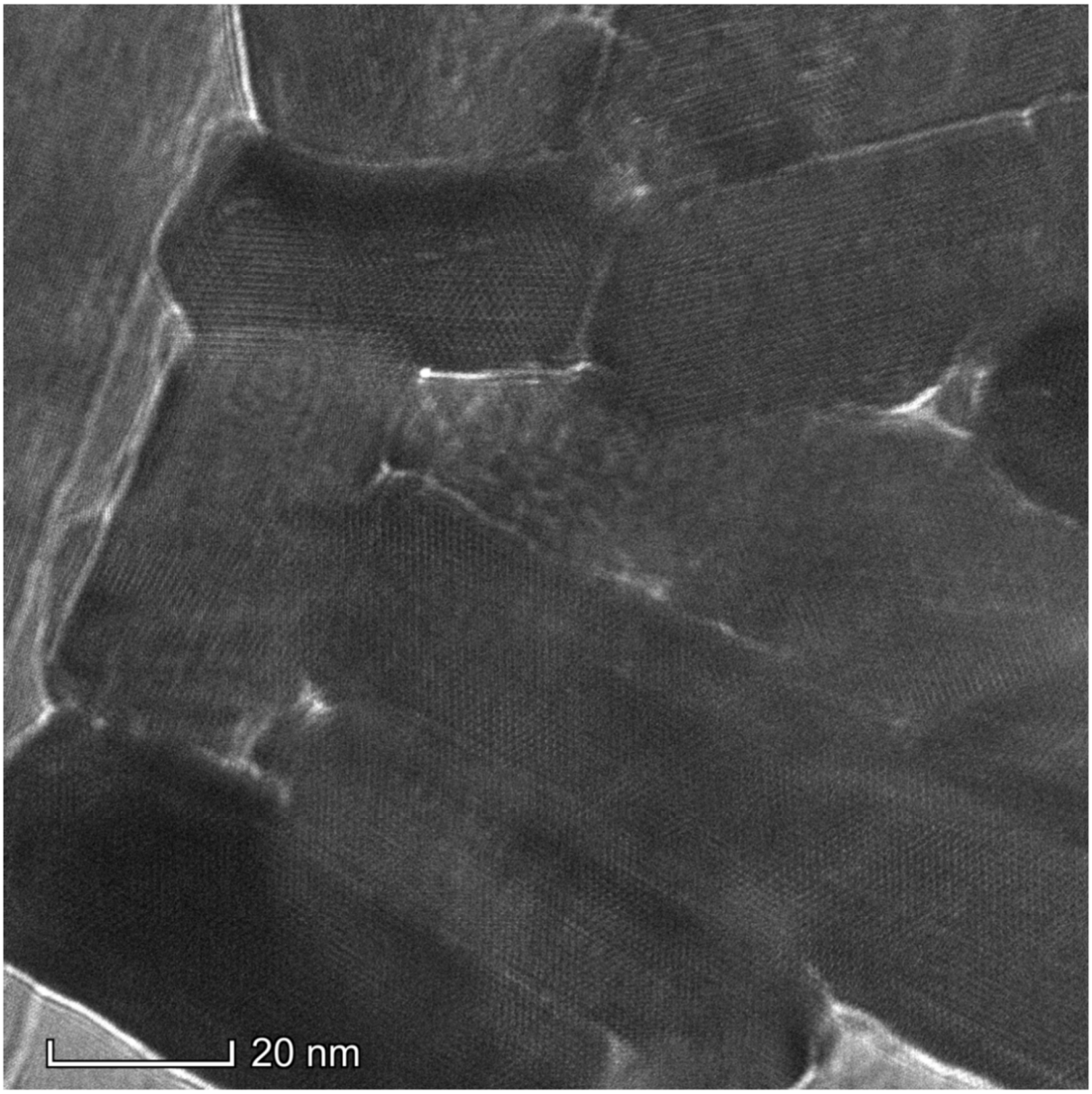

Figure 18: TEM image of a sample that was treated with KOH solution showing several HAP-crystallites in perpendicular orientation to the image plane with a resolution of 4096x4096 px, resulting in approximately 34.4 px per nm. The lattice planes of the crystallites are visible. Crystallite boundaries manifest either as a thin white line or can be distinguished by the different orientations of the lattices the crystallites. Crystallites are overlapping and, in some cases, seem to be in contact with each other. The darker spots appearing all over the picture are artifacts due to the fabrication of the lamella or onset of beam damage.

5.1.3 Structure of Dental Enamel after Deproteinization

The macroscopic structure and the local crystal structure of dental enamel before and after treatment were examined by SEM and TEM. Figure 19 shows the structure of untreated enamel in comparison with enamel after KOH and H_2O_2-treatment (chemical treatment). At small magnifications, the structure of the chemically treated enamel appears similar to the untreated with rod boundaries that are just barely visible after the etching. Larger magnifications also reveal no obvious difference in the crystal morphology between untreated and treated enamel. Figure 20 shows the structure of the sample after heat treatment at selected temperatures (300°C and 600°C) after 15 min or 24 h holding period in nitrogen atmosphere and the complementary SEM images for air atmosphere can be found in the supplementary information B.5. Small magnifications showing the macroscopic structure of the 300°C heated enamel reveal no dramatic changes to the structure compared to the untreated enamel. At larger magnifications however, it becomes obvious that there are changes to the structure of the crystallites: The crystals no longer have always clearly defined boundaries but start to fuse together. This sintering behavior is intensified with the longer holding period of 24h and higher temperatures >400°C. The enamel heated to 600°C exhibits the most drastic changes, with the formation of large cracks even after the comparably short holding time of 15 min. Additionally, the rod boundaries appear much wider and the sintering of the crystallites is more pronounced than in the otherwise treated enamel. Increasing the time of the heat treatment (24h) or changing the atmosphere to air results in the same changes. For heat treatment in air atmosphere, the structure is more affected than with nitrogen treatment, even at low temperatures.

Three enamel regions (innermost, inner and outer enamel) of untreated and KOH-treated enamel have been investigated by TEM (Figure 21). In the untreated enamel, the boundaries present as discontinuous structures with frequent direct mineral to mineral contacts and bridging filaments, as described previously (ch. 5.1.1). The KOH-treated enamel shows a similar crystallite morphology. Here, the boundaries are again characterized by frequent direct mineral to mineral contact, however, the gaps between these contact areas appear wider. In general, the images generate the impression that the KOH-treated enamel is more porous. The pore fraction determined of the KOH sample was determined as 44.50 ± 7.47 area% by image analysis with the Fiji software [159]. The small, fibrous connections described as bridging filaments, that were present in the untreated enamel could not be found in the KOH-treated enamel.

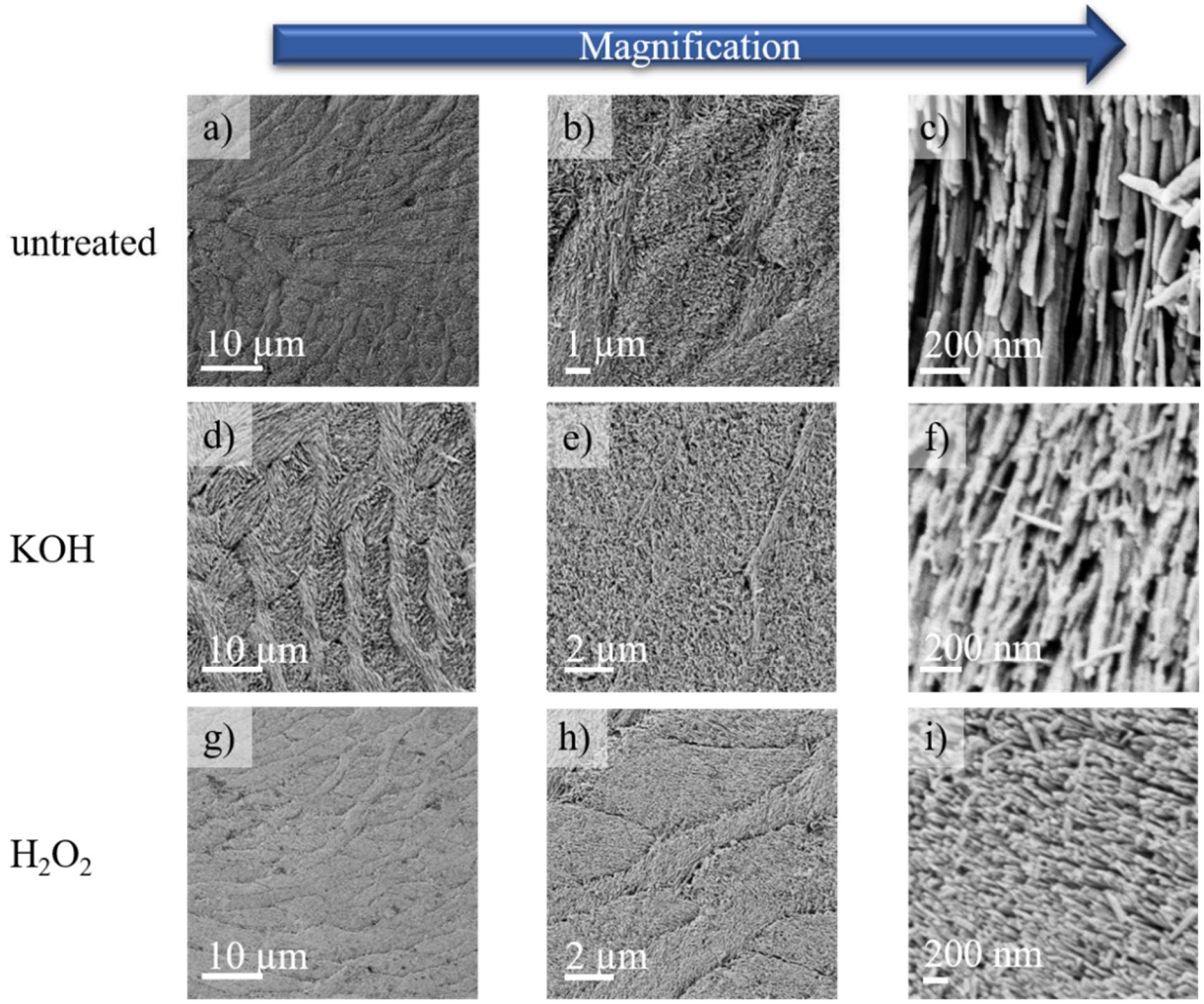

Figure 19: SEM images of untreated (a-c), KOH-treated (d-f) and H_2O_2-treated enamel (g-i). The macroscopic and crystal structure keep intact.

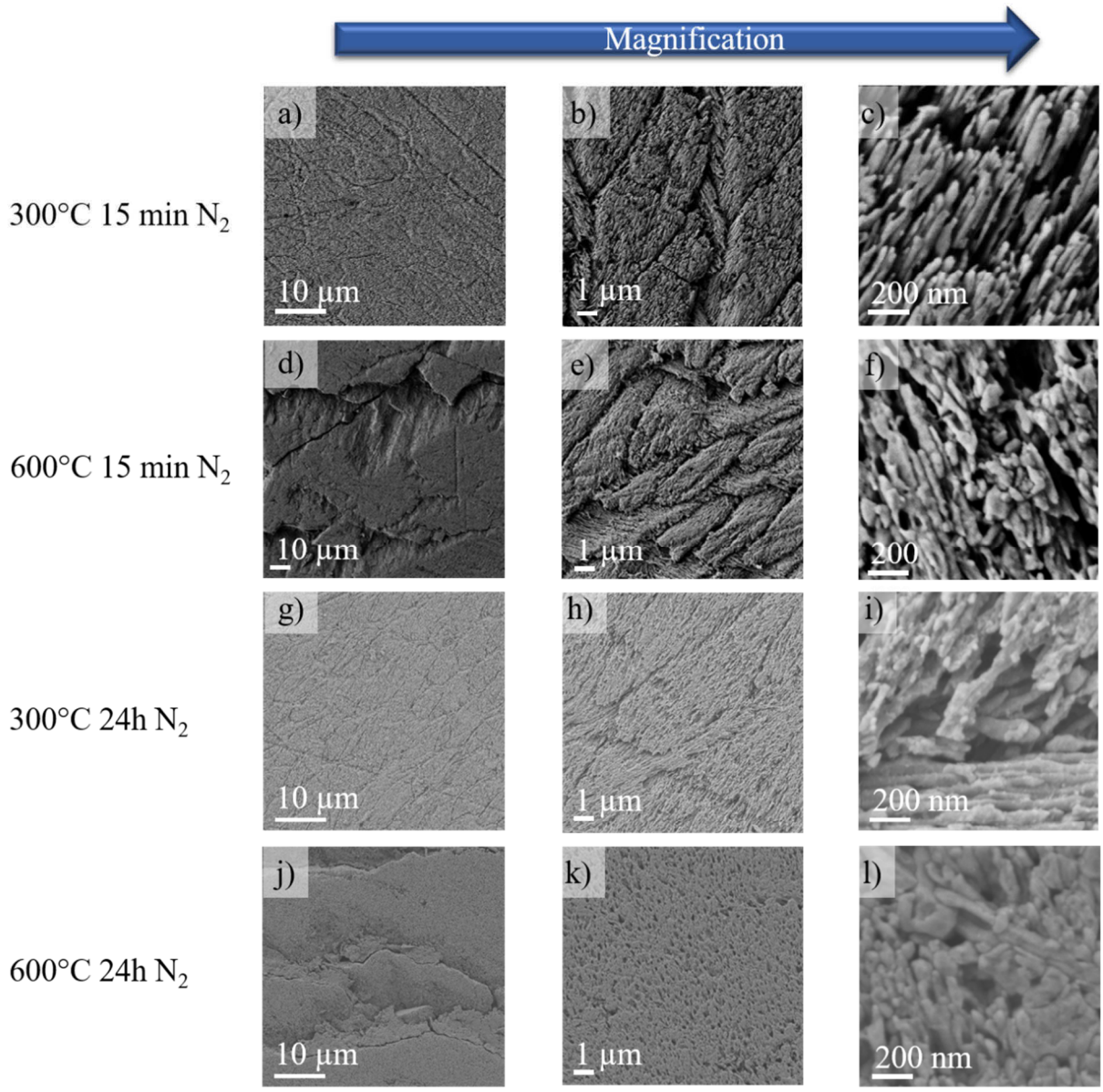

Figure 20: SEM images of heat-treated enamel in nitrogen at 300°C for 15 min (a-c) and 24 h (g-i) and 600°C for 15 min (d-f) and 24 h (j-l). After heat treatment the crystallites start to sinter. The higher the temperature or the longer the holding time, the stronger is this effect. Additionally, high temperatures cause large cracks in the samples (d and j).

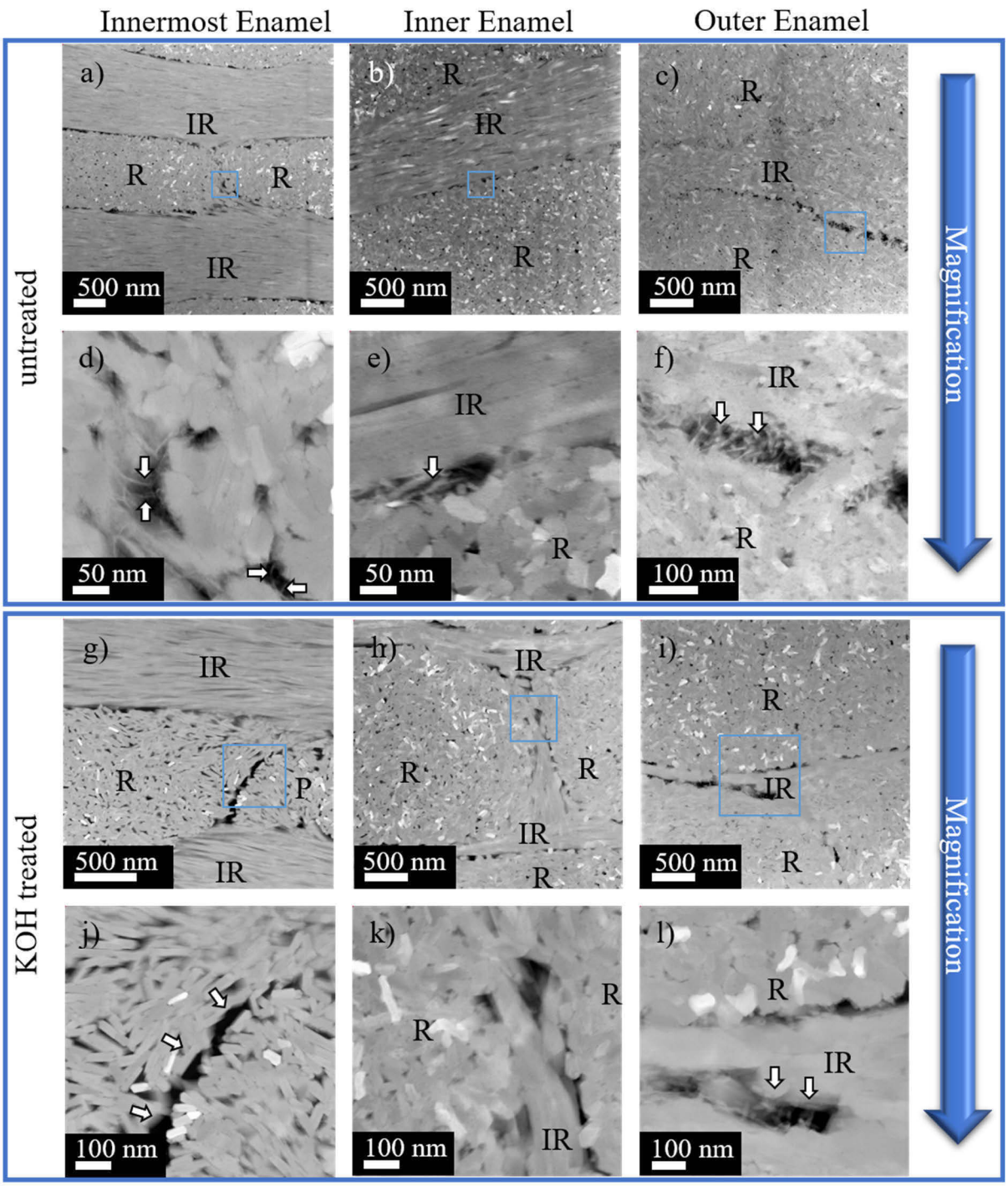

Figure 21: STEM images of untreated (a-f) and KOH-treated (g-j) enamel with rod and interrod enamel distingushible (R and IR, respectively). The boundaries appear as porous structures with frequent mineral-to-mineral contacts, regardless of treatment. Small fibrous connection can be found in the untreated enamel (d-f, arrows) but are absent in the KOH-treated enamel (j-l, arrows). There is no obvious difference in the crystal structure between both treatments.

5.2 Composition

The composition of dental enamel before and after deproteinization treatments has been analyzed by various methods, as described in chapter 4.4, in order to verify if the removal of the proteins has been successful.

For the TGA, samples from synthetic HAP, untreated enamel and chemically deproteinized enamel (n = 5, respectively) were analyzed. The curves were averaged, data was smoothed (FFT Filter with 100 points window), derived and a Gaussian multiple peak fitting was carried out. For all samples there is constant mass loss across the complete temperature range (25-900°C) (Figure 22). After derivation four peaks at ca. 305, 400, 550 and 730°C for enamel and three peaks at ca. 220, 410 and 720°C for HAP could be identified (for detailed peak locations and areas see supplementary C.1). In literature, the evaporation of organic material is attributed to the temperature range 200-600°C, with the strongest loss around 350°C, but as additionally also carbonate and structurally incorporated water evaporate, the mass loss of this region cannot be equated with the organic content [19,21,25,26,52]. The peak at ca. 720°C is attributed to loss of mineral CO_3 [19] and was not further considered for the determination of organic content. In this work, the peak areas of all peaks in the 200-600°C range was calculated and compared across the different samples (Figure 21). The mass losses for the region 200-600°C, i.e. the sum of the peak areas, are: 1.5 ± 0.02 w% for HAP, 1.9 ± 0.01 w% for the untreated enamel, 1.4 ± 0.01 w% for the KOH-treated enamel and 2.3 ± 0.01 w% for the H_2O_2-treated enamel (TGA accuracy of ± 0.2% of the sample mass).

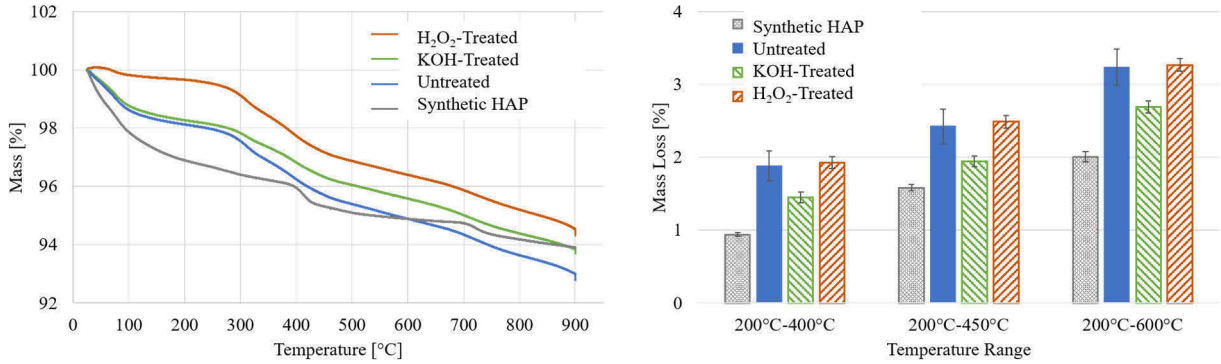

Figure 22: TGA curves (mean, n = 5) for N_2 atmosphere (left) and mass loss for several temperature ranges (right). High mass loss until 200°C is a result of water evaporation. Loss of bound water and organic matter occur in the range 200-600°C, with strongest loss around 350°C. For enamel, a peak at about 400°C could be observed and temperature ranges were selected accordingly. The KOH-treated enamel shows smaller mass loss than untreated enamel in all temperature ranges while the H_2O_2-treated enamel always shows the same mass loss as the untreated enamel. The HAP shows the lowest mass loss, but nevertheless some mass loss occurs in the temperature range 200-600°C. The raw TGA data was collected by Annika Holzschuh under the supervision of Jasmin Koldehoff.

As the mass loss during TGA cannot be solely attributed to organic material additional analyzes were performed. Thus, deproteinized (chemical and heat treatment) and untreated enamel and HAP samples were analyzed by FTIR (Figure 23). In all samples, there is a strong peak at about 1200 - 930 cm^{-1} which can be attributed to strong PO_4^{-3} [160]. Peaks of organic origin are usually attributed to the region 2000 - 2500 cm-1 [160] and in enamel a peak for amide I has previously been identified at 1650 cm^{-1} [160,161]. However, these peaks could not be identified in this work. Instead, a distinct peak can be found at 1550 cm^{-1} in the untreated enamel. This peak is also present in the treated enamel, but is reduced after heat treatments, and is absent in the HAP. Additionally, for untreated enamel there is a shoulder in the peak at 1425 cm^{-1} that is reduced after deproteinization and with heat treatment. The respective graphs for the heat treatments in different conditions (difference in holding times and atmosphere) can be found in the supplementary information 0 and show a similar behavior to the selected graphs in Figure 23.

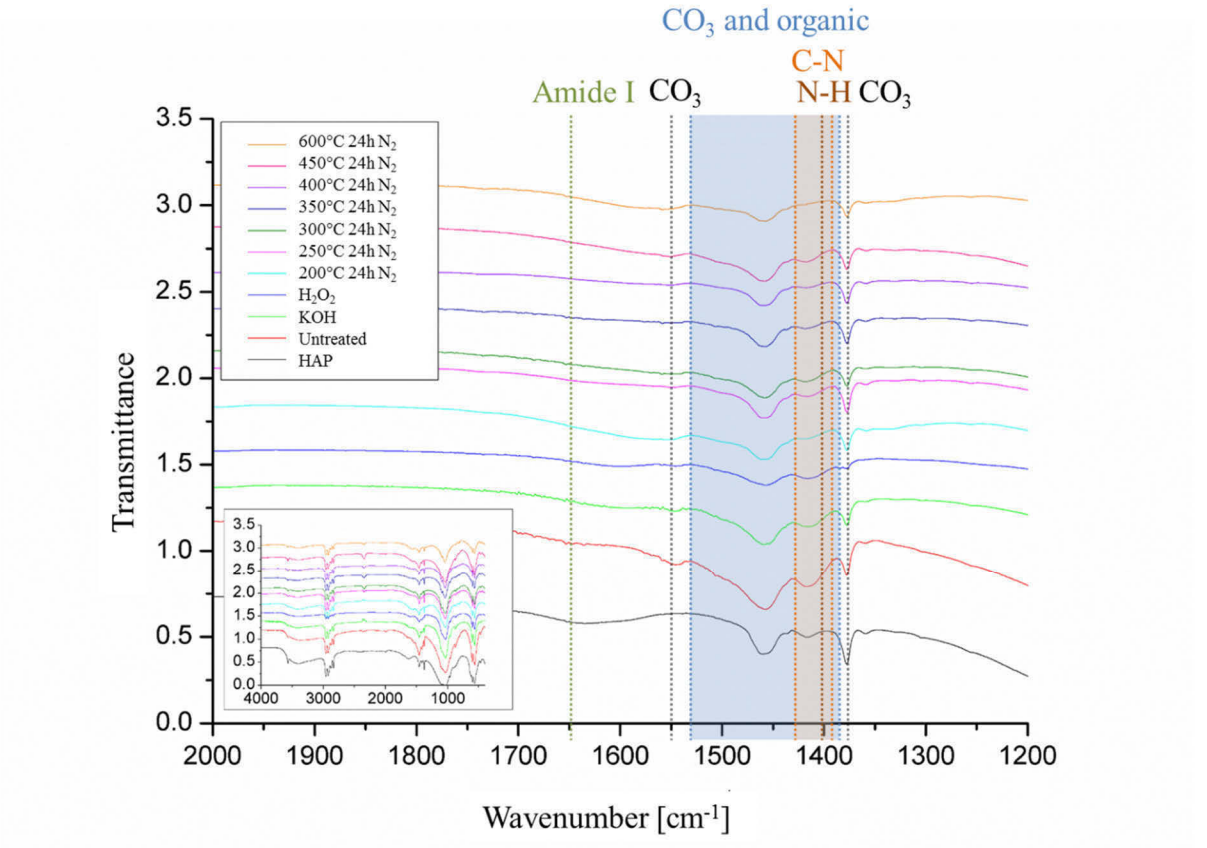

Figure 23: FTIR spectra of HAP, untreated and treated enamel. The spectra are similar for all samples. No amide I peak can be seen. A shoulder at 1425cm^{-1} can be seen in the untreated enamel that is reduced after deproteinization and with heat treatment. Aditionally, there is overlap with CO_3 peaks. .

Total Organic Carbon (TOC) and amino acid content were determined by elemental analysis (NCHS) and HPLC in the Central Laboratory for Chemical Analysis at the Hamburg University of Technology (Figure 24). The untreated enamel has the highest amount of TOC and amino acids which is reduced to approx. half the amount after chemical treatment. While TOC is on a similar level for the KOH and H_2O_2-treated enamel, the H_2O_2-treated enamel show a by one order of magnitude lower concentration of amino acids compared to the KOH-treated enamel. TOC in the heat-treated enamel is also lower than in the untreated enamel, with the lowest amount present after heating to 900°C. The same trend can be observed for the amino acid concentration where no amino acids could be detected for the 900°C-heated enamel (detection limit <0.3 µmol/g).

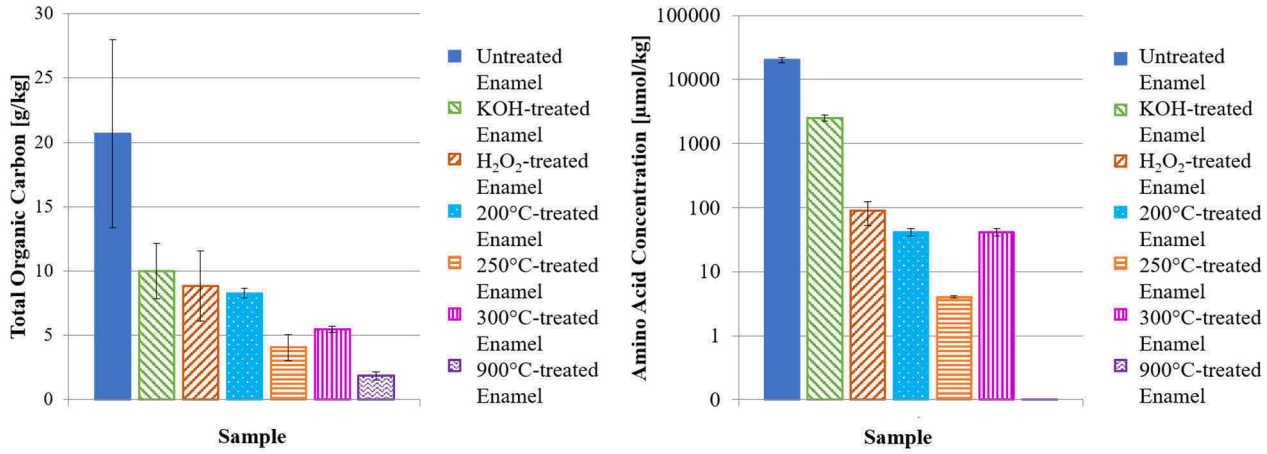

Figure 24: Total organic carbon (left) and amino acids (right) in treated and untreated enamel (n=3, respectively). Note the logarithmic scale for the amino acid concentration. The chemically treated enamel shows a lower amount of TOC and a lower concentration of amino acids than the untreated enamel, whereby the H_2O_2-treated enamel has a lower concentration of amino acids than the KOH-treated. The heat treated enamel also shows lower TOC than the untreated enamel, with the lowest amount present after heating to 900°C. The same trend is present for the amino acid concentration, where no amino acids could be detected for the 900°C heated enamel (detection limit <0.3 µmol/g).

5.3 Elastic Modulus & Hardness

The elastic modulus and hardness of the untreated enamel and after chemical and heat treatments were determined by nanoindentation. For untreated and chemically treated enamel both properties are in the same range, considering their standard deviations (Figure 25). Heat treatment in nitrogen at relatively low temperatures (200-350°C) leads to an increase in both properties, but after heating above 400°C modulus and hardness decrease. This trend occurs as well for the samples heat-treated in air and the accompanying data can be found in the supplementary (D.1).

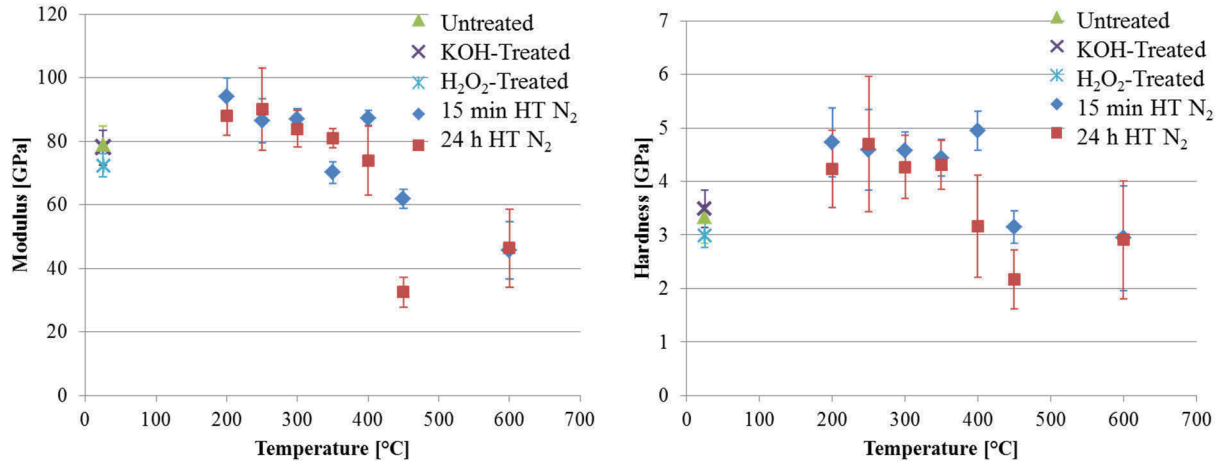

Figure 25: Elastic modulus (left) and hardness (right) of the untreated, chemically treated and heat-treated enamel. After chemical treatment no change in properties can be observed. After heating the sample to temperatures <400°C an increase in elastic modulus and hardness is present but after heating to ≤400°C, a strong drop in both properties occurs.

5.4 Creep

In order to illustrate the viscoelastic properties of dental enamel, creep tests were carried out as described in chapter 4.6. First experiments were carried out using method 1 (ch. 4.6.3) according to He and Swain [154] with a high maximum load of 250 mN and a sharp Berkovich tip. In the enamel samples this resulted in strong crack formation and even buckling of the enamel rods. In the load displacement curves this was also evident by strong 'pop-in' events (Figure 26). Therefore, tests with a spherical tip and lower loads (method 2 and 3, ch. 4.6.3) were carried out to avoid damage to the enamel structure and be able to gain insight into visco-elastic behavior of the enamel samples. The data for part of the 5 µm tests and all of the 50 µm were collected and analyzed (drift correction and averaging) by Katherina Lewandowski under the supervision of Jasmin Koldehoff.

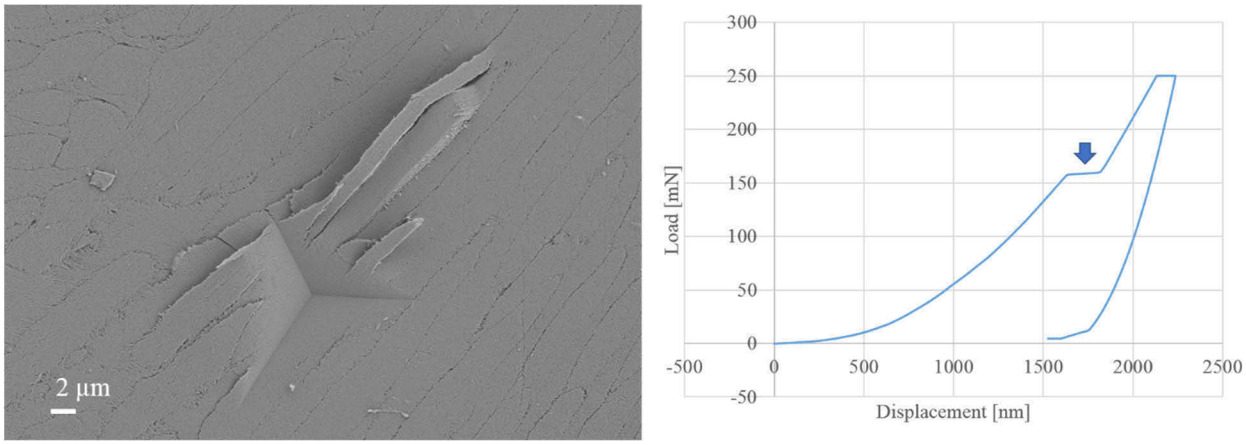

Figure 26: Exemplary residual impression after an indentation with the Berkovich tip using method 1 (left). It can be seen that the rods are pushed upwards by the indenter tip. In the exemplary load-displacement curve (right) this damage to the structure manifests as a pop-in (arrow).

5.4.1 Drift Correction

Due to thermal expansion in the electronics of the nanoindentation system, some changes in the measured displacement can occur. This behavior is referred to as thermal drift. To avoid the influence of thermal drift on the measurement, the test will not be started if the drift rate is >0.05 nm/s. Additionally, the indenter offers a built-in drift correction, where after unloading to about 90% of the maximum load the load is held constant for 75 s (50 s to determine the drift after an initial settling time of 25 s), the change in displacement is recorded and fitted by a linear regression. This linear function is then used to correct the measured displacement.

For the creep experiments with method 2 (see ch. 4.6.3), where the load was held for an extended time period it could be observed that the drift rate is not constant, and the linear regression used by the indenter is not accurate to determine drift. Therefore, the built-in drift correction by the indenter was not used and a manual drift correction procedure was developed and verified by analyzing SiO_2 and Al_2O_3 (see Supplementary D.2). For the low load of 5 mN and a spherical indenter tip of radius 5 µm, no creep was expected to occur in alumina and silica, therefore after the correction the displacement at maximum load should stay constant over time. The same is true for backcreep, hence the displacement after unloading should also be constant.

The drift correction procedure was as follows (see also visual representation of the process in Figure 27)

1) Creating a continuous displacement-time curve $h_{hold}(t)$ from only the hold segments. This is done by removing the loading and unloading ramps, as the time to load or unload is very short compared to the hold segments and any drift that may occur can be disregarded. To remove the ramps the starting times of the ramps are subtracted from the measured elapsed time and the displacement at the start of the hold segment was set equal to the last data point of the previous segment. This can be defined as:

   $t_{0,new} = t_1 - t_1 = 0$

   $t_{1,new} = t_2 - t_1$

   $t_{2,new} = t_4 - t_3 + t_{1,new}$

   $t_{3,new} = t_6 - t_5 + t_{2,new}$

   With

   $h_{hold}(t_{0,new}) = h(t_1) - h(t_1) = 0$

   $h_{hold}(t_{1,new}) = h(t_2) - h(t_1) = h(t_3) - (h(t_3) - h(t_2)) - h(t_1)$

   $h_{hold}(t_{2,new}) = h_{hold}(t_{1,new}) + h(t_4) - h(t_3)$

   $h_{hold}(t_{3,new}) = h_{hold}(t_{2,new}) + h(t_6) - h(t_5)$

   This results in a curve as shown in Figure 27 b) and Figure 28.

2) For the enamel samples where actual creep occurs, 'jumps' could be seen in the such created curve $h_{hold}(t)$ (see Figure 28 b). Hence parts of the curve needed to be removed before fitting the curve in order to be able to use those segments for creep evaluation. The first 100s or 50% of the 900s hold segments ($t_{1,new}$ to $t_{2,new}$ and $t_{2,new}$ to $t_{3,new}$, respectively) were removed. In the latter case the complete shorter 50 s hold segment ($t_{0,new}$ up to $t_{1,new}$) was also omitted.

3) Just removing the segments however does not account for the large change in displacement caused by the creep in the sample. The segments were thus shifted in y-direction, such that the space between them could be connected by a strictly monotonously increasing or decreasing continuous function. This was done by calculating the change in displacement due to the 'jump' in the curve $h_{hold}(t_{new})$ (see Figure 28 b) and subtracting it from the curve resulting in:

   $h_{hold,shifted}(t_{0,new}) = h(t_1) - h(t_1) = 0$

   $h_{hold,shifted}(t_{1,new}) = h(t_3) - (h(t_3) - h(t_2)) - h(t_1) - y_{shift,1} = h(t_2) - h(t_1) - y_{shift,1}$

   $h_{hold,shifted}(t_{2,new}) = h_{hold}(t_{1,new}) + h(t_4) - h(t_3) - y_{shift,2}$

$h_{hold,shifted}(t_{3,new}) = h_{hold}(t_{2,new}) + h(t_6) - h(t_5)$

With $y_{shift,1} = h_{hold}(t_{jump,1}) - h_{hold}(t_1)$ and $y_{shift,2} = h_{hold}(t_{jump,2}) - h_{hold}(t_2)$

As for the '50% cut + moved' the complete first segment was omitted, here $h_{hold,shifted}(t_{1,new}) = -y_{shift,1}$

4) The such resulting curve was subsequently fitted with a 4th order polynomial:

$$h_d(t) = a_0 + a_1 t + a_2 t^2 + a_3 t^3 + a_4 t^4 \quad (36)$$

With $a_0 = 0$ so that $h_I(t = 0) = h(0) - h_d(0) = 0$ and hence for the corrected load-displacement curve $F(h = 0) = 0$ holds true. After fitting, the y-shift of the segments was adjusted if the resulting fitted curve deviated from a strictly monotonously increasing or decreasing continuous function between the omitted segments, by choosing a different $t_{jump,i}$.

5) Lastly the displacement due to drift was calculated and subtracting it from the measured displacement $h(t)$ to calculate the true indentation depth (from (35) $h_I(t) = h(t) - h_d(t)$).

All $h_{hold}(t_{new})$ and $h_{hold,shifted}(t_{new})$ (with 100s or 50% cut, respectively) were calculated and fitted for each individual test in order to gauge the appropriateness of the y-shift and the resulting fitting function. The final drift correction was carried out with the $h_{hold,shifted}(t_{new})$ were 50% were removed, as this led to the best results (i.e. least amount of creep) in the silica references. This correction was applied to the raw data of each individual test manually.

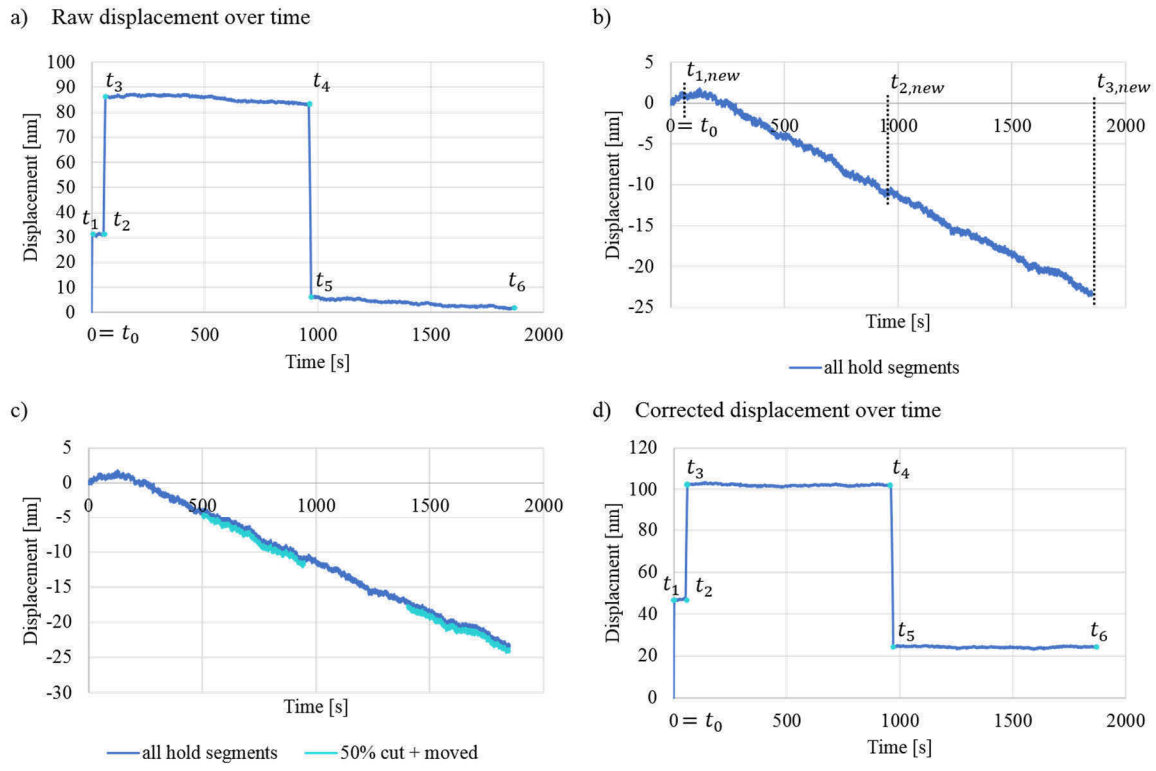

Figure 27: a) Displacement-time $h(t)$ as recorded by the indenter. b) Continuous curve created from all hold segments $h_{hold}(t)$ c) Curve from all hold segments $h_{hold}(t)$ and additionally curve from all hold segments $h_{hold}(t)$ with 50% cut and moved d) Corrected displacement-time curve $h_I(t)$

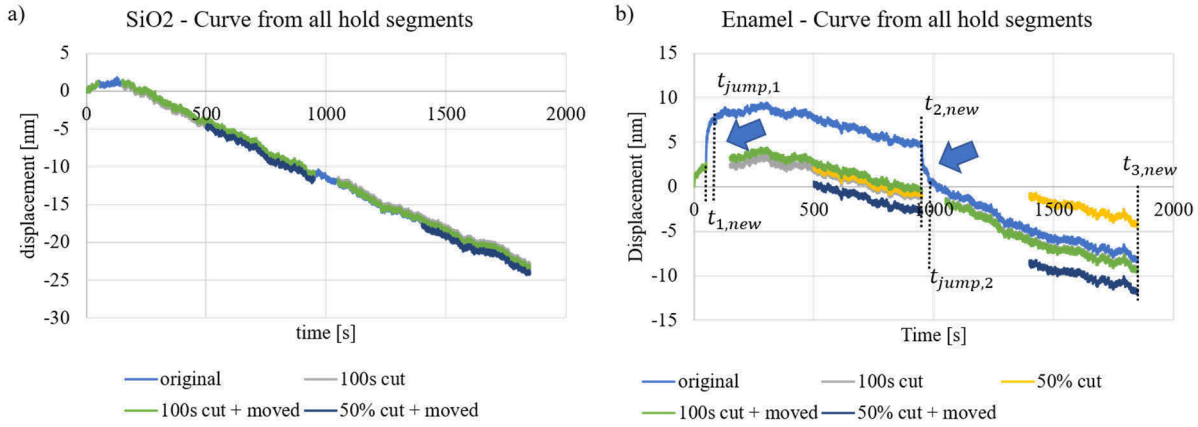

Figure 28: Exemplary curves for a) SiO_2 and b) untreated enamel showing displacement over time stitched together from all hold segments. 100s or the first 50% (including the complete first hold segment) were cut from the curve and it was shifted in y-direction to create a continuous curve without local maxima or minima between the segments. This was necessary as in untreated enamel 'jumps' (arrows), where the slope suddenly changes, occur in the curve that are due to events in the sample rather than drift.

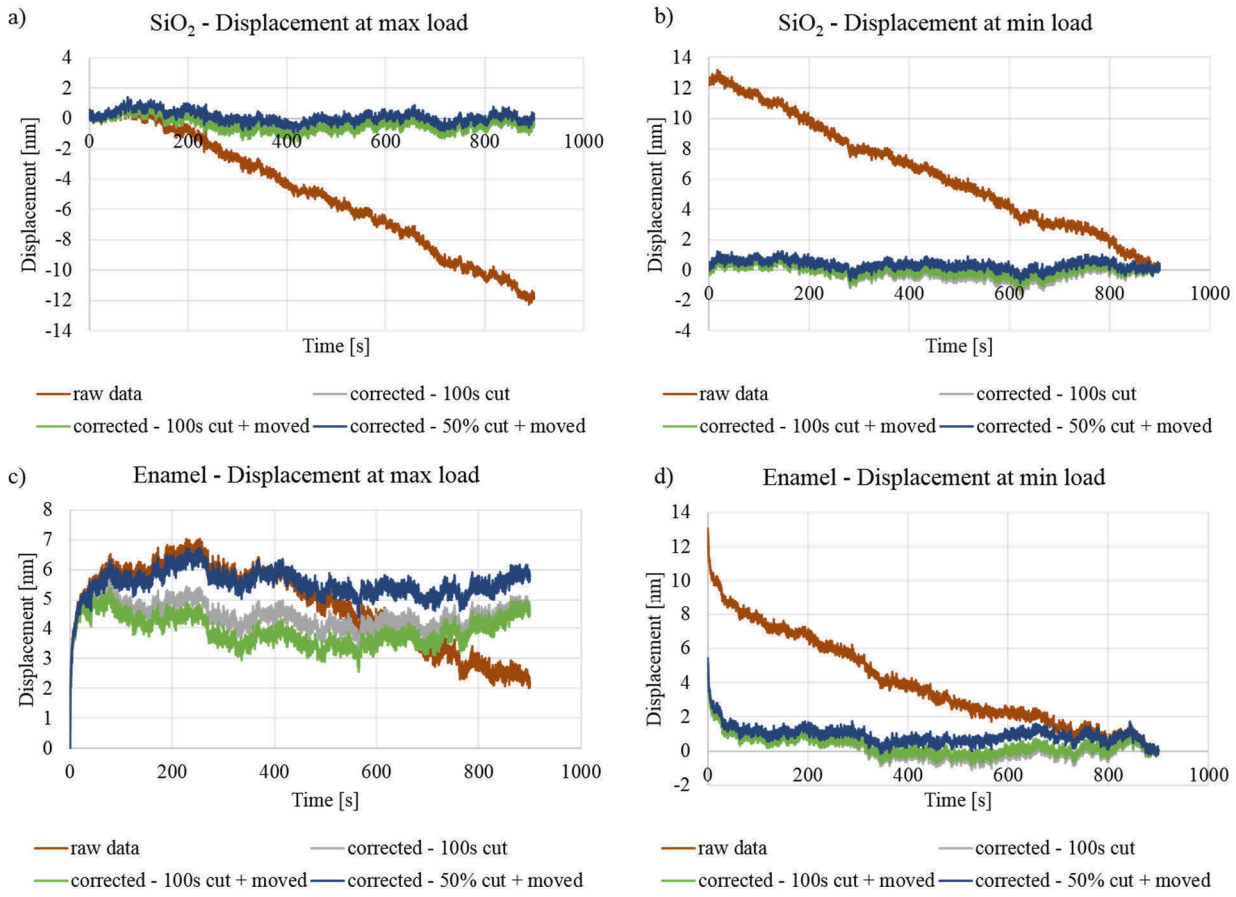

Figure 29: Exemplary raw displacement and corrected data of the SiO_2 sample during hold at a) max and b) min load. After drift correction the SiO_2 sample shows almost no creep (displacement <1.5 nm). c) and d) show exemplary raw displacement and corrected data of the untreated enamel during hold at max. and min. load, respectively. After drift correction still some creep is present, but after 100-200s almost no changes in displacement occur.

For the creep experiments with varied load rates (method 3), again the built-in drift correction was not adequate, and a manual drift correction was applied. Here a linear regression was performed on the last 20 s of the hold segment at maximum load ($h(t_1)$ to $h(t_2)$) where creep effects are expected to have died down, according to the observations during the experiments with method 2. The recorded displacement was then corrected with the such determined drift rate. This approach was again verified on silica.

5.4.2 Load Displacement

Figure 30 shows the load-displacement curves, after correction and averaged, for the ceramic refence materials (silica, alumina and sintered HAP) and the enamel samples. It can be seen that alumina and silica show an elastic behavior where loading and unloading curves lie perfectly on top of each other, while the HAP and enamel samples show some degree of plastic deformation.

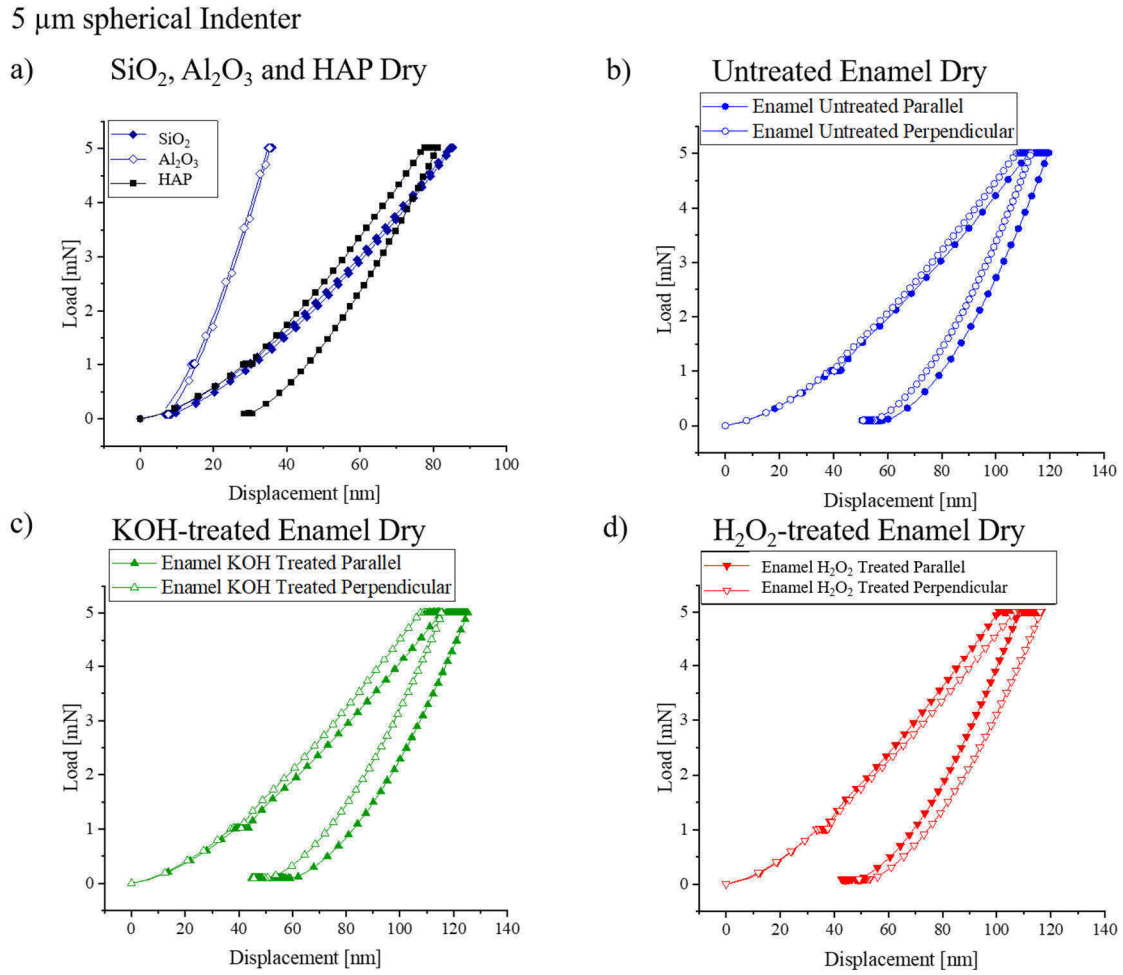

Figure 30: Load displacement curves for a) silica, alumina and HAP b) untreated enamel c) KOH-treated enamel and d) H_2O_2-treated enamel in dry state for the creep experiments with 900s hold segments (method 2) with a 5 µm indenter tip. Silica and alumina show perfect elastic behavior, whereas in HAP and in enamel energy loss occurs. For the enamel samples both loading directions show similar behavior. All enamel samples show more displacement at max. load than the HAP sample.

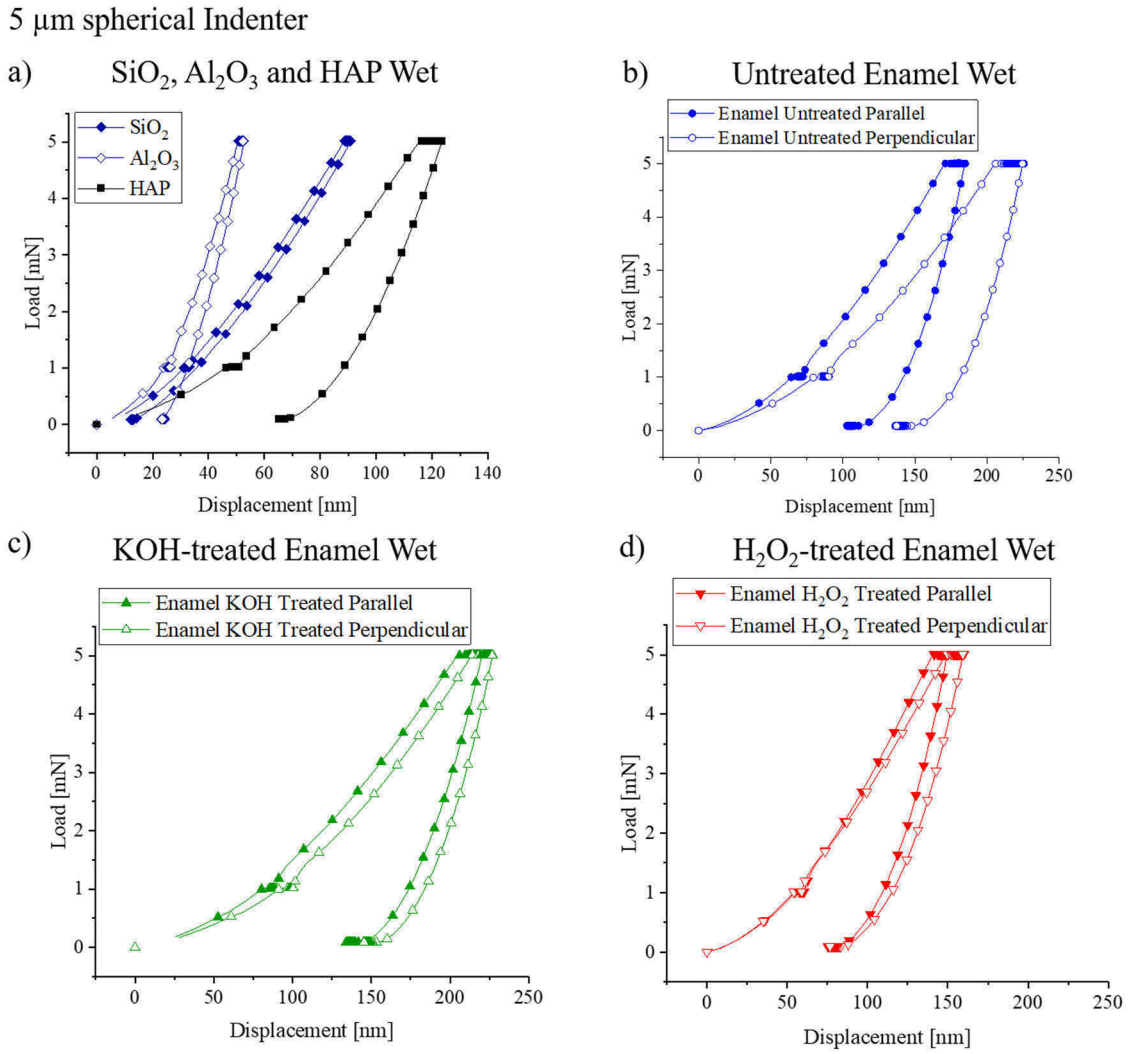

Figure 31: Load displacement curves for a) silica, alumina and HAP b) untreated enamel c) KOH-treated enamel and d) H_2O_2-treated enamel in wet state for the creep experiments with 900s hold segments (method 2) with a 5 µm indenter tip. Silica and alumina show almost perfect elastic behavior, whereas in HAP and in enamel energy loss occurs. For the treated enamel samples both loading directions show similar behavior, whereas the untreated enamel tested in perpendicular direction shows a higher displacement at max. load. All enamel samples show more displacement at max. load than the HAP sample.

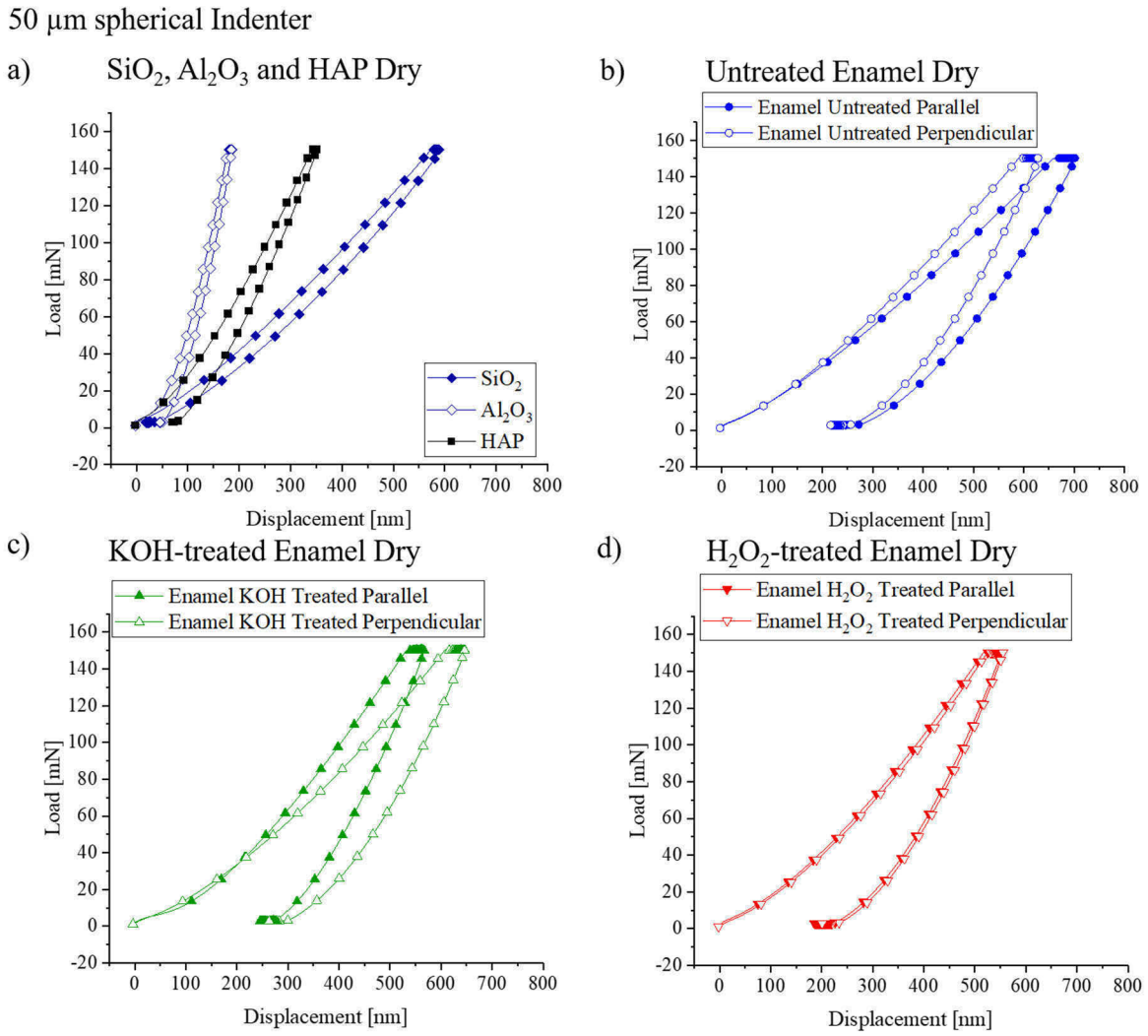

Figure 32: Load displacement curves for a) silica, alumina and HAP b) untreated enamel c) KOH-treated enamel and d) H_2O_2-treated enamel in dry state for the creep experiments with 900s hold segments (method 2) with a 50 µm indenter tip. Silica and alumina show almost perfect elastic behavior, whereas in HAP and in enamel energy loss occurs. For the enamel samples both loading directions show similar behavior. All enamel samples show more displacement at max. load than the HAP sample

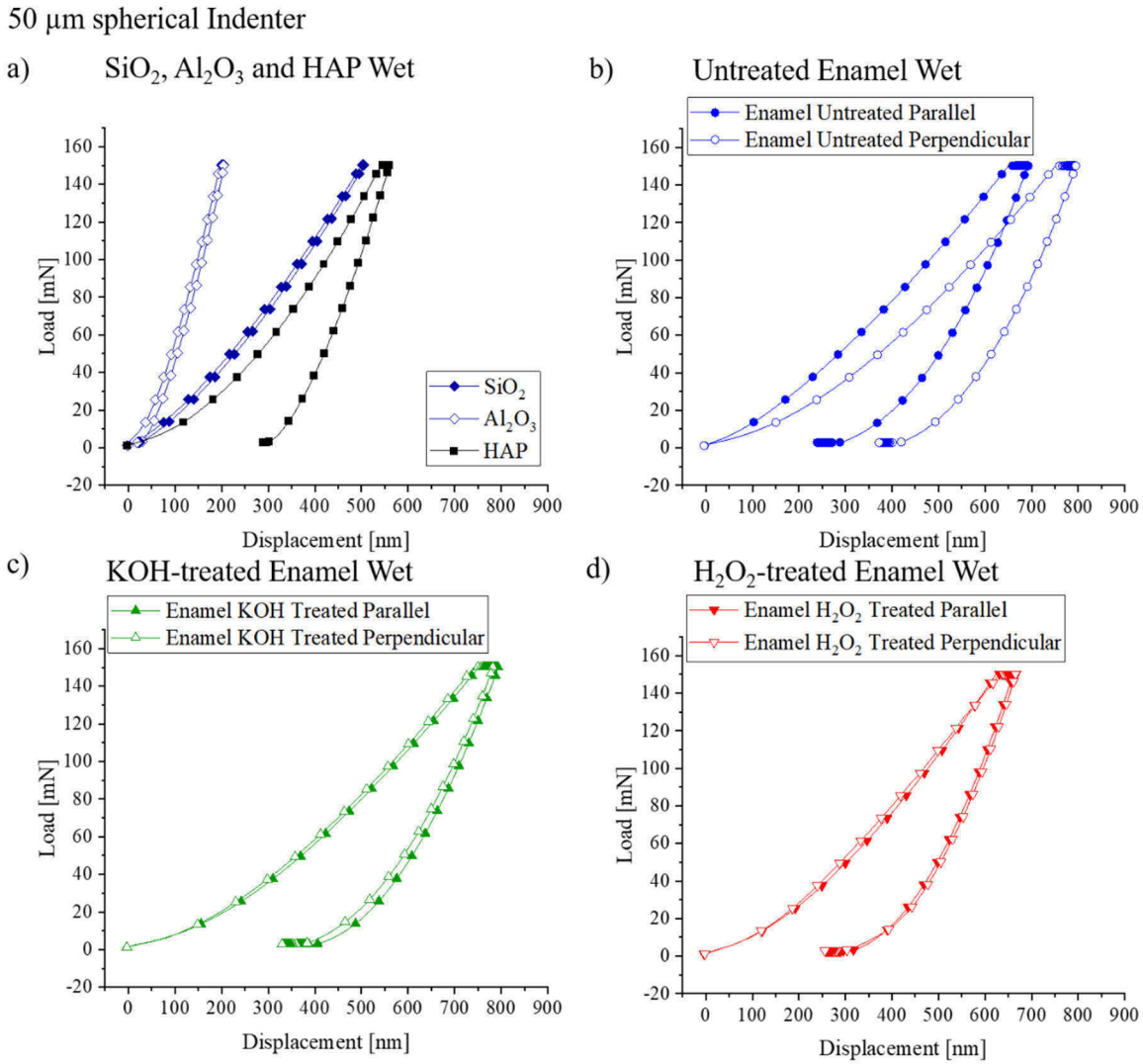

Figure 33: Load displacement curves for a) silica, alumina and HAP b) untreated enamel c) KOH-treated enamel and d) H_2O_2-treated enamel in wet state for the creep experiments with 900s hold segments (method 2) with a 50 µm indenter tip. Silica and alumina show almost perfect elastic behavior, whereas in HAP and in enamel energy loss occurs. For the treated enamel samples both loading directions show similar behavior, whereas the untreated enamel tested in perpendicular direction shows a higher displacement. All enamel samples show slightly more displacement at max. load than the HAP sample.

The elastic modulus was calculated by fitting the loading curve with the Hertz equation for an elastic contact and from unloading using the method described by Oliver and Pharr [147]. The results are presented in Figure 34 and in the supplementary information D.4 (Supplementary Table 5). In the case of silica, the values from loading and unloading determined with the 5 µm tip agree with each other and are close to its nominal modulus of 70 GPa (not shown in the graph). The modulus determined with the 50 µm tip however are lower than the nominal

modulus. For the HAP and all enamel samples (except untreated enamel in perpendicular direction) the modulus determined from unloading is higher than the modulus from loading. For the untreated enamel in parallel direction and the treated enamel in both directions the modulus from loading is roughly twice as high as for loading. The moduli from loading for the wet samples are consistently lower than for the dry state. In contrast the modulus from unloading generally is higher in the wet state than in the dry state. The moduli determined with the 5 µm tip are generally in a similar range as the moduli determined for the 50 µm tip, barring a few exceptions.

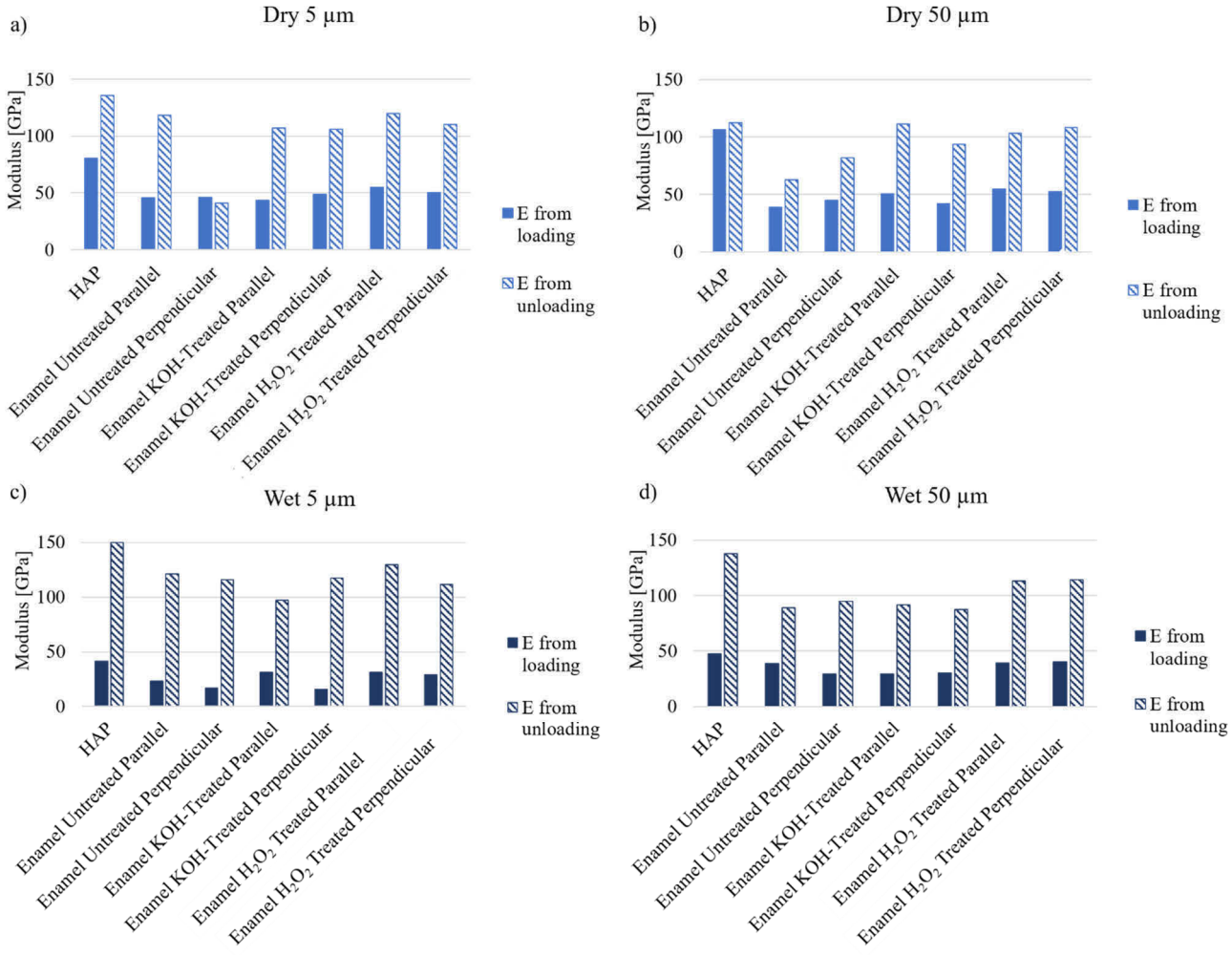

Figure 34: Elastic Moduli from loading (Hertz fit) and unloading (Oliver and Pharr) for all tested enamel samples in a)-b) dry and c)-d) wet condition with either the 5 or the 50 µm tip. While both calculations yield a similar elastic modulus for the untreated enamel in perpedicular direction with the 5 µm tip, in all other cases the modulus from unloading is higher. The moduli from loading for the wet samples are consistently lower than for the dry state. In contrast the modulus from unloading generally is higher in the wet state than in the dry state.

5.4.3 Evolution of Displacement during Constant Load

Creep tests were carried out with a spherical tip according to the adapted CLH protocol reported in chapter 4.6.3 (method 2) with a maximum load of 5 mN and a spherical tip with a nominal radius of 5 µm to test multiple crystallites at the first hierarchical level, and with a maximum load of 150 mN with a tip with nominal tip radius of 50 µm to test multiple rods at the second hierarchical level. The tip calibration has revealed the actual indenter tip radii as 5.31 µm and 36.31 µm respectively (see Supplementary Information A.1). For the sake of conciseness, the respective tips will be identified by their nominal radii in the following. Drift correction of the raw data was carried out as described in the previous chapter. In order to compare the evolution during the second hold segments (hold at maximum load of 5 or 150 mN) the curves were normalized such that all start at zero displacement and zero seconds. To compare the recovery after unloading the displacement at the end of the third hold segment (min load of 95% of max. load) was set to zero and the time of the beginning was set to zero seconds. The curves for the separate tests (5-10 indents) were averaged using the software OriginLab (averaged over full X range with linear interpolation and 1000 points).

5.4.3.1 Level 1 – Multiple Crystallites

The tests on multiple crystallites were carried out with a 5 µm tip. Two loading directions were employed: parallel and perpendicular to the predominant crystallite orientation. Figure 35 shows the displacement at maximum load for the dry samples. For SiO_2 and Al_2O_3 the displacement varies only slightly over the hold period. The inset shows the complete 900 s of the hold segment, where it can be seen, that the displacement of the other samples reaches a plateau quite early, after about 100 s. Therefore, this more interesting part of the curves will be the focus of the analysis. For the enamel and the HAP sample, after reaching the load of 5 mN, the displacement shows a sharp increase for about 25 s. Then it slows down and reaches a plateau of ~2 nm for HAP and 5-9 nm for the enamel samples. The exact values for the displacement at maximum load and amount of recovery for all sample states can be found in Supplementary Table 4. The untreated enamel sample tested perpendicular to the load direction has the lowest maximum displacement. After unloading to 95% of the maximum load (Figure 36) the HAP, SiO_2 and Al_2O_3 sample show an almost constant displacement. The enamel samples, however, show recovery. The displacement decreases rapidly over 25-50 s from the initial value of 3.5-5 nm, when it slows down and reaches a plateau after about 100 s. The untreated enamel sample in parallel direction shows the largest recovery, recovering about 72%

of the displacement at maximum load (recovery of 4.7 nm from a displacement at maximum load of 6.5 nm).

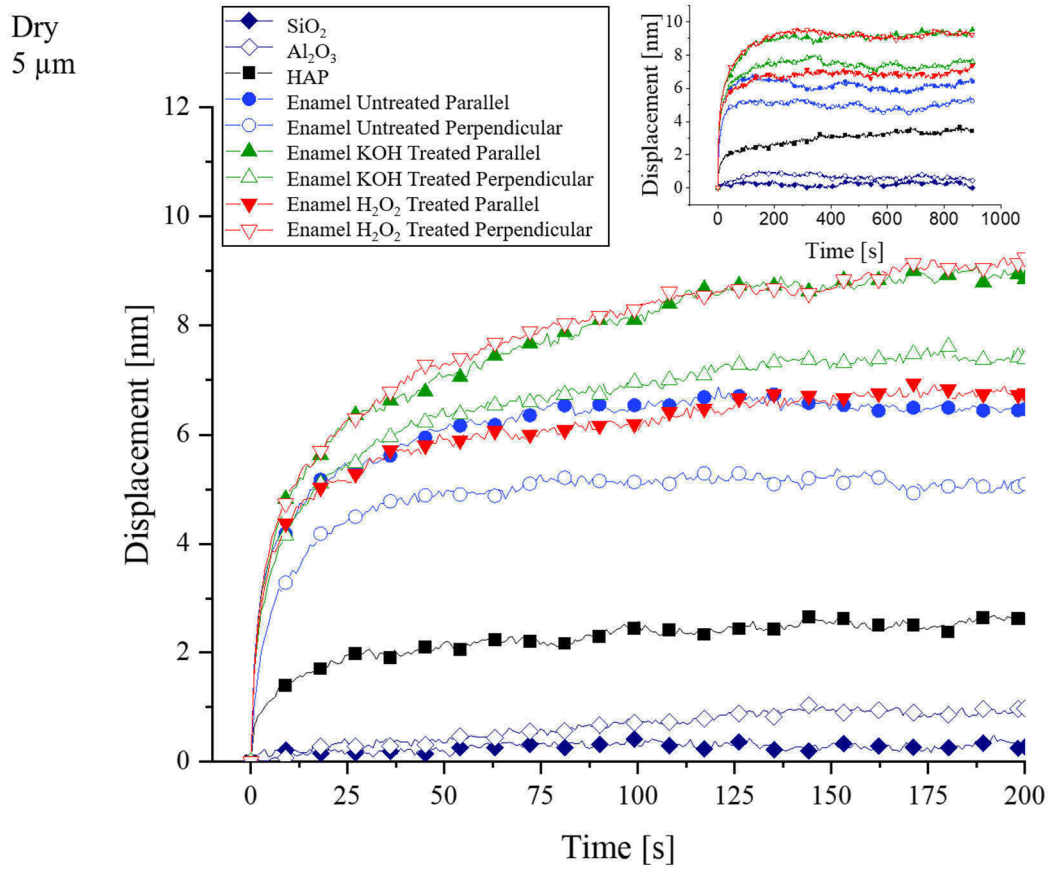

Figure 35: Average displacement over time during the first 200 s of the hold segment at max. load (5 mN) and during the complete 900 s (inset) in dry state. A plateau is reached after about 100 s, after which the displacement only varies slightly. For Al_2O_3 and SiO_2 the displacement stays almost constant, showing no creep. HAP shows some creep but considerably less than the enamel samples. Between the enamel samples some variation can be seen, with the untreated enamel in perpendicular direction showing the least creep of all enamel samples.

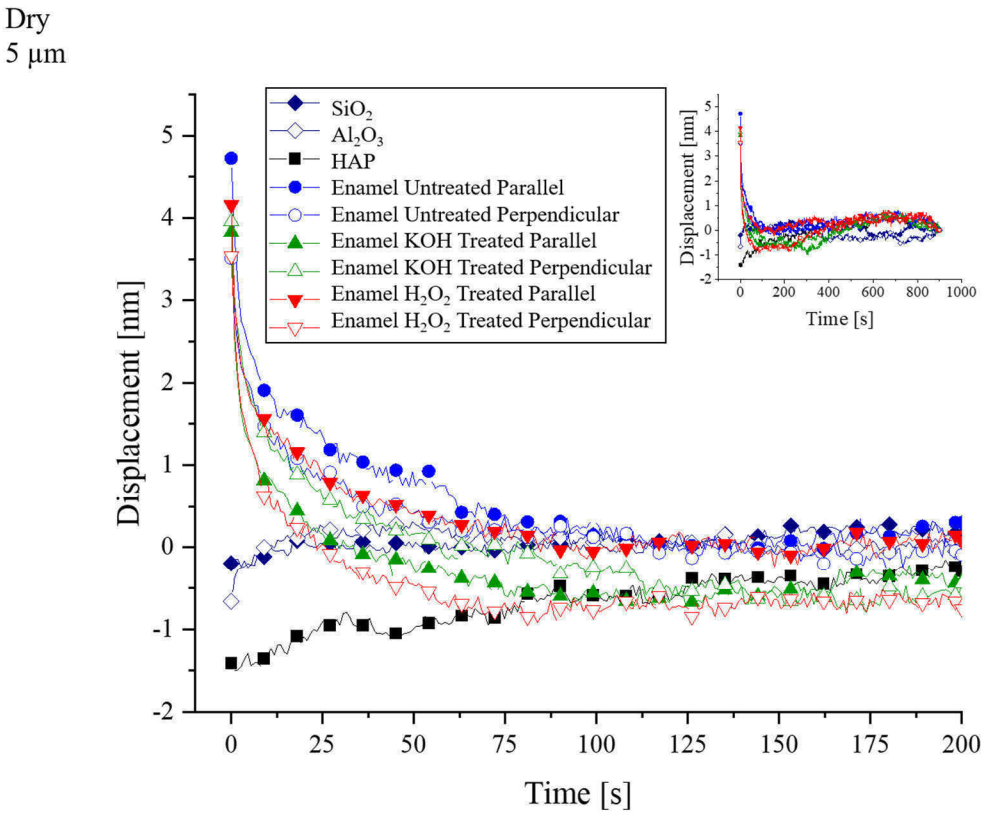

Figure 36: Average displacement over time during the first 200 s of the hold segment at min. load (95% of max. load) and during the complete 900 s (inset) in dry state. A plateau is reached after about 100 s, after which the displacement only varies slightly. For Al_2O_3, SiO_2 and HAP the displacement stays almost constant, showing no recovery. Between the enamel samples some variation can be seen, with the untreated enamel in perpendicular direction showing the least recovery of all enamel samples.

The displacement at maximum load and recovery after unloading for the wet samples tested with the 5 µm tip are shown in Figure 37 and Figure 38, respectively. The general behavior is similar to the dry state. After reaching the maximum load the displacement continues to increase sharply until a plateau is reached after about 100 s. Similarly, after unloading the displacement is also not changing considerably anymore after about 100 s. Thus, only the first 200 s of the respective hold segment are shown. The silica and alumina also show no creep or recovery in the wet state. However, the enamel samples all show roughly twice the amount of creep and recovery compared to their dry state. In this case, the highest amount of creep is observed for the untreated enamel in perpendicular direction with about 20 nm, whereas the untreated enamel in parallel direction only reaches a creep of about 15 nm. Of the enamel samples, the H_2O_2-treated enamel shows the least amount of creep with about 10 nm and only minor differences

between the two loading directions. As for the dry enamel, no clear dependence of the creep on the loading direction could be observed.

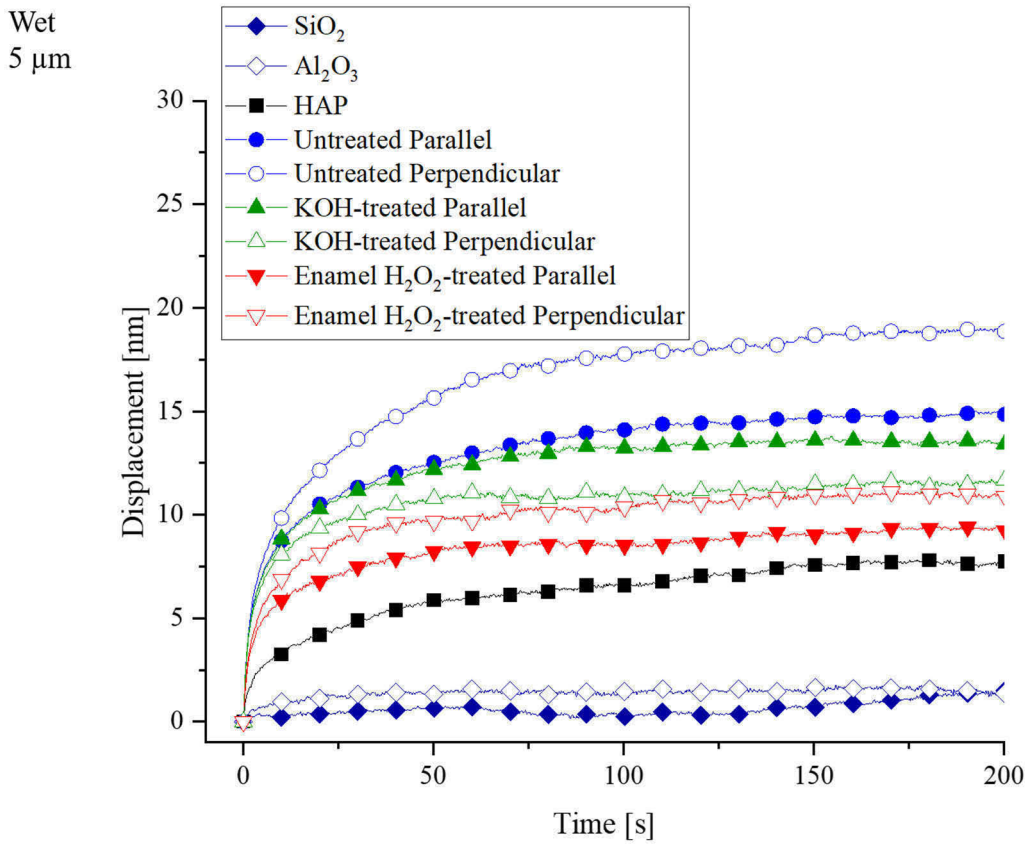

Figure 37: Average displacement over time during the first 200 s of the hold segment at max. load (5 mN) in wet state. For Al_2O_3 and SiO_2 the displacement stays almost constant, showing no creep. HAP shows some creep but less than the enamel samples. Between the enamel samples some variation can be seen, with the untreated enamel in perpendicular direction showing the most creep of all enamel samples and the H_2O_2-treated enamel showing only slightly more creep than the HAP.

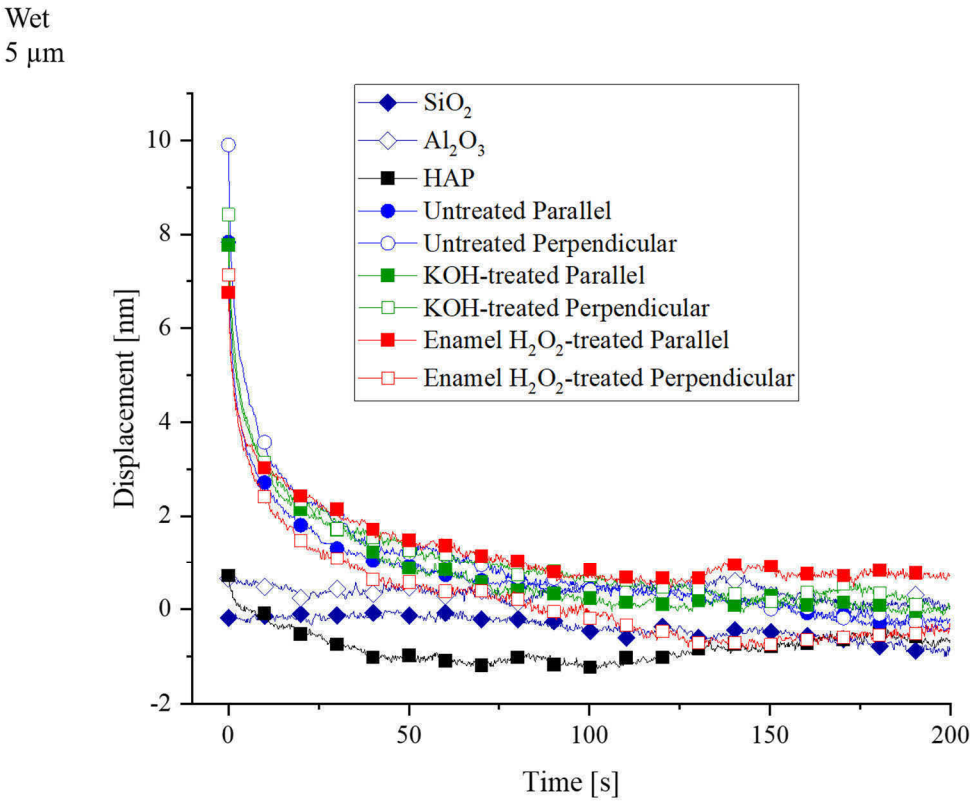

Figure 38: Average displacement over time during the first 200 s of the hold segment at min. load (95% of max. load) in wet state. For Al_2O_3, SiO_2 and HAP the displacement stays almost constant, showing no recovery. Between the enamel samples some variation can be seen, with the untreated enamel in perpendicular direction showing the most recovery of all enamel samples.

5.4.3.2 Level 2 – Multiple Enamel Rods

The tests on multiple enamel rods were carried out with a 50 µm tip. Two loading directions were employed: parallel and perpendicular to the predominant rod orientation. Figure 39 and Figure 40 show the change in displacement at maximum load and the recovery after unloading for the dry samples, respectively. The exact values for the displacement at maximum load and amount of recovery for both the wet and dry state can be found in Supplementary Table 4.

After reaching the maximum load the displacement still rapidly increases for about 25 s after which it slows down, and a plateau is reached after about 100 s. This mirrors the behavior of the creep observed with the 5 µm tip. For Al_2O_3, SiO_2 and HAP the displacement stays almost constant, showing no creep. Between the enamel samples some variation can be seen, with the untreated enamel in parallel direction showing the most creep of all enamel samples with roughly 36 nm creep. Of the enamel samples, the H_2O_2-treated enamel shows the least amount

of creep with ~27 nm. Untreated enamel in perpendicular direction shows less creep (32 nm) than in parallel direction, whereas for the treated enamel only minor differences occur.

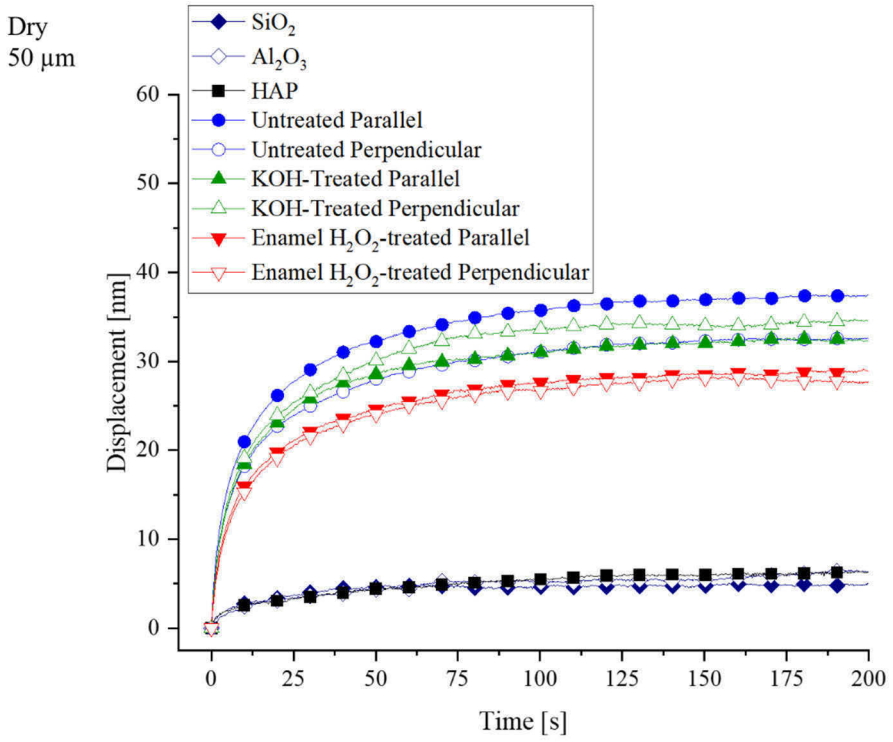

Figure 39: Average displacement over time during the first 200 s of the hold segment at max. load (150 mN) in dry state. For Al_2O_3, SiO_2 and HAP the displacement stays almost constant, showing no creep. Between the enamel samples some variation can be seen, with the untreated enamel in parallel direction showing the most creep of all enamel samples and the H_2O_2-treated enamel showing the least amount of creep.

Similarly, the recovery behavior mirrors the curve for the measurements with the 5 µm tip. In the enamel samples at first a sharp decrease in displacement occurs and a plateau is quickly reached. The untreated enamel measured with loading direction parallel to the HAP crystallites shows the highest recovery with ~30 nm. Here the KOH-treated enamel measured in parallel direction shows the least amount of recovery (~19 nm). Except for the KOH-treated enamel, no difference in recovery depending on loading direction can be observed. Al_2O_3, SiO_2 and HAP show no considerably recovery.

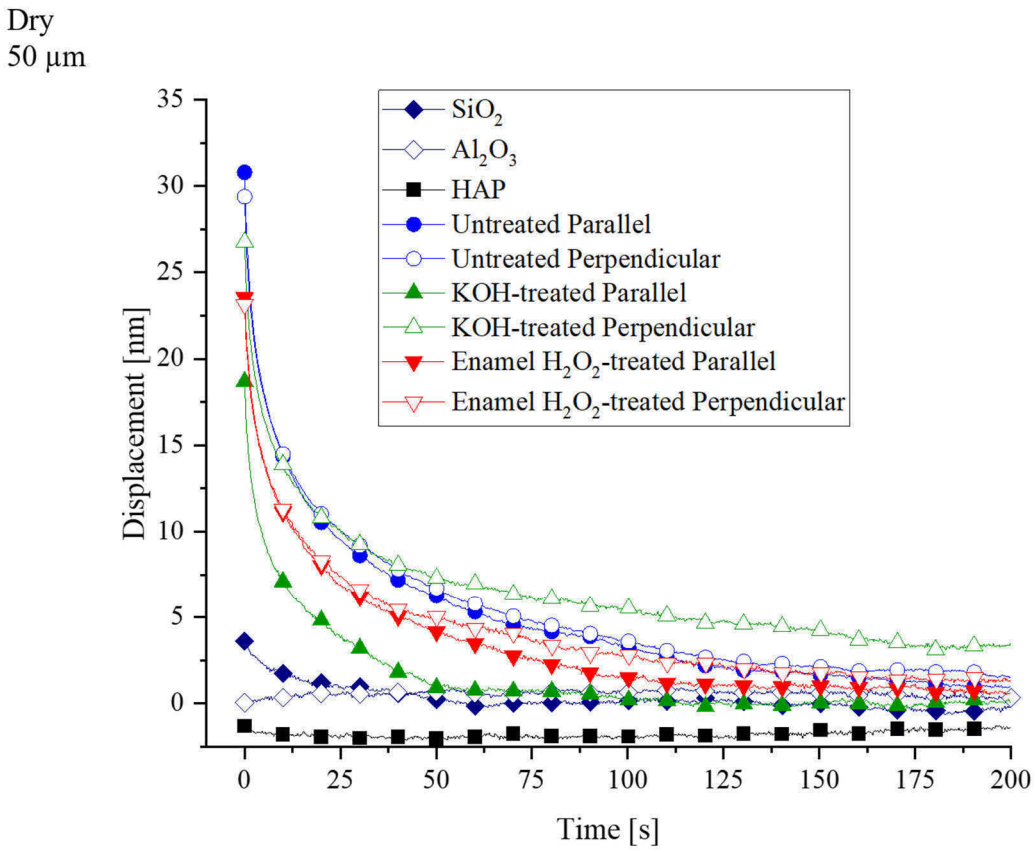

Figure 40: Average displacement over time during the first 200 s of the hold segment at min. load (95% of max. load) in dry state. For Al_2O_3, SiO_2 and HAP the displacement stays almost constant, showing no recovery. Between the enamel samples some variation can be seen, with the untreated enamel in parallel direction showing the most recovery of all enamel samples.

The creep and recovery behavior of the wet samples (Figure 41 and Figure 42) is similar to their dry state with a sharp increase/ decrease at first followed by a plateau afterwards. As for the dry samples, the untreated enamel in parallel direction also shows the most creep in the wet state with ~43 nm. The KOH-treated enamel shows almost the same behavior and amount of creep, whereas the creep in the H_2O_2-treated enamel is lower (~31 nm). No differences between loading directions can be seen for the enamel samples. The creep in the HAP sample is increased about two-fold compared to its dry state. In contrast silica and alumina show no creep when measured in the wet state.

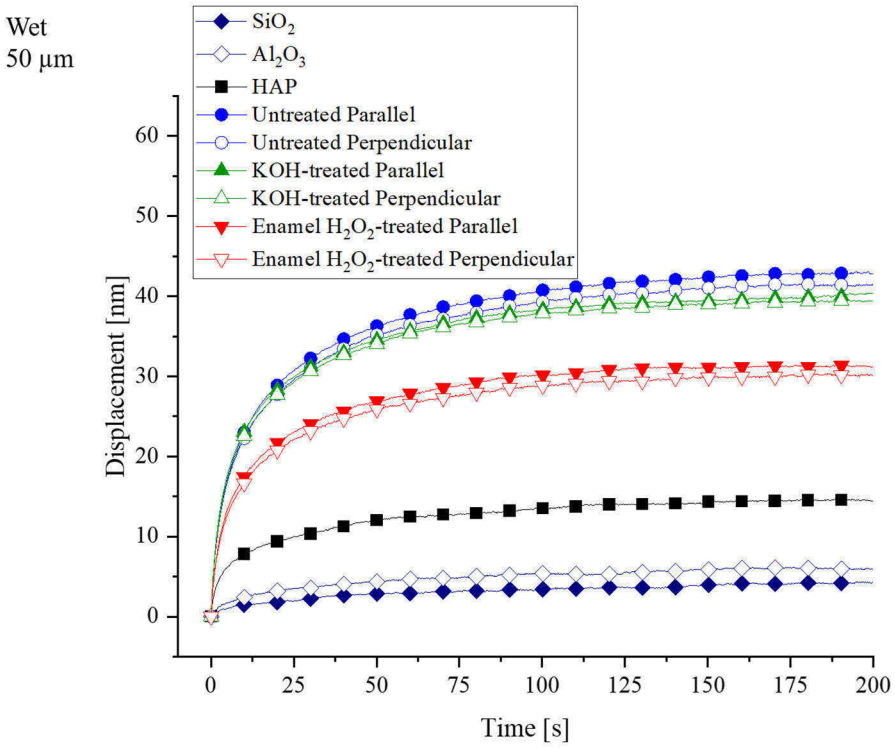

Figure 41: Average displacement over time during the first 200 s of the hold segment at max. load (150 mN) in wet state. For Al_2O_3 and SiO_2 the displacement stays almost constant, showing no creep. HAP shows some creep but considerably less than the enamel samples. Between the enamel samples some variation can be seen, with the untreated enamel in parallel direction showing the most creep of all enamel samples and the H_2O_2-treated enamel showing the least creep.

The recovery follows again the same behavior as before: a sharp decrease followed by a plateau. The silica and alumina samples show no recovery. The HAP sample however recovers some displacement (~8 nm). For the enamel samples considerably more recovery as for the synthetic ceramics can be observed. Untreated enamel measured in parallel direction again shows the highest amount of recovery with about 43 nm. The H_2O_2-treated enamel shows the lowest amount of recovery with about 32 nm. While for untreated enamel in perpendicular direction less recovery (~37 nm), than for the parallel direction could be observed, for the treated enamel the loading direction did not have an influence on recovery.

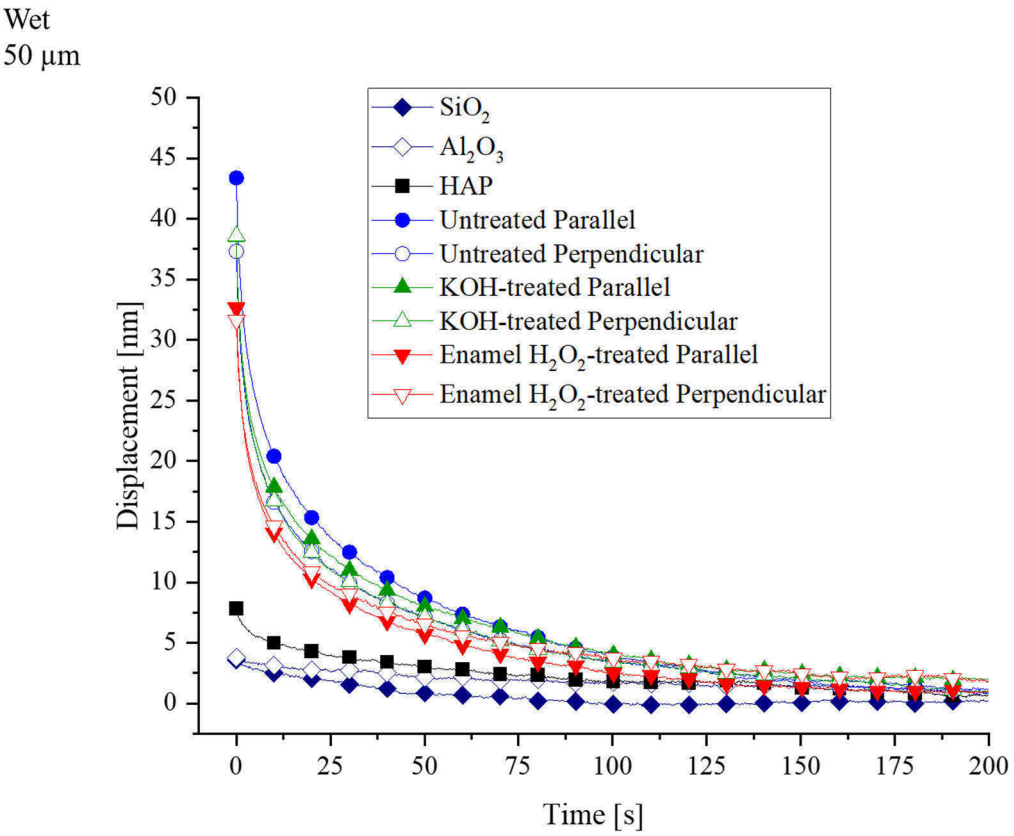

Figure 42: Average displacement over time during the first 200 s of the hold segment at min. load (95% of max. load) in wet state. For Al_2O_3, SiO_2 and HAP the displacement stays almost constant, showing no recovery. Between the enamel samples some variation can be seen, with the untreated enamel in parallel direction showing the most recovery of all enamel samples

5.4.4 Load Rate Effects

The load displacement curves for the creep experiments with the CLH method with 3 hold segments in total (method 2), show that plastic deformation occurs during the loading of dental enamel. As the creep process seems to occur quite rapidly in dental enamel, it was considered that creep occurs already during the loading to maximum load. In order to test this hypothesis, indentations with varied load rates (where load and unload rate are equal) and a shorter hold segment at max. load (100 s), as described for method 3, were carried out on the enamel samples and the silica reference.

Figure 43 and Figure 44 show the averaged (n = 4-10) load displacement curves of the silica and enamel samples measured in dry and wet state respectively. The drift corrected data was shifted to the left such that the end point of the hold segment was at zero displacement for all

samples in order make the curves more comparable. The slopes for the dry silica sample for the different load rates during loading and unloading are similar. In the dry enamel samples however, the loading slope is less steep than the unloading slope, for all sample treatments. The slope also appears to be dependent on the load rate. For all sample treatments the loading slope for the faster load rates (5 and 10 mN/s) are steeper than for the slower rates. The load displacement curves for dry untreated enamel and the dry deproteinized samples are very similar.

Looking at the onset of the loading and the onset of unloading, some observations can be made: With faster load rates, the initial part of the loading deviates from the Hertzian curve that would be expected for an elastic contact. Additionally, at the onset of unloading the slope is almost vertical for the faster load rates. This occurs for all enamel samples and even the silica sample. Comparing the displacement at maximum load and after unload, it can be seen, that the segments increase in length for faster load rates, which would speak to time dependent processes occurring. As these features could even be observed in the silica at fast load rates, instrument issues are suspected and will be discussed in detail at a later point (ch. 6.4.1).

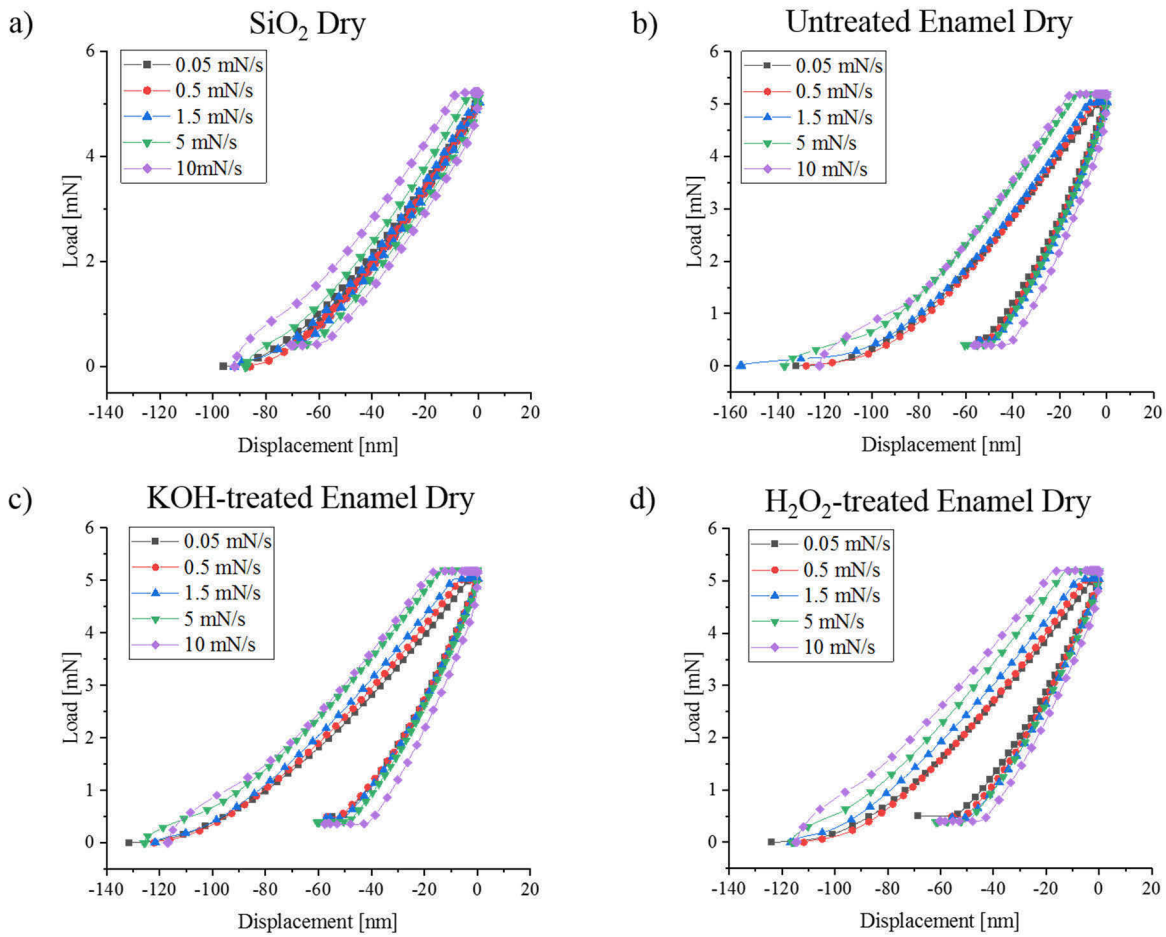

Figure 43: Averaged load displacement curves for the silica sample (a) and different enamel samples (b-d) in dry state. For the enamel samples the slope of the load and unload differ. Faster load rates (5 and 10 mN/s) in enamel samples show a steeper slope compared to slower ones (0.05-1.5 mN/s). However, the enamel samples show similar behavior, regardless of their treatment.

The measurements in wet state (Figure 44) show the same observations regarding the influence of the load rate as observed for the dry state: with faster rates loading and unloading slopes get steeper and the displacement at maximum load increases for all samples. While for the silica sample the dry and wet measurements show no difference (i.e. similar slope during loading and unloading and similar total displacement) there are differences for the enamel samples. Whereas in the dry state the displacement at max. load was ~120-140 nm, for all sample treatments, for the wet enamel displacements ≥ 160 nm were recorded. This changes the slope of the curve and speaks to a lower elastic modulus. For the KOH-treated enamel again the increase in displacement at max. load with a faster load rate is visible, whereas for the untreated and H_2O_2-treated enamel, there is no clear effect of the load rate.

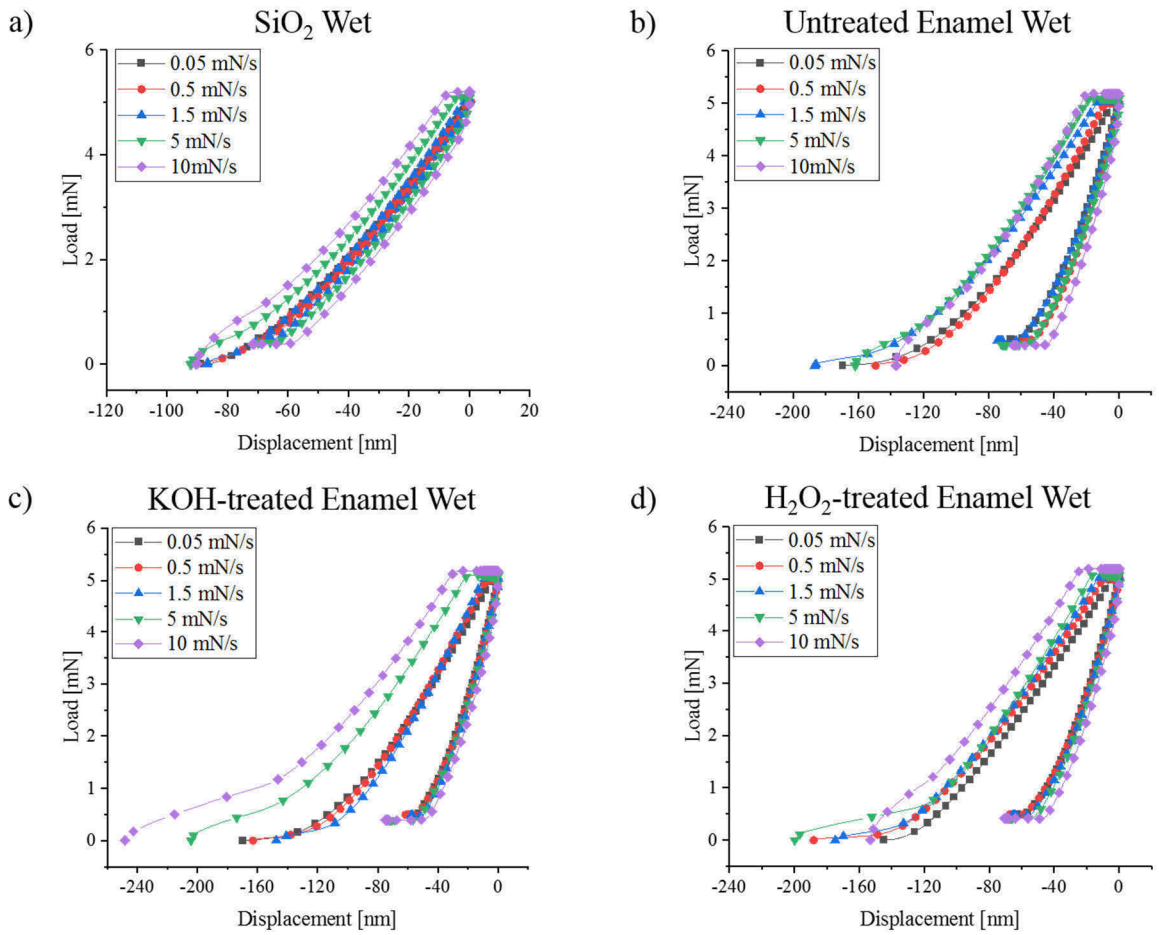

Figure 44: Averaged load displacement curves for the silica sample (a) and different enamel samples (b-d) in wet state. For the enamel samples the slope of the load and unload differ. Faster load rates (5 and 10 mN/s) in enamel samples show a steeper slope compared to slower ones (0.05-1.5 mN/s). However, the enamel samples show similar behavior, regardless of their treatment.

The elastic moduli have been calculated by fitting the loading curve, excluding values below 1 mN, with the Hertz equation for a perfect elastic contact (equation (16)). In order to compare unloading with loading, the elastic modulus has also been calculated from the unloading curve, excluding values above 4 mN and below 2.5 mN, according to the method from Oliver and Pharr [147]. In both cases the averaged curves for the respective sample treatments and load rates (as shown in Figure 43 and Figure 44) were used. Figure 45 shows the calculated values for the different load rates, sample treatments and measurement conditions. The moduli calculated from unloading, ranging from ~45 to 80 GPa (with on outlier at ~9 GPa for the KOH-treated wet enamel at 10 mN/s where fitting of the curve did not work well), are higher than from loading, ranging from ~20 to 50 GPa. Generally, the elastic modulus of wet enamel is about 10 GPa lower than for dry enamel. There is neither a clear trend in elastic modulus

depending on the load rate, neither on sample treatment. Dry deproteinized and untreated enamel samples all show a mean elastic modulus, across all load rates of ~50 GPa (loading) or ~60 GPa (unloading), whereas wet enamel samples have a mean elastic modulus of ~30 GPa (loading) or ~50 GPa (unloading). The exact values and standard deviations can be found in Supplementary Table 6.

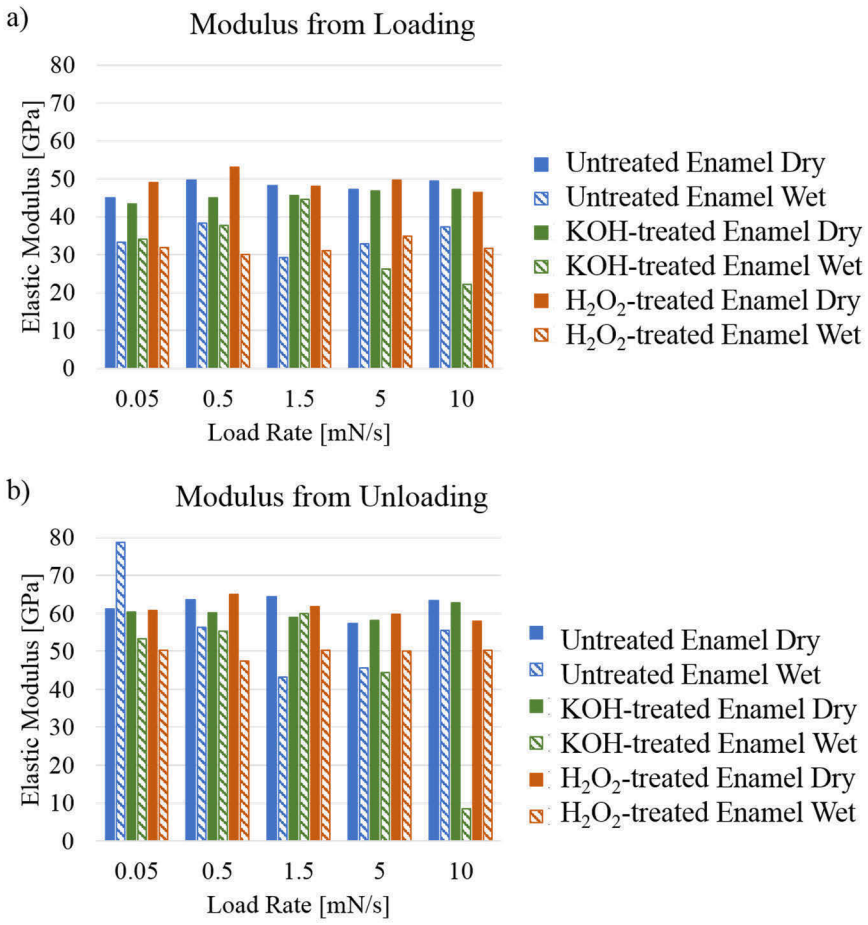

Figure 45: Elastic moduli calculated from Hertzian fit on the loading curve or the Oliver and Pharr method using the unloading curve (range from 4 mN to 2.5 mN). The moduli calculated from unloading are higher than from loading (with on outlier where fitting of the curve did not work well). Barring a couple of exceptions, the elastic modulus of wet enamel is lower than for dry enamel with little difference between deproteinized and untreated enamel. No clear trend with regard to the load rate is recognizable.

Figure 46 and Figure 47 show the averaged (n = 4-10) displacement over time at maximum load for the dry and wet state respectively. The displacement at the start of the creep segment was set to zero in order to compare all measurements with each other. The start point of the hold segment is automatically marked by the indenter software. However, it was observed that

the indenter speed still changed for the first two measurement points in the silica data. Hence, these two data points were omitted for all samples and treatments. The displacement in dry silica stays mostly constant at a low level during the holding period, while in the enamel samples, there is a fast increase in displacement during the first ~20s after which a plateau is reached. The creep in enamel samples is similar, regardless of their treatment. In all enamel samples the least creep occurs with the slowest load rate of 0.05 mN/s, but there is little difference between the creep with faster load rates. The total creep is similar for the untreated and deproteinized samples with ~3-4 nm for the slowest load rate and ~6 nm for the faster rates.

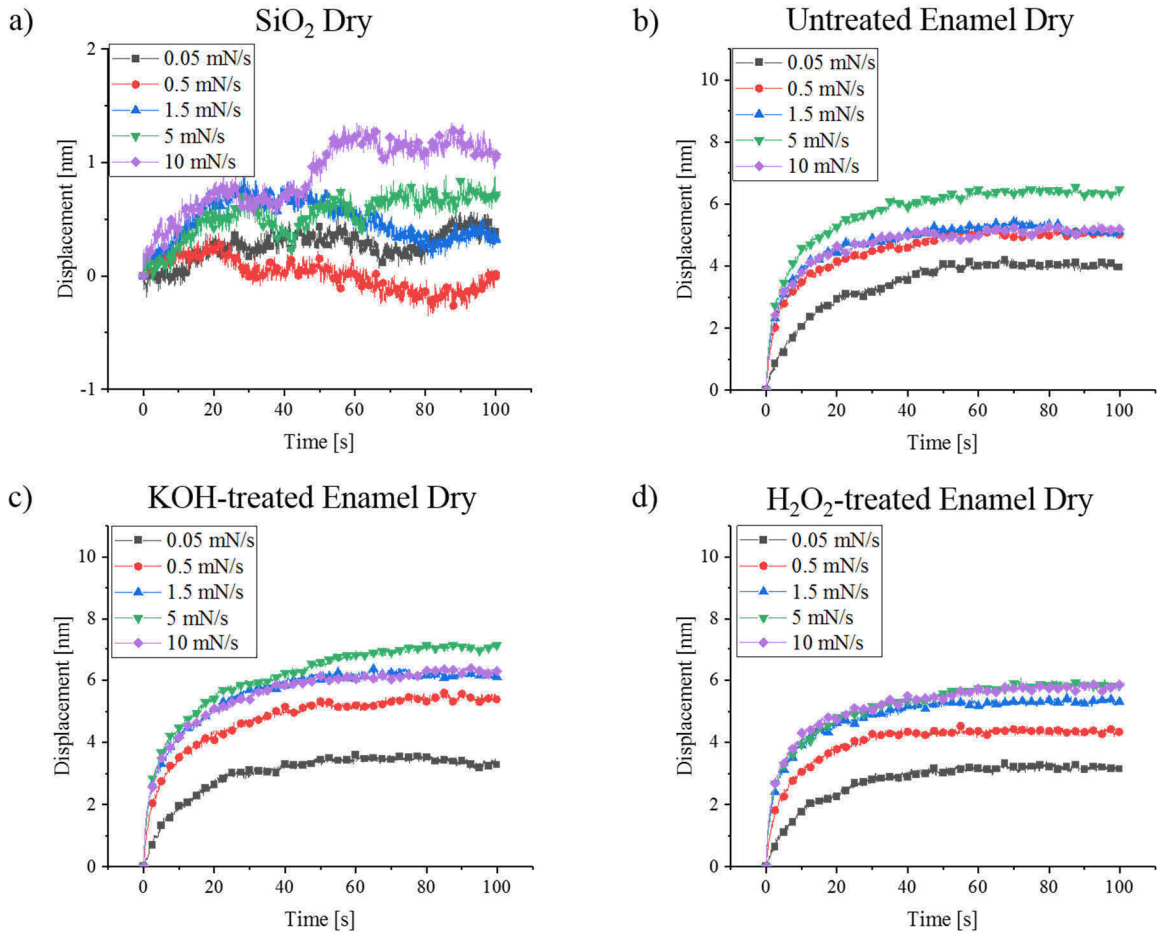

Figure 46: Displacement over time during the hold segment at maximum load for the different load rates on dry samples a) SiO_2 crystal b) untreated enamel c) KOH-treated enamel and d) H_2O_2-treated enamel.

Except for the silica, all wet samples show more creep in wet state (Figure 47) compared to their dry state. Wet silica shows the same behavior as dry silica, with an almost time-independent displacement at a low level. In general, all enamel samples show a similar behavior, with a steep increase in the beginning and a plateau that is reached after ~40s.

However, the total displacement is higher for the wet samples, reaching up to 14 nm for the KOH-treated wet enamel at 10 mN/s load rate. The untreated wet enamel also shows twice the displacement than recorded for the dry sample, whereas the H_2O_2 sample shows a 1.5-fold increase in displacement (10 nm). For the all enamel samples there are clear differences between the slowest and fastest load rate, but the trend for the intermediate load rates is less clear. For the KOH sample no difference can be observed between the 0.5 and 1.5 mN/s load rate, and the 1.5 and 5 mN/s load rate. For the untreated and H_2O_2-treated enamel the load rates above 0.05 mN/s all show roughly the same creep and no clear trend can be seen.

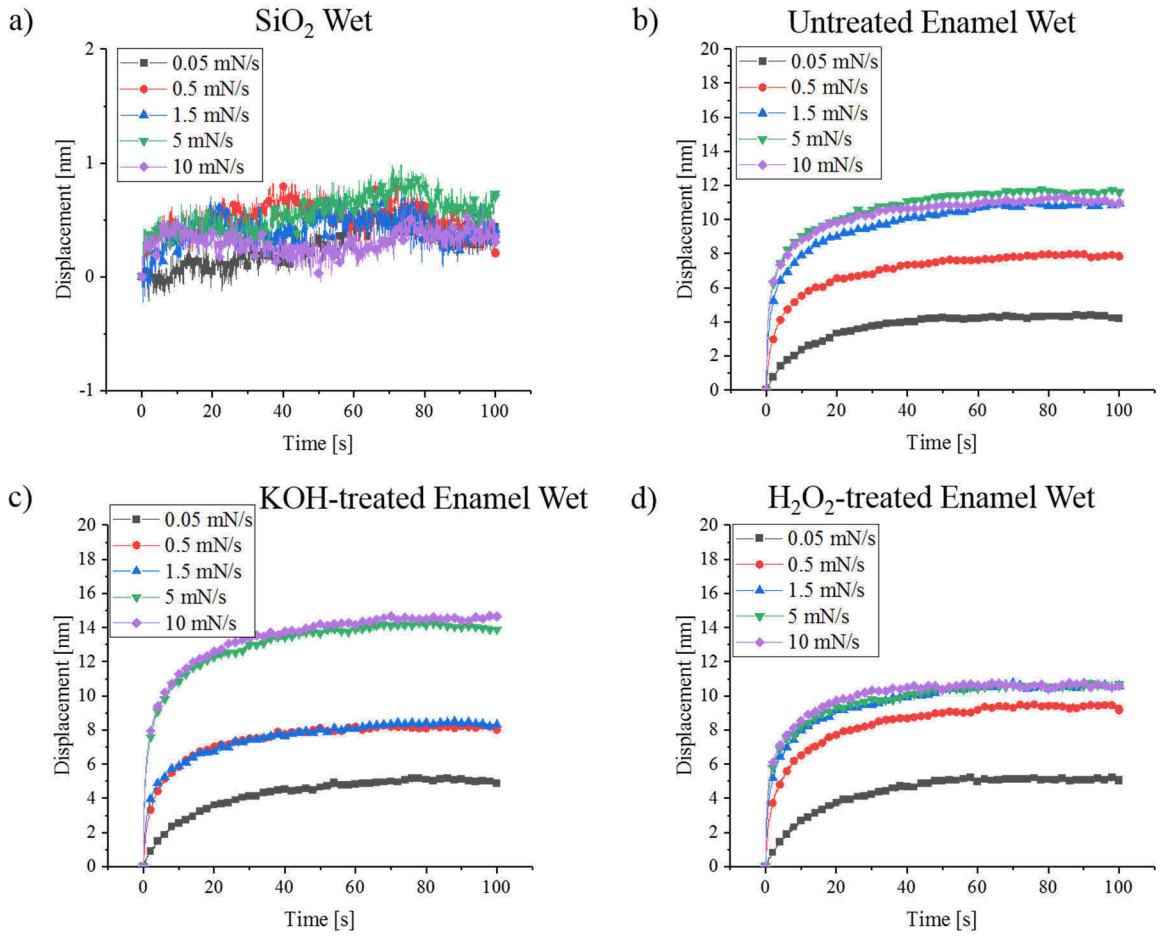

Figure 47: Displacement over time during the hold segment at maximum load for the different load rates on wet samples a) SiO_2 crystal b) untreated enamel c) KOH-treated enamel and d) H_2O_2-treated enamel.

5.4.5 Modelling of Experimental Data

The averaged displacement-time curves for the creep experiments with both method 2 and method 3 were fitted with three different models using combinations of springs and dashpots according to Menčík et al. [162] as shown in Figure 48. In order to perform the curve fitting the relationship resulting from forming the compliance function related to the spring and damper properties (37) needs to be transformed into a function suitable for computational regression analysis (38).

$$h^{\frac{3}{2}}(t) = PK_S\left[C_0 + c_v\left(t - \frac{t_R}{2}\right) + \sum C_i\left(1 - \rho_i e^{-t/\tau_i}\right)\right] \quad (37)$$

$$h^{\frac{3}{2}}(t) = PK_S\left[B + c_v t - \sum D_i e^{-t/\tau_i}\right] \quad (38)$$

With load P, geometric constant for the spherical indenter $K_S = \frac{3}{8\sqrt{R}}$, compliance constants C_i, ramp time t_R, retardation time τ_i, viscous compliance c_v related to the dynamic viscosity as $c_v = 1/\eta_v$ and ramp correction factor ρ_i. From the relationships (39) - (41) the compliance constants and viscosity can be determined from the regression constants.

$$\rho_i = \frac{\tau_i}{t_R}\left(e^{t_R/\tau_i} - 1\right), \text{ with } i = 1, 2, 3 \ldots \quad (39)$$

$$C_i = \frac{D_i}{\rho_i}, \text{ with } i = 1, 2, 3 \ldots \quad (40)$$

$$C_0 = B + \frac{c_v t_R}{2} - \sum_{i=1}^{n} C_i \quad (41)$$

[162].

Only the first 200 s were used for the tests with method 2 and only the creep at maximum load was used for the experiments conducted with method 3. The resulting time constants and coefficient of determination R^2 are given in Supplementary Table 7 - Supplementary Table 12.

a) Model 1

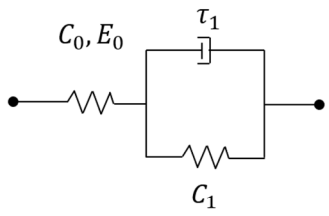

$$h^{\frac{3}{2}}(t) = PK_S\left[C_0 - C_1\left(1 - e^{-t/\tau_1}\right)\right]$$

b) Model 2

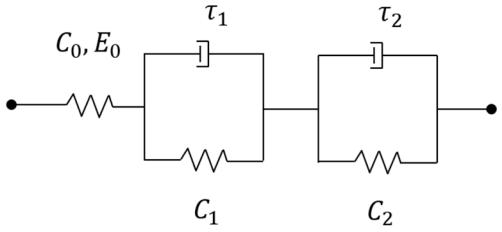

$$h^{\frac{3}{2}}(t) = PK_S\left[C_0 - C_1\left(1 - e^{-t/\tau_1}\right) - C_2\left(1 - e^{-t/\tau_2}\right)\right]$$

c) Model 3

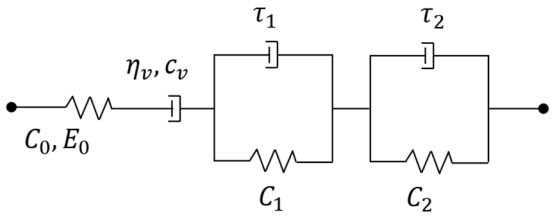

$$h^{\frac{3}{2}}(t) = PK_S\left[C_0 + c_v\left(t - \frac{t_R}{2}\right) - C_1\left(1 - e^{-t/\tau_1}\right) - C_2\left(1 - e^{-t/\tau_2}\right)\right]$$

Figure 48: Spring and dashpot models to fit creep behavior according to Menčík et al. [162], with geometric constant for the spherical indenter $K_S = \frac{3}{8\sqrt{R}}$*, load P and the spring and dashpot constants* C_i, E_i c_v, η_i *and* τ_i.

Figure 49 and Figure 50 show the time constants for model 1 exemplary for the creep tests with 900 s hold segments (method 2) and the creep tests with varied load rates (method 3), respectively. It can be seen that for the tests carried out with method 2 the time constants for the recovery are much lower than for than for the creep at maximum load. HAP showed no recovery; therefore, fitting was not possible in this case and no time constant could be determined. There is no clear trend for either sample treatment or loading direction. Similarly, the results of the fitting for the creep experiments carried out with method 3 show no clear trend neither for the sample treatment (dry or wet as well as untreated or deproteinized) nor for the load rates applied. However, the time constants calculated for these tests are lower than for the tests carried out with method 2 even for the case where the load rates for both experiments is equal (0.5 mN/s).

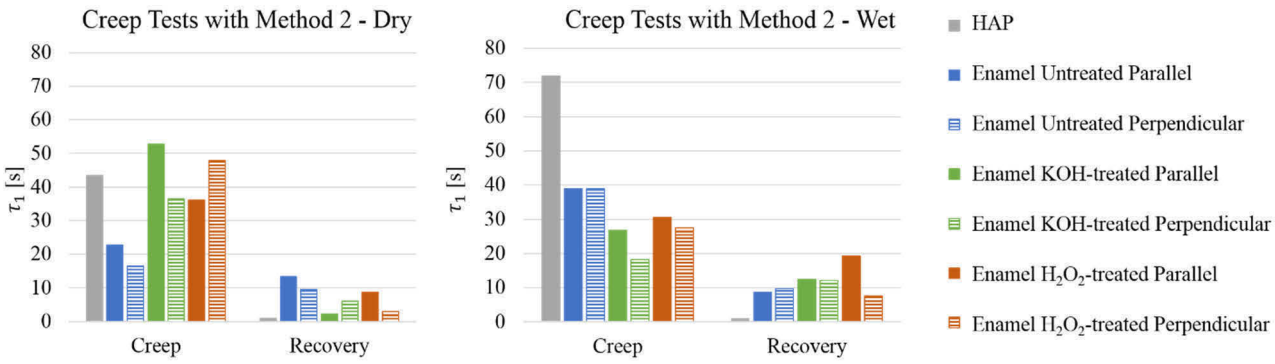

Figure 49: Time constant for creep at maximum load and recovery after partial unloading for HAP and enamel tested with creep method 2 in dry and wet state with the 5 µm indenter. HAP showed no recovery after unloading therefore no time constant could be determined. The time constants for recovery are much lower than for creep.

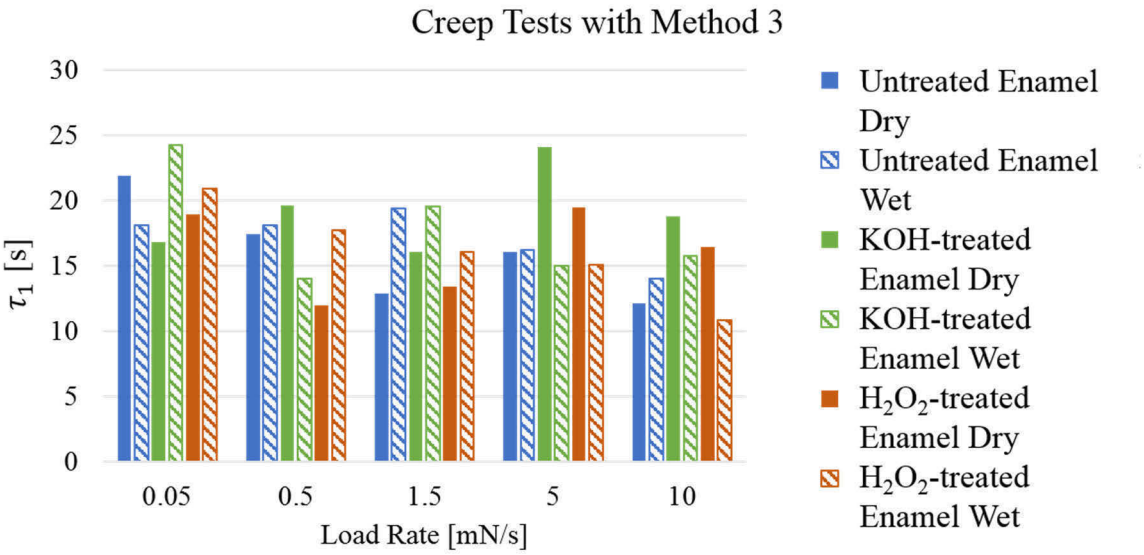

Figure 50: Time constant for creep at maximum load for enamel tested with creep varied load rates (method 3) and the 5 µm indenter. No clear trend depending on sample treatment (dry or wet) and load rates can be distinguished.

6. Discussion

In the following chapter the results from the structural and compositional analyses will be discussed. The discussion of the structural investigation has been published in *Acta Biomaterialia* with the title 'The geometrical structure of interfaces in dental enamel: A FIB-STEM investigation' [63]. The discussion of the structural investigation after deproteination treatment and the compositional analyses has been published in *Materialia* with the title 'Effect of deproteinization treatments on the structure and mechanical properties of dental enamel'. Additionally, the results from the mechanical characterization via nanoindentation and nanoindentation creep tests will be discussed, which has partially been published in *Materialia* with the title 'Effect of deproteinization treatments on the structure and mechanical properties of dental enamel'.

6.1 Morphology of Dental Enamel

The arrangement of rod and interrod bovine enamel differs with distance from dentin as can be seen at lower magnifications (Supplementary Figure 5 and Supplementary Figure 6). In the innermost and inner enamel, the rods seem to be neatly stacked on top of each other and are separated by a sheet of interrod enamel. In contrast, in outer enamel the rod boundaries are more open, with frequent interconnections with interrod enamel. The structure in outer bovine enamel seems to be similar to the one found in human enamel, with rod and interrod enamel appearing as 'keyhole shapes'. A detailed structural description of bovine enamel has been given by Yilmaz et al. [18] and in the following only the new features, observed by TEM will be discussed.

6.1.1 Interfaces in Dental Enamel

As illustrated in chapter 5.1 the rod boundaries in dental enamel are discontinuous structures where crystallites bridge the boundary frequently and confluence between rod and interrod enamel along an area of the rod boundary exists. Additionally, in the STEM images of the untreated enamel (Figure 14, Figure 15 and Figure 21), thin filaments, bridging the rod boundaries, could be observed. The STEM images were collected with HAADF detector (a Z-contrast sensitive technique) and there is little contrast between the filaments and surrounding HAP crystallites, indicating that the filaments also consist of mineral. They are also not more susceptible to beam damage, which would be expected for an organic material. The

deproteinized (KOH-treated) sample, however, did not show these filaments (Figure 21 and Supplementary Figure 6), which indicates an organic material as the basis of the filaments. One possible explanation combining these seemingly contradicting observations could be that the filaments are organic filaments onto which dissolved mineral has precipitated during drying in the vacuum.

The apparent discontinuous nature of the rod boundaries is in good agreement with previous structural descriptions. Several researchers noted a discontinuous nature of the rod sheaths [42,88,89,163] or described them as being absent in mature enamel [71,77,78,87]. Nevertheless, such findings are entirely disregarded in the materials science literature which instead describes the rod boundary as a 'protein sheath' surrounding the enamel rods [8,45,96,103,115,158]. During enamel formation protein 'sheaths' are present and govern the growth of the HAP crystallites and rods, however, the proteins are largely removed by proteases during maturation and these regions are mineralized [67,87,89,164]. This apparent confusion regarding the nature of the 'sheath' may have arisen due to the broad utilization of this term during both the formation and maturation stages of enamel, as laid out in chapter 2.4. Still, some proteins and remnants thereof undoubtedly exist in mature enamel and must be present in unmineralized spaces.

The size (~50 nm in the wider axis and ~25 nm in the short axis) and shape of the crystallites observed in this work is in good agreement with the literature. Selvig and Halse [165] measured a mean width of 45 nm and Xue et al. [102] reported widths of 10-24 nm and lengths of 12-50 nm for mature mouse and human enamel, respectively. In addition, Selvig and Halse also observed variations in the crystallites' shape. In the outer enamel regions, more regular hexagonal crystal shapes dominated, whereas in the inner enamel regions the profiles changed to more irregular shapes. The crystallites were mostly separated by a thin electron lucent line, but some crystallites seemed to be in direct contact with each other [165]. Crystallites have also been described as fusing with each other during remineralization processes [166], adjoining [88] or pressing against each other and interlocking [86]. These findings are in good agreement with the narrow gap size between the crystallites observed in this work. In Figure 16 approximately the cross-section of one enamel rod can be seen and its area porosity has been determined as 2.5% by image analysis. On the one hand, there are large areas where crystallites are in direct contact with each other. On the other hand, there are some larger gaps, where possibly, crystallites were broken out during sample preparation. The width of the interface

region between two crystallites varies and may span a few Å up to about 2 nm (Figure 17 and Figure 18). Concerning the existence of proteins in the interface between crystallites, the size of the gap and the organic structures must be considered. Proteins are chains of peptides and can reach large sizes, which by far exceed a couple of nanometers. The dental enamel proteins have mostly been characterized in the developmental stage of enamel formation. Here, amelogenin is present as nanospheres with a diameter of about 20 nm [35] and with a molecular weight of circa 20 kDa [69] it is one of the smaller enamel proteins. However, during maturation the proteins are mostly broken down and removed so that only remnants and amino acids are left [41,80,82,167]. These remnants, as well as small proteins, might fit into the larger gaps between the crystallites, especially if the proteins assume an elongated shape. Still, with only very limited space available between the crystallites, it remains questionable that every crystal is covered by a complete organic sheath; a conclusion that has already been previously doubted by various researchers [61,65]. Therefore, based upon these images it is far more plausible that protein remnants would be found, not on the crystal faces, but in the triple junctions where there are larger gaps. This was also recently reported by two research groups where organic precipitates could be found with atom probe tomography (APT) at such triple junction points. It was also noted that the interface between the crystallites was found to be an amorphous mineral phase with a high Mg content [109,110].

6.2 Influence of Deproteinization on Composition & Structure

In the following chapter the results of the compositional analysis with regards to the success of the removal of the proteins and the effect of the various deproteination methods on the enamel's structure will be discussed.

6.2.1 Verification of Deproteinization

The TGA curves (Figure 22) of dental enamel show a continuous mass loss across the whole temperature range. This behavior has been observed before and is due to biological apatite not being stoichiometric and containing carbonate, which will be evaporated and decomposed already beginning at 100°C and continuing at higher temperatures [52]. The HAP shows different decomposition peaks than the enamel samples as it does not contain organic material and is less carbonated than biological apatite. Specifically, for the HAP, there is no peak at 550°C, hence in this work, this peak was attributed to the loss of organic material. For enamel, there are two peaks at 305 and 400°C, which is in the temperature range attributed to loss of organic (200-600°C). However, they also occur in HAP, albeit slightly shifted, and thus cannot

solely be attributed to the loss of organic. There are some variations between the TGA curves of the enamel samples below 200°C, which are related to a variation in water content, and in the range 200-450°C. After 200°C the curves for the untreated and the H_2O_2-treated enamel are running parallel which means that the same decomposition processes take place in both.

Literature gives a wide range of literature values for organic content with 0.3-11 w% (for human and bovine enamel) [5,19–22]. The mass losses of all samples (1.4-2.3 w%) determined in this work lie within this range. However, the mass loss in this temperature range is attributed to the loss of organic material, carbonate and structurally incorporated water and therefore cannot be equated with the organic content. Holcomb and Young saw a sharp loss of structurally incorporated water at 250-300°C and a strong CO_2 evolution at 360°C and 460°C, starting as early as 180°C [52]. In this work, the enamel samples show two peaks at about 300°C and about 400°C, which are slightly moved compared to the synthetic HAP sample. This might be due to additional organic matter and different binding energy of structurally incorporated water adding a shoulder to the peak.

Compared to enamel, HAP shows a lower mass loss, which was expected as it does not contain any organic material. The KOH-treated enamel shows a lower mass loss compared to the untreated enamel, suggesting a lower organic content and therefore a successful deproteinization. This is supported by the fact that the mass loss across the complete temperature range for the KOH-treated enamel and the HAP are almost the same (compare TGA curves in Figure 22) and that the mass loss for 200-600°C is similar. The H_2O_2-treated enamel, however, has an even higher mass loss than the untreated enamel and therefore seems to still contain organic material. This finding might result from the different deproteinization process of both chemical deproteinization methods. During the KOH-treatment the sample is placed in KOH solution for 9 days; the OH-ions split the peptide bond of the amino acids and the proteins are dissolved. Yahyazadehfar et al. controlled the progress of deproteinization by measuring the protein concentration in the solution via UV-Vis [49]. During H_2O_2-treatment, the tooth is treated with a peroxide containing gel. Here, the peptide bonds are also attacked by the ions; however, it seems likely that due to the much shorter treatment time, the protein fragments remain inside the tooth. Rathsam et al. showed a significant reduction in protein content after H_2O_2-treatment, via protein assay [40], but as this method is based on molecular weight, small protein fragments would not be detected. This fragmentation would affect the

proteins in their functionality but would not be detected by TGA as here only weight loss is measured.

The FTIR measurements revealed several interesting features that warrant discussion. For instance, the 200°C sample shows less intense peaks than all other samples This might be due to an unfavorable distribution of enamel material or other defects in the KBr pellet. Distinct organic peaks that were described in literature (2000-2500 cm^{-1} [160]) and the amide I peak (1650 cm^{-1} [160,161]) were absent in this work. This could be the result of the only minor amount of organic material in dental enamel, which is at the detection limit of the FTIR [48]. A distinct peak at 1550 cm^{-1} has been identified in untreated enamel but is absent in HAP. Its intensity is reduced in the heat-treated enamel samples. This peak is likely related to CO_3, which is present in the untreated enamel but is removed with treatment at increasing temperatures [26]. CO_3 ions are commonly substituted in biological HAP [29,31] and the crystal structure of HAP is known to change during heat treatment due to the loss of water and carbonate [52]. The intensity of this peak is also reduced in the chemically treated enamel, which means that the deproteinization agents interact with the carbonate. Another weak peak (shoulder) can be seen at 1425 cm^{-1} for the untreated enamel. Literature gives peaks in this region as N-H vibrations of organic components [26,168] or as 'organic material' (1530–1380 cm^{-1}). However, several CO_3 peaks are also present in this region [26,160,169] - with a prominent double peak at 1456 and 1422 cm^{-1} which is related to type B carbonate [169,170] - which may be overlapping with signals of organic components. The signal from untreated enamel shows a shoulder in the peak at 1425 cm^{-1}, which is absent in HAP, therefore resulting from the overlap with an additional organic component. For the chemically deproteinized enamel this shoulder is less pronounced and the intensity decreases with increasing temperatures during heat treatment indicating successful deproteinization.

The organic content may be overestimated by not accounting for the loss of carbonate and water as part of the weight loss during TGA as discussed earlier. Excluding studies that determined the organic content by TGA [19–21,171], the reported organic content of dental enamel is given as 0.6-4.4 w% [5,22,171]. The measured TOC for the untreated enamel (20.67 ± 7.32 g/kg or 2.07 ± 0.73 w%) is well in this range, but slightly lower than the TOC of 4 w% (4.4 g/100 g) reported by Teruel et al. [21]. Chemically treated enamel has a lower TOC than untreated, which shows that the organic was, at least partially, removed. This is further supported by the by orders of magnitude lower amino acid content in both chemically treated enamel. However, the amino

acid concentration in the H_2O_2-treated enamel is one order of magnitude lower than in the KOH-treated enamel while the TOC is in a similar range. This might imply that the H_2O_2-treatment is more successful at cleaving the amino acids than the KOH-treatment, so that they can no longer be detected by the HPLC analysis. In contrast, the organic carbon of the cleaved organic molecules can still be detected by elemental analysis (TOC). After heat treatment at 200°C enamel has a similar TOC and amino acid concentration than after H_2O_2-treatment, whereas the TOC decreases after heating to 250°C and 300°C. The amino acid concentration in the 300°C heated enamel is similar to the H_2O_2-treated, while the 250°C heated enamel shows both a lower TOC and amino acid concentration than the 300°C heated. As no feasible explanation for an increase in organic content with heat treatment at higher temperatures can be found, this is attributed to the natural variance in the tooth samples. The 900°C sample only shows a low amount of TOC and no amino acids could be detected (detection limit <0.02 mg/g). Therefore, it can be assumed after heating to 900°C the enamel is fully deproteinized.

Based on the fact that the elemental analysis and the TGA are using the same principle: heating the sample and measuring the weight loss, plus in the case of the elemental analysis additionally analyzing the evolved gases, similar outcomes for both analyses were expected. However, contradicting results were observed with the H_2O_2-treated enamel showing the same mass loss as the untreated in the TGA studies, while the TOC was considerably reduced. One explanation here could be that these results differ due to the natural variance in teeth which is evident from the wide range of values for the organic content given in literature (0.3-11 w%) [5,19–22]. Another possible explanation could be that the mass loss that is detected via TGA is not only related to the organic content but also other processes, as described earlier. When heated enamel loses a considerable amount of water and mineral CO_3. It could be the case that the amount of these two components is higher in the H_2O_2-treated enamel and therefore the total mass loss reaches a similar level to the untreated enamel. Due to the additional decomposition of inorganic parts the origin of the mass loss during TGA is uncertain and thus cannot provide a reliable value for the organic content in dental enamel.

Although there are some insecurities and variance between enamel samples, a lower organic content after chemical treatment was measured by several methods, therefore confirming that (partial) deproteinization has been successful. Some organic material might remain in the sample; however, it is not clear whether the tertiary structure and bonds of these proteins remain intact after treatment. Heat treatment, especially at high temperatures, removes organic more

completely but some alteration in the HAP composition can be observed in FTIR, even at temperatures as low as 100°C, and have been described in the literature [52].

6.2.2 Influence of the deproteinization treatments on the structure

The SEM images (Figure 19) show that the macroscopic structure and the crystal structure are not affected by the chemical deproteinization treatments. This is confirmed by an unaltered crystal structure after chemical treatment measured by FTIR and XRD, reported by other research groups [46,98,172]. In contrast, heating the enamel samples resulted in massive changes in the structure. Starting at 300°C sintering of the crystallites could be observed, which intensified at higher temperatures. Opposed to these findings, He and Swain found that heating to 300°C (5 min in vacuum) did not affect enamel structure. However, they used lower magnifications in their SEM and EDX investigation and only observed the structure on a higher hierarchical level than the crystallites themselves [47]. Similarly, Baldassari et al. did not detect changes to the mineral phase in the FTIR spectra after plasma ashing of the enamel samples (4h in O_2) [48]. Either changes in the crystallites were not obvious under these conditions or the shorter heating period combined with the vacuum affected the crystallites less. As sintering of the crystallites increased with longer heating times and in air atmosphere, the latter is plausible. In general, the chemical composition is not altered when sintering occurs, therefore would neither be apparent in EDX. Zenóbio et al. reported a phase change in the enamel mineral after heating above 400°C. While the predominant phase was still hydroxyapatite (<60%), the amount of whitlockite increased from <3% to <10% [19]. In this work (Figure 20), drastic changes in the enamel structure after heating to temperatures >400°C could be observed. After heating to temperatures of ≥400°C and with increasing holding times, large cracks are formed inside the sample. Sui et al. [173] reported similar findings with a change in crystal size when heating enamel >400°C, accompanied by cracking of the sample.

Comparing the FTIR spectra of the untreated enamel to the chemically treated, there are no obvious changes to the PO_4^{-3} peaks (1200-930 cm^{-1}) which would indicate changes to the crystallites. However, the intensity of the CO_3 peak at 1550 cm^{-1} is also reduced in the chemically treated enamel, which might result from the deproteinization agent interacting with the carbonate. But the intensity of this peak is also very weak in the untreated enamel. Therefore, the differences that could be observed here might also be due to natural variations between teeth. Similarly, Taube et al. did not find an influence on KOH on the carbonate content

[172]. Thus, it can be assumed that the chemical deproteinization does not affect the mineral phase significantly.

In contrast, the PO_4^{-3} peaks in the heat-treated enamel samples get narrower with increased temperature and the double peak at 1456 and 1422 cm^{-1} which is related to type B carbonate [169,170] gets diminished after heating. This is in agreement with the reported loss of CO_3 (evolved as CO_2) and subsequent alteration of the crystal structure during heat treatment of dental enamel [52]. The content of inorganic CO_2 was determined as 1.09 w% for HAP [21] and ca. 3.6 w% for enamel [21,161], with the latter varying significantly (interval of 1.8-4.5%) [161]. In this work, the HAP showed a mass loss of 1.95 w% during TGA (sum of total peak areas 200-900°C; see supplementary information C.1), which is higher than the content given by Teruel et al. [21], but in the same order of magnitude. This difference may be the result of variances in water content or HAP samples in this work may have a higher CO_2 content than reported by Teruel et al. due to a different production route or lower purity. The mass losses of the enamel (1.96-3.24 w% over 200-900°C) lie in the interval given by Teruel et al., even considering the insecurities about the amount of organic and water present.

Comparison of the TEM images (Figure 21) of untreated and KOH-treated enamel confirm that there is no obvious change to the crystal structure after treatment. However, the rod boundaries in the KOH-treated enamel appear more pronounced than in the untreated. Analysis of the pore percentage showed that that, counterintuitive to the first impression, boundaries in the KOH-treated enamel (44.50 ± 7.47 vol%.) are less porous than in the untreated enamel (57.04 ± 15.22 vol%). Due to the large standard deviation, the limitations of the analysis and the expected variation between different teeth, it can be assumed that there is no considerable difference in the porosity of the boundaries between the untreated and KOH-treated enamel. As the width of the boundaries is not considered in the porosity analysis (details in [63]) it is feasible that the boundaries of the KOH-treated enamel are wider and result in the impression of more pronounced boundaries. Taube et al. found that KOH solutions had an etching effect on enamel surfaces [172], removing material from the boundaries.

6.3 Mechanical Properties

Elastic modulus and hardness as basic mechanical properties were determined for untreated, chemically deproteinized and heat-treated enamel samples. Afterwards a structural model based

on the findings from the morphological characterization is proposed and its behavior under load is qualitatively discussed.

6.3.1 Influence of the Deproteinization Treatments on Elastic Modulus & Hardness

There is a considerable drop in the elastic modulus and hardness after heating the samples to temperatures >400°C for 24h, regardless of the atmosphere used. For the 15 min holding time this change is not as prominent at 400°C but occurs after heating to 450°C. The structural analysis has revealed that at these temperatures large cracks begin to form in the sample. Even though the tested areas were carefully selected in some distance to obvious defects, it is possible that the area underneath the indents was already damaged, leading to reduced mechanical properties. Sui et al. also observed a decrease in elastic modulus and hardness after heating enamel >400°C. Structurally, they reported cracks forming inside the samples and additionally an increased size of the HAP crystallites after heating enamel. They attributed the reduced mechanical properties to the increased defect number due to the larger crystal size. [173] Heating at lower temperatures (250-350°C) leads to slightly increased elastic modulus and hardness. The structural analysis revealed sintering of the crystallites at these temperatures. Sintering is known to result in an increased density and reduction of inherent defects or pores which is accompanied by an increased elastic modulus, hardness and strength in ceramic materials [174].

Comparing the chemically treated and the untreated enamel, the elastic modulus and hardness are in a similar range, considering the variation of these properties can be large across a single sample [99,115,175]. However, an increase in elastic modulus and hardness can already be seen for the 200°C heat-treated enamel, both in air in nitrogen atmosphere. At these temperatures no morphological changes in the crystallites were apparent in the structural analysis, but the FTIR data and previous studies show that even at low temperatures CO_3^{2-} is removed. B-type carbonate (substituting PO_4^{3-}) is transformed firstly into A-type carbonate (substituting OH^-). CO_3 then is removed by a reaction with water, which is incorporated into enamel, and retained in the crystal as CO_2. At the same time there is an increase in OH groups with a higher degree of ordering up to temperatures of 400°C, accompanied by a-lattice contraction due to loss of incorporated water [52]. As a result of this increased number of OH groups and the smaller atomic distances, the atomic interactions may get stronger. The high mobility of the OH and CO_3 during heating can plausibly also lead to healing of defects in the structure. Both effects

could result in an increased elastic modulus and hardness. Furthermore, the TOC and amino acids concentrations in the 200°C treated enamel are at a similar level as the H_2O_2-treated enamel. Therefore, the difference in their basic mechanical properties cannot solely be attributed to a difference in organic content.

As illustrated in chapter 2.3, enamel consist not only of proteins and mineral, but also contains a considerable amount of water (up to 9 vol% [22]). This is more than four times the organic content and it seems therefore reasonable that the water content may influence the mechanical behavior of dental enamel greatly. In fact, the influence of the moisture in dental enamel on the mechanical properties, especially the visco-elastic behavior, has been highlighted in recent studies [162,176,177]. The measurement of elastic modulus and hardness in this work have been conducted on samples that have been air dried due to greater ease of measurement and sample handling, and under these conditions no influence of the protein content could be observed. The time-dependent behavior of dental enamel under load has been investigated with regards to the water content and will be discussed at a later point (ch. 6.4.4).

6.3.2 Structural Model

The mechanical behavior and the structure of a material are very closely related, resulting in a variety of structural models that are used to explain the processes occurring inside materials during mechanical loading and are applied to dental enamel. For instance, in the analytical mechanical model by Gao and co-workers [13] for biological hierarchical materials the mineral component is described as being completely surrounded by proteins in a well aligned, quasi self-similar, brick and mortar structure (see also chapter 2.1). Since this first model of biological materials, models have been developed further to and adapted to the structure of the specific biological material they describe. For example, a generalized numerical model by Dimas at al. replaces the organic layer of the Gao-model by a brittle porous silicon layer [178] and a recent numerical model by Pro and Barthelat [179] incorporates for the first time an approximation for the decussation of the rods in dental enamel. However, the latter does not include the HAP crystallites as the constitutive units of the rods. Although Pro and Barthelat acknowledge the more complex internal structure and uncertainties about the exact nature of the interfaces between two rods, some simplifications had to be made for the sake of usability of the model [179].

The structural investigation undertaken in this work reveals that these models are not yet sophisticated enough to model the complex structure of dental enamel. Instead of continuous protein layers making up the interfaces, crystallites are bridging the rod boundaries and crystallites converge from the interrod region into the rod. There is direct contact between interlocking crystallites inside rod and interrod enamel and many crystallites are not separated by gaps. It appears as if the crystallites are not running parallel to each other but are intertwined like threads in a rope, albeit more randomly arranged. Figure 51 shows a schematic of the structure of bovine enamel including the observed structural features like intertwined crystallites and connections between rod and interrod enamel. Note that there are some minor differences in structure for the different regions of enamel. In innermost and inner enamel regions the rod boundaries surround more of the enamel rod (referred to as 'closed boundaries' after a classification coined by Boyde [80]) whereas in outer enamel the boundaries surround less of the rod circumference (open boundaries). Additionally, the thickness of the interrod layer varies with a thick layer present in inner enamel and only a thin layer in outer enamel.

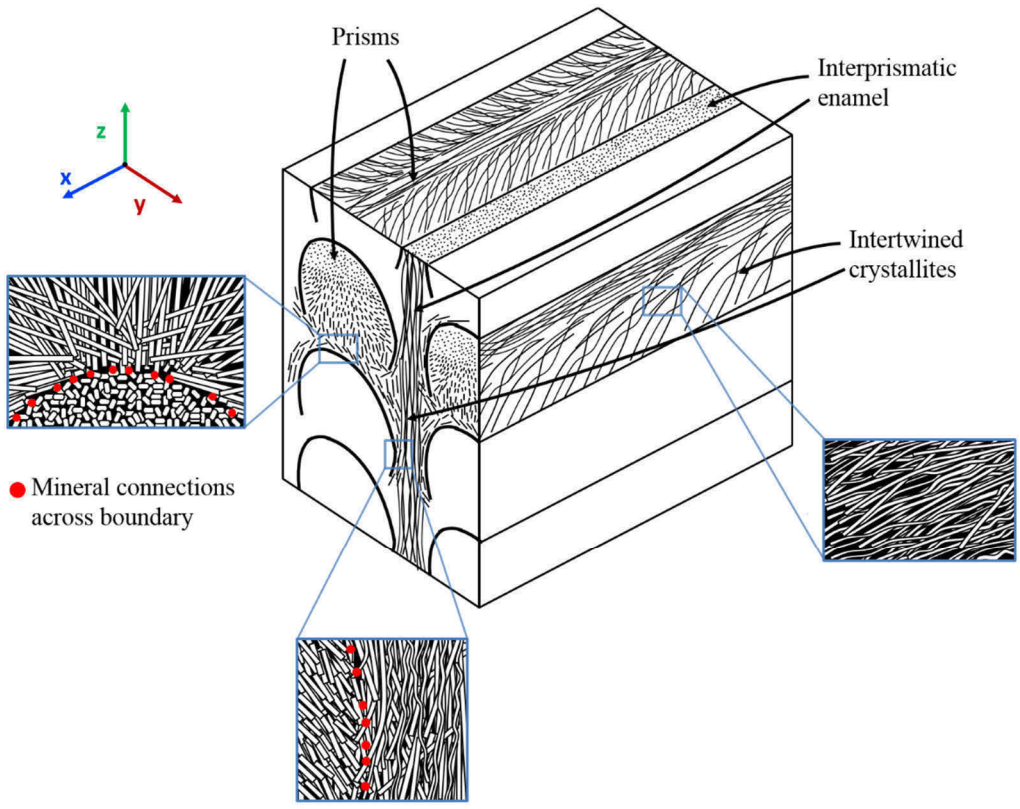

Figure 51: Structure of bovine enamel. Crystallites are intertwined and there is continuity between rod and interrod enamel. The magnifications of the boundary areas show that there are direct mineral connections between rod and interrod enamel (colored in red).

In the following the implications of the identified geometrical structure shown in Figure 51 for the mechanical properties of enamel will be described qualitatively. If this structure experiences a compressive load in the x-direction, parallel to the rods, it will experience high resistance as the crystallites are mostly aligned in loading direction and load can be transferred along them. While buckling is prohibited by the presence of the interrod enamel, sliding of crystallites and rods is possible, but hindered by the mineral connections at the boundary between rod and interrod enamel as well as the intertwining of the crystallites. Depending on the nature of the interface, several mechanisms may occur: If a protein is connecting the crystallites via electrostatic interactions and H-bonds [180], load transfer is possible from one crystallite to the other and protein shearing would be the leading deformation mechanism, resulting in energy dissipation by the unfolding of the proteins and breaking of the bonds. Such movement will however be hindered by the interlocking of many of the crystallites. For a direct contact between the crystallites or an amorphous mineral interface, the leading deformation mechanism would be frictional sliding of the crystallites. Similarly, sliding of the rods can occur but is also hindered by the mineral connections at the interfaces, as well as by their decussation in the inner regions of enamel. Fluid inside the porous rod boundaries could also enable viscoelastic behavior in the enamel structure as compression of a viscous fluid in one area of the enamel can lead to movement in other areas and thus enable the structure to creep [181]. The creep behavior of dental enamel will be discussed in more detail in chapter 6.4. Mineral fibers bridging the boundaries exist, but they have a very small diameter of about 50 nm and therefore would be able to bend quite significantly without fracturing [182] still allowing the movement of the rods. Subjecting the structure to tensile stress in x-direction is probably more critical, as the interfaces of both crystallites and rod and interrod enamel are at risk of being pulled apart. Therefore, resistance to this deformation is determined by the bond strength of these interfaces. The intertwining and interlocking of the crystallites hinder the displacement of the crystallites and as such increases the resistance of the structure to tension. Similarly, the mineral connections between the crystallites and their intertwined nature - and on a larger scale the same is true for the rods - increases the resistance to shear. At the rod interfaces not only do the weaker proteins - if present - carry some of the load but also mineral connections have to be broken, preventing the interface from being pulled apart.

The structure will likely behave similarly if subjected to load in the y- and z-direction. Due to interlocking of the crystallites in the rod and interrod enamel, both structural units are expected to show similar isotropic behavior in compression and tension. Buckling of the crystallites

could be a problem when subjected to compression but is prohibited as they are clamped by the larger structural units (i.e. rods and interrod enamel). An almost isotropic behavior for compression of a single rod in different directions irrespective of crystallite orientation has been previously reported by Yilmaz et al. [122]. Topologically interlocked materials built out of brittle building blocks - like the interlocking motifs of the crystallites - possess damage tolerance, tunable stiffness and a pseudo-ductile response [183] and microcracking, most likely at the bonded interfaces, can allow for stress dissipation [184] which could present as a pseudo-plastic behavior in enamel. On top of that, microcracking is an important toughening mechanism [18,184] which would also more readily allow for slip between rods and crystallites.

Another toughening mechanism is the decussating and bifurcating nature of the interrod and rod enamel. Cracks reaching a bifurcation spot must either penetrate the interrod enamel by propagating between the crystallites or be will be diverted and follow a path with weaker interfaces, thereby dissipating energy. Sharp angled changes in direction lead to crack arrest thus effectively toughen the material. The influence of the decussation pattern of the rods has been modelled in detail by Pro and Barthelat, showing that decussation is essential for crack deflection and trapping, therefore increasing fracture toughness [179]. In addition, the decussation has a significant influence on the elastic modulus, which partially explains the difference between the outer and inner enamel regions that have been observed experimentally by several researchers who attributed this to a variation in protein content [45,47,48]. However, even a higher protein content in some enamel regions is not contradictory to the observed nature of the boundary in this work, as the organic component is most likely present in the pores.

A limited number of studies investigated the difference between hardness and elastic modulus of the rod and the ‘sheath’ by nanoindentation and reported a significant difference [158]. Different moduli and hardness of deproteinized and untreated enamel were also reported and attributed to the variation in protein content [45,47,48]. It has to be noted however, that Ge and co-workers investigated a ‘prism sheath’ in human enamel that has a width of 800–1000 nm [158]. This is much wider than the thin area that separates rod and interrod enamel which is termed ‘prism sheath’ in other studies. The width these researchers observed is in the same size range as the width of the layer of interrod enamel in Figure 14 and Figure 15. Thus, it seems likely that in this study actually interrod enamel was compared to rod enamel. The actual size of the indent was only approximately 80 nm in width [158] and as such only probes a handful of HAP nanofibers (diameter of 50 nm) whereas in the study of Yilmaz et al., where isotropic

behavior was observed, pillars with a diameter of approximately 2 µm were compressed [122]. Only small areas where crystallites are interlocking are expected on the nanoscale, resulting in anisotropy of the elastic modulus due to crystallite orientation. On top of that, there is an inherent anisotropy in elastic modulus of a single HAP crystallite [185]. In contrast, the interlocking crystallites provide the structure with an almost isotropic behavior on a larger length scale.

Even though Ge at al. probably measured a larger area than the small boundary between the rod and the interrod enamel, a mechanical difference between a 'sheath' and rod is still reasonable when considering a porous structure of the boundary. Despite the frequent mineral on mineral contact, there are also frequent gaps or pores along the boundary in which the organic remnants and fluid are most likely confined. Probing an organic-rich region would lead to a reduced elastic modulus and hardness, compared to a more mineralized region, due to the much lower inherent modulus of the organic. The same however would be expected in a comparison between a densely packed mineral material with a more porous one, in which the pores are empty. Still the term 'rod sheath' implies a continuous coverage of the complete rod, which is not accurate as there are frequent areas of confluence between interrod and rod enamel as previously described by several researchers [5,83–85] and the term 'protein-rich sheath' or 'protein-rich region' as used by some researchers is considered more appropriate [99–101,118].

The organic was largely removed with the chemical treatments and no difference between hardness and elastic modulus of treated and untreated enamel has been observed, showing that the organic matter has no major influence on these properties. Instead, the intertwining nature of the HAP crystallites is suggested to have a far greater impact on the elastic modulus, resulting in a quasi-isotropic modulus [18,122]. In order to compare the influence of the structure on the mechanical properties of a single rod, the composite elastic modulus was calculated using four different models (see Figure 52a). Even though fluid makes up a large part of enamel structure and might influence the mechanical properties, this was not further considered in these simple models. Model 1 (E_1) is the classical Voigt model (equation (42)) using the modulus of the HAP E_{HAP} and protein $E_{Protein}$ as well as the mineral volume fraction φ_{HAP}. The value of the elastic modulus of a single HAP fiber was taken as 150 GPa [185] whereas for the elastic modulus of the organic part values of 10 MPa, 1 GPa (comparable to collagen in a mammalian tendon [186]), 10 GPa (for comparison the elastic modulus of an epoxy resin is about 4 GPa [187]) and 40 GPa (comparable to chitin [188]) were assumed. The latter values are relatively

high as the elastic modulus of many proteins rather lies in the MPa range [186] but due to their confined arrangement higher elastic moduli than for free standing proteins can be expected. Only the direction parallel to the HAP crystallites was considered as it was already demonstrated by Yilmaz et al. that due to the isotropy of the elastic modulus of a single rod the classical Reuss model is not appropriate to describe its behavior [122].

$$E_1 = \varphi_{HAP} \cdot E_{HAP} + (1 - \varphi_{HAP}) \cdot E_{Protein} \quad (42)$$

Model 2 (E_2) is an adapted version of the Voigt model including mineral connections between the HAP crystallites used by Yilmaz et al. [122] for enamel to include the observed mineral to mineral contact (equations (43)-(44)). Here it was assumed that protein and HAP bridges both have the same volume fraction ($v_{HAP} = 0.5$) in the shared interlayer between the mineral. The combined modulus of this layer can be calculated using the Reuss model (equation (44)) [122].

$$E_2 = \varphi_{HAP} \cdot E_{HAP} + (1 - \varphi_{HAP}) \cdot E_{HAP+\,Protein} \quad (43)$$

$$\frac{1}{E_{HAP+\,Protein}} = \frac{v_{HAP}}{E_{HAP}} + \frac{(1 - v_{HAP})}{E_{\,Protein}} \quad (44)$$

Models 3 and 4 (E_3 and E_4) were recently developed by Jelitto and Schneider to determine the modulus of porous materials [189]. For a single enamel rod the porosity was measured as 2.5%, therefore closed porosity is more likely. Nevertheless, the elastic modulus was calculated using both models for closed (Model 3) and open porosity (Model 4) (Equation (45) and Equation (46)) with d as the thickness of the material ligaments depending on the porosity Φ (equation (46) and equation (49)). After the elastic moduli for each model were calculated in such a way, they were normalized with respect to the elastic modulus of HAP ($E_i^* = E_i/E_{HAP}$).

$$E_3 = \left(\frac{1 - d_3}{-{d_3}^2 + 2d} + \frac{1}{-d_3 + 2 + (1 - d_3)^2 \cdot {d_3}^{-1/2}} \right)^{-1} \cdot E_{HAP} \quad (45)$$

$$d_3 = 1 - \Phi^{\frac{1}{3}} \quad (46)$$

$$E_4 = \left(\frac{-2{d_4}^3 + 3{d_4}^2}{2{d_4}^2 - 4d_4 + 3} \right) \cdot E_{HAP} \quad (47)$$

$$d_4 = \cos\left(\frac{1}{3} \cdot (2\pi - \cos^{-1}(2\Phi - 1)) \right) + \frac{1}{2} \quad (48)$$

Figure 52 b shows the calculated values for the elastic modulus, depending on volume fraction or porosity. As expected, for very low volume fraction of the protein or porosity there is no

pronounced difference between the models, as the influence of the HAP is dominant. With increasing porosity there is an increasing difference between the models. The moduli of the porous models (models 3 and 4) are smaller than the Voigt model (model 1), whereas the adapted Voigt model (model 2) has the highest modulus values. With decreasing elastic modulus of the protein however the difference between E_1, E_2, E_3 and E_4 decreases. This is reasonable, as the lower the elastic modulus of the proteins, the more similar they to empty spaces that do not possess substantial load bearing capability, i.e. pores. On top of that, the difference between the Voigt model (model 1) and the adapted Voigt model (model 2) becomes almost negligible for low elastic moduli of the protein, because the modulus of the protein has a large influence on the modulus of the combined layer of protein and HAP bridges $E_{HAP+\,Protein}$. For very low elastic moduli of the protein, the difference between $E_{HAP+\,Protein}$ and $E_{Protein}$ is minimal. The overall composite modulus is only minimally influenced by the interface layer, instead it is dominated by the HAP crystallites due to their high volume fraction.

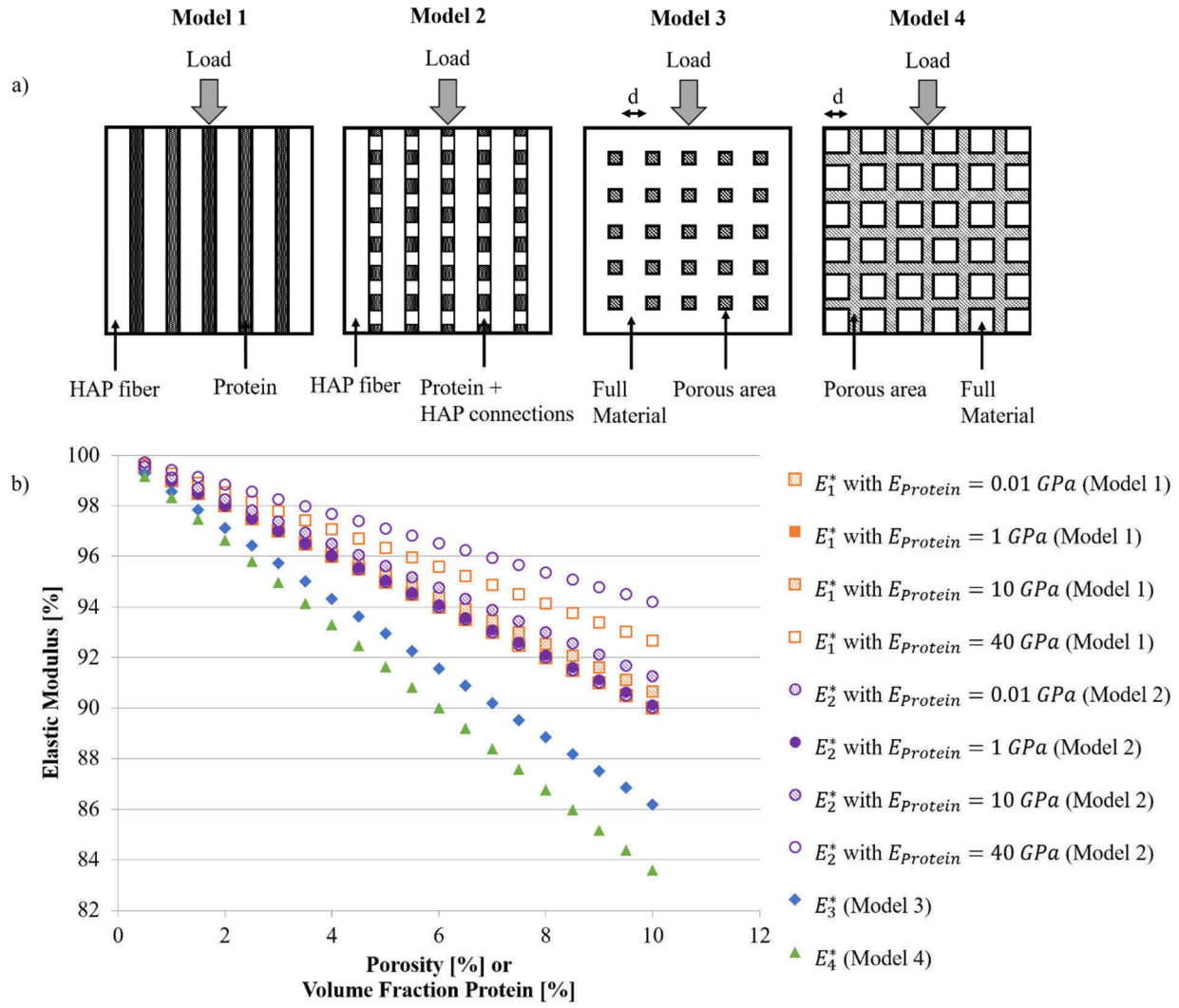

Figure 52: a) Schematic representation of the models used for the calculation of the composite elastic modulus. Model 1 is the classical Voigt model for a composite, model 2 is an adapted Voigt model with mineral slabs interconnecting the HAP crystallites as used in [122] and models 3 and 4 are geometric models for materials with closed and open porosity respectively (taken from [189]). b) Calculated normalized composite modulus E^* for models 1-4 and assumed values of the elastic modulus of the protein covering almost 3 orders of magnitude. The modulus E^*_4 calculated with the model for open porosity acts as a lower boundary for the elastic modulus. Note that the data points for E^*_1 and E^*_2 with $E_{Protein}$ = 1 GPa and $E_{Protein}$ = 0.01 GPa lie directly on top of each other.

There is only a small difference between all the models at these values for porosity or protein volume fraction leading to the conclusion, that at least the elastic behavior of enamel can be explained by employing the model of a porous material. The observed interlocking motifs of the crystallites, which inhibits sliding between them, strengthens the assumption of interconnected mineral motifs as assumed in models 2, 3 and 4. As from the TEM investigation

it is not clear if the pores or gaps that are present between the crystallites are filled by protein or not, as such models 3 and 4 may have to be adapted to incorporate the protein content. Model 2 accounts for the proteins by incorporating HAP bridges into the protein layer, but unlike the models for porous materials, no real interconnection of the mineral is incorporated. For a protein content of 2 vol% as given in literature [22] there is virtually no influence of the protein on the elastic modulus, regardless of the mechanical model used and the elastic modulus of the protein. On top of that, experimental data has confirmed that deproteinization has virtually no effect on the elastic modulus. Thus, it can be concluded that, the structural arrangement of the crystallites is the main contributor to the elasticity and hardness of dental enamel. Nevertheless, the organic content appears to have an influence on enamel's ability to creep and recover from deformation, as has been shown by He and Swain [118,154].

6.4 Creep Behavior

The creep behavior of dental enamel was analyzed by two kind of experiments as described in chapter 4.6.3: An adapted CLH method with 3 load hold segments (900 s hold at maximum load) and a five-step CLH method with 100 s hold at maximum load where the load rates where varied. A spherical tip was used as the Berkovich tip combined with the high load resulted in considerable damage to the enamel structure. Under these conditions the measured change in displacement is most likely due to plastic deformation and not a reliable indication for creep in sample. Therefore, the approach with the Berkovich tip was discarded and a spherical tip with much lower loads was used. In order to validate the applied drift correction, alumina and silica samples were analyzed in the same way. From Figure 35, Figure 37, Figure 39 and Figure 41, showing the data from the adapted CLH method, it can be seen that the alumina and silica samples show no creep at all, which is expected and confirms that the drift correction procedure is appropriate. The displacement at maximum load for the silica sample with different load rates in dry and wet state (Figure 46 and Figure 47) also show no obvious creep. This confirms that the water has no direct effect on the creep measurement. However, in all cases the creep in alumina and silica is non-zero. Instead values of ~1-2 nm for 5 µm tip and ~5 nm for the 50 µm tip can be reached. As the curve does not show the typical shape of a creep event where displacement steadily increases but instead the displacement oscillates and even adopts negative values, this can be attributed to the uncertainty of the measurement itself. Hence, when interpreting the data from the measured samples, differences in the range of 1-2 nm and 5 nm for the 5 µm and 50 µm respectively, cannot be attributed to a difference in the materials' behavior with certainty. Enamel's creep behavior is complex and influenced by protein and

water content as well as hierarchy, which are all interconnected. Nevertheless, in the following chapters these influence factors will be discussed separately before combining the results to form a consistent explanation for the creep mechanisms in dental enamel.

6.4.1 Determination of Elastic Moduli from Creep Tests

The elastic moduli of enamel were determined by fitting the loading curves with the Hertz function for elastic contact and from unloading by the Oliver and Pharr method [147]. With only two exceptions (silica and dry untreated enamel with the 5 µm tip in perpendicular direction), there was a difference of at least 50 GPa in the value of both such determined moduli. In the case of enamel this means a 100% increase of modulus from unloading, compared to loading. For the alumina sample it is evident from the load-displacement diagram that loading and unloading have the same slope. The discrepancy between the moduli determined with the two methods may results from the fact that for the comparatively low loads employed in this work (5 and 150 mN) the contact between indenter tip and sample surface may be ill defined, especially in very hard materials such as alumina. Small asperities will have a large effect on the actual contact area and thereby on the calculated elastic modulus. The Hertz fit on the loading curve males use of the radius of the indenter tip, which is calibrated on the silica. Hence for silica there is a good agreement in the moduli determined by both methods. During calibration it was however evident that at low loads the scatter for the determined radius was large, confirming this as a potential issue. The elastic moduli determined for enamel from unloading during the creep experiments with the 5 µm tip were higher than those determined with the CSM method and Berkovich tip as presented in ch. 5.3. This can be explained by the fact that the creep experiments used a much smaller load, resulting in a smaller contact area, thereby probing only multiple crystallites and not multiple enamel rods. A single HAP crystallite is estimated to have a modulus of 150 GPa [185] whereas other studies give the elastic modulus of the first hierarchical level of dental enamel as 100-110 GPa [190], which is close to what is calculated here. The moduli determined from the experiments with the 50 µm tip, thus probing multiple rods, are lower than the ones from the 5 µm tip, supporting this explanation. However, they are still slightly higher than the moduli determined from the Berkovich-indentations. This could result from the fact that there is less plastic deformation, especially chipping and cracking at the edges of the indentations which can alter the calculated elastic modulus as the calculation are based on a perfectly elastic contact. The elastic moduli of both treated and untreated enamel lie in a similar range, showing no influence of the deproteination treatment, as already shown for the experiments with the Berkovich indenter.

Typically, in a case where the slope of loading and unloading do not agree plastic deformation is expected. Curiously in this case the loading curve perfectly followed the Hertz equation and no elastic-plastic transition could be found (see Figure 53). This pseudo-elastic behavior of enamel was thought to result from creep already occurring during the loading of the sample and has already been observed for corneal tissue [191]. Hence, further experiments with varied load rates and shorter holding periods were conducted (method 3, results see ch. 5.4.4).

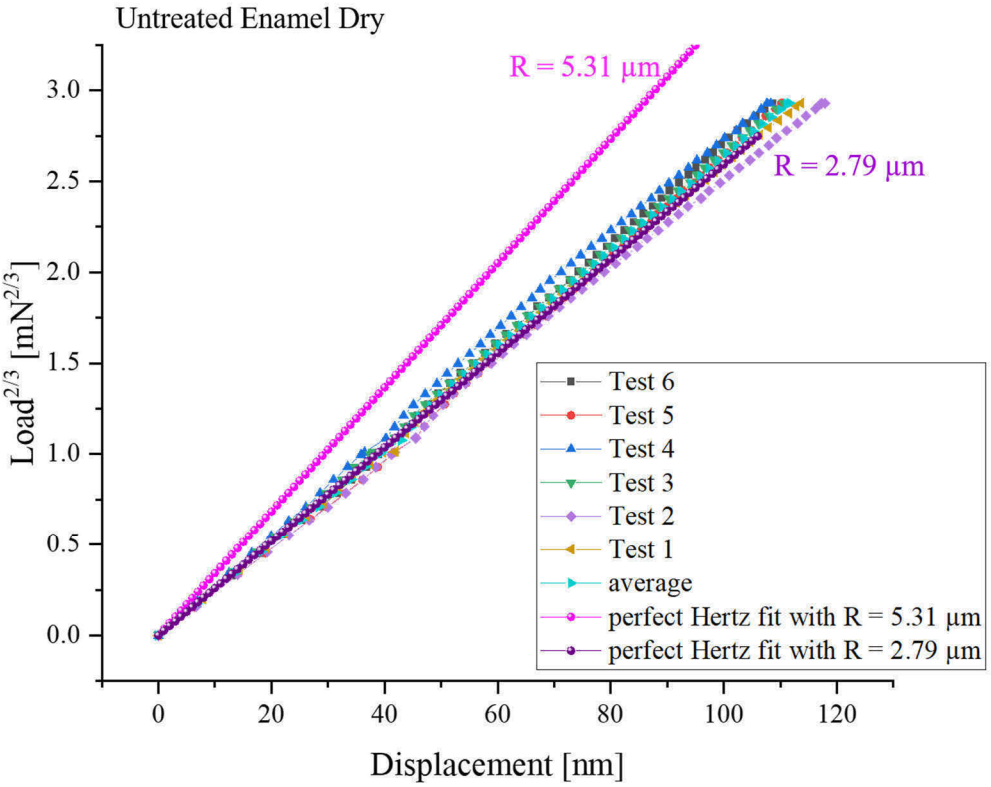

Figure 53: Plot of Load$^{2/3}$ vs displacement for untreated dry enamel. It can be seen that the measured curves show a perfectly linear behavior, which would mean perfect elastic behavior. When using the elastic modulus from the CSM based nanoindentation $E_r = 76.8\,GPa$ the measurement data can be fitted with the Hertz equation with an effective indenter radius of $R = 2.79\,\mu m$. The Hertz curve with the same elastic modulus and the calibrated indenter radius $R = 5.31\,\mu m$ is plotted for comparison. Fitting the load displacement curve with the Hertz equation with the calibrated indenter radius was possible by varying the elastic modulus.

During the experiments with varied load rates, all dry enamel samples showed the same behavior during loading and unloading (Figure 43). With faster load rates the slope appears to be increasing, however some of this effect is due to the technical issues discussed in ch. 6.4.2.

Calculating the elastic modulus from the parts of the curve that were less affected by instrument issues revealed no clear trend in elastic modulus depending on load rate. Analyzing only the change in displacement at maximum load, shows that there is only a clear difference in creep between the slowest load rate of 0.05 mN/s and all other load rates. No difference larger than the measurement uncertainty could be found between load rates of 0.5 mN/s and above. Therefore, it appears that enamel shows time dependent behavior, i.e. creep during loading, but this only affects the measurement below a certain threshold. On top of that, there is no difference between the untreated and deproteinized samples. All enamel samples show the least creep (~2 nm) for the slowest load rate and the creep for the faster load rates is ~4-6 nm. In contrast to the creep experiments with long hold periods (method 2), the elastic modulus from unloading in this experiment (method 3) is only ~50% higher compared to the modulus from loading. The moduli from loading for both variants of the creep experiments (method 2 and 3) are in the same range. A possible explanation could be a difference in fluid content in the samples. While the creep experiments with method 2 were conducted shortly after SEM investigation, where the samples were subjected to a high vacuum, the later creep tests with method 3 were conducted after a longer storage period in ambient conditions during which enamel could possibly rehydrate.

6.4.2 Technical Issues during Creep Experiments

The creep data is normalized to start at zero at the start of the segment where the load is held constant. Depending how the starting point of this segment is chosen, there is a discrepancy in the amount of the creep at maximum load depending. From the load displacement curves (Figure 43 and Figure 44) it can be seen the segment at maximum load is extended with faster load rates, meaning more creep occurs, even in the silica, which is not expected at the measurement conditions (spherical tip 5 µm radius and 5 mN maximum load). Looking at the raw data the load of 5 mN is reached already before the datapoint where the indenter determined the start of the hold segment. The reason for this is a technical issue with the measurement. The indenter is controlled by a PID controller. The experiment is set up such that the indenter movement should stop once the maximum load of 5 mN is reached. However, there is a time delay (~0.1-0.2 s) between the instrument reaching and measuring the load and the signal to stop the indenter movement. For the faster load rates, this dramatically affects the collected date as the time to load is much shorter than for the slower rates. The indenter marks the hold segment at the point where an indenter speed of 0 nm/s is first reached. However, analyzing the indenter speed at the start of the hold segment, it was noticed that consistently two additional

measurement points were required for the indenter speed to stabilize near zero (Figure 54). Hence, the first two data points were excluded in the creep analysis. While for slower load rates ≤ 1.5 mN/s this made no difference in the creep data, the creep in SiO_2 measured for the fast load rates was reduced by ~2 nm and resulted in the data presented in chapter 5.4.4, with the expected values close to zero creep, whereas in the load-displacement curves the segment at maximum load still appears longer compared to the slower load rates.

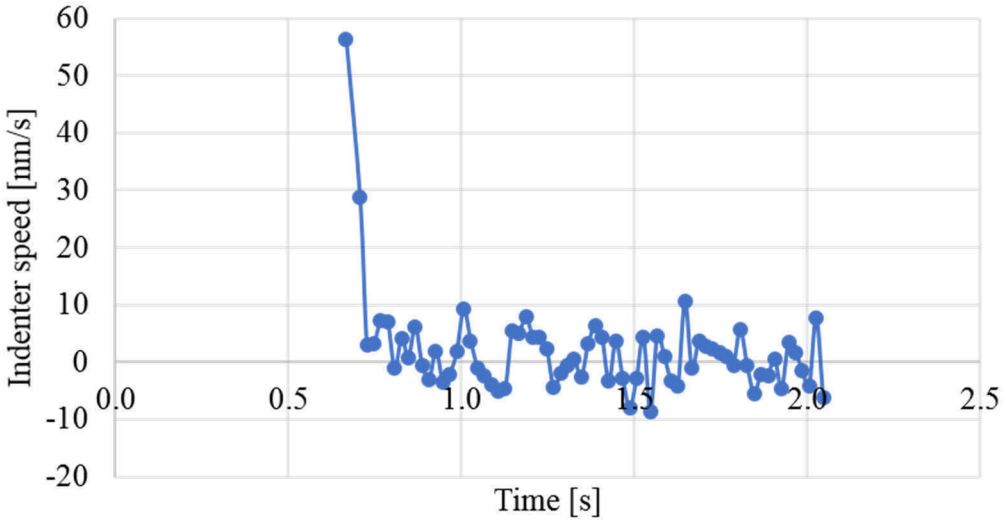

Figure 54: Indenter speed during the initial part of the hold segment, exemplary graph for a load rate of 10 mN/s. The hold segment starts after ~0.7 s of the experiment have passed and the load of 5 mN has been reached. The first data point in the plot is the first point of the segment as determined by the indenter program. It can be seen that the indenter speed still changes considerably for the first two measurement points before stabilizing around 0 nm/s.

A similar problem occurs in the roll-over from the hold segment to unloading. Again, here the indenter speed changes dramatically during the initial measurement points due to a delay between recorded load and controller. Especially for the faster load rates this results in the observed almost vertical slope during the initial unloading. When considering the unloading slope, this segment should therefore be excluded.

Additionally, there are some issues with the initial loading part. Especially for faster load rates and wet samples in some cases the automatic surface finding conducted by the indenter is not accurate. This may result in long segments where load and displacement are not increasing considerably, because the indenter has not made good contact with the surface yet. On the other hand, with faster load rates, sometimes a similar problem with vastly changing indenter speed,

as for the onset of the hold and unload segment can be seen. This may even result in a decreasing displacement initially. More typically it results in a fast-increasing displacement during the initial segment as can be seen for the faster load rates. The contact between indenter tip and sample seems to only be reliably established at loads ≥1 mN, such that data before that point must be treated carefully. In general, the load displacement curves, especially for the fast load rates of 5 and 10 mN/s, should be interpreted very carefully if at all due to these various issues.

For the wet measurements the sample is completely submerged under water. This can cause some issues with the initial contacting of the surface. Due to the surface tension in the water layer, some forces may act on the indenter tip, causing the automated surface finding process to register this as the initial point of contact even though the indenter tip may not already contact the sample surface. Therefore, a correction of the initial contact point needs to be carried out by shifting the load displacement curve to the left. Additionally, the water will evaporate as time passes during the measurement. The evaporation speed of the water layer on the sample in the ambient room conditions was measured repeatedly on different days and it was determined that for at least 6 h the water covers the sample surface. Thus, only experiments that were completed under 6 h measurement time were considered for the evaluation of the wet data.

6.4.3 Influence of Proteins on Creep Behavior

The creep behavior of enamel was first investigated with a CLH method with comparatively long hold segments of 900 s (method 2). The creep responses of the chemically deproteinated and untreated enamel samples are similar and differ from the silica and alumina references. After a sharp increase during the first ~25 s the increase in displacement slows down and reaches a plateau. This is a different behavior than described for typical creep curves, e.g. for metals. Here, the strain rate will reach a constant value during steady state creep, but $\dot{\varepsilon} \neq 0$ and the displacement continues to increase constantly (see chapter 4.6). The creep in all enamel samples tested in dry state with the 5 µm tip, except untreated loaded perpendicular to the rod direction are similar (differences between curves are in the range of 1-2 nm which is in the range of the uncertainty associated with the device), but considerably higher than in the sintered HAP, which shows a low amount of creep. The untreated enamel loaded perpendicular to the rod direction shows the same behavior in general but reaches a lower total displacement, which is almost half of the enamel with the most creep (4 nm and 8 nm respectively). While the total displacement for the enamel loaded perpendicular to the rods is lower for the untreated and KOH-treated enamel, the H_2O_2-treated enamel shows the opposite behavior. While in the wet

state (5 µm tip) the creep in general is higher than in the dry state, the differences between the enamel samples are again mostly small (1-2 nm). But it should be noted that here the untreated enamel in perpendicular direction shows the most amount of creep (~17 nm) whereas the H_2O_2-treated enamel shows less creep (~7 and 10 nm). The latter values are also close to the creep that is observed in HAP (~6 nm). However, already the untreated enamel in parallel direction is very similar to the KOH-treated enamel (difference of ~1 nm), such that differences between enamel samples are hard to interpret given the relatively large uncertainty in the measurement. This and the relatively small number of tests (5-10) means that these observed differences may be due to statistical errors. On top of that, although care was taken to select similar enamel regions, differences due to local variation of chemistry or variance between the tested teeth cannot be ruled out.

The recovery behavior or back-creep (Figure 36) with the 5 µm tip shows similar trends to the creep behavior. While the SiO_2, Al_2O_3 and HAP samples show no recovery, regardless if tested in wet or dry state, all enamel samples show some extent of recovery. Again, most of the time-dependent behavior occurs during the first 25 s and then reaches a standstill. There are differences between the two loading directions, with the perpendicularly loaded untreated enamel and H_2O_2-treated enamel showing a faster recovery than the parallel loaded ones, in the dry state. For the KOH-treated enamel this trend is the other way around. On top of that the untreated parallel enamel shows the largest recovery in the dry state whereas in the wet state the untreated perpendicular enamel has the largest recovery. For the wet tests there is only a larger difference (>2 nm) between the untreated perpendicular and the H_2O_2-treated enamel. In all other cases the observed differences between the treated enamel samples, in the dry and wet state respectively, are small (1-2 nm) and must be treated carefully as they are in the range of uncertainty.

Regarding the creep with the 50 µm tip, a similar behavior can be observed. The SiO_2 and Al_2O_3 reference samples show only a negligible amount of creep in both wet and dry state, which was expected and confirm that the applied drift correction was appropriate. While the HAP sample in dry state has a creep behavior similar to SiO_2 and Al_2O_3, it shows some amount of creep in the wet state. This could be caused by water accumulating tin the pores and grain boundaries, facilitating some movement of the grains. The creep in the enamel samples in all cases is however much higher than for any of the synthetic ceramics. Comparing the treated and untreated enamel in the dry state, there are no considerable differences between the untreated

and KOH-treated enamel. The H_2O_2-treated enamel, in both directions, shows a lower creep than the untreated enamel in parallel direction (a difference of about 10 nm which is ~ 30% less creep in the H_2O_2-treated enamel compared to the untreated parallel enamel), however compared to the KOH-treated enamel and the untreated enamel in perpendicular direction the differences are in the range of the uncertainty of the measurement (~5 nm). The loading direction only seems to affect the amount of creep in untreated enamel in dry state, where in parallel direction more creep occurs than in perpendicular direction. In the wet measurements there is no difference between measurement directions in any enamel sample. In the wet state the difference in creep between the untreated enamel and H_2O_2-treated enamel is even more pronounced with almost 40% percent (~15 nm) less creep in the H_2O_2-treated compared to the untreated enamel, while there is no difference between the KOH-treated and untreated enamel. The measurement of recovery mirrors the behavior observed for the creep, regarding SiO_2, Al_2O_3 and HAP. The largest amount of recovery is observed for the untreated enamel in parallel direction in both wet and dry state, whereas the treated enamel shows less recovery. More considerable differences occur when comparing the untreated with the H_2O_2-treated and the KOH-treated enamel in the dry state, and the untreated with the H_2O_2-treated enamel in the wet state. Comparing the amount of displacement that is recovered with the amount of displacement that occurs during creep, in the dry state the treated enamel samples recover considerably less of their creep displacement than the untreated counterparts (Figure 55 and Supplementary Table 4).

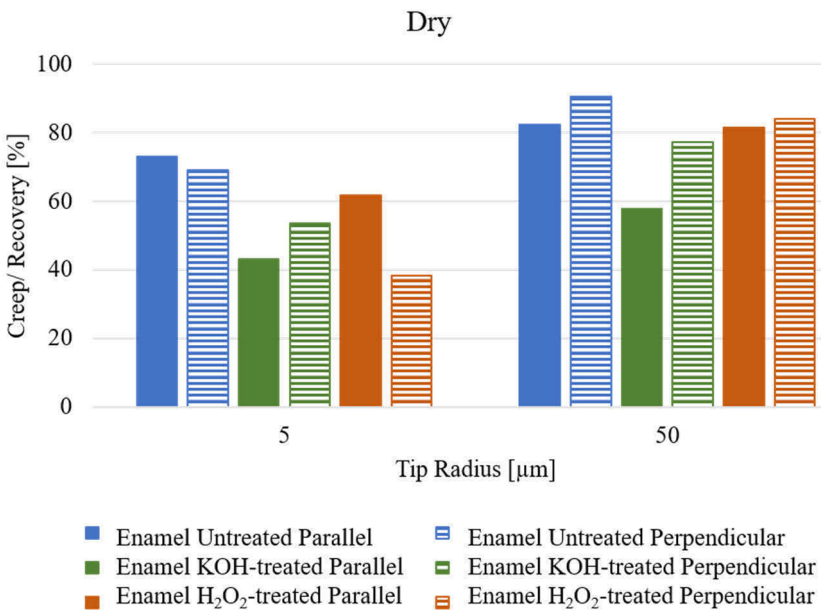

Figure 55: Amount of recovery compared to the creep in dry treated and untreated enamel samples. The dry untreated enamel shows more recovery than the treated enamel.

In conclusion, only minor differences between treated and untreated enamel can be observed that seem to be interdependent on the water content and hierarchical level, which will be discussed in the next chapters (ch. 6.4.4 and 6.4.5). Additionally, no clear effect of the loading direction could be observed. This is contrary to the typical explanation given for the creep and recovery in enamel, which is as follows: When loaded, the HAP crystallites are sheared against each other. The protein connection between crystallites may act as springs bearing tensile forces, with a time-dependent unfolding of peptide chains and sacrificial bonds, as proposed by He and Swain. After the load is removed, they assume their original position, the peptide chains refold and the displacement of the indenter tip into the surface is recovered [47]. As the proteins are largely removed in the KOH and H_2O_2-treated enamel and no difference in creep behavior to the untreated enamel could be observed in this work, however another mechanism must be the origin of creep. Nevertheless, the proteins might be more important to the recovery of the displacement than for the creep, as here the untreated enamel consistently showed the largest amount of recovery and in the dry state recovered considerably more of its displacement than the treated enamel.

6.4.4 Influence of Water Content on Creep Behavior

All creep tests were conducted in dry and wet environment. As shown in ch. 5.4.4 there was no difference between the dry and wet silica and alumina. For the comparatively low loads that were applied no creep was expected to occur in both ceramic materials, independent of sample condition and load rate, which is confirmed by the observed results. In dental enamel a clear effect of water content on the creep behavior could be observed, with more creep occurring in the wet samples compared to their dry state. Comparing the ratio of creep and recovery (Figure 56), it can be seen that the water content is extremely important for the recovery. The wet enamel recovers considerably more of its displacement compared to its dry counterparts. Especially, when tested on the larger length scale (50 µm) an extraordinary recovery of all enamel samples of about 100% of the displacement can be observed. Additionally, the creep was more strongly affected by the load rate, with more creep occurring during the hold segment with the fast load rates than for the slow load rates. This shows that the viscoelastic or -plastic effects in the material are strongly dependent on water. Although material behavior dependent on water content has also been observed for other biological materials such as nacre and bone [2,192], this large influence of water content on the creep behavior of dental enamel is quite surprising considering its high mineral content.

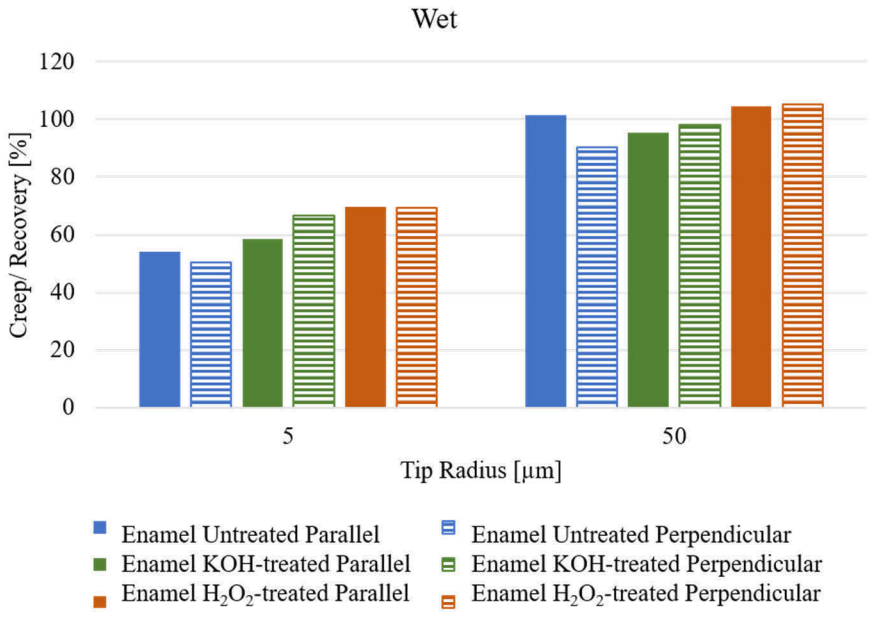

Figure 56: Amount of recovery compared to the creep in wet treated and untreated enamel samples. Compared to the dry samples a larger percentage of displacement is recovered in the wet samples, with almost all of it recovered for the larger indenter tip.

An influence of the water content on enamel's viscoelastic behavior has previously been observed by He and Swain. They measured creep in hydrated, desiccated, re-hydrated and burnt samples as well as dehydrated samples, where water was replaced by ethanol. The hydrated and re-hydrated enamel showed the largest amount of creep, while the burnt and de-hydrated enamel showed only very limited creep. The desiccated enamel showed a creep value between the burnt and hydrated enamel. He and Swain explained this variance in behavior with the influence of the water on the proteins. They hypothesized that the ethanol affected the conformation of the peptide chains such that the proteins could no longer act unfold when loaded. The heat treatment at 300°C removes the proteins and hence would also remove the capabilities of any time-dependent behavior in enamel caused by the proteins [47]. In contrast, this work has revealed that the capability of enamel to creep is not affected by protein content but by water content. Furthermore, it has been shown that heat treatment at 300°C affects the HAP crystallites, changing enamels microstructure and resulting in a stiffer and harder material. In their study, He and Swain observed that removal of water resulted in less creep in enamel. The more complete the removal of water was (dehydration with ethanol and heat treatment) the less amount of creep occurred [47]. This goes hand in hand with the observations in this work that wet enamel showed more creep compared to dried samples and possible creep mechanisms in enamel will be discussed in more detail in chapter 6.4.6.

6.4.5 Influence of Hierarchy on Creep Behavior

The creep experiments with the 900 s hold segments (method 2) were conducted with a 5 µm tip and a 50 µm tip in order to investigate the influence of the hierarchical level on the creep behavior of dental enamel. The maximum applied load of 5 mN with the 5 µm tip resulted in a contact radius of approximately 0.8 µm, thus with this experiment only a single enamel rod, or more precisely, multiple HAP crystallites (first hierarchical level) were probed. Depending on where the indent was placed however, it is possible that a rod boundary was below the indent. The maximum load of 150 mN for the 50 µm was chosen such that a contact radius of ~4.5 µm resulted, probing at least two enamel rods (second hierarchical level). While for the first hierarchical level no remaining indents could be seen, for the second hierarchical level, some plastic deformation could be observed by SEM. The indent boundaries were hard to distinguish, making it impossible to determine the contact radius of the plastic deformation, but it could be seen that multiple enamel rods were contacted by the indenter, validating that these experiments probe the second hierarchical level.

In general, the overall displacement in the experiments on the second hierarchical level is higher than on the first hierarchical level, which is easily explained by the higher load that is applied. Compared to level 1, level 2 also shows a higher amount of creep in wet as well as in dry state. This might also be explained by the application of a higher load, forcing the HAP crystallites, or rather the rods to move a larger distance. Comparing the amount of creep to the amount of deformation (the displacement into the surface at maximum load), we see that in untreated enamel (parallel) at level 1, creep makes up for roughly 5% of deformation (6 nm creep and 120 nm displacement) in dry state, whereas in the wet state it increased to ~10% (15 nm creep and 150 nm displacement). While the absolute numbers of creep and displacement on the second hierarchical level are much larger, the percentage of creep of the total displacement on the second hierarchical level is the same with ~5% (700 nm displacement and 35 nm creep) dry and ~10% (800 nm displacement and 40 nm creep) in the wet untreated enamel (parallel). Therefore, it seems that the hierarchical level only has a minor influence on the creep behavior of dental enamel.

However, the recovery of the displacement on the second hierarchical level is increased compared to the first hierarchical level in both wet and dry state. While in the dry state ~80% of the displacement during creep are recovered (with the exception of KOH-treated enamel in parallel direction), in the wet state up to 100% of displacement can be recovered. Typically, this behavior would be easily explained by higher protein content on the second hierarchical level (located in the rod boundaries), where unfolding of the proteins and breaking and reforming of bonds may be valid mechanisms for time dependent deformation behavior. However, as we do not see differences between the deproteinized and untreated enamel samples, the increased ability of recovery may simply be related to the more porous nature of the interfaces between enamel rods. Here fluid may move more freely allowing a faster recovery of the displacement (more detailed explanation of the mechanism in ch. 6.4.6).

6.4.6 Creep Mechanisms in Dental Enamel

Typically, viscous behavior in biological materials is attributed and is owed to the description of their hierarchical structure. In the TSC model by Gao et al. bone is described as structure built from HAP nanoparticles that only carry tension and are connected by protein layers that transport load between the particles as shear. Logically in such a structure the visco-elastic properties of the proteins would be the main cause for creep as for any creep occurring in the HAP single crystals high loads beyond the failure strength of the protein, which are typically

< 1 GPa, would be required. This model has been directly transferred to enamel with the assumption that proteins mostly fill the spaces between crystallites and rods. However, this assumption is not accurate for dental enamel. On the one hand, the HAP crystallites in dental enamel are much longer as in bone and are intertwined with each other. On the other hand, is has been known for a long time that the majority of the proteins is removed during maturation such that HAP crystallites are in direct contact with each other. In this work it was also revealed that the interfaces between enamel rods are also not discontinuous open spaces bit also have numerous direct mineral-to-mineral contacts. In addition, the experiments in this work have revealed that water influences the creep behavior of dental enamel with wet samples showing up to twice the creep compared to dry samples and an increased recovery of displacement reaching up to 100% for the second hierarchical level. Fluid accounts for approximately 9-10% volume (4% weight [22,26]), which is much larger compared to the ~1% weight of the remnant organic, thus water content can conceivably influence the material's properties. On top of that., recent APT studies have found an amorphous mineral phase in the interfaces between HAP crystallites. All these structural features could cause viscous material behavior in different ways.

Chapter 4.6 briefly described creep mechanisms occurring in ceramics, typically only at very high temperatures, such as the formation and expansion of cavities at grain boundaries, especially at triple points. Still material behavior at the nanoscale can be different than known from the macroscale. For example, it is well known that nanoparticles are sintering much faster due to their large surface energy. Similarly, small loads at the macro scale can cause high stresses in nanosized structures and provide the needed energy to initiate processes that would typically only occur at high temperatures. Considering that dental enamel is a highly porous structure with pores not only present at the rod boundaries, but also inside the rods, where HAP crystallites border each other it is possible that the pores, especially at triple contact points expand under steady load as the crystallites are slowly pushed away from each other. The HAP crystallites are also interlocking, hindering each other's movement. Barthelat described that loading structures with interlocking features can exhibit large deflection with pseudo-ductile behavior. The non-linear behavior is caused by the building blocks sliding against each other. Energy is dissipated by friction and frictional forces hinder the sliding. [183] These mechanisms can conceivably also occur with the interlocking HAP crystallites.

Another mechanism of creep in ceramics is the viscous flow of an amorphous phase in the grain boundaries. A similar situation has already been modelled for dental enamel and fit experimental results well, albeit here the amorphous phase was assumed to be of proteinaceous nature [181]. With the recent discovery of an amorphous mineral phase, however a new interpretation is possible: under load this amorphous mineral phase may start to flow and cause the crystallites to glide along each other, resulting in creep in the structure. Nonetheless, the influence of the water must not be forgotten. As the porosity of a single rod has been determined as only approximately 2.5%, a substantial part of the fluid must be confined to the more porous boundaries. This fluid may be a mixture of water, organic matter and amorphous mineral. During loading the fluid is displaced, resulting in a time dependent behavior of the structure. This is reflected in the experiments where more creep occurs when the load is applied faster, even though an upper limit seems to be reached already with a load rate of 0.5 mN/s. Schneider et al. showed previously that dental enamel's creep behavior can be adequately modelled with a viscous flow model [181]. Although Schneider et al. assumed the viscous fluid inside enamel's pores to be of proteinaceous origin, their theory could be applied for water inside the porous structure (ch. 6.4.7). The recovery after unloading is also a time dependent process which is consistent with the assumption that the creep in enamel is related to fluid flow in the pores. After unloading, local stresses in the sample relax and fluid can flow back into the pores of which it was pressed out during loading. The pores may assume their original shape and some displacement is recovered. This also holds true in the dry state, as the enamel will not be perfectly dry and still contain some water as is evident from TGA measurements (Supplementary Information C.3). Even though the enamel is measured in dry condition and has been air dried for at least 24 h, samples have been stored at ambient conditions before measurement and will rehydrate to some extent during the storage period [24].

Considering all dry enamel samples, at most only small differences slightly above the level of uncertainty inherent to the experiment occurred. However, for the wet samples there was a more pronounced difference (~5 nm) between the untreated enamel in perpendicular direction (5 µm tip, method 2) and the treated enamel. On the larger length scale (50 µm tip, method 2) there was an even more pronounced difference (~10 nm) between untreated and H_2O_2-treated enamel. However, there was no difference between the KOH-treated and untreated enamel during these experiments. Additionally, the KOH-treated enamel shows slightly more creep for load rates of 5 and 10 mN/s (method 3, 5 µm tip), compared to the untreated and H_2O_2-treated enamel. As both the H_2O_2-treated and KOH-treated enamel contain a similar amount of organic

matter (ch. 5.2, Figure 24), which is less than in untreated enamel the different creep behavior cannot be attributed solely to the organic component.

From the measurement of the protein concentration in the KOH solution by Yahyazadehfar and Arola [49] we know that with KOH-treatment the proteins are removed from the enamel structure. In contrast the treatment time during H_2O_2-treatment is comparatively short and here the proteins may only be fragmented such that they could no longer be found with the protein assay (relying on molecular weight), but the fragments may remain in the enamel. from the elemental analysis conducted in this work, we also see a lower concentration of amino acids in the H_2O_2-treated than in the KOH-treated enamel, while the amount of TOC is similar. This could support the hypothesis that the H_2O_2-treatment is more successful in cleaving the proteins into their constituents, even down to an atomistic level, while the cleavage products partly remain inside the material. This could result in a comparatively more porous material in the case of the KOH-treated enamel, whereas the protein fragments in the H_2O_2-treated enamel may hinder the movement of water through the pores, thus reducing the ability to creep. And in fact, the structural characterization has shown that the KOH-treated enamel has wider boundaries and the sample in general appears more porous. In the case of the untreated enamel an interplay between proteins or amino acids and water may make the latter more pliant by allowing deformation, as discussed by He and Swain [154], resulting in an increased creep compared to the H_2O_2-treated enamel.

Similarly, the water content influenced on the amount of recovery in enamel, here the untreated enamel consistently showed the highest amount of recovery. However, on the first hierarchical level the differences between treated and untreated enamel were only minor, and a considerable influence of protein content could only be observed at the second hierarchical level between the untreated and H_2O_2-treated enamel. All enamel samples, even those tested in dry state, showed a considerable recovery of displacement, which was increased if water was present (when considering the absolute values). Considering the ratio between creep and recovery, for the second hierarchical level (50 µm tip) in wet condition, even up to 100% of displacement could be recovered, whereas the untreated enamel showed the largest amount of recovery in the dry state. As explained above, a recovery of displacement could be explained by fluid flowing back into the pores. This would again be a time dependent process, during which energy would be dissipated by friction. In a load-displacement curve this would manifest as a hysteretic curve, which is what can be observed in this work, supporting this hypothesis. As the untreated enamel

shows the most recovery (in absolute values and in dry state percentage wise) it might be the case that the presence of proteins aids the recovery. If proteins unfolded under loading, they may refold when the load is removed pulling the displaced HAP crystallites back into their original position. While in the treated enamel the recovery is solely due to the movement of the fluid back into the pore channels. In the wet state the positive effect of the proteins may be negated by the fact that they block the narrow pore space and hinder the fluid movement, thus resulting in less recovery of the displacement as observed for the untreated enamel in wet state (percentage wise).

During SEM investigations carried out after the (dry) indentations it was not possible to find the residual indentations on the first hierarchical level and the indents were barely visible on the second hierarchical level. This might mean that either no plastic deformation occurred, which is not consistent with the observed load-displacement curves, where a residual displacement remains after unloading or a significant amount of deformation could be recovered maybe even after a long time period after loading. Even though during measurement of the recovery, a plateau is reached quickly (after about 25 s), this might be mostly related to viscoelastic effects while plastic deformation might be recovered as well, but take more time. Recovery of significant plastic deformation has also been reported by Rivera et al. [193], where even the partial closure of cracks was observed after storing enamel in distilled water for some time. In summary, water is clearly important for the time dependent deformation of dental enamel and further studies are warranted.

6.4.7 Modelling of Enamel Behavior

Creep in dental enamel has already been studied to some extent, mainly by a research group based around Michael V. Swain. This group has modelled enamel's creep behavior with two main approaches. One approach is to model the behavior by combining Kelvin-Voigt and Maxwell bodies [162] as illustrated in chapter 4.6. The other approach is to consider the proteins as a viscous fluid confined to the pores inside the enamel structure [181]. Both approaches showed a good agreement between the modelled behavior and the experimental data.

The applicability of both the Kelvin-Voigt model and the viscous fluid model were tested in this work. While the creep and back-creep could be fitted with various combinations of springs and dampers the basic assumption of proportionality between the displacement and time for the viscous fluid model did not hold true. For a Berkovich indenter $h^2(t) \propto t$ whereas for a

spherical indenter $h^{3/2}(t) \propto t$ due to the geometry. The experimental data agreed well with a model employing a spring and a Kelvin-Voigt body in series ($R^2 \geq 0.92$ for creep and $R^2 \geq 0.90$ for back-creep data, except HAP which did not converge). More elaborate models using a Maxwell body or a spring and two Kelvin-Voigt bodies in series also fit most of the datasets well, but the fitting failed to converge in some cases and did not show improvement of R^2. Explaining the function of these multiple elements by physical processes inside the enamel was also considered overly complicated, thus these models were deemed as not appropriate to describe enamel's creep behavior. For a simple series of spring and Kelvin-Voigt body however a simple physical representation can be found. The spring represents the instantaneous elastic deformation of the material under load, representing the mineral in enamel. The Kelvin-Voigt body describes the time dependent elastic deformation. This deformation is usually attributed to the proteinaceous phase [154,162], however as in this work the protein content had no influence on the creep behavior it must be attributed to water or an amorphous phase in the enamel (maybe in combination with the protein). As it has been shown that not all deformation could be recovered, these models still lack a representation of the plastic behavior.

In this work, it was shown that the creep behavior of enamel is dependent on the water content and to some extent, on the applied load rate. On top of that, the load-displacement curves revealed a pseudo-elastic behavior, similar to the behavior Swain et al. observed during the investigation of creep in corneal tissue [191]. Here the material's behavior could be well described by considering the tissue as a poro-elastic material. Analogous to the classical Kelvin-Voigt model, one might consider two components that govern the materials response. One is the elastic modulus and the other the permeability. By including a so-called hydraulic conductivity K_{hyd} into the Hertz equation the load-displacement curve could be described as:

$$F(h) = \frac{4}{3} E R^{1/2} h^{3/2} + \frac{1}{K_{hyd}} (2Rh)^{3/2} \frac{dh}{dt} \qquad (49)$$

[191].

The general approach to consider biological tissues as poro-elastic has also been applied to bone [194] and could also be valid for dental enamel. The development of such a model however lay beyond the scope of this work.

7. Conclusion & Outlook

In this work a thorough structural and mechanical characterization of untreated and deproteinized dental enamel was carried out. Enamel was deproteinized by chemical treatment with KOH-solution and H_2O_2 containing bleaching agents and by heat treatment. Advanced microscopy techniques such as FIB and TEM revealed that the interfaces between single HAP crystallites likely cannot accommodate organic structures due to their narrow gap size of often <1 nm. Furthermore, the boundaries between enamel rods are discontinuous, porous structures and there is no complete organic layer engulfing the rods. In untreated enamel frequent bridging filaments could be found that might be of organic origin and were not present in the deproteinized enamel. While chemical treatment did not affect the crystal structure and arrangement, heating enamel leads to decomposition of inorganic components and sintering of the HAP crystallites. Additionally, at high temperatures large cracks are formed in the sample which lead to a largely reduced elastic modulus and hardness. Chemical treatment on the other hand did not affect the modulus and hardness, showing that the protein content is not the decisive factor for those properties. Nanoindentation creep studies confirmed that the protein content does not have a large influence on the mechanical behavior of dental enamel, as virtually no differences could be observed between deproteinized and untreated enamel. However, a pseudo-elastic behavior of enamel and a noticeable influence of water on the mechanical properties of enamel could be observed. Wet enamel, both deproteinized and untreated, had a lower elastic modulus and showed considerably more creep (~10% of the complete deformation) and recovery than dry enamel on both the first and second hierarchical level. It is proposed that the predominant creep mechanism in dental enamel is frictional sliding of the HAP crystallites which is facilitated by the water that is present in the pores and interfaces.

It was observed that enamel is able to recover a considerable amount of deformation after unloading. Further studies where a nanoindentation experiment is couple with an AFM may shed light on how much of the deformation is recovered in which timeframe, as the optical and electron microscopy methods are not adequate to visualize very small deformations in the enamel surface. Furthermore, an adequate model to describe the creep and pseudo-elastic behavior on several hierarchical levels should be developed to gain a better understanding of these processes.

Bibliography

[1] M.A. Meyers, P.-Y. Chen, A.Y.-M. Lin, Y. Seki, *Biological materials: Structure and mechanical properties*, Prog. Mater. Sci. 53 (2008) 1–206. https://doi.org/10.1016/j.pmatsci.2007.05.002.

[2] J. Sun, B. Bhushan, *Hierarchical structure and mechanical properties of nacre: a review*, RSC Adv. 2 (2012) 7617. https://doi.org/10.1039/c2ra20218b.

[3] P. Fratzl, R. Weinkamer, *Nature's hierarchical materials*, Prog. Mater. Sci. 52 (2007) 1263–1334. https://doi.org/10.1016/j.pmatsci.2007.06.001.

[4] U.G.K. Wegst, H. Bai, E. Saiz, A.P. Tomsia, R.O. Ritchie, *Bioinspired structural materials*, Nat. Mater. 14 (2015) 23–36. https://doi.org/10.1038/nmat4089.

[5] A.R. TenCate, A. Nanci, *Ten Cate's oral histology*: *Development, structure, and function,* seventh. ed., Mosby/Elsevier, St. Louis, Mo., 2008.

[6] J. Moradian-Oldak, *Protein-mediated enamel mineralization*, Front. Biosci. (Landmark Ed) 17 (2012) 1996–2023. https://doi.org/10.2741/4034.

[7] G.W. Marshall, M. Balooch, R.R. Gallagher, S.A. Gansky, S.J. Marshall, *Mechanical properties of the dentinoenamel junction*: *AFM studies of nanohardness, elastic modulus, and fracture*, J. Biomed. Mater. Res. 54 (2001) 87–95. https://doi.org/10.1002/1097-4636(200101)54:1<87:AID-JBM10>3.0.CO;2-Z.

[8] H. Chai, J.J.-W. Lee, B.R. Lawn, *Fracture of tooth enamel from incipient microstructural defects*, J. Mech. Behav. Biomed. Mater. 3 (2010) 116–120. https://doi.org/10.1016/j.jmbbm.2009.08.002.

[9] B.R. Lawn, J.J.-W. Lee, H. Chai, *Teeth: Among Nature's Most Durable Biocomposites*, Annu. Rev. Mater. Res. 40 (2010) 55–75. https://doi.org/10.1146/annurev-matsci-070909-104537.

[10] B. Ji, H. Gao, *Mechanical Principles of Biological Nanocomposites*, Annu. Rev. Mater. Res. 40 (2010) 77–100. https://doi.org/10.1146/annurev-matsci-070909-104424.

[11] M.E. Launey, M.J. Buehler, R.O. Ritchie, *On the Mechanistic Origins of Toughness in Bone*, Annu. Rev. Mater. Res. 40 (2010) 25–53. https://doi.org/10.1146/annurev-matsci-070909-104427.

[12] F. Barthelat, C.-M. Li, C. Comi, H.D. Espinosa, *Mechanical properties of nacre constituents and their impact on mechanical performance*, J. Mater. Res. 21 (2006) 1977–1986. https://doi.org/10.1557/jmr.2006.0239.

[13] H. Gao, *Application of Fracture Mechanics Concepts to Hierarchical Biomechanics of Bone and Bone-like Materials*, Int. J. Fract. 138 (2006) 101–137. https://doi.org/10.1007/s10704-006-7156-4.

[14] I. Jäger, P. Fratzl, *Mineralized Collagen Fibrils: A Mechanical Model with a Staggered Arrangement of Mineral Particles*, Biophysical Journal 79 (2000) 1737–1746. https://doi.org/10.1016/S0006-3495(00)76426-5.

[15] S. Bechtle, S.F. Ang, G.A. Schneider, *On the mechanical properties of hierarchically structured biological materials*, Biomaterials 31 (2010) 6378–6385. https://doi.org/10.1016/j.biomaterials.2010.05.044.

[16] H. Gao, *Mechanical Principles of a Self-Similar Hierarchical Structure*, MRS Online Proceedings Library 1188 (2009) 23–34. https://doi.org/10.1557/PROC-1188-LL01-01.

[17] W.V. Koenigswald, W.A. Clemens, *Levels of complexity in the microstructure of mammalian enamel and their application in studies of systematics*, Scanning Microsc. 6 (1992) 195-217; discussion 217-8.

[18] E.D. Yilmaz, J. Koldehoff, G.A. Schneider, *On the systematic documentation of the structural characteristics of bovine enamel*: *A critic to the protein sheath concept*, Dent. Mater. 34 (2018) 1518–1530. https://doi.org/10.1016/j.dental.2018.06.006.

[19] M.A.F. Zenóbio, M.S.N. Tavares, E.G. Zenóbio, T.A. Silva, *Elemental composition of dental biologic tissues: study by means of different analytical techniques*, J Radioanal Nucl Chem 289 (2011) 161–166. https://doi.org/10.1007/s10967-011-1067-1.

[20] J. Holager, *Thermogravimetric Examination of Enamel and Dentin* (1970).

[21] J.d.D. Teruel, A. Alcolea, A. Hernández, A.J.O. Ruiz, *Comparison of chemical composition of enamel and dentine in human, bovine, porcine and ovine teeth*, Arch. Oral Biol. 60 (2015) 768–775. https://doi.org/10.1016/j.archoralbio.2015.01.014.

[22] J.K. Avery, P.F. Steele, N. Avery (Eds.), *Oral development and histology,* 3rd ed., Thieme, Stuttgart, 2002.

[23] M.F. Little, F.S. Casciani, *The nature of water in sound human enamel*, Arch. Oral Biol. 11 (1966) 565–571. https://doi.org/10.1016/0003-9969(66)90222-6.

[24] G.H. Dibdin, *The stability of water in human dental enamel studied by proton nuclear magnetic resonance*, Arch. Oral Biol. 17 (1972) 433–437. https://doi.org/10.1016/0003-9969(72)90058-1.

[25] D. Ying, G.K. Chuah, C.-Y.S. Hsu, *Effect of Er*: *YAG laser and organic matrix on porosity changes in human enamel*, J. Dent. 32 (2004) 41–46. https://doi.org/10.1016/S0300-5712(03)00138-6.

[26] M.A. Larmas, H. Häyrynen, L.H. Lajunen, *Thermogravimetric studies on sound and carious human enamel and dentin as well as hydroxyapatite*, Scand. J. Dent. Res. 101 (1993) 185–191. https://doi.org/10.1111/j.1600-0722.1993.tb01102.x.

[27] R.M. Wilson, S.E.P. Dowker, J.C. Elliott, *Rietveld refinements and spectroscopic structural studies of a Na-free carbonate apatite made by hydrolysis of monetite*, Biomaterials 27 (2006) 4682–4692. https://doi.org/10.1016/j.biomaterials.2006.04.033.

[28] S.V. Dorozhkin, *Calcium Orthophosphates and Man: A Historical Perspective from the 1770s to 1940*, in: R.B. Heimann (Ed.), Calcium Phosphate: Structure, synthesis, properties, and applications, Nova Publishers, New York, NY, 2014, pp. 1–40.

[29] M.E. Fleet, *The Carbonate Ion in Hydroxylapatite and Biological Apatite*, in: R.B. Heimann (Ed.), Calcium Phosphate: Structure, synthesis, properties, and applications, Nova Publishers, New York, NY, 2014, pp. 41–61.

[30] M. Mathew, S. Takagi, *Structures of Biological Minerals in Dental Research*, J. Res. Natl. Inst. Stand. Technol. 106 (2001) 1035–1044. https://doi.org/10.6028/jres.106.054.

[31] V. Uskoković, *The Role of Hydroxyl Channel in Defining Selected Physicochemical Peculiarities Exhibited by Hydroxyapatite*, RSC Adv. 5 (2015) 36614–36633. https://doi.org/10.1039/C4RA17180B.

[32] F. Brudevold, D.E. Gardner, F.A. Smith, *The distribution of fluoride in human enamel*, J. Dent. Res. 35 (1956) 420–429. https://doi.org/10.1177/00220345560350031301.

[33] J.C. Elliott, *Calcium Phosphate Biominerals*, Rev. Mineral. Geochem. 48 (2002) 427–453. https://doi.org/10.2138/rmg.2002.48.11.

[34] J.D. Pasteris, *Structurally Incorporated Water in Bone Apatite: A Cautionary Tale*, in: R.B. Heimann (Ed.), Calcium Phosphate: Structure, synthesis, properties, and applications, Nova Publishers, New York, NY, 2014, pp. 63–94.

[35] A.G. Fincham, J. Moradian-Oldak, T.G. Diekwisch, D.M. Lyaruu, J.T. Wright, P. Bringas, H.C. Slavkin, *Evidence for amelogenin "nanospheres" as functional components of secretory-stage enamel matrix*, J. Struct. Biol. 115 (1995) 50–59. https://doi.org/10.1006/jsbi.1995.1029.

[36] A.G. Fincham, J. Moradian-Oldak, J.P. Simmer, *The Structural Biology of the Developing Dental Enamel Matrix*, J. Struct. Biol. (1999) 270–99. https://doi.org/10.1006/jsbi.1999.4130.

[37] J.D. Bartlett, J.P. Simmer, *Proteinases in Developing Dental Enamel*, Crit. Rev. Oral Biol. M. 10 (1999) 425–441. https://doi.org/10.1177/10454411990100040101.

[38] S.N. White, W. Luo, M.L. Paine, H. Fong, M. Sarikaya, M.L. Snead, *Biological organization of hydroxyapatite crystallites into a fibrous continuum toughens and controls anisotropy in human enamel*, J. Dent. Res. 80 (2001) 321–326. https://doi.org/10.1177/00220345010800010501.

[39] T. Uchida, C. Murakami, K. Wakida, N. Dohi, Y. Iwai, J.P. Simmer, M. Fukae, T. Satoda, O. Takahashi, *Sheath proteins: synthesis, secretion, degradation and fate in forming enamel*, Eur. J. Oral Sci. 106 (1998) 308–314. https://doi.org/10.1111/j.1600-0722.1998.tb02191.x.

[40] C. Rathsam, R.M. Farahani, P.G. Hains, V.A. Valova, N. Charadram, H. Zoellner, M. Swain, N. Hunter, *Characterization of inter-crystallite peptides in human enamel rods reveals contribution by the Y allele of amelogenin*, J. Struct. Biol. 204 (2018) 26–37. https://doi.org/10.1016/j.jsb.2018.06.006.

[41] O. Duverger, E. Beniash, M.I. Morasso, *Keratins as components of the enamel organic matrix*, Matrix Biol. 52-54 (2016) 260–265. https://doi.org/10.1016/j.matbio.2015.12.007.

[42] V. Dusevich, C. Xu, Y. Wang, M.P. Walker, J.P. Gorski, *Identification of a protein-containing enamel matrix layer which bridges with the dentine-enamel junction of adult human teeth*, Arch. Oral Biol. 57 (2012) 1585–1594. https://doi.org/10.1016/j.archoralbio.2012.04.014.

[43] J.D. McGuire, M.P. Walker, V. Dusevich, Y. Wang, J.P. Gorski, *Enamel organic matrix: potential structural role in enamel and relationship to residual basement membrane constituents at the dentin enamel junction*, Connect. Tissue Res. 55 Suppl 1 (2014) 33–37. https://doi.org/10.3109/03008207.2014.923883.

[44] J.D. McGuire, M.P. Walker, A. Mousa, Y. Wang, J.P. Gorski, *Type VII collagen is enriched in the enamel organic matrix associated with the dentin-enamel junction of mature human teeth*, Bone 63 (2014) 29–35. https://doi.org/10.1016/j.bone.2014.02.012.

[45] H.M. Elfallah, L.E. Bertassoni, N. Charadram, C. Rathsam, M.V. Swain, *Effect of tooth bleaching agents on protein content and mechanical properties of dental enamel*, Acta Biomater. 20 (2015) 120–128. https://doi.org/10.1016/j.actbio.2015.03.035.

[46] G.V. Lubarsky, P. Lemoine, B.J. Meenan, S. Deb, I. Mutreja, P. Carolan, N. Petkov, *Enamel proteins mitigate mechanical and structural degradations in mature human enamel during acid attack*, Mater. Res. Express 1 (2014) 25404. https://doi.org/10.1088/2053-1591/1/2/025404.

[47] L.H. He, M.V. Swain, *Influence of environment on the mechanical behaviour of mature human enamel*, Biomaterials 28 (2007) 4512–4520. https://doi.org/10.1016/j.biomaterials.2007.06.020.

[48] M. Baldassarri, H.C. Margolis, E. Beniash, *Compositional Determinants of Mechanical Properties of Enamel*, J. Dent. Res. 87 (2008) 645–649.

[49] M. Yahyazadehfar, D. Arola, *The role of organic proteins on the crack growth resistance of human enamel*, Acta Biomater. 19 (2015) 33–45. https://doi.org/10.1016/j.actbio.2015.03.011.

[50] R.A. Young, S. Spooner, *Neutron diffraction studies of human tooth enamel*, Arch. Oral Biol. 15 (1970) 47–63. https://doi.org/10.1016/0003-9969(70)90144-5.

[51] C.H. Yoder, J.D. Pasteris, K.N. Worcester, D.V. Schermerhorn, *Structural water in carbonated hydroxylapatite and fluorapatite: confirmation by solid state (2)H NMR*, Calcif. Tissue Int. 90 (2012) 60–67. https://doi.org/10.1007/s00223-011-9542-9.

[52] D.W. Holcomb, R.A. Young, *Thermal decomposition of human tooth enamel*, Calcif. Tissue Int. 31 (1980) 189–201. https://doi.org/10.1007/bf02407181.

[53] C.-D. Pham, C.E. Smith, Y. Hu, J.C.-C. Hu, J.P. Simmer, Y.-H.P. Chun, *Endocytosis and Enamel Formation*, Front. Physiol. 8 (2017) 529. https://doi.org/10.3389/fphys.2017.00529.

[54] J.P. Simmer, J.C. Hu, *Dental enamel formation and its impact on clinical dentistry*, J. Dent. Educ. (2001) 896–905.

[55] Y. Bai, Z. Yu, L. Ackerman, Y. Zhang, J. Bonde, W. Li, Y. Cheng, S. Habelitz, *Protein nanoribbons template enamel mineralization*, Proc. Natl. Acad. Sci. U.S.A. 117 (2020) 19201–19208. https://doi.org/10.1073/pnas.2007838117.

[56] E. Beniash, R.A. Metzler, R.S.K. Lam, P.U.P.A. Gilbert, *Transient amorphous calcium phosphate in forming enamel*, J. Struct. Biol. 166 (2009) 133–143. https://doi.org/10.1016/j.jsb.2009.02.001.

[57] T.G. Diekwisch, *Subunit compartments of secretory stage enamel matrix*, Connect. Tissue Res. 38 (1998) 101-11; discussion 139-45. https://doi.org/10.3109/03008209809017026.

[58] C. Robinson, P. Fuchs, J.A. Weatherell, *The appearance of developing rat incisor enamel using a freeze fracturing technique*, J. Cryst. Growth 53 (1981) 160–165. https://doi.org/10.1016/0022-0248(81)90062-2.

[59] J.P. Simmer, A.S. Richardson, Y.-Y. Hu, C.E. Smith, J. Ching-Chun Hu, *A post-classical theory of enamel biomineralization… and why we need one*, Int. J. Oral Sci. 4 (2012) 129–134. https://doi.org/10.1038/ijos.2012.59.

[60] C. Robinson, P. Fuchs, J.A. Weatherell, *The fate of matrix proteins during the development of dental enamel*, Calc. Tis. Res. 22 Suppl (1977) 185–190.

[61] G. Daculsi, B. Kerebel, *High-resolution electron microscope study of human enamel crystallites*: *Size, shape, and growth*, J. Ultrastruct. Res. 65 (1978) 163–172. https://doi.org/10.1016/S0022-5320(78)90053-9.

[62] A. Boyde, *The Development of Enamel Structure*, Section of Odontology (1967).

[63] J. Koldehoff, M.V. Swain, G.A. Schneider, *The geometrical structure of interfaces in dental enamel: A FIB-STEM investigation*, Acta Biomater. 104 (2020) 17–27. https://doi.org/10.1016/j.actbio.2019.12.040.

[64] D.F. Travis, M.J. Glimcher, *The Structure And Organization Of, And The Relationship Between The Organic Matrix And The Inorganic Crystals Of Embryonic Bovine Enamel*, J. Cell Biol. 23 (1964) 447–497. https://doi.org/10.1083/jcb.23.3.447.

[65] H. Warshawsky, *Organization of crystals in enamel*, Anat. Rec. (1989). https://doi.org/10.1002/ar.1092240214.

[66] J.C.-C. Hu, Y.-H.P. Chun, T. Al Hazzazzi, J.P. Simmer, *Enamel formation and amelogenesis imperfecta*, Cells Tissues Organs 186 (2007) 78–85. https://doi.org/10.1159/000102683.

[67] R.M. Frank, J. Nalbandian, *Comparative Aspects of Development of Dental Hard Structures*, J. Dent. Res. 42 (1963) 422–437. https://doi.org/10.1177/00220345630420014901.

[68] N.W. Johnson, *Some aspects of the ultrastructure of early human enamel caries seen with the electron microscope*, Arch. Oral Biol. (1967) 1505–1518. https://doi.org/10.1016/0003-9969(67)90186-0.

[69] M.L. Paine, S.N. White, W. Luo, H. Fong, M. Sarikaya, M.L. Snead, *Regulated gene expression dictates enamel structure and tooth function*, Matrix Biol. 20 (2001) 273–292. https://doi.org/10.1016/S0945-053X(01)00153-6.

[70] D.B. Scott, *The Electron Microscopy of Enamel and Dentin*, Annals of the New York Academy of Sciences 60 (1955) 575–584. https://doi.org/10.1111/j.1749-6632.1955.tb40052.x.

[71] E. Rönnholm, *The amelogenesis of human teeth as revealed by electron microscopy*, J. Ultrastruct. Res. 6 (1962) 249–303. https://doi.org/10.1016/S0022-5320(62)80036-7.

[72] J.-E. Glas, M.U. Nylen, *A correlated electron microscopic and microradiographic study of human enamel*, Arch. Oral Biol. 10 (1965) 893-IN13. https://doi.org/10.1016/0003-9969(65)90083-X.

[73] C.C. Hu, M. Fukae, T. Uchida, Q. Qian, C.H. Zhang, O.H. Ryu, T. Tanabe, Y. Yamakoshi, C. Murakami, N. Dohi, M. Shimizu, J.P. Simmer, *Sheathlin: cloning, cDNA/polypeptide sequences, and immunolocalization of porcine enamel sheath proteins*, J. Dent. Res. 76 (1997) 648–657. https://doi.org/10.1177/00220345970760020501.

[74] T. Nakata, K. Yamamoto, S. Matsuo, T. Nishimoto, E. Kitano, M. Akai, *Nature and distribution of mucosubstances in human mature enamel identified by enzyme electron microscopy*, Arch. Oral Biol. 27 (1982) 431–433. https://doi.org/10.1016/0003-9969(82)90154-6.

[75] Q. Ruan, J. Moradian-Oldak, *Amelogenin and Enamel Biomimetics*, J. Mater. Chem. B 3 (2015) 3112–3129. https://doi.org/10.1039/C5TB00163C.

[76] R.M. Frank, R.F. Sognnaes, *Electron microscopy of matrix formation and calcification in rat enamel*, Arch. Oral Biol. (1960) 339–342. https://doi.org/10.1016/0003-9969(60)90095-9.

[77] A.H. Meckel, W.J. Griebstein, R.J. Neal, *Structure of mature human dental enamel as observed by electron microscopy*, Arch. Oral Biol. 10 (1965) 775–783. https://doi.org/10.1016/0003-9969(65)90131-7.

[78] H. Warshawsky, *A light and electron microscopic study of the nearly mature enamel of rat incisors*, Anat. Rec. 169 (1971) 559–583. https://doi.org/10.1002/ar.1091690307.

[79] J.G. Helmcke, *Ultrastructure of Enamel*, in: A. Mills (Ed.), Structural and Chemical Organization of Teeth, second ed., Elsevier Science, Burlington, 1967, pp. 135–163.

[80] M.C. Maas, E.R. Dumont, *Built to last: The structure, function, and evolution of primate dental enamel*, Evol. Anthropol. (1999). https://doi.org/10.1002/(SICI)1520-6505(1999)8:4<133:AID-EVAN4>3.0.CO;2-F.

[81] F.-Z. Cui, J. Ge, *New observations of the hierarchical structure of human enamel, from nanoscale to microscale*, J. Tissue Eng. Regen. Med. 1 (2007) 185–191. https://doi.org/10.1002/term.21.

[82] M.J. Glimcher, P.T. Levine, *Studies of the proteins, peptides and free amino acids of mature bovine enamel*, Biochem. J. 98 (1966) 742–753.

[83] S. Risnes, D. Septier, D.D.d. Periere, M. Goldberg, *TEM Observations on the Ameloblast/Enamel Interface in the Rat Incisor*, Connect. Tissue Res. 43 (2002) 496–504. https://doi.org/10.1080/03008200290000899.

[84] S. Risnes, *Growth tracks in dental enamel*, J. Hum. Evol. 35 (1998) 331–350. https://doi.org/10.1006/jhev.1998.0229.

[85] H. Warshawsky, K. Josephsen, A. Thylstrup, O. Fejerskov, *The development of enamel structure in rat incisors as compared to the teeth of monkey and man*, Anat. Rec. 200 (1981) 371–399. https://doi.org/10.1002/ar.1092000402.

[86] C.E. Smith, *Cellular and Chemical Events During Enamel Maturation*, Crit. Rev. Oral Biol. M. (1998) 128–161. https://doi.org/10.1177/10454411980090020101.

[87] E. Johansen, *Microstructure of Enamel and Dentin*, J. Dent. Res. 43 (1964) SUPPL:1007-20.

[88] Z. Xie, N.M. Kilpatrick, M.V. Swain, P.R. Munroe, M. Hoffman, *Transmission electron microscope characterisation of molar-incisor-hypomineralisation*, J. Mater. Sci. Mater. Med. 19 (2008) 3187–3192. https://doi.org/10.1007/s10856-008-3441-2.

[89] Z.-H. Xie, E.K. Mahoney, N.M. Kilpatrick, M.V. Swain, M. Hoffman, *On the structure-property relationship of sound and hypomineralized enamel*, Acta Biomater. 3 (2007) 865–872. https://doi.org/10.1016/j.actbio.2007.05.007.

[90] Y.L. Chan, A.H.W. Ngan, N.M. King, *Degraded prism sheaths in the transition region of hypomineralized teeth*, J. Dent. 38 (2010) 237–244. https://doi.org/10.1016/j.jdent.2009.11.003.

[91] D. Bajaj, D. Arola, *Role of prism decussation on fatigue crack growth and fracture of human enamel*, Acta Biomater. 5 (2009) 3045–3056. https://doi.org/10.1016/j.actbio.2009.04.013.

[92] Z. Xie, M.V. Swain, M.J. Hoffman, *Structural integrity of enamel*: *Experimental and modeling*, J. Dent. Res. 88 (2009) 529–533. https://doi.org/10.1177/0022034509337130.

[93] A. Boyde, L. Martin, *The Microstructure of Primate Dental Enamel*, in: D.J. Chivers, B.A. Wood, A. Bilsborough (Eds.), Food Acquisition and Processing in Primates, Springer US, Boston, MA, s.l., 1984, pp. 341–367.

[94] C. Robinson, S. Connell, S.J. Brookes, J. Kirkham, R.C. Shore, D.A.M. Smith, *Surface chemistry of enamel apatite during maturation in relation to pH: implications for protein removal and crystal growth*, Arch. Oral Biol. 50 (2005) 267–270. https://doi.org/10.1016/j.archoralbio.2004.11.017.

[95] L.H. He, N. Fujisawa, M.V. Swain, *Elastic modulus and stress-strain response of human enamel by nano-indentation*, Biomaterials 27 (2006) 4388–4398. https://doi.org/10.1016/j.biomaterials.2006.03.045.

[96] J. Zhou, L.L. Hsiung, *Depth-dependent mechanical properties of enamel by nanoindentation*, J. Biomed. Mater. Res. A 81 (2007) 66–74. https://doi.org/10.1002/jbm.a.31012.

[97] L.H. He, M.V. Swain, *Understanding the mechanical behaviour of human enamel from its structural and compositional characteristics*, J. Mech. Behav. Biomed. Mater. 1 (2008) 18–29. https://doi.org/10.1016/j.jmbbm.2007.05.001.

[98] G.V. Lubarsky, R.A. D'Sa, S. Deb, B.J. Meenan, P. Lemoine, *The role of enamel proteins in protecting mature human enamel against acidic environments*: *A double layer force spectroscopy study*, Biointerphases 7 (2012) 14. https://doi.org/10.1007/s13758-011-0014-6.

[99] B. An, R. Wang, D. Arola, D. Zhang, *The role of property gradients on the mechanical behavior of human enamel*, J. Mech. Behav. Biomed. Mater. 9 (2012) 63–72. https://doi.org/10.1016/j.jmbbm.2012.01.009.

[100] B. An, R. Wang, D. Zhang, *Role of crystal arrangement on the mechanical performance of enamel*, Acta Biomater. 8 (2012) 3784–3793. https://doi.org/10.1016/j.actbio.2012.06.026.

[101] Y.-F. Jia, F.-Z. Xuan, *Anisotropic wear behavior of human enamel at the rod level in terms of nanoscratching*, Wear 290-291 (2012) 124–132. https://doi.org/10.1016/j.wear.2012.04.020.

[102] J. Xue, A.V. Zavgorodniy, B.J. Kennedy, M.V. Swain, W. Li, *X-ray microdiffraction, TEM characterization and texture analysis of human dentin and enamel*, J. Microsc. 251 (2013) 144–153. https://doi.org/10.1111/jmi.12053.

[103] P.W. Lucas, S.M. Philip, D. Al-Qeoud, N. Al-Draihim, S. Saji, A. van Casteren, *Structure and scale of the mechanics of mammalian dental enamel viewed from an evolutionary perspective*, Evol. Dev. 18 (2016) 54–61. https://doi.org/10.1111/ede.12169.

[104] S. Myoung, J. Lee, P. Constantino, P. Lucas, H. Chai, B. Lawn, *Morphology and fracture of enamel*, J. Biomech. 42 (2009) 1947–1951. https://doi.org/10.1016/j.jbiomech.2009.05.013.

[105] I. Scheider, T. Xiao, E. Yilmaz, G.A. Schneider, N. Huber, S. Bargmann, *Damage modeling of small-scale experiments on dental enamel with hierarchical microstructure*, Acta Biomater. 15 (2015) 244–253. https://doi.org/10.1016/j.actbio.2014.11.036.

[106] S. Bargmann, I. Scheider, T. Xiao, E.D. Yilmaz, G.A. Schneider, N. Huber, *Towards bio-inspired engineering materials*: *Modeling and simulation of the mechanical behavior of hierarchical bovine dental structure*, Computational Materials Science 79 (2013) 390–401. https://doi.org/10.1016/j.commatsci.2013.06.028.

[107] I.R. Spears, *A three-dimensional finite element model of prismatic enamel: a re-appraisal of the data on the Young's modulus of enamel*, J. Dent. Res. 76 (1997) 1690–1697. https://doi.org/10.1177/00220345970760101101.

[108] H. Gao, B. Ji, I.L. Jager, E. Arzt, P. Fratzl, *Materials become insensitive to flaws at nanoscale: Lessons from nature*, Proc. Natl. Acad. Sci. U.S.A. (2003) 5597–5600. https://doi.org/10.1073/pnas.0631609100.

[109] L.M. Gordon, D. Joester, *Mapping residual organics and carbonate at grain boundaries and the amorphous interphase in mouse incisor enamel*, Front. Physiol. 6 (2015) 57. https://doi.org/10.3389/fphys.2015.00057.

[110] A. La Fontaine, A. Zavgorodniy, H. Liu, R. Zheng, M. Swain, J. Cairney, *Atomic-scale compositional mapping reveals Mg-rich amorphous calcium phosphate in human dental enamel*, Sci. Adv. 2 (2016) e1601145. https://doi.org/10.1126/sciadv.1601145.

[111] E. Beniash, C.A. Stifler, C.-Y. Sun, G.S. Jung, Z. Qin, M.J. Buehler, P.U.P.A. Gilbert, *The hidden structure of human enamel*, Nat. Commun. 10 (2019) 4383. https://doi.org/10.1038/s41467-019-12185-7.

[112] S. Bechtle, S. Habelitz, A. Klocke, T. Fett, G.A. Schneider, *The fracture behaviour of dental enamel*, Biomaterials 31 (2010) 375–384. https://doi.org/10.1016/j.biomaterials.2009.09.050.

[113] E.D. Yilmaz, G.A. Schneider, M.V. Swain, *Influence of structural hierarchy on the fracture behaviour of tooth enamel*, Philos. Trans. A Math. Phys. Eng. Sci. 373 (2015). https://doi.org/10.1098/rsta.2014.0130.

[114] S. Bechtle, H. Özcoban, E.T. Lilleodden, N. Huber, A. Schreyer, M.V. Swain, G.A. Schneider, *Hierarchical flexural strength of enamel*: *Transition from brittle to damage-tolerant behaviour*, J. R. Soc. Interface 9 (2012) 1265–1274. https://doi.org/10.1098/rsif.2011.0498.

[115] J.L. Cuy, A.B. Mann, K.J. Livi, M.F. Teaford, T.P. Weihs, *Nanoindentation mapping of the mechanical properties of human molar tooth enamel*, Arch. Oral Biol. 47 (2002) 281–291. https://doi.org/10.1016/S0003-9969(02)00006-7.

[116] L.-H. He, Z.-H. Yin, L.J. van Vuuren, E.A. Carter, X.-W. Liang, *A natural functionally graded biocomposite coating--human enamel*, Acta Biomater. 9 (2013) 6330–6337. https://doi.org/10.1016/j.actbio.2012.12.029.

[117] S. Park, D.H. Wang, D. Zhang, E. Romberg, D. Arola, *Mechanical properties of human enamel as a function of age and location in the tooth*, J. Mater. Sci. Mater. Med. 19 (2008) 2317–2324. https://doi.org/10.1007/s10856-007-3340-y.

[118] L.-H. He, M.V. Swain, *Enamel--a functionally graded natural coating*, J. Dent. 37 (2009) 596–603. https://doi.org/10.1016/j.jdent.2009.03.019.

[119] Y.L. Chan, A.H.W. Ngan, N.M. King, *Nano-scale structure and mechanical properties of the human dentine-enamel junction*, J. Mech. Behav. Biomed. Mater. 4 (2011) 785–795. https://doi.org/10.1016/j.jmbbm.2010.09.003.

[120] S. Bechtle, G.A. Schneider, K. Schulte, *On the mechanical properties of dental enamel*: *A multi-scale approach*. *Zugl.: Hamburg-Harburg, Techn. Univ., Institut für Keramische Hochleistungswerkstoffe, Diss., 2011,* first Aufl., Dr. Hut, München, 2011.

[121] E.D. Yilmaz, S. Bechtle, H. Özcoban, A. Schreyer, G.A. Schneider, *Fracture behavior of hydroxyapatite nanofibers in dental enamel under micropillar compression*, Scripta Mater. 68 (2013) 404–407. https://doi.org/10.1016/j.scriptamat.2012.11.007.

[122] E.D. Yilmaz, H. Jelitto, G.A. Schneider, *Uniaxial compressive behavior of micro-pillars of dental enamel characterized in multiple directions*, Acta Biomater. 16 (2015) 187–195. https://doi.org/10.1016/j.actbio.2015.01.015.

[123] E.D. Yilmaz, G.A. Schneider, *Mechanical behavior of enamel rods under micro-compression*, J. Mech. Behav. Biomed. Mater. 63 (2016) 183–194. https://doi.org/10.1016/j.jmbbm.2016.06.017.

[124] S.F. Ang, E.L. Bortel, M.V. Swain, A. Klocke, G.A. Schneider, *Size-dependent elastic/inelastic behavior of enamel over millimeter and nanometer length scales*, Biomaterials 31 (2010) 1955–1963. https://doi.org/10.1016/j.biomaterials.2009.11.045.

[125] S. Bechtle, H. Özcoban, E.D. Yilmaz, T. Fett, G. Rizzi, E.T. Lilleodden, N. Huber, A. Schreyer, M.V. Swain, G.A. Schneider, *A method to determine site-specific, anisotropic fracture toughness*

in biological materials, Scripta Mater. 66 (2012) 515–518. https://doi.org/10.1016/j.scriptamat.2011.12.027.

[126] S.F. Ang, A. Schulz, R. Pacher Fernandes, G.A. Schneider, *Sub-10-micrometer toughening and crack tip toughness of dental enamel*, J. Mech. Behav. Biomed. Mater. 4 (2011) 423–432. https://doi.org/10.1016/j.jmbbm.2010.12.003.

[127] D. Bajaj, D.D. Arola, *On the R-curve behavior of human tooth enamel*, Biomaterials 30 (2009) 4037–4046. https://doi.org/10.1016/j.biomaterials.2009.04.017.

[128] M. Yahyazadehfar, J. Ivancik, H. Majd, B. An, D. Zhang, D. Arola, *On the Mechanics of Fatigue and Fracture in Teeth*, Appl. Mech. Rev. 66 (2014) 308031–3080319. https://doi.org/10.1115/1.4027431.

[129] M. Yahyazadehfar, D. Bajaj, D.D. Arola, *Hidden contributions of the enamel rods on the fracture resistance of human teeth*, Acta Biomater. 9 (2013) 4806–4814. https://doi.org/10.1016/j.actbio.2012.09.020.

[130] B. He, S. Huang, J. Jing, Y. Hao, *Measurement of hydroxyapatite density and Knoop hardness in sound human enamel and a correlational analysis between them*, Arch. Oral Biol. 55 (2010) 134–141. https://doi.org/10.1016/j.archoralbio.2009.12.005.

[131] H. Eimar, E. Ghadimi, B. Marelli, H. Vali, S.N. Nazhat, W.M. Amin, J. Torres, O. Ciobanu, R.F. Albuquerque Junior, F. Tamimi, *Regulation of enamel hardness by its crystallographic dimensions*, Acta Biomater. 8 (2012) 3400–3410. https://doi.org/10.1016/j.actbio.2012.06.002.

[132] C.A. Stifler, J.E. Jakes, J.D. North, D.R. Green, J.C. Weaver, P.U.P.A. Gilbert, *Crystal misorientation correlates with hardness in tooth enamels*, Acta Biomater. 120 (2021) 124–134. https://doi.org/10.1016/j.actbio.2020.07.037.

[133] Y.L. Chan, A.H.W. Ngan, N.M. King, *Use of focused ion beam milling for investigating the mechanical properties of biological tissues*: *A study of human primary molars*, J. Mech. Behav. Biomed. Mater. 2 (2009) 375–383. https://doi.org/10.1016/j.jmbbm.2009.01.006.

[134] S. Bechtle, T. Fett, G. Rizzi, S. Habelitz, A. Klocke, G.A. Schneider, *Crack arrest within teeth at the dentinoenamel junction caused by elastic modulus mismatch*, Biomaterials 31 (2010) 4238–4247. https://doi.org/10.1016/j.biomaterials.2010.01.127.

[135] J. Koldehoff, G.A. Schneider, *Effect of deproteinization treatments on the structure and mechanical properties of dental enamel*, Materialia 16 (2021) 101088. https://doi.org/10.1016/j.mtla.2021.101088.

[136] C.J. Soares, L. Barbosa, F.R. Santana, P.B.F. Soares, A.S.d. Mota, G.R.d. Silva, *Fracture strength of composite fixed partial denture using bovine teeth as a substitute for human teeth with or without fiber-reinforcement*, Braz. Dent. J. 21 (2010) 235–240. https://doi.org/10.1590/S0103-64402010000300011.

[137] P. Laurance-Young, L. Bozec, L. Gracia, G. Rees, F. Lippert, R.J.M. Lynch, J.C. Knowles, *A review of the structure of human and bovine dental hard tissues and their physicochemical behaviour in relation to erosive challenge and remineralisation*, J. Dent. 39 (2011) 266–272. https://doi.org/10.1016/j.jdent.2011.01.008.

[138] C. Wang, Y. Li, X. Wang, L. Zhang, Tiantang, B. Fu, *The enamel microstructures of bovine mandibular incisors*, Anat. Rec. (Hoboken) 295 (2012) 1698–1706. https://doi.org/10.1002/ar.22543.

[139] R.F. Egerton, *Physical principles of electron microscopy*: *An introduction to TEM, SEM, and AEM,* Corr. third. print, Springer, New York, NY, 2008.

[140] A.A. Tseng, *Recent developments in nanofabrication using focused ion beams*, Small 1 (2005) 924–939. https://doi.org/10.1002/smll.200500113.

[141] U. Muehle, S. Jansen, L. Hillmann, H.-J. Engelmann, D. Rafaja, *FIB-based target preparations of complex material systems for advanced TEM investigations*, in: A. Mendez-Vilas, J. Díaz (Eds.), Microscopy: Science, technology, applications and education, Formatex, Badajoz, 2010, pp. 1704–1716.

[142] D.B. Williams, C.B. Carter, *Transmission electron microscopy*: *A textbook for materials science,* secondnd ed., Springer, New York, 2008.

[143] R. Wirth, *Focused Ion Beam (FIB) combined with SEM and TEM*: *Advanced analytical tools for studies of chemical composition, microstructure and crystal structure in geomaterials on a nanometre scale*, Chemical Geol. 261 (2009) 217–229. https://doi.org/10.1016/j.chemgeo.2008.05.019.

[144] H. Dietrich, A. Stahl, H. Frerichs, *NCHS-Elementaranalyse*: *M02.001. 02*, 2019. https://www.tuhh.de/zentrallabor/methoden/m02001.html (accessed 10 December 2020).

[145] A.-L. Schulze, H. Frerichs, *Aminosäuren-Analyse mittels HPLC-FLD nach OPA-Derivatisierung*: *M03.003. 03*, 2019. https://www.tuhh.de/zentrallabor/methoden/m03003.html (accessed 10 December 2020).

[146] C. Berthomieu, R. Hienerwadel, *Fourier transform infrared (FTIR) spectroscopy*, Photosynth Res 101 (2009) 157–170. https://doi.org/10.1007/s11120-009-9439-x.

[147] W.C. Oliver, G.M. Pharr, *An improved technique for determining hardness and elastic modulus using load and displacement sensing indentation experiments*, J. Mater. Res. 7 (1992) 1564–1583. https://doi.org/10.1557/JMR.1992.1564.

[148] A.C. Fischer-Cripps, *Nanoindentation*, Springer, New York, NY, 2013.

[149] R.E. Smallman, A.H.W. Ngan, *Chapter 5 - Characterization and Analysis*, in: R.E. Smallman, A.H.W. Ngan (Eds.), Modern physical metallurgy, Eighth edition, Butterworth-Heinemann, Oxford, 2014, pp. 159–250.

[150] J.S. Field, M.V. Swain, *A simple predictive model for spherical indentation*, J. Mater. Res. 8 (1993) 297–306. https://doi.org/10.1557/JMR.1993.0297.

[151] X. Li, B. Bhushan, *A review of nanoindentation continuous stiffness measurement technique and its applications*, Mater. Character. 48 (2002) 11–36. https://doi.org/10.1016/S1044-5803(02)00192-4.

[152] V. Maier, B. Merle, M. Göken, K. Durst, *An improved long-term nanoindentation creep testing approach for studying the local deformation processes in nanocrystalline metals at room and elevated temperatures*, J. Mater. Res. 28 (2013) 1177–1188. https://doi.org/10.1557/jmr.2013.39.

[153] D. Munz, T. Fett, *Ceramics*: *Mechanical properties, failure behaviour, materials selection,* Corr. second. print, Springer, Berlin, 2001.

[154] L.-H. He, M.V. Swain, *Nanoindentation creep behavior of human enamel*, J. Biomed. Mater. Res. A 91 (2009) 352–359. https://doi.org/10.1002/jbm.a.32223.

[155] A. Leitner, V. Maier-Kiener, D. Kiener, *Essential refinements of spherical nanoindentation protocols for the reliable determination of mechanical flow curves*, Mater. Design 146 (2018) 69–80. https://doi.org/10.1016/j.matdes.2018.03.003.

[156] T.H. Zhang, J.H. Ye, Y.H. Feng, Y. Ma, *On the spherical nanoindentation creep of metallic glassy thin films at room temperature*, Mat. Sci. Eng. A-Struct. 685 (2017) 294–299. https://doi.org/10.1016/j.msea.2017.01.018.

[157] O. Prach, C. Minnert, K.E. Johanns, K. Durst, *A new nanoindentation creep technique using constant contact pressure*, J. Mater. Res. 34 (2019) 2492–2500. https://doi.org/10.1557/jmr.2019.188.

[158] J. Ge, F.Z. Cui, X.M. Wang, H.L. Feng, *Property variations in the prism and the organic sheath within enamel by nanoindentation*, Biomaterials 26 (2005) 3333–3339. https://doi.org/10.1016/j.biomaterials.2004.07.059.

[159] J. Schindelin, I. Arganda-Carreras, E. Frise, V. Kaynig, M. Longair, T. Pietzsch, S. Preibisch, C. Rueden, S. Saalfeld, B. Schmid, J.-Y. Tinevez, D.J. White, V. Hartenstein, K. Eliceiri, P. Tomancak, A. Cardona, *Fiji: an open-source platform for biological-image analysis*, Nat. Methods 9 (2012) 676–682. https://doi.org/10.1038/nmeth.2019.

[160] L. Bachmann, R. Diebolder, R. Hibst, D.M. Zezell, *Infrared Absorption Bands of Enamel and Dentin Tissues from Human and Bovine Teeth*, Appl. Spectrosc. Rev. 38 (2003) 1–14. https://doi.org/10.1081/ASR-120017479.

[161] F. Taube, M. Marczewski, J.G. Norén, *Deviations of inorganic and organic carbon content in hypomineralised enamel*, J. Dent. 43 (2015) 269–278. https://doi.org/10.1016/j.jdent.2014.09.003.

[162] J. Mencík, L.H. He, M.V. Swain, *Determination of viscoelastic-plastic material parameters of biomaterials by instrumented indentation*, J. Mech. Behav. Biomed. Mater. 2 (2009) 318–325. https://doi.org/10.1016/j.jmbbm.2008.09.002.

[163] S. Bernick, R.F. Baker, R.L. Rutherford, O. Warren, *Electron Microscopy of Enamel and Dentin*, J. Am. Dent. Assoc. 45 (1952) 689–696. https://doi.org/10.14219/jada.archive.1952.0245.

[164] M. Al-Mosawi, G.R. Davis, A. Bushby, J. Montgomery, J. Beaumont, M. Al-Jawad, *Crystallographic texture and mineral concentration quantification of developing and mature human incisal enamel*, Sci. Rep. 8 (2018) 14449. https://doi.org/10.1038/s41598-018-32425-y.

[165] K.A. Selvig, A. Halse, *Crystal growth in rat incisor enamel*, Anat. Rec. 173 (1972) 453–468. https://doi.org/10.1002/ar.1091730406.

[166] T. Yanagisawa, Y. Miake, *High-resolution electron microscopy of enamel-crystal demineralization and remineralization in carious lesions*, J. Electron Microsc. (2003) 605–613. https://doi.org/10.1093/jmicro/52.6.605.

[167] C. Robinson, J. Hudson, *Tuft protein: protein cross-linking in enamel development*, Eur. J. Oral Sci. 119 Suppl 1 (2011) 50–54. https://doi.org/10.1111/j.1600-0722.2011.00906.x.

[168] R. Salzer, S. Thiele, L. Suemmchen, S. Machill, *Analytische Chemie*: *IR/Raman-Spektroskopie - Interpretation von C,H,O-Verbindungen*, 2016. http://www.chemgapedia.de/vsengine/vlu/vsc/de/ch/3/anc/ir_spek/cho_verbindungen.vlu/Page/vsc/de/ch/3/anc/ir_spek/schwspek/spektreninterpretation/ir_13_4_7_6/amid.vscml.html (accessed 24 June 2020).

[169] A.B. Sønju Clasen, I.E. Ruyter, *Quantitative determination of type A and type B carbonate in human deciduous and permanent enamel by means of Fourier transform infrared spectrometry*, Adv. Dent. Res. 11 (1997) 523–527. https://doi.org/10.1177/08959374970110042101.

[170] C. Rey, B. Collins, T. Goehl, I.R. Dickson, M.J. Glimcher, *The carbonate environment in bone mineral: a resolution-enhanced Fourier Transform Infrared Spectroscopy Study*, Calcif. Tissue Int. 45 (1989) 157–164. https://doi.org/10.1007/BF02556059.

[171] J.E. Eastoe, *Organic Matrix of Tooth Enamel*, Nature 187 (1960) 411. https://doi.org/10.1038/187411b0.

[172] F. Taube, R. Ylmén, A. Shchukarev, S. Nietzsche, J.G. Norén, *Morphological and chemical characterization of tooth enamel exposed to alkaline agents*, J. Dent. 38 (2010) 72–81. https://doi.org/10.1016/j.jdent.2009.09.006.

[173] T. Sui, M.A. Sandholzer, E. Le Bourhis, N. Baimpas, G. Landini, A.M. Korsunsky, *Structure-mechanical function relations at nano-scale in heat-affected human dental tissue*, J. Mech. Behav. Biomed. Mater. 32 (2014) 113–124. https://doi.org/10.1016/j.jmbbm.2013.12.014.

[174] H. Salmang, H. Scholze, *Keramik*, Springer Berlin Heidelberg, 2007.

[175] C. Xu, R. Reed, J.P. Gorski, Y. Wang, M.P. Walker, *The distribution of carbonate in enamel and its correlation with structure and mechanical properties*, Journal of Materials Science 47 (2012) 8035–8043. https://doi.org/10.1007/s10853-012-6693-7.

[176] M.V. Swain, *Role of Fluid on the Contact Deformation Response of Biological Tissue*, Acta Polytech. CTU Proc. 27 (2020) 22–31. https://doi.org/10.14311/APP.2020.27.0022.

[177] L.C. Hua, W.Y. Wang, M.V. Swain, C.L. Zhu, H.B. Huang, J.K. Du, Z.R. Zhou, *The dehydration effect on mechanical properties of tooth enamel*, J. Mech. Behav. Biomed. Mater. 95 (2019) 210–214. https://doi.org/10.1016/j.jmbbm.2019.04.013.

[178] L.S. Dimas, G.H. Bratzel, I. Eylon, M.J. Buehler, *Tough Composites Inspired by Mineralized Natural Materials: Computation, 3D printing, and Testing*, Adv. Funct. Mater. 23 (2013) 4629–4638. https://doi.org/10.1002/adfm.201300215.

[179] J.W. Pro, F. Barthelat, *Discrete element models of tooth enamel, a complex three-dimensional biological composite*, Acta Biomater. 94 (2019) 536–552. https://doi.org/10.1016/j.actbio.2019.04.058.

[180] X. Chen, T. Wu, Q. Wang, J.-W. Shen, *Shield effect of silicate on adsorption of proteins onto silicon-doped hydroxyapatite (100) surface*, Biomaterials 29 (2008) 2423–2432. https://doi.org/10.1016/j.biomaterials.2008.02.002.

[181] G.A. Schneider, L.H. He, M.V. Swain, *Viscous flow model of creep in enamel*, J. Appl. Phys. 103 (2008) 14701. https://doi.org/10.1063/1.2827987.

[182] D. Hull, T.W. Clyne, *An Introduction to Composite Materials,* second ed., Cambridge University Press, Cambridge, 1996.

[183] F. Barthelat, *Architectured materials in engineering and biology*: *Fabrication, structure, mechanics and performance*, International Materials Reviews 60 (2016) 413–430. https://doi.org/10.1179/1743280415Y.0000000008.

[184] H. Özcoban, E.D. Yilmaz, G.A. Schneider, *Hierarchical microcrack model for materials exemplified at enamel*, Dent. Mater. 34 (2018) 69–77. https://doi.org/10.1016/j.dental.2017.11.007.

[185] S. Saber-Samandari, K.A. Gross, *Micromechanical properties of single crystal hydroxyapatite by nanoindentation*, Acta Biomater. 5 (2009) 2206–2212. https://doi.org/10.1016/j.actbio.2009.02.009.

[186] J. Gosline, M. Lillie, E. Carrington, P. Guerette, C. Ortlepp, K. Savage, *Elastic proteins: biological roles and mechanical properties*, Philos. Trans. R. Soc. Lond. ,. B,. Biol. Sci. 357 (2002) 121–132. https://doi.org/10.1098/rstb.2001.1022.

[187] X. Xu, M.M. Thwe, C. Shearwood, K. Liao, *Mechanical properties and interfacial characteristics of carbon-nanotube-reinforced epoxy thin films*, Appl. Phys. Lett. 81 (2002) 2833. https://doi.org/10.1063/1.1511532.

[188] T. Nishino, R. Matsui, K. Nakamae, *Elastic modulus of the crystalline regions of chitin and chitosan*, J. Polym. Sci. Pol. Phys. 37 (1999) 1191–1196. https://doi.org/10.1002/(SICI)1099-0488(19990601)37:11<1191:AID-POLB13>3.0.CO;2-H.

[189] H. Jelitto, G.A. Schneider, *A geometric model for the fracture toughness of porous materials*, Acta Mater. 151 (2018) 443–453. https://doi.org/10.1016/j.actamat.2018.03.018.

[190] S.F. Ang, M. Saadatmand, M.V. Swain, A. Klocke, G.A. Schneider, *Comparison of mechanical behaviors of enamel rod and interrod regions in enamel*, J. Mater. Res. 27 (2012) 448–456. https://doi.org/10.1557/jmr.2011.409.

[191] M.V. Swain, J. Nohava, P. Eberwein, *A simple basis for determination of the modulus and hydraulic conductivity of human ocular surface using nano-indentation*, Acta Biomater. 50 (2017) 312–321. https://doi.org/10.1016/j.actbio.2016.12.007.

[192] N. Sasaki, A. Enyo, *Viscoelastic properties of bone as a function of water content*, J. Biomech. 28 (1995) 809–815. https://doi.org/10.1016/0021-9290(94)00130-V.

[193] C. Rivera, D. Arola, A. Ossa, *Indentation damage and crack repair in human enamel*, J. Mech. Behav. Biomed. Mater. 21 (2013) 178–184. https://doi.org/10.1016/j.jmbbm.2013.02.020.

[194] S.C. Cowin, *Bone poroelasticity*, J. Biomech. 32 (1999) 217–238. https://doi.org/10.1016/S0021-9290(98)00161-4.

[195] A.J. Bushby, N.M. Jennett, *Determining the Area Function of Spherical Indenters for Nanoindentation*, MRS Online Proceedings Library 649 (2000) 7171–7176. https://doi.org/10.1557/PROC-649-Q7.17.

[196] S.R. Kalidindi, S. Pathak, *Determination of the effective zero-point and the extraction of spherical nanoindentation stress–strain curves*, Acta Mater. 56 (2008) 3523–3532. https://doi.org/10.1016/j.actamat.2008.03.036.

[197] R.Z. LeGeros, G. Bonel, R. Legros, *Types of "H2O" in human enamel and in precipitated apatites*, Calc. Tis. Res. 26 (1978) 111–118. https://doi.org/10.1007/BF02013245.

Supplementary Information

A Theoretical Basis

A.1 Spherical Tip Calibration

The ideal elastic contact between a sphere and a planar surface can be described by the well-known Hertzian equation

$$h_e = \left(\frac{9}{3}\right)^{1/3} \left(\frac{P}{E_r}\right)^{2/3} \left(\frac{1}{R}\right)^{1/3} \tag{50}$$

With load P, radius of the sphere R and composite elastic modulus E_r, which is equivalent to equation (16). In a real experiment, several factors influence the depth measured by the indenter and the elastic depth h_e is described as

$$h_e = h + h_0 - C_f P = \left(\frac{9}{3}\right)^{1/3} \left(\frac{P}{E_r}\right)^{2/3} \left(\frac{1}{R_{eff}}\right)^{1/3} \tag{51}$$

where h is the measured penetration depth, h_0 is the penetration depth correction associated with contacting the surface, C_f is the instrument frame compliance, and R_{eff} is the effective indenter radius and is a function of the depth of the sphere in contact with the surface. To obtain the function describing R_{eff}, indentations into materials with a known elastic modulus have to be carried out and R_{eff} can be determined from (49) [195].

In this work, to calibrate the tip indentations into fused silica at various maximum loads within the elastic range of the material have been carried out (Supplementary Figure 1 and Supplementary Figure 2). The indenter radius was then determined by fitting the loading portion of the load-displacement curve with:

$$P = \frac{4}{3} E_r R^{1/2} h^{3/2} \tag{52}$$

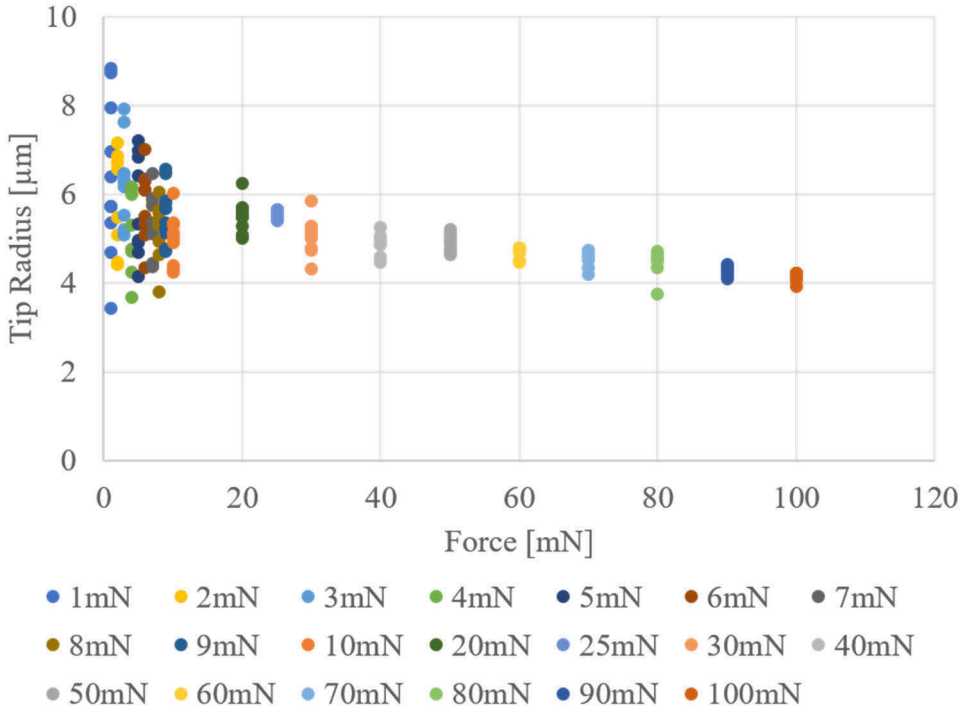

Supplementary Figure 1: Tip radius dependent on force on fused silica. At low loads contact between tip and surface is not well established and the deviation is large. Between 70 and 80mN elastic-plastic transition occurs and the apparent tip radius is decreased.

In total 153 and 221 fitted curves were considered for the determination of the 5 and 50 µm tip radius, respectively. Curves where contact between tip and surface was not well established were not considered. For the 5 µm tip this was the case for the curves with maximum load 1 mN and for curves with maximum load of 10 mN for the 50 µm tip. Additionally, curves where initial contact deviated majorly from the Hertzian relationship, hence resulting in a bad fit with lower R^2 value were not included. For the 5 µm tip on Silica, a transition from purely elastic contact to elastic-plastic contact was observed between 70 and 80 mN. Hence measurements with maximum loads ≥ 80 mN were not considered either. In Supplementary Figure 1 this transition is represented by the decreasing tip radius after 80 mN. The indenter radius has such been determined as 5.31 ± 0.76 µm, which is close to the nominal value of 5 µm. For the 50 µm tip no such transition was observed and the indenter radius has been determined as 36.31 ± 8.32 µm, which has a large deviation from the nominal radius of 50 µm.

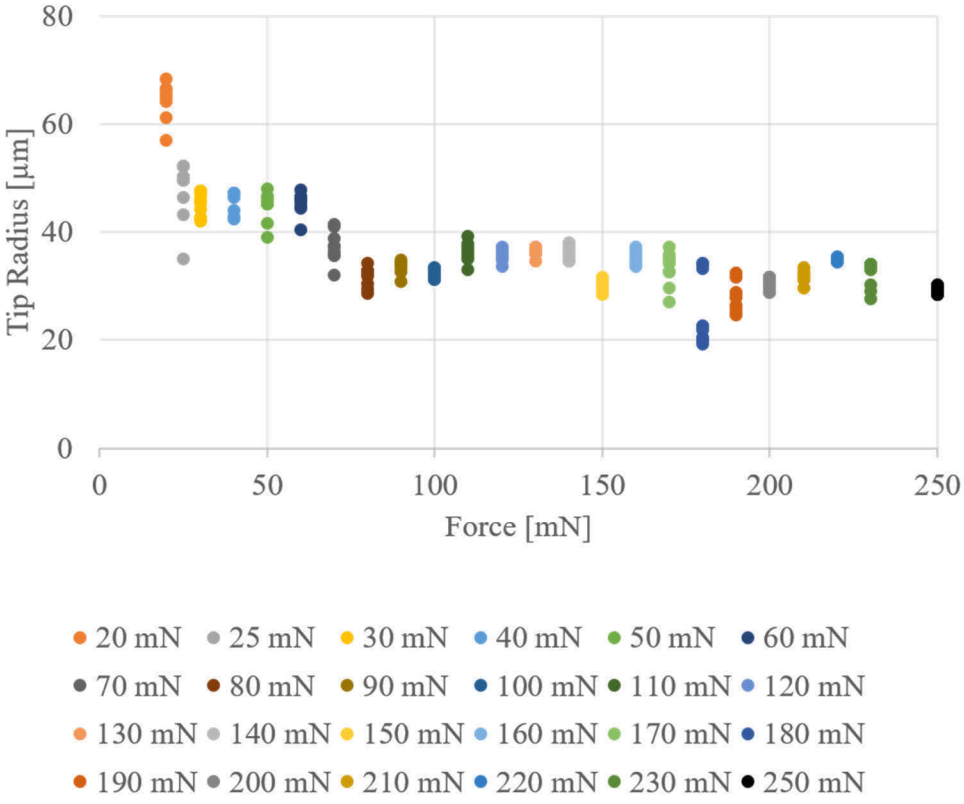

Supplementary Figure 2: Tip radius dependent on force on fused silica. At a load of 10 mN contact between tip and surface is not well established and the deviation is large.

While the approach described here, to indirectly measure R of the indenter by a series from indentation, is a common procedure, it is not without criticisms. This approach implicitly assumes that the contact radius between indenter and surface independent from the respective material. However, the inherent material response should have an important role for the geometry of the contact [196]. As currently there are no reliable and easy methods to measure the indenter radius with the required accuracy, the indirect approach is however widely accepted and was employed in this work.

A.2 Correction of Initial Point of Contact

Although, the nanoindentation system automatically determines a point of initial contact by observing the change in contact stiffness, the point of initial contact is not accurately determined as can be seen in the raw data. For the CSM based experiments to determine the elastic modulus and hardness this was a negligible influence as the overall displacement and load were high. However, for the creep experiments were small loads were applied and small changes in

displacement should be detected during the holding period, a correction of the data was necessary. The point of initial contact for a spherical tip can be determined by fitting the initial loading with the adapted Hertzian function in the form of:

$$P = k(h - h_0)^{1.5} \tag{53}$$

Where h_0 denotes the displacement at zero load and is subsequently subtracted from the measured displacement. Note that by introducing the constant k, the function can be fitted without knowledge about the elastic modulus or indenter tip radius which are required from the Hertzian equation (16). The true load for the initial loading is then calculated by the fitting function until the recorded load and calculated load match. Supplementary Figure 3 shows an exemplary initial load displacement curve for untreated enamel. The fit agrees very well with the raw data at a displacement of ≥ 20 nm. The corrected curve starts with positive values, any negative displacement values are discarded as the corrected load cannot be calculated.

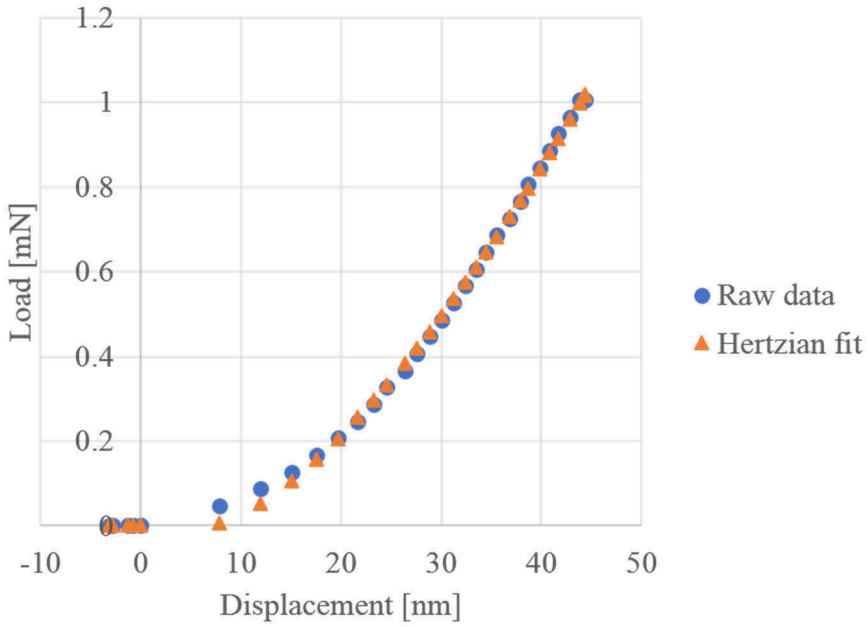

Supplementary Figure 3: Exemplary curve of the raw data and Hertzian fit for the initial loading for untreated enamel. It can be seen that after a displacement of ~20 nm the fit and raw data overlap very well. For displacements <0 the Hertzian function is not valid and is shown at a load of 0 mN.

A.3 Determination of Elastic Modulus

The elastic modulus in nanoindentation experiments can be determined by a method described by Oliver & Pharr. If the stiffness of the contact is known, the modulus of the contact between two bodies can be calculated by (11) and the elastic modulus of the sample can be found by (9), as described in chapter 4.5. With the underlying assumption that the unloading is purely elastic, the Hertzian equations for elastic contact between two bodies can be applied to the unloading. The stiffness of the contact is thus determined by fitting the first 50% of the unloading segment with a power law fit:

$$P = k(h - h_r)^m \tag{54}$$

With k as a constant and h_r as the residual depth caused by plastic deformation. For a spherical tip and a perfect Hertzian curve the exponent $m = 1.5$. The stiffness is then calculated from

$$S = \frac{dP}{dh} = mk(h - h_r)^{m-1} \tag{55}$$

[147].

B Electron Microscopy

This supplementary chapter gives additional information to the electron microscopy techniques and image analyses that were conducted in this work. Similar descriptions have been published in *Acta Biomaterialia* with the title 'The geometrical structure of interfaces in dental enamel: A FIB-STEM investigation' [63] (SI B.1 - B.4) and in *Materialia* with the title 'Effect of deproteinization treatments on the structure and mechanical properties of dental enamel' [135] (SI B.5).

B.1 Fabrication of TEM lamellae

The TEM lamellae were fabricated with the aid of the FIB system. In the following the fabrication steps will be described in more detail. The first step was to choose suitable areas of the enamel where the structure of enamel could easily be distinguished. The sample was orientated in a way that the enamel rods would be cut perpendicular to the lamella. A Pt protection layer was deposited to prevent damage to the underlying structure, two trenches were milled with a current of 21 nA (see schematic in Supplementary Figure 4). This was followed by cleaning procedures with currents of 0.79 nA and 0.43 nA to remove milling artifacts and to guarantee a smooth surface. Then the lamella was cut free on two sides, attached to the nanomanipulator and completely cut free. With the help of the nanomanipulator the lamella was attached onto a copper lift-out grid. Subsequently, several thinning steps with currents of 0.79 nA, 0.23 nA, 80 pA and finally 40 pA followed to achieve electron transparency of the lamella (a thickness of roughly 100 nm). More details on the preparation of TEM samples by FIB can be found in ref. [141].

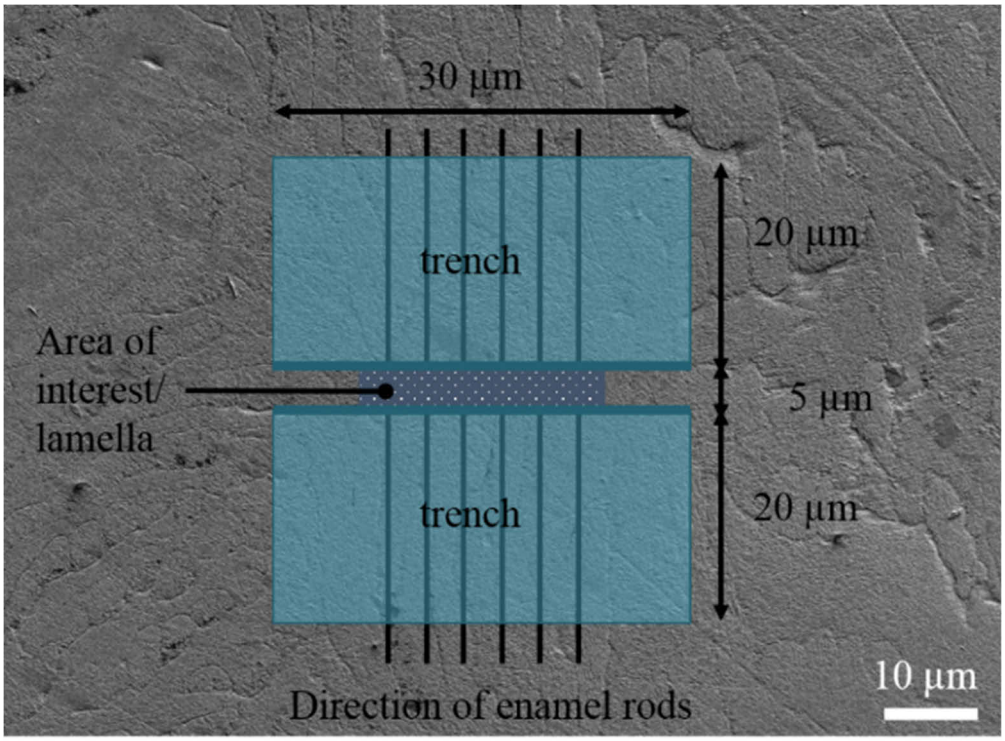

Supplementary Figure 4: For FIB fabrication of the TEM samples (lamellae) first the area of interest is chosen and protected from FIB damage by a Pt-layer (dark blue). FIB is used to mill trenches (light blue) around the area of interest and several cleaning/ polishing steps follow. After lift-out the lamella is then further thinned to about 100 nm.

B.2 FIB lamellae from different enamel areas

Supplementary Figure 5 and Supplementary Figure 6 show lamellae that were prepared by FIB from different regions from untreated and KOH-treated enamel respectively. An overview of the respective lamella can be seen in low magnification images (Supplementary Figure 5 a-c and Supplementary Figure 6 a-c). In both cases, the rods are oriented mostly perpendicular to the chosen cutting direction and can be seen in cross-section. Rod and interrod enamel are arranged in a sandwich structure where the layer of the interrod enamel has approximately the same thickness as the rod layer. The rod boundaries clearly appear as dark lines surrounding the rods and have a closed shape. In the KOH-treated enamel, the boundaries appear wider. Higher magnifications (Supplementary Figure 5 d-f) reveal that these rod boundaries are not mineral free gaps or thin organic sheaths. Instead there is frequent contact between the rod and interrod enamel or between two rods. Crystallites are bridging the boundary creating mineral on mineral contact between those entities and with gaps in between the contacts. However, from the STEM images it cannot be determined whether these gaps are filled by some organic material that is postulated to be present in the zone surrounding the rods or whether they are empty pores. Higher magnification images of the boundaries in untreated enamel (Supplementary Figure 5 g-i) reveal that the crystallites bridging the boundary seem to fuse with the ones in the rod or interrod enamel so that in some cases it is not clear where one structure begins and the other ends. Supplementary Figure 5 g highlights this feature, showing two rods that apparently are in direct contact with each other. Additionally, thin filaments (a few nanometer wide) bridging the boundary could be detected (Supplementary Figure 5 g-i) which seem to have the same grey value as the surrounding HAP crystallites and therefore likely are of mineral origin as discussed in chapter 6.1. These bridging filaments appear to be absent in the deproteinized enamel (Supplementary Figure 6 g-i) where there are large dark gaps visible in the boundary. Other than the absence of the bridging filaments there are no obvious differences between the structures of the untreated and KOH-treated enamel.

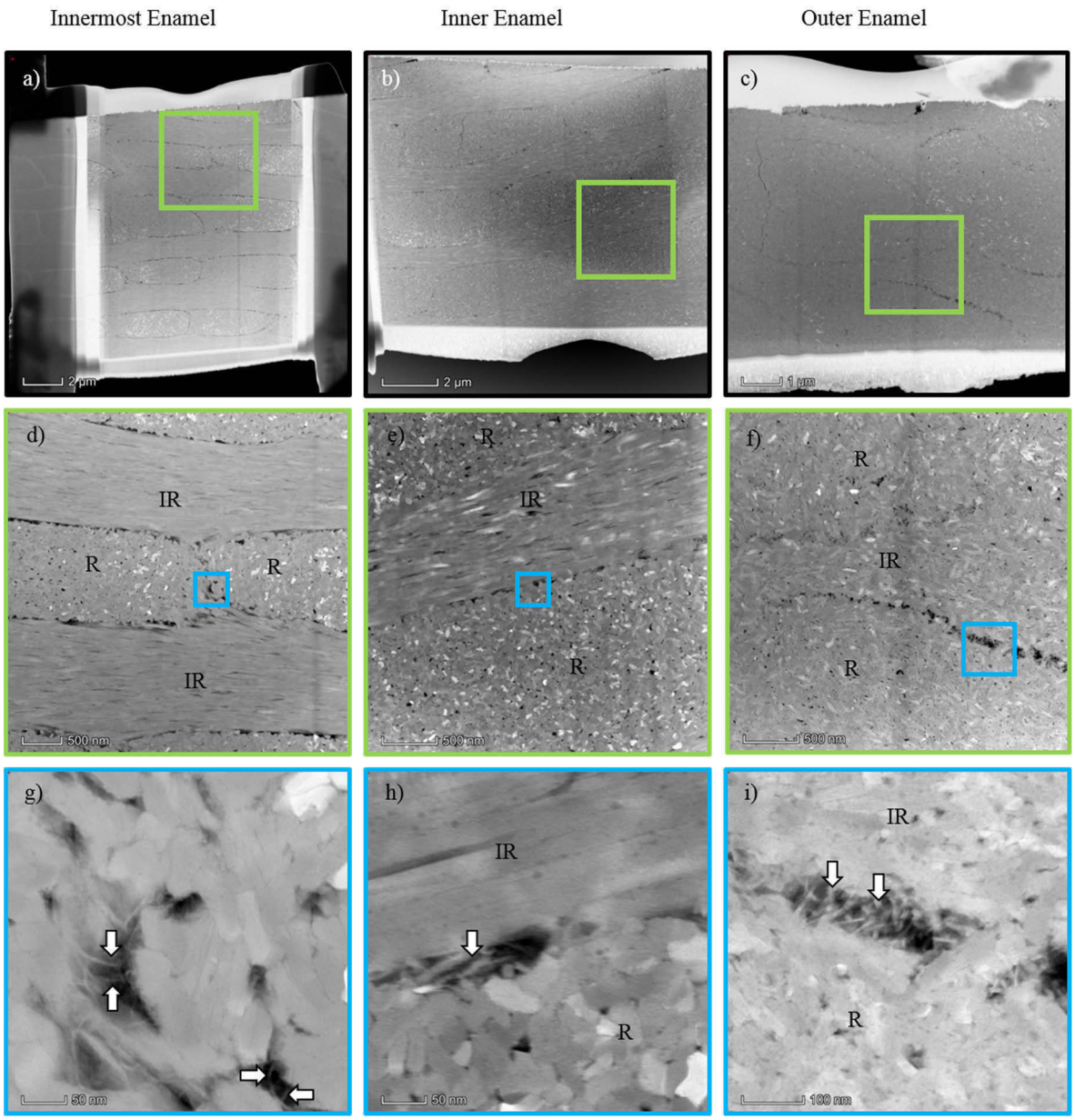

Supplementary Figure 5: STEM images of lamellae from different enamel regions prepared by FIB. Brighter appearing crystallites don't have a different Z-value but are simply in the right orientation for Bragg scattering to occur which gives an additional signal to the detector. 1st row (a-c): Overview of the prepared lamella. 2nd row (d-f): Magnified image of marked area (green square). Rod (R) and interrod enamel (IR) can be distinguished. Rod boundaries appear as discontinuous structures with frequent crystallite on crystallite contact. Higher magnifications (3rd row g-i) of marked areas (blue square) show some bridging filaments or bridging crystallites (arrows) across rod boundaries.

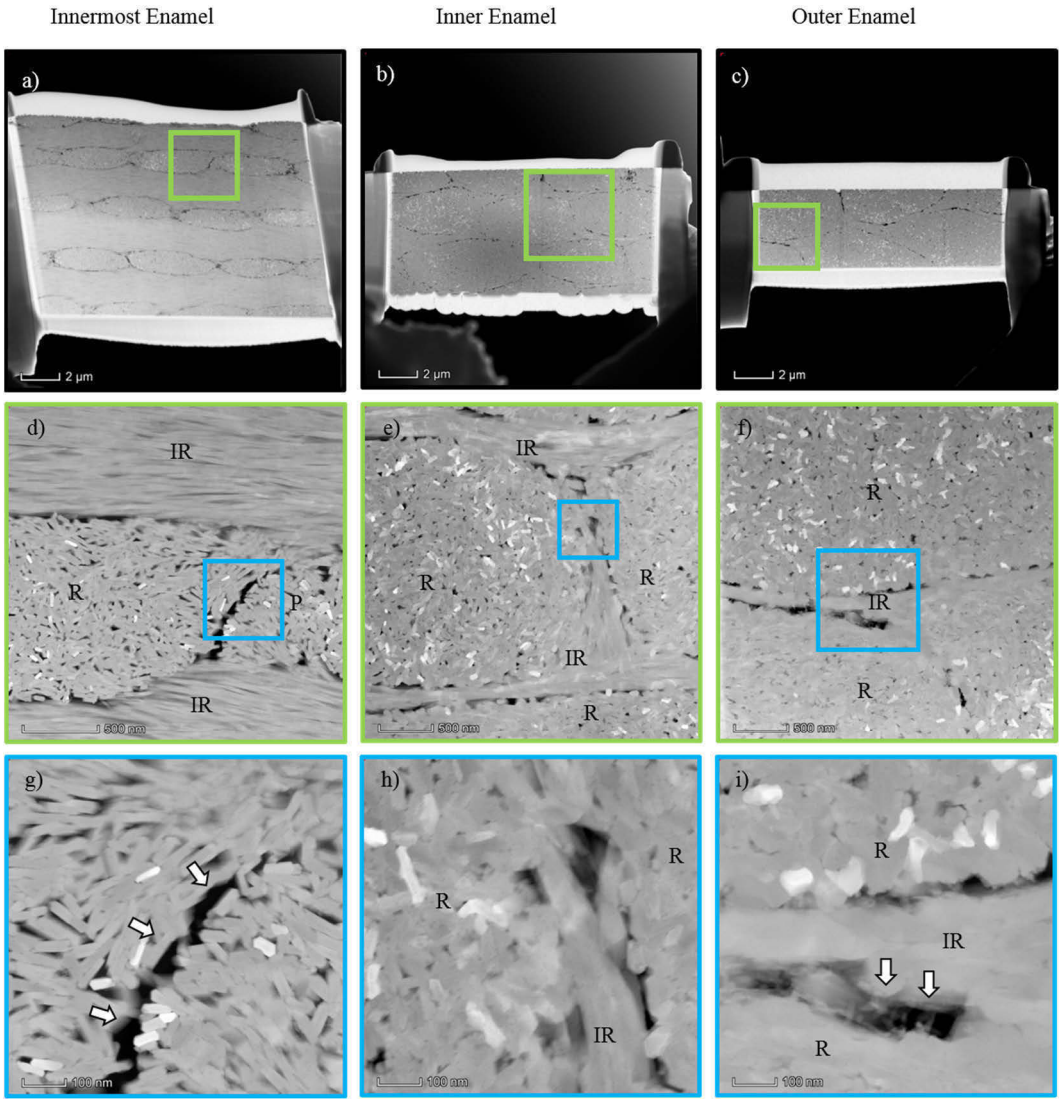

Supplementary Figure 6: STEM images of lamellae from different enamel regions from a KOH-treated enamel sample prepared by FIB. Brighter appearing crystallites don't have a different Z-value but are simply in the right orientation for Bragg scattering to occur which gives an additional signal to the detector. 1st row (a-c): Overview of the prepared lamella. 2nd row (d-f): Magnified image of marked area (green square). Rod (R) and interrod enamel (IR) can be distinguished. Rod boundaries appear as discontinuous structures with frequent crystallite on crystallite contact. Compared to sound enamel, these boundaries appear wider. The bridging filaments that could be seen in the untreated enamel do not seem to be present in the deproteinated sample at higher magnifications (3rd row g-i) of marked areas (blue square) show.

B.3 Determination of the porous area of the rod interfaces

The determination of the porous area in a rod interface was carried out with the image processing software Fiji [159]. To determine the percentage of pores in the interface the

following steps were performed: The image was converted from an RGB-image to an 8-bit image to obtain grey values only. With the function ‘Set Scale’ the image size was set to the correct values utilizing the scale bar. With the function ‘Adjust Threshold’ the threshold was manually chosen in a way that mostly the darker pores and not the lighter crystallites were selected (see Supplementary Figure 7). The threshold was then applied which transformed the image into one with only black or white pixels. A segmented line profile was then drawn across the length of the interface, with the function ‘Plot Profile’ the distribution of black and white pixels can be given and the datapoints can be exported. The length of the line that cuts across white pixels was determined and related to the total length of the line, which determined the percentage of the porous area of the interface. In total 15 interfaces were measured in this way and the average percentage of these pores related to the total interface was determined to be 57 ± 15%. For the KOH-treated enamel the same analysis was carried out on 14 interfaces and the porosity of the interface was determined as 45 ± 8%.

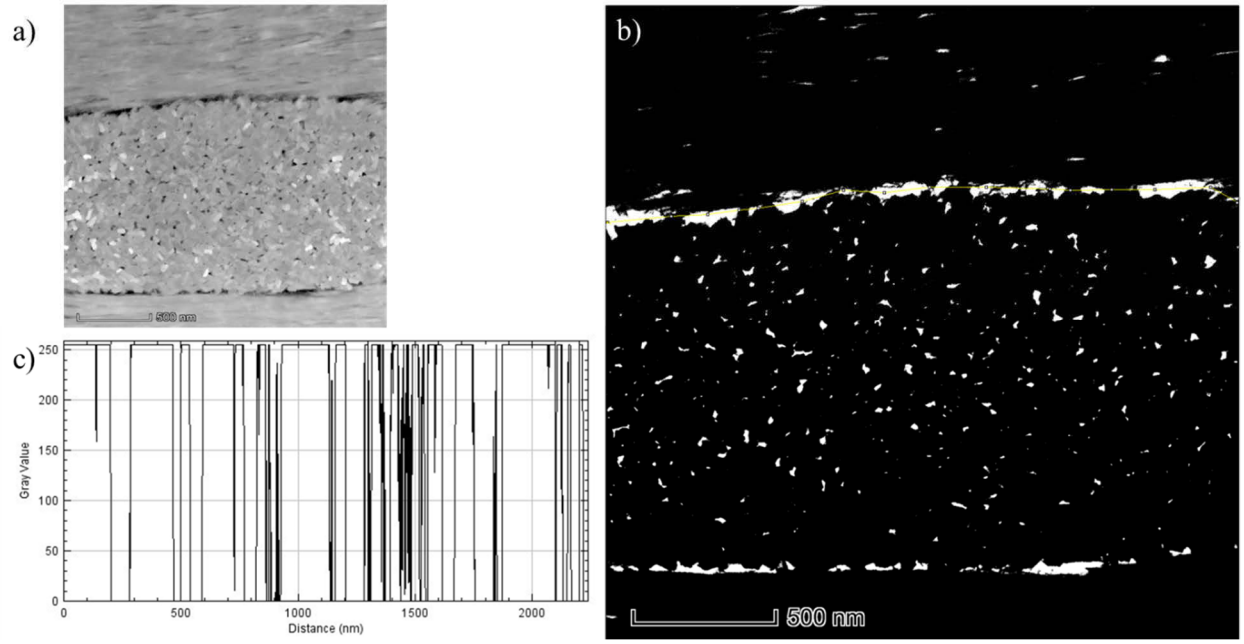

Supplementary Figure 7: a) Original TEM image b) Image after applying the threshold function and segmented line profile drawn in the top rod boundary (yellow line) c) Plot of the pixels’ grey values along the line profile

B.4 Determination of the porosity from TEM pictures

As Figure 16 in chapter 5.1.2 shows roughly the area of one rod, this picture was used to determine the porosity of a rod exemplary. The determination of the porosity was carried out with the image processing software Fiji [159] via the following steps: Conversion from an RGB-image to an 8-bit image to obtain grey values only. The image was then cropped so that roughly the cross-sectional area of a single rod was selected, and the imprinted scale bar was removed in order to not count those pixels into the porosity (a scale bar was re-inserted later). With the function 'Adjust Threshold' the threshold was manually chosen in a way that mostly the darker pores and not the lighter crystallites were selected (a value of 36 which led to 2.68% of the image marked) (see Supplementary Figure 8). The threshold was then applied which transformed the image into one with only black or white pixels. With the function 'Histogram' now the exact numbers of black and white pixels can be determined, and the percentage calculated (or it can be read directly from the percentage given when applying the threshold).

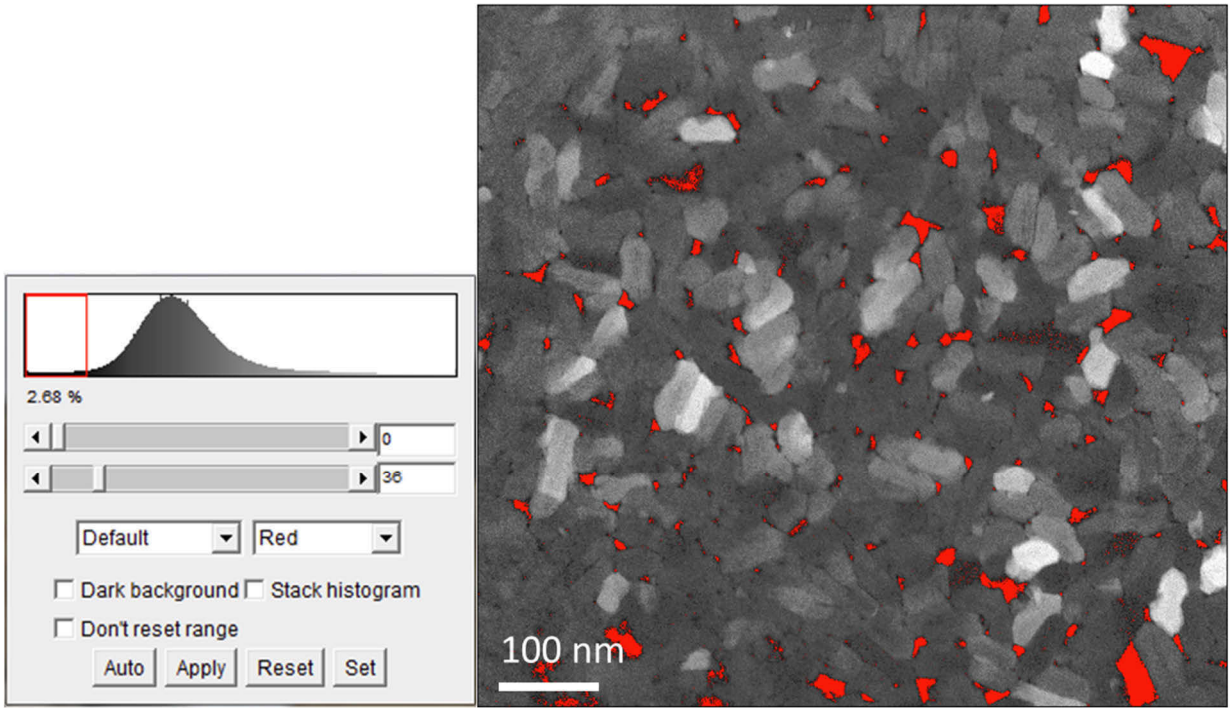

Supplementary Figure 8: Cropped image with threshold applied in a way that porous areas are marked in red. The scale bar was re-inserted after the determination of the porosity.

B.5 Structure of Enamel after Heat Treatment in Air

Supplementary Figure 9 shows the structure of the enamel after heating in air for selected temperatures. As for heating in nitrogen, it can be seen that at 300°C the structure is still

relatively intact, however for a holding time of 24 h the crystallites already start to sinter. For 600°C the sintering is very pronounced and large cracks are formed.

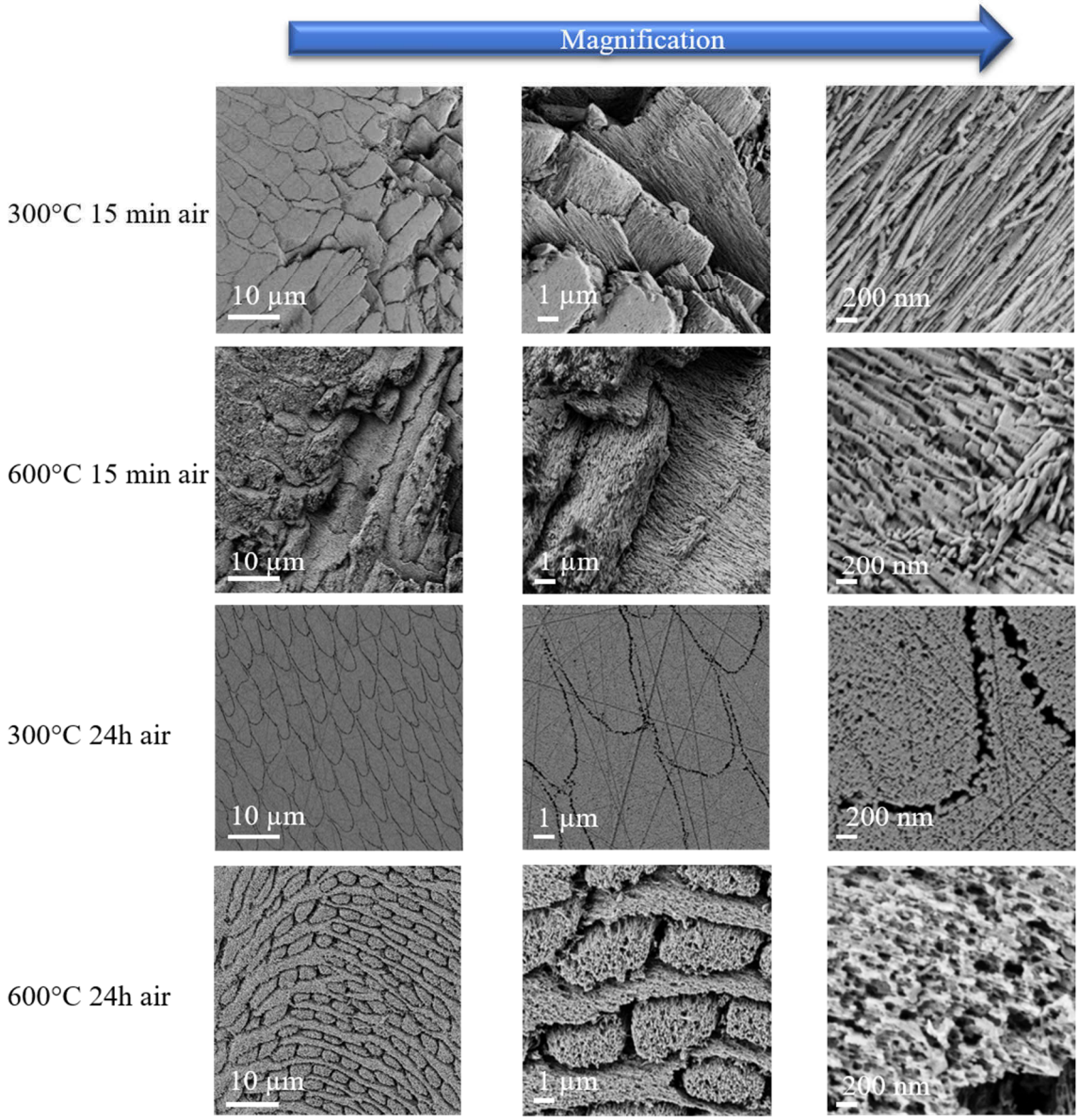

Supplementary Figure 9: SEM images of the enamel after heat treatment in air.

B.6 Plastic Deformation after Indentation

After the creep experiments the remaining indentations were observed via SEM in order to gauge the amount of plastic deformation that occurred. For the 5 µm spherical tip no remaining indentations could be observed. For the 50 µm tip however some plastic deformation occurred. Supplementary Figure 10 shows that the indent contour is just barely visible, but in the middle of the indent it can be seen that the HAP crystallites have been pressed together. This is

especially evident when regarding the rod boundaries which appear much less porous than the boundaries next to the indent. Due to the lack of clarity on the indent boundaries, the radius of the remaining indentation and subsequently the depth of plastic deformation could not be determined.

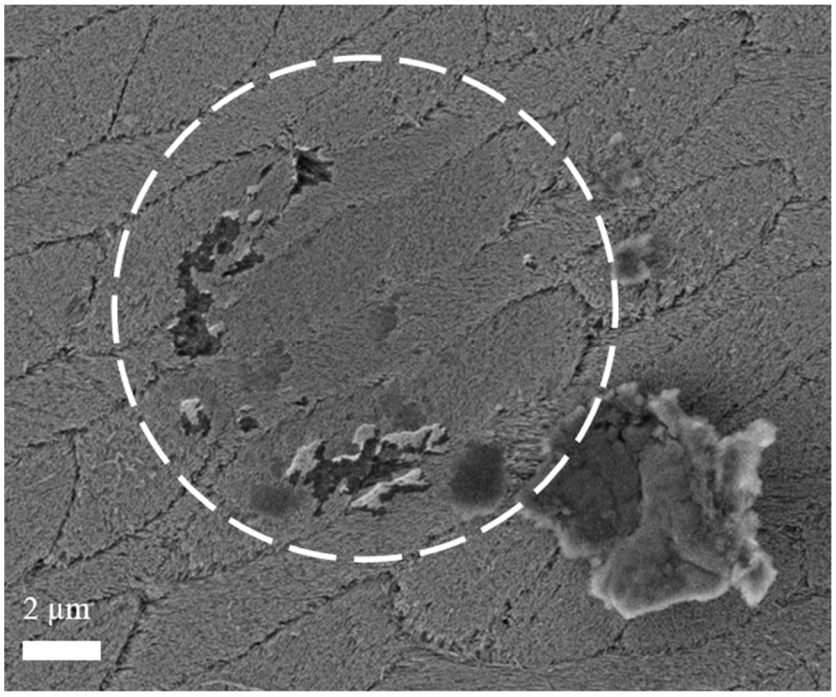

Supplementary Figure 10: SEM of an indent with 50 µm tip on the untreated enamel with loading direction perpendicular to the enamel rods. The circle denotes the apparent circumference of the remaining indentation.

C Composition

The composition was analyzed by several techniques as described in chapter 5.2. The following chapters contain additional measurement data from the TGA and FTIR measurements and have been already published in *Materialia* with the title 'Effect of deproteinization treatments on the structure and mechanical properties of dental enamel' [135] (SI C.1 and C.2).

C.1 TGA Peak Analysis

The peak locations and their areas including the standard errors as given from the fitting computed with the software OriginLab can be found in Supplementary Table 1. Here the sum of the areas, the cumulative standard error and the adjusted R^2 values as an indicator for the accuracy of the fit are given as well.

Supplementary Table 1: Peak locations and areas for TGA

		Peak 1	Peak 2	Peak 3	Peak 4	Sum 200-900°C	Sum 200-600°C (Organic region)	R^2
HAP	Peak Location (X)	246.41	412.66	n.a.	724.64			0.92
	Std. Error	3.53	0.03	n.a.	0.07			
	Peak Area	0.96	0.54	n.a.	0.31	1.81	1.50	
	Std. Error	0.023	0.001	n.a.	0.001	0.03	0.02	
Untreated Enamel	Peak Location (X)	307.24	392.20	553.48	728.71			0.97
	Std. Error	0.05	0.10	0.45	0.15			
	Peak Area	0.60	1.13	0.20	0.56	2.48	1.92	
	Std. Error	0.002	0.004	0.003	0.003	0.01	0.01	
KOH-treated Enamel	Peak Location (X)	308.17	398.21	547.45	712.46			0.94
	Std. Error	0.08	0.10	0.44	0.19			
	Peak Area	0.32	0.91	0.13	0.59	1.96	1.37	
	Std. Error	0.002	0.003	0.002	0.003	0.01	0.01	
H_2O_2-treated Enamel	Peak Location (X)	306.20	390.71	526.13	736.23			0.98
	Std. Error	0.07	0.11	0.27	0.73			
	Peak Area	0.67	1.29	0.34	0.94	3.24	2.30	
	Std. Error	0.003	0.007	0.005	0.007	0.02	0.01	

C.2 FTIR

The FTIR spectra of the samples heat treated in nitrogen for 15 min, in air for 15 min and 24 h are shown in Supplementary Figure 11 - Supplementary Figure 13. For all cases trend is similar than for the samples treated in nitrogen for 24 h, presented in ch. 5.2. After heating, the peaks in the C-N area get diminished. However, interpretation of the spectra is difficult as there is an overlap with the CO_3 peaks in the range 1530–1380 cm^{-1}. The amide I peak could not be found for any of the enamel samples.

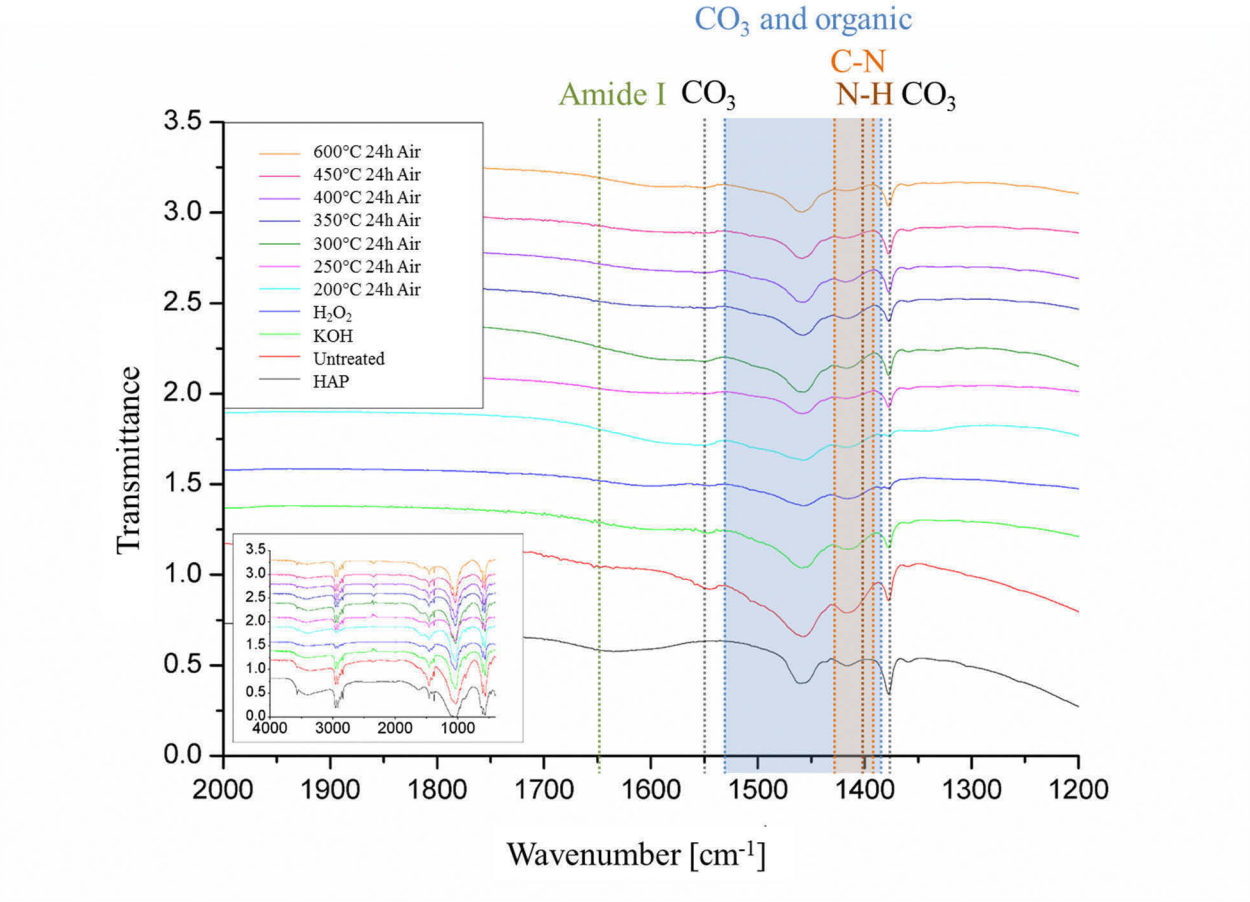

Supplementary Figure 11: FTIR spectra of the enamel heat-treated 24 h in air. HAP, untreated and chemically treated enamel as references.

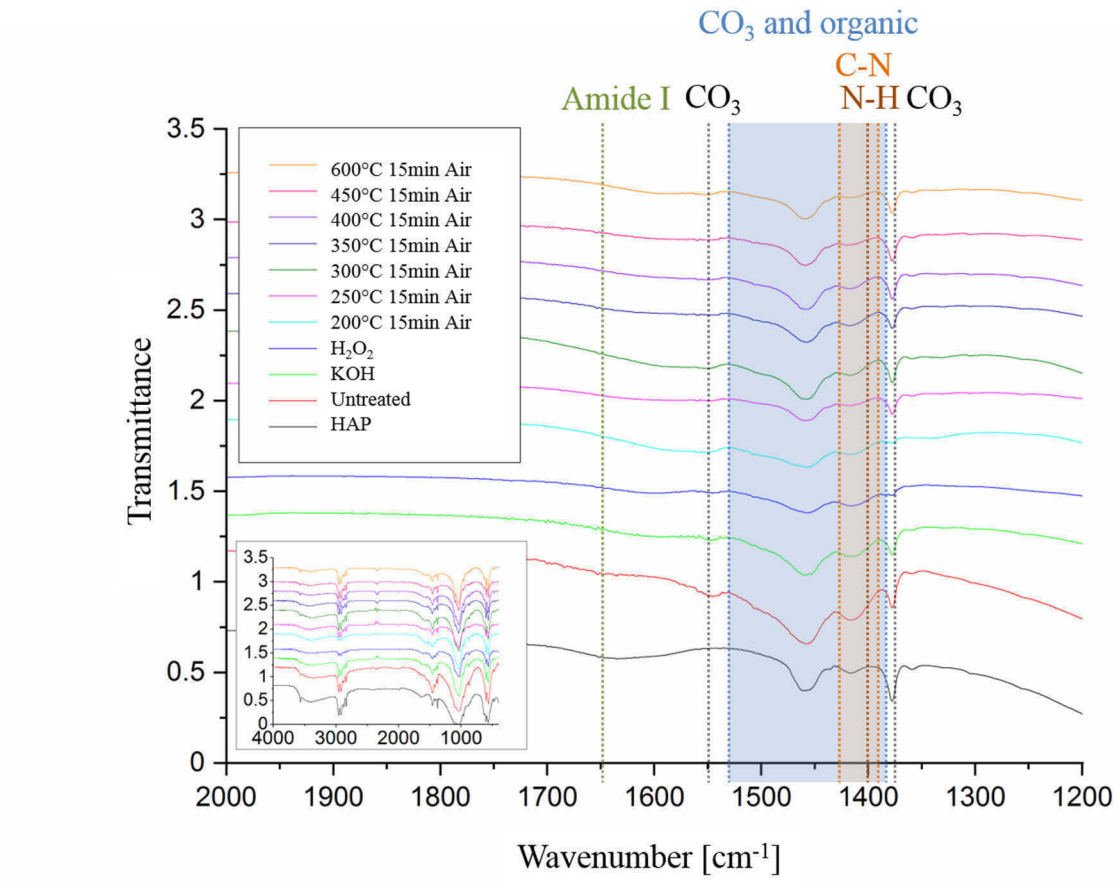

Supplementary Figure 12: FTIR spectra of the enamel heat-treated 15 min in air. HAP, untreated and chemically treated enamel as references.

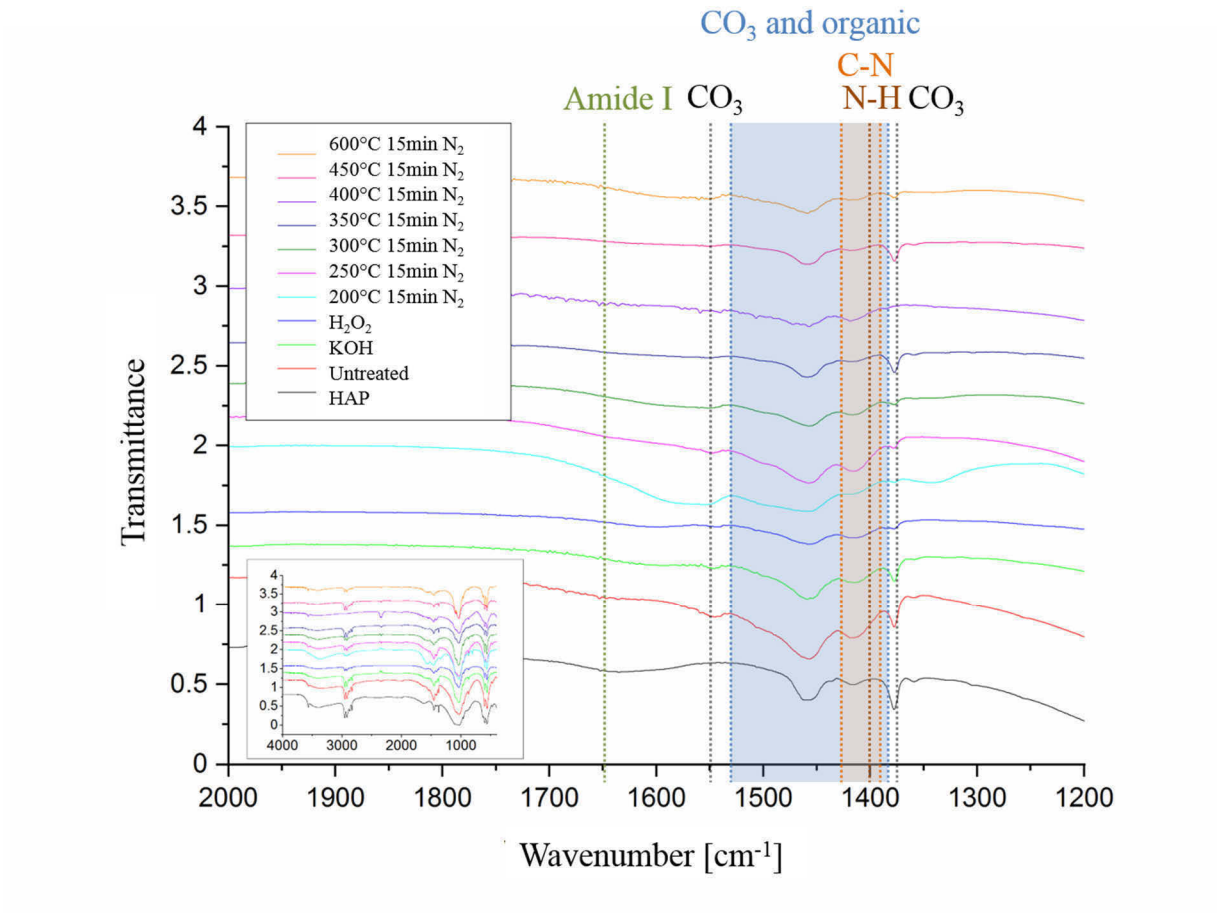

Supplementary Figure 13: FTIR spectra of the enamel heat-treated 15 min in nitrogen. HAP, untreated and chemically treated enamel as references.

C.3 Water Content in Wet Enamel Samples

In order to rehydrate the as prepared samples for the wet nanoindentation experiments, they were store in distilled water for at least 24h before the nanoindentation tests. To validate if this was sufficient to rehydrate the samples, enamel bars (dentin was removed) were analyzed by TGA. Treated and untreated enamel bars were either stored in air (ambient conditions) or distilled water for ≥ 24h, before the TGA measurement. Samples stored at ambient conditions underwent an additional drying treatment for 60 min in a desiccator directly before TGA measurement. Wet samples were taken out of water directly before the TGA measurement and briefly dabbed dry with a tissue to remove surface water. This method will introduce some uncertainty to the measurement, as the surface area of the samples will vary.

TGA was carried out with a STA 449 F5 Jupiter TGA (NETZSCH Holding, Selb, Germany), by heating the samples from 25 to 200°C (1 K/min) under N_2-atmosphere. From the TGA measurements as shown in ch. 5.2 it can be seen there is a steep mass loss between 25-100°C, which is where most of the loosely bound water would evaporate, even in the dry samples used in those experiments. In literature water evaporation has been described to occur mainly from 25-200°C [197], hence the mass loss across the complete temperature range was evaluated by a peak fitting, analogous to ch. C.1. The resulting mass losses and standard deviations are shown in Supplementary Figure 14 and Supplementary Table 2.

It can be seen that even the dry enamel contains some water. As samples have been stored at ambient conditions before measurement they will not dehydrate completely and may even exchange water with the environment to some extent during the storage period [24]. Even though the standard deviations are large, the dry enamel contains ~1 w% less water than the wet, which is roughly the amount of water that is readily mobile (able to be removed and reincorporated) [19,20,23–26], thus, supporting the claim, that enamel could be successfully rehydrated by storage in distilled water for 24h.

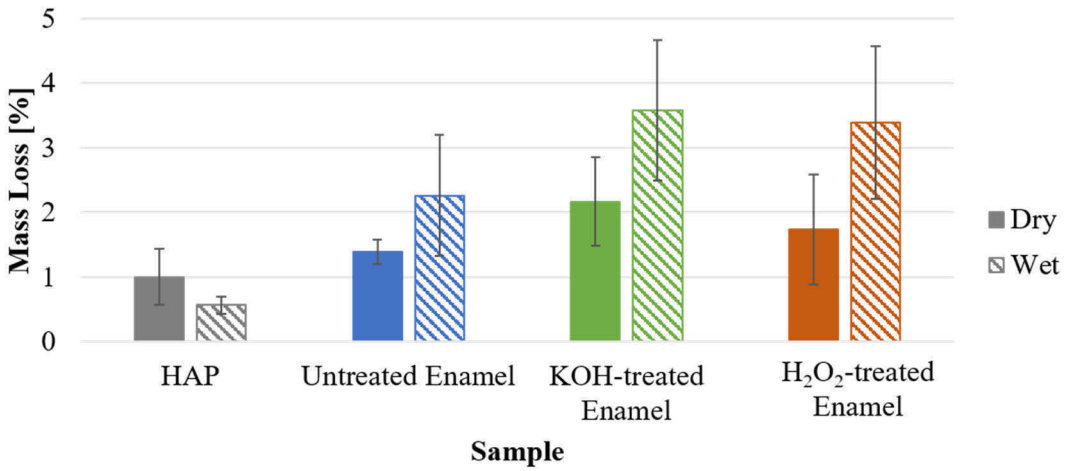

Supplementary Figure 14: Mass losses and standard deviations (n = 5) for the dry and wet (rehydrated) HAP and enamel.

Supplementary Table 2: Mass losses and standard deviations (n = 5) for the dry and wet (rehydrated) HAP and enamel.

Sample (n=5)	**Mass Loss (Mean ± SD) [%]**	
	Dry	**Wet**
HAP	1.0 ± 0.4	0.6 ± 0.1
Untreated Enamel	1.4 ± 0.2	2.3 ± 0.9
KOH-treated Enamel	2.2 ± 0.7	3.6 ± 1.1
H2O2-treated Enamel	1.7 ± 0.9	3.4 ± 1.2

D Mechanical Characterization

D.1 Hardness and Elastic Modulus

This chapter contains additional data from the nanoindentation measurements and has previously been published in *Materialia* with the title 'Effect of deproteinization treatments on the structure and mechanical properties of dental enamel' [135].

Supplementary Figure 15 shows the elastic modulus and hardness for the untreated, chemically treated and enamel heated in air. The elastic modulus and hardness of the untreated and chemically treated enamel are in the same range. After heating to 200°C an increase in both properties can be observed. However, there is a strong drop in both hardness and elastic modulus after heating above 400°C. The measured values and their standard deviations can be found in Supplementary Table 3.

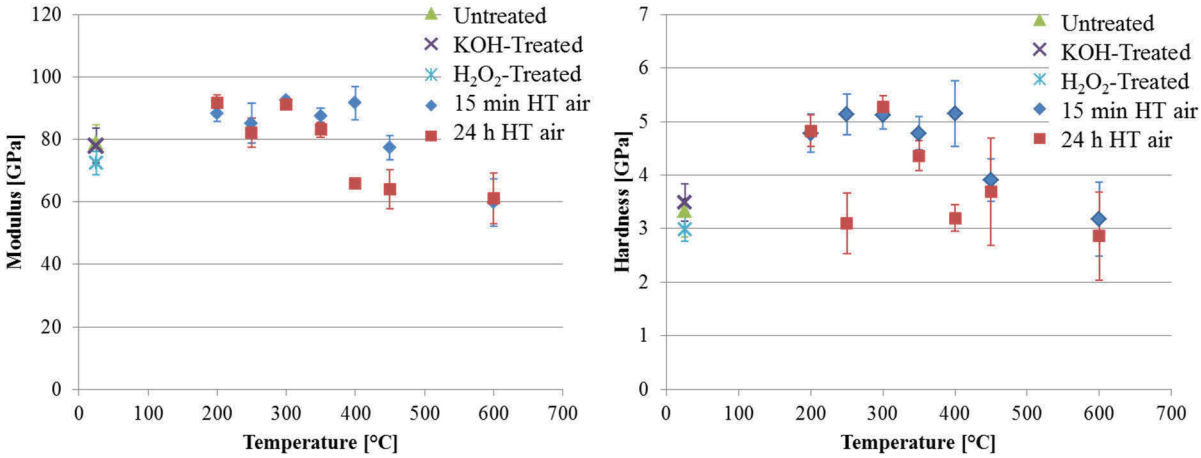

Supplementary Figure 15: Elastic modulus (left) and hardness (right) of the untreated, chemically treated and heat-treated enamel. After chemical treatment no change in properties can be observed. After heating the enamel an increase in elastic modulus and hardness is present until temperatures >400°C after which there occurs a strong drop in both properties. For hardness one outlier at 250°C can be observed.

Supplementary Table 3: Results from nanoindentation in CSM mode with a Berkovich tip

Sample Treatment	Temper-ature [°C]	Number of Indents	Modulus [GPa]	Modulus Std. Deviation [GPa]	Hardness [GPa]	Hardness Std. Deviation [GPa]
Untreated	25	26	76.80	5.40	3.65	0.47
KOH-Treated	25	34	78.00	5.50	3.49	0.35
H_2O_2-Treated	25	33	72.50	3.70	2.99	0.22
15 min HT N_2	200	24	94.00	5.90	4.73	0.64
	250	26	86.50	6.90	4.59	0.76
	300	28	87.10	3.10	4.57	0.36
	350	24	70.20	3.40	4.44	0.34
	400	23	87.40	2.40	4.95	0.36
	450	24	61.90	2.90	3.15	0.30
	600	31	45.80	9.00	2.94	0.98
24 h HT N2	200	26	88.00	6.20	4.23	0.72
	250	24	90.20	12.90	4.70	1.26
	300	32	84.00	5.80	4.27	0.59
	350	21	81.00	3.10	4.31	0.46
	400	25	74.00	10.80	3.16	0.95
	450	25	32.60	4.70	2.17	0.55
	600	21	46.40	12.20	2.91	1.10
15 min HT Air	200	24	88.40	2.70	4.78	0.36
	250	30	85.20	6.40	5.13	0.38
	300	30	92.40	1.20	5.12	0.26
	350	30	87.60	2.30	4.78	0.31
	400	22	91.60	5.20	5.15	0.61
	450	30	77.30	3.90	3.91	0.40
	600	29	59.70	7.60	3.18	0.69
24 h HT Air	200	23	91.70	2.60	4.83	0.30
	250	29	82.10	4.72	3.10	0.56
	300	29	91.10	1.60	5.28	0.21
	350	28	83.10	2.30	4.36	0.28
	400	27	65.80	1.60	3.20	0.25
	450	27	64.10	6.20	3.69	1.00
	600	23	61.10	8.10	2.86	0.82

D.2 Verification of Drift Correction during Creep Experiments

For the creep experiments a manual drift correction was necessary. To verify the method used to correct the drift measurements on alumina and silica were carried out, where no creep was expected to occur at the low loads and ambient temperature employed during the test. The procedure for the drift correction for the 7-step CLH method (method 2) is described in chapter

5.4.1. Supplementary Figure 16 and Supplementary Figure 17 show representative curves for the measurements on silica and alumina, respectively, with the original data and after application of the correction developed for silica. After the correction is applied, both samples show a constant displacement over time during the hold segment. Additionally, the load displacement curve shows an elastic behavior. This shows that the developed method reliably results in the expected behavior of alumina and can be used to correct the measured data for drift.

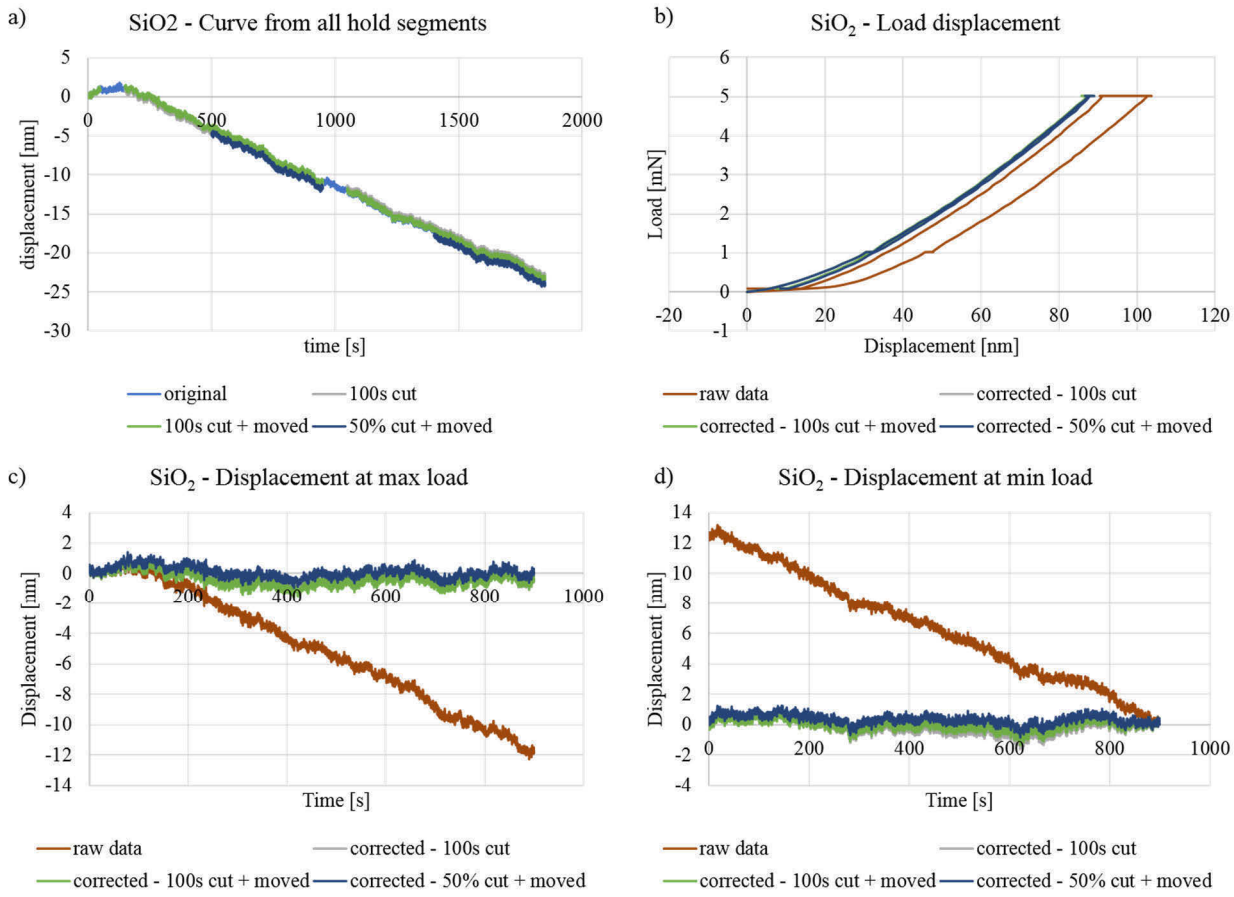

Supplementary Figure 16: Exemplary curves for the SiO_2 sample. a) raw displacement during all hold segments shifted and put together into a continuous curve. b) raw and corrected load displacement curves. After correction the unloading directly follows the loading, showing elastic behavior of the sample. c) Raw and corrected displacement at maximum load. d) Raw and corrected displacement at minimum load. After drift correction the alumina sample shows almost no creep or recovery (displacement <1.5 nm).

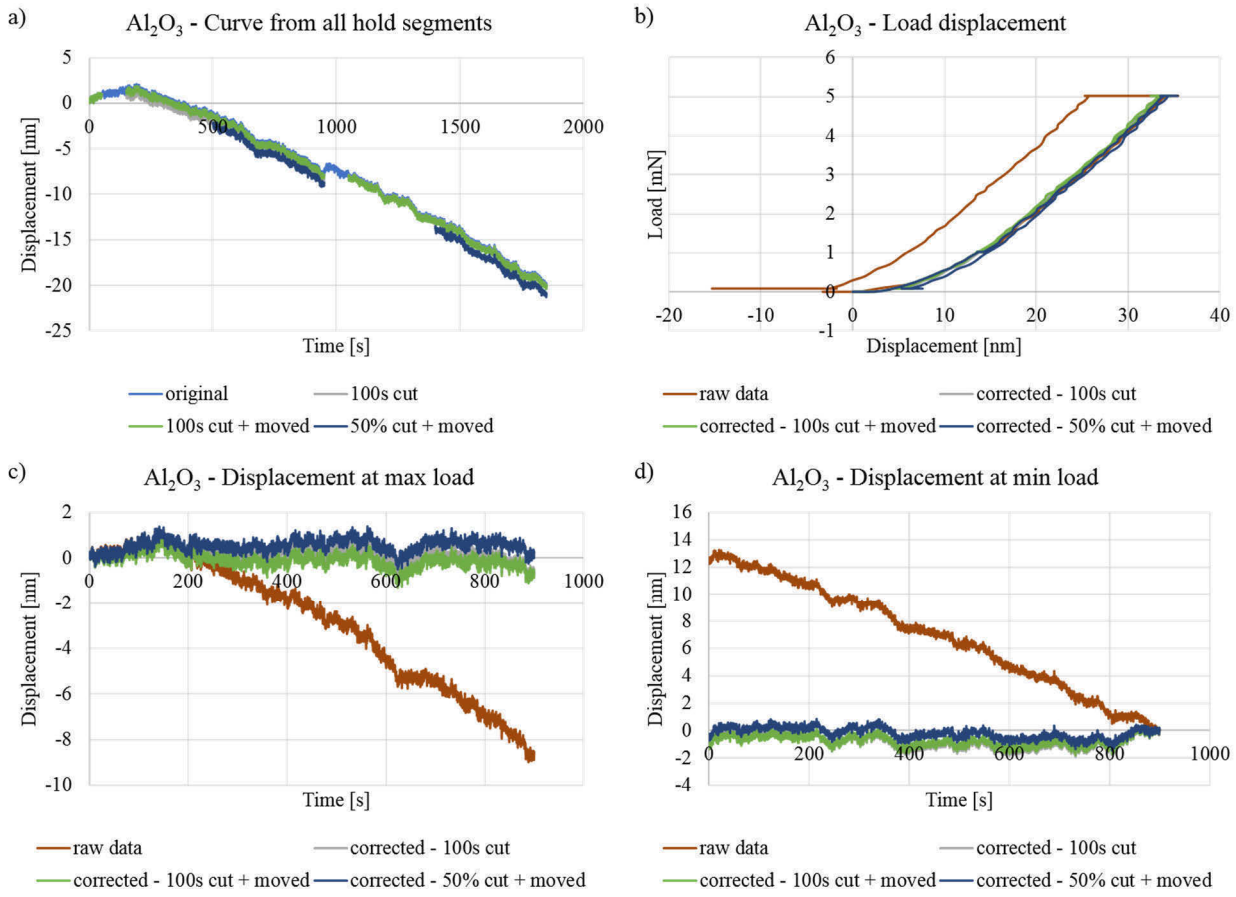

Supplementary Figure 17: Exemplary curves for the Al_2O_3 sample. a) raw displacement during all hold segments shifted and put together into a continuous curve. b) raw and corrected load displacement curves. After correction the unloading directly follows the loading, showing elastic behavior of the sample. c) Raw and corrected displacement at maximum load. d) Raw and corrected displacement at minimum load. After drift correction the alumina sample shows almost no creep or recovery (displacement <1.5 nm).

Supplementary Figure 18 shows the corrected displacement over time at maximum load for the silica and alumina sample. It can be seen that only small changes in displacement occur after the correction, showing its reliability. Still the displacement is non-zero, meaning that the accuracy of the measurement is equal to the changes in displacement observed in these samples (as no creep occurs under these conditions). Thus, the accuracy of the creep experiments is ~1.5 nm.

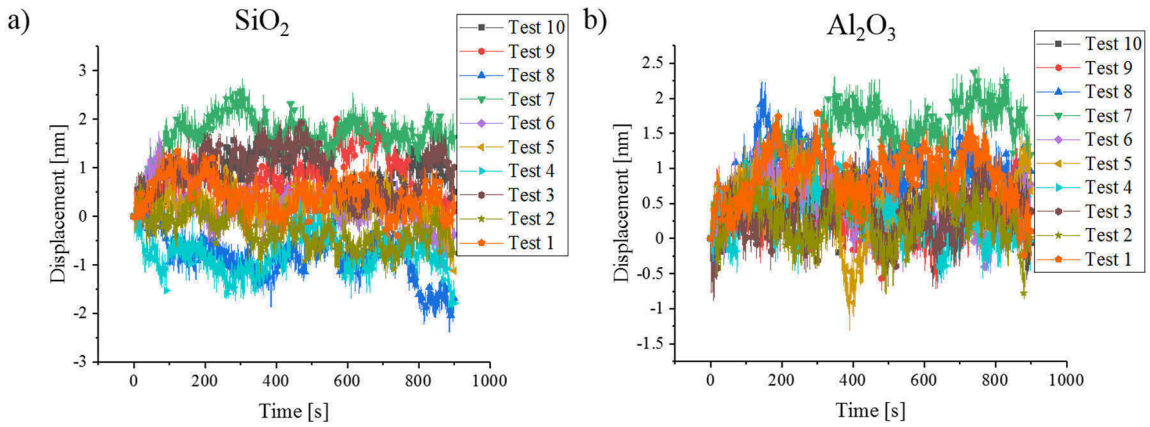

Supplementary Figure 18: Corrected displacement at maximum load for a) silica and b) alumina. After correction both samples show only small changes in displacement, but there is a residual insecurity of ~1.5 nm.

For the creep experiments where different load rates were used (method 3) another manual drift correction was performed. In this case a linear regression was performed on the last 20 s of the hold segment at maximum load where creep effects are expected to have died down, according to the observations during the experiments with method 2. The recorded displacement was then corrected with the such determined drift rate. This approach was again verified on silica and the data before and after drift correction can be seen in Supplementary Figure 19.

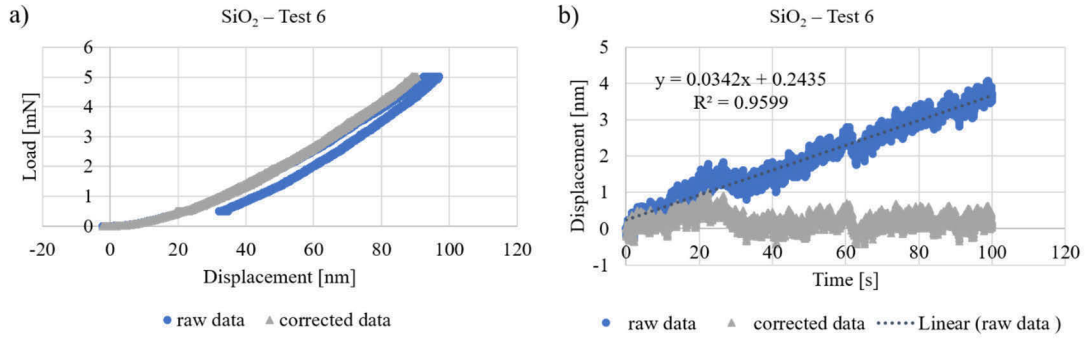

Supplementary Figure 19: a) Exemplary load-displacement curve of silica before and after drift correction. b) Exemplary displacement-time curve of silica before and after drift correction. Correction was carried out by linear regression on the last 20 s of displacement-time curve. Linear regression function shown in the graph.

D.3 Creep and Recovery

Supplementary Table 4 shows the amount of creep (displacement at maximum load after 200 s) and the amount of recovery (amount of displacement that is recovered during the first 200 s after unloading the sample to 95% of the maximum load) that were measured during the experiments with 900 s holding periods (method 2).

Supplementary Table 4: Creep and recovery with their respective standard deviations (SD) for the tests carried out with method 2 (900 s hold segments).

Sample	R_{Tip} [µm]	Creep [nm]	SD Creep [nm]	Recovery [nm]	SD Recovery [nm]	Creep/ Recovery [%]
SiO_2 Dry	5	0.3	0.6	-0.2	0.9	-69.4
	50	5.0	0.4	3.6	2.2	71.8
SiO_2 Wet	5	1.5	0.8	-0.2	1.8	-13.9
	50	4.3	0.8	3.6	0.9	83.5
Al_2O_3 Dry	5	1.0	0.5	-0.7	0.7	-68.2
	50	6.3	1.0	0.0	2.3	0.7
Al_2O_3 Wet	5	1.4	0.8	0.7	0.6	47.5
	50	6.0	1.6	3.8	2.8	63.4
HAP Dry	5	2.6	1.0	-1.4	0.5	-54.1
	50	6.2	0.4	-1.3	1.5	-21.3
HAP Wet	5	7.7	2.7	1.6	3.7	20.9
	50	14.4	1.7	7.8	2.9	54.2
Untreated Dry Parallel	5	6.5	0.5	4.7	0.4	73.1
	50	37.4	5.0	30.8	3.4	82.3
Untreated Wet Parallel	5	14.9	3.3	8.1	1.7	54.2
	50	42.8	6.9	43.4	5.1	101.4
Untreated Dry Perpendicular	5	5.1	1.5	3.5	0.8	69.2
	50	32.5	2.7	29.4	2.1	90.4
Untreated Wet Perpendicular	5	18.9	1.8	9.5	1.4	50.4
	50	41.3	5.0	37.3	3.0	90.2
KOH-treated Dry Parallel	5	8.9	1.4	3.8	1.2	43.2
	50	32.4	3.0	18.7	4.8	57.7
KOH-treated Wet Parallel	5	13.5	1.6	7.9	1.2	58.4
	50	40.4	3.5	38.6	1.5	95.4

KOH-treated Dry Perpendicular	5	7.4	0.7	4.0	0.9	53.6
	50	34.7	3.2	26.8	3.8	77.2
KOH-treated Wet Perpendicular	5	11.7	2.4	7.8	2.3	66.5
	50	39.4	3.4	38.6	3.4	98.0
H_2O_2-treated Dry Parallel	5	6.7	1.1	4.2	1.0	61.6
	50	28.9	2.8	23.5	1.5	81.4
H_2O_2-treated Wet Parallel	5	9.1	0.6	6.4	1.6	69.7
	50	31.2	1.6	32.6	1.3	82.9
H_2O_2-treated Dry Perpendicular	5	9.2	1.0	3.5	0.9	38.3
	50	27.5	2.2	23.1	1.3	84.1
H_2O_2-treated Wet Perpendicular	5	11.0	2.6	7.6	0.9	69.3
	50	31.2	1.6	31.6	1.0	101.3

D.4 Calculation of Elastic Moduli

Elastic moduli were calculated by fitting the averaged loading curves with the Hertz equation as well as fitting the unloading curve with a power law fit, according to Oliver and Pharr [147]. The results are shown in Supplementary Table 5 for indentations done with method 2 and Supplementary Table 6 for indentations done with method 3. Additionally, mean and standard deviation across load rates were calculated.

Supplementary Table 5: Elastic moduli from the creep tests with 900 s hold segments (method 3) with a 5 and 50 µm indenter tip calculated by fitting the loading and unloading curves

Sample	R_{Tip} [µm]	E from Loading [GPa]	E from Unloading [GPa]
SiO_2 Dry	5	71.06	65.79
	50	48.09	36.87
SiO_2 Wet	5	65.55	64.56
	50	58.11	50.45
Al_2O_3 Dry	5	312.81	365.99
	50	301.62	489.41
Al_2O_3 Wet	5	146.96	394.85
	50	273.34	242.86
HAP Dry	5	80.22	135.62
	50	106.20	112.43
HAP Wet	5	41.07	149.62
	50	47.26	137.52
Untreated Dry Parallel	5	45.47	118.52
	50	38.76	62.47
Untreated Wet Parallel	5	22.95	120.85
	50	38.39	88.80
Untreated Dry Perpendicular	5	46.08	40.70
	50	45.15	82.08
Untreated Wet Perpendicular	5	16.97	115.62
	50	29.20	94.58
KOH-treated Dry Parallel	5	43.54	106.90
	50	50.59	111.24
KOH-treated Wet Parallel	5	30.86	96.95
	50	29.20	91.64
KOH-treated Dry Perpendicular	5	48.55	106.19
	50	42.07	93.74

KOH-treated Wet Perpendicular	5	15.59	117.12
	50	30.01	87.64
H_2O_2-treated Dry Parallel	5	54.67	119.92
	50	54.57	103.35
H_2O_2-treated Wet Parallel	5	31.05	129.56
	50	39.21	113.14
H_2O_2-treated Dry Perpendicular	5	50.42	109.94
	50	52.70	108.26
H_2O_2-treated Wet Perpendicular	5	29.00	111.41
	50	39.93	114.31

Supplementary Table 6: Elastic moduli from the creep tests with varied load rates (method 3) with a 5 µm indenter tip calculated by fitting the loading and unloading curves.

Sample	Load Rate [mN/s]	E from Loading [GPa]	E from Unloading [GPa]
Untreated Dry	0.05	44.93	61.21
	0.5	49.58	63.69
	1.5	48.29	64.47
	5	47.27	57.33
	10	49.40	63.43
	Mean ± SD	**47.89 ± 1.70**	**62.03 ± 2.59**
Untreated Wet	0.05	33.25	78.74
	0.5	38.28	56.27
	1.5	29.34	43.31
	5	32.84	45.64
	10	37.25	55.54
	Mean ± SD	**34.19 ± 3.23**	**55.90 ± 12.54**
KOH-treated Dry	0.05	43.35	60.45
	0.5	45.06	60.12
	1.5	45.51	59.05
	5	46.71	58.06
	10	47.20	62.75
	Mean ± SD	**45.57 ± 1.35**	**60.09 ± 1.58**
KOH-treated Wet	0.05	34.19	53.25
	0.5	37.72	55.30
	1.5	44.54	59.97
	5	26.21	44.35
	10	22.10	8.48
	Mean ± SD	**32.95 ± 8.02**	**44.27 ± 18.60**
H_2O_2-treated Dry	0.05	48.99	60.87
	0.5	53.03	64.96
	1.5	47.97	61.77

	5	49.55	59.73
	10	46.41	57.98
	Mean ± SD	**49.19 ± 2.20**	**61.06 ± 2.33**
H_2O_2-treated Wet	0.05	31.82	50.29
	0.5	30.14	47.40
	1.5	31.03	50.38
	5	34.87	50.05
	10	31.74	50.33
	Mean ± SD	**31.92 ± 1.59**	**49.69 ± 1.15**

D.5 Fitting of Creep behavior

The averaged displacement-time curves for the creep experiments with both method 2 and method 3 were fitted with three different models according to Menčík et al. [162] as described in ch. 5.4.5. For the tests with method 2 only the first 200 s were used and the resulting fitting parameters, spring, damper and time constants, and coefficient of determination R^2 are given in Supplementary Table 7 - Supplementary Table 12. Supplementary Table 13 gives the resulting fitting parameters, spring, damper and time constants, and coefficient of determination R^2 for the tests conducted with method 3 (varying load rates).

Supplementary Table 7: Fitting parameters, time, spring and damper constants for creep curve of the tests conducted with method 2. Fitting with a Kelvin-Voigt body (model 1) with ramp time of 60 s and load of 5 mN.

Sample	R_{Tip} [µm]	B	D_1	τ_1 [s]	ρ_1 [s]	C_1	C_0	R^2
HAP Dry	5	1.56E-13	1.17E-13	43.38	2.16	5.41E-14	1.02E-13	0.93
	50	5.67E-14	5.12E-14	73.47	1.74	2.94E-14	2.73E-14	0.99
HAP Wet	5	8.78E-13	7.36E-13	71.78	1.56	4.71E-13	4.07E-13	0.98
	50	1.87E-13	1.49E-13	44.27	2.62	5.68E-14	1.30E-13	0.99
Untreated Dry Parallel	5	6.50E-13	4.99E-13	22.68	4.95	1.01E-13	5.49E-13	0.97
	50	7.62E-13	6.38E-13	31.40	4.14	1.54E-13	6.08E-13	0.99
Untreated Wet Parallel	5	2.21E-12	1.66E-12	38.84	2.39	6.95E-13	1.51E-12	0.98
	50	9.39E-13	7.86E-13	35.68	3.42	2.30E-13	7.09E-13	0.99
Untreated Dry Perpendicular	5	4.52E-13	4.04E-13	16.52	10.13	3.99E-14	4.12E-13	0.97
	50	6.23E-13	5.15E-13	33.54	3.74	1.38E-13	4.85E-13	0.99
Untreated Wet Perpendicular	5	3.15E-12	2.63E-12	38.91	2.38	1.10E-12	2.05E-12	0.99
	50	8.93E-13	7.47E-13	35.78	3.40	2.20E-13	6.74E-13	0.99
KOH-treated Dry Parallel	5	1.05E-12	8.15E-13	52.73	1.86	4.38E-13	6.16E-13	0.98
	50	6.13E-13	5.24E-13	27.82	5.13	1.02E-13	5.11E-13	0.99
KOH-treated Wet Parallel	5	1.92E-12	1.47E-12	26.89	3.73	3.95E-13	1.53E-12	0.98
	50	8.43E-13	6.85E-13	31.89	4.04	1.70E-13	6.74E-13	0.98
KOH-treated Dry Perpendicular	5	7.74E-13	5.98E-13	36.49	2.54	2.35E-13	5.38E-13	0.97
	50	6.81E-13	5.94E-13	29.66	4.56	1.30E-13	5.51E-13	0.99
KOH-treated Wet Perpendicular	5	1.46E-12	1.10E-12	18.24	7.85	1.40E-13	1.32E-12	0.95
	50	8.25E-13	6.82E-13	31.44	4.13	1.65E-13	6.60E-13	0.99
H_2O_2-treated Dry Parallel	5	6.66E-13	4.53E-13	36.03	2.57	1.76E-13	4.90E-13	0.92
	50	5.18E-13	4.35E-13	33.11	3.81	1.14E-13	4.04E-13	0.99
H_2O_2-treated Wet Parallel	5	1.06E-12	7.67E-13	30.64	3.11	2.47E-13	8.13E-13	0.95
	50	5.90E-13	4.90E-13	33.31	3.78	1.30E-13	4.60E-13	0.99
H_2O_2-treated Dry Perpendicular	5	1.06E-12	8.24E-13	47.94	1.99	4.13E-13	6.43E-13	0.98
	50	4.98E-13	4.26E-13	32.16	3.99	1.07E-13	3.91E-13	0.99
H_2O_2-treated Wet Perpendicular	5	1.38E-12	1.05E-12	27.50	3.60	2.91E-13	1.08E-12	0.96
	50	5.54E-13	4.59E-13	33.53	3.74	1.23E-13	4.31E-13	0.99

Supplementary Table 8: Fitting parameters, time, spring and damper constants for backcreep curve of the tests conducted with method 2. Fitting with a spring and a Kelvin-Voigt body (model 1). with ramp time of 10 s and load of 0.1 mN.

Sample	R_{Tip} [µm]	B	D_1	τ_1 [s]	ρ_1 [s]	C_1	C_0	R^2
HAP Dry	5	n.a.	n.a.	n.a.	n.a.	n.a.	n.a.	0.00
	50	n.a.	n.a.	n.a.	n.a.	n.a.	n.a.	0.00
HAP Wet	5	5.19E-15	1.11E-12	0.87	8803.33	1.27E-16	5.06E-15	0.98
	50	2.11E-13	2.35E-12	38.75	1.40	1.67E-12	-1.46E-12	0.97
Untreated Dry Parallel	5	1.34E-13	5.02E-12	13.42	1.49	3.38E-12	-3.24E-12	0.90
	50	7.64E-13	1.84E-11	16.54	2.34	7.85E-12	-7.09E-12	0.95
Untreated Wet Parallel	5	8.84E-13	2.54E-11	8.76	1.87	1.36E-11	-1.27E-11	0.93
	50	1.04E-12	2.99E-11	18.17	2.15	1.39E-11	-1.29E-11	0.95
Untreated Dry Perpendicular	5	1.10E-13	3.77E-12	9.53	1.77	2.13E-12	-2.02E-12	0.95
	50	8.56E-13	1.69E-11	19.29	2.05	8.25E-12	-7.39E-12	0.95
Untreated Wet Perpendicular	5	1.19E-12	3.70E-11	9.69	1.75	2.11E-11	-1.99E-11	0.93
	50	8.98E-13	2.37E-11	16.25	2.38	9.98E-12	-9.08E-12	0.94
KOH-treated Dry Parallel	5	2.40E-13	5.08E-12	2.26	18.60	2.73E-13	-3.36E-14	0.94
	50	1.08E-13	9.51E-12	9.74	4.68	2.03E-12	-1.92E-12	0.96
KOH-treated Wet Parallel	5	4.73E-13	2.59E-11	12.39	1.54	1.68E-11	-1.64E-11	0.94
	50	1.16E-12	2.41E-11	17.98	2.17	1.11E-11	-9.94E-12	0.94
KOH-treated Dry Perpendicular	5	1.61E-13	4.76E-12	6.11	2.53	1.88E-12	-1.72E-12	0.95
	50	1.72E-12	1.39E-11	18.97	2.08	6.68E-12	-4.96E-12	0.94
KOH-treated Wet Perpendicular	5	1.06E-12	2.70E-11	12.13	1.55	1.74E-11	-1.63E-11	0.91
	50	1.01E-12	2.48E-11	15.00	2.58	9.62E-12	-8.61E-12	0.94
H_2O_2-treated Dry Parallel	5	1.03E-13	4.35E-12	8.66	1.88	2.31E-12	-2.21E-12	0.90
	50	3.46E-13	1.32E-11	15.40	2.51	5.26E-12	-4.91E-12	0.96
H_2O_2-treated Wet Parallel	5	1.38E-12	1.80E-11	19.35	1.31	1.37E-11	-1.23E-11	0.94
	50	6.58E-13	1.94E-11	14.84	2.61	7.46E-12	-6.80E-12	0.94
H_2O_2-treated Dry Perpendicular	5	1.52E-13	4.67E-12	2.84	9.29	5.03E-13	-3.51E-13	0.98
	50	6.44E-13	1.23E-11	16.49	2.34	5.25E-12	-4.60E-12	0.95
H_2O_2-treated Wet Perpendicular	5	7.61E-13	2.41E-11	7.63	2.07	1.17E-11	-1.09E-11	0.95
	50	1.06E-12	1.89E-11	15.82	2.44	7.73E-12	-6.67E-12	0.95

Supplementary Table 9: Fitting parameters, time, spring and damper constants for creep curves of the tests conducted with method 2. Fitting with a spring and two Kelvin-Voigt bodies (model 2) with ramp time of 60 s and load of 5 mN.

Sample	R_{Tip} [µm]	B	D_1	D_2	τ_1 [s]	τ_2 [s]	ρ_1 [s]	ρ_2 [s]	C_1	C_2	C_0	R^2
HAP Dry	5	1.72E-13	8.93E-14	7.43E-14	95.64	8.46	1.39	169.30	6.42E-14	4.39E-16	1.07E-13	0.96
	50	5.67E-14	2.56E-14	2.56E-14	73.48	73.48	1.74	1.74	1.47E-14	1.47E-14	2.73E-14	0.99 (failed)
HAP Wet	5	1.02E-12	2.70E-13	7.05E-13	14.01	138.54	16.70	1.25	1.62E-14	5.63E-13	4.42E-13	0.99
	50	1.93E-13	5.71E-14	1.29E-13	5.75	58.88	35101.54	2.02	1.63E-18	6.36E-14	1.29E-13	1.00
Untreated Dry Parallel	5	6.54E-13	4.22E-13	2.33E-13	27.53	2.01	3.60	3.00E+11	1.17E-13	7.76E-25	5.37E-13	0.98
	50	7.80E-13	2.93E-13	4.78E-13	7.03	45.48	4048.64	2.55	7.25E-17	1.88E-13	5.92E-13	1.00
Untreated Wet Parallel	5	2.26E-12	1.39E-12	8.04E-13	52.46	4.49	1.87	47555.58	7.44E-13	1.69E-17	1.52E-12	1.00
	50	9.66E-13	3.42E-13	6.09E-13	7.48	51.37	2255.33	2.26	1.52E-16	2.69E-13	6.97E-13	1.00
Untreated Dry Perpendicular	5	4.54E-13	1.32E-13	3.22E-13	3.80	20.47	458170.50	6.05	2.89E-19	5.32E-14	4.01E-13	0.98
	50	6.37E-13	4.03E-13	2.31E-13	47.11	6.27	2.46	13151.25	1.64E-13	1.76E-17	4.73E-13	1.00
Untreated Wet Perpendicular	5	3.20E-12	7.65E-13	2.37E-12	4.30	45.91	82440.90	2.06	9.28E-18	1.15E-12	2.05E-12	1.00
	50	9.17E-13	5.87E-13	3.16E-13	50.57	7.26	2.30	2974.11	2.56E-13	1.06E-16	6.62E-13	1.00
KOH-treated Dry Parallel	5	1.10E-12	3.64E-13	7.25E-13	4.90	73.55	16990.00	1.55	2.14E-17	4.69E-13	6.32E-13	0.99
	50	6.33E-13	3.06E-13	3.10E-13	51.01	10.22	2.28	209.76	1.34E-13	1.48E-15	4.97E-13	1.00
KOH-treated Wet Parallel	5	1.94E-12	7.08E-13	1.19E-12	3.64	34.95	8.66E+05	2.66	8.18E-19	4.47E-13	1.50E-12	1.00
	50	8.64E-13	5.20E-13	3.35E-13	46.51	6.16	2.49	15831.29	2.09E-13	2.12E-17	6.55E-13	1.00
KOH-treated Dry Perpendicular	5	8.20E-13	4.18E-13	3.61E-13	71.15	8.39	1.57	178.37	2.66E-13	2.02E-15	5.52E-13	0.99
	50	6.86E-13	5.29E-13	1.69E-13	34.09	3.69	3.65	3.23E+07	1.45E-13	5.21E-21	5.41E-13	1.00
KOH-treated Wet Perpendicular	5	3.13E-12	1.07E-12	1.83E-12	11.26	1397.48	38.43	1.02	2.78E-14	1.79E-12	1.31E-12	0.99

	50	8.43E-13	5.30E-13	3.07E-13	43.88	6.00	2.65	21625.17	2.00E-13	1.42E-17	6.42E-13	1.00
H_2O_2-treated Dry Parallel	5	7.42E-13	3.26E-13	3.84E-13	104.28	6.41	1.35	1239.32	2.41E-13	3.10E-16	5.01E-13	0.99
	50	5.29E-13	3.45E-13	1.82E-13	45.09	6.25	2.57	13594.85	1.34E-13	1.34E-17	3.95E-13	1.00
H_2O_2-treated Wet Parallel	5	8.82E-10	8.81E-10	6.90E-13	6.62E+05	14.73	1.00	14.18	8.81E-10	4.87E-14	8.52E-13	0.98 (failed)
	50	6.00E-13	1.97E-13	4.02E-13	5.39	43.49	79372.31	2.67	2.48E-18	1.51E-13	4.50E-13	1.00
H_2O_2-treated Dry Perpendicular	5	1.11E-12	3.72E-13	7.08E-13	5.69	70.45	3625.70	1.58	1.03E-16	4.49E-13	6.59E-13	1.00
	50	5.06E-13	3.49E-13	1.59E-13	41.43	5.82	2.82	30370.42	1.24E-13	5.22E-18	3.82E-13	1.00
H_2O_2-treated Wet Perpendicular	5	1.48E-12	5.36E-13	8.35E-13	87.69	10.13	1.44	62.83	3.73E-13	1.33E-14	1.10E-12	0.99
	50	5.67E-13	2.01E-13	3.56E-13	6.82	47.35	5391.28	2.45	3.73E-17	1.46E-13	4.21E-13	1.00

Supplementary Table 10: Fitting parameters, time, spring and damper constants for backcreep curve of the tests conducted with a spring and two Kelvin-Voigt bodies (model 2). Fitting with model 2 with ramp time of 10 s and load of 0.1 mN.

Sample	R_{Tip} [µm]	B	D_1	D_2	τ_1 [s]	τ_2 [s]	ρ_1 [s]	ρ_2 [s]	C_1	C_2	C_0	R^2
HAP Dry	5	n.a.	n.a.	n.a.	n.a.	n.a.	n.a.	n.a.	n.a.	n.a.	n.a.	n.a.
	50	n.a.	n.a.	n.a.	n.a.	n.a.	n.a.	n.a.	n.a.	n.a.	n.a.	n.a.
HAP Wet	5	n.a.	n.a.	n.a.	n.a.	n.a.	n.a.	n.a.	n.a.	n.a.	n.a.	n.a.
	50	1.01E-13	1.92E-12	1.36E-12	57.17	4.30	1.25	57.63	1.53E-12	2.36E-14	-1.46E-12	0.99
Untreated Dry Parallel	5	4.98E-14	1.24E-11	7.33E-12	1.70	27.04	60.84	1.21	2.03E-13	6.06E-12	-6.21E-12	0.99
	50	2.53E-13	1.01E-11	1.58E-11	34.65	3.55	1.47	163.31	6.90E-12	9.68E-14	-6.74E-12	1.00
Untreated Wet Parallel	5	4.63E-13	2.49E-11	1.42E-11	1.40	17.78	177.00	1.34	1.41E-13	1.05E-11	-1.02E-11	0.99
	50	3.51E-13	2.49E-11	1.90E-11	2.90	32.00	647.64	1.52	3.85E-14	1.25E-11	-1.22E-11	1.00
Untreated Dry Perpendicular	5	9.74E-14	6.72E-12	5.66E-12	1.77	17.66	50.20	1.35	1.34E-13	4.21E-12	-4.25E-12	0.99
	50	3.93E-13	1.04E-11	1.40E-11	35.67	3.42	1.45	203.86	7.19E-12	6.87E-14	-6.86E-12	1.00
Untreated Wet Perpendicular	5	3.57E-13	3.43E-11	1.83E-11	2.17	22.70	21.67	1.26	1.58E-12	1.46E-11	-1.58E-11	0.99
	50	3.18E-13	2.09E-11	1.38E-11	2.93	31.80	587.71	1.52	3.56E-14	9.10E-12	-8.82E-12	1.00
KOH-treated Dry Parallel	5	-1.45E-13	9.65E-12	5.00E-12	0.87	8.92	8580.29	1.84	1.12E-15	2.71E-12	-2.86E-12	1.00
	50	1.64E-14	6.84E-12	6.26E-12	1.65	15.23	245440.39	2.54	2.79E-17	2.47E-12	-2.45E-12	1.00
KOH-treated Wet Parallel	5	6.94E-14	2.32E-11	1.57E-11	1.95	22.26	32.40	1.26	7.16E-13	1.24E-11	-1.31E-11	1.00
	50	5.36E-13	1.48E-11	2.12E-11	33.45	2.88	1.49	680.41	9.97E-12	3.12E-14	-9.47E-12	1.00
KOH-treated Dry Perpendicular	5	4.28E-14	7.91E-12	7.15E-12	1.19	12.02	539.17	1.56	1.47E-14	4.58E-12	-4.55E-12	1.00
	50	1.02E-12	7.06E-12	1.26E-11	49.52	4.66	1.30	39.58	5.43E-12	3.17E-13	-4.72E-12	0.99
KOH-treated Wet Perpendicular	5	3.66E-13	2.83E-11	1.35E-11	2.27	29.60	18.40	1.19	1.54E-12	1.13E-11	-1.25E-11	0.99

	50	3.91E-13	2.28E-11	1.37E-11	2.87	31.42	701.54	1.53	3.24E-14	8.94E-12	-8.58E-12	1.00
H_2O_2-treated Dry Parallel	5	4.96E-14	1.04E-11	5.93E-12	1.17	18.93	590.27	1.32	1.76E-14	4.50E-12	-4.47E-12	1.00
	50	1.29E-13	8.07E-12	9.82E-12	26.72	3.13	1.66	367.70	4.87E-12	2.67E-14	-4.77E-12	1.00
H_2O_2-treated Wet Parallel	5	1.12E-12	1.35E-11	1.78E-11	27.60	1.44	1.21	151.66	1.12E-11	1.18E-13	-1.02E-11	0.99
	50	2.32E-13	1.11E-11	1.75E-11	29.33	2.68	1.58	1203.67	7.05E-12	1.46E-14	-6.83E-12	1.00
H_2O_2-treated Dry Perpendicular	5	-1.00E-14	6.06E-12	6.92E-12	0.92	5.36	4988.56	2.93	1.21E-15	2.36E-12	-2.37E-12	1.00
	50	3.18E-13	6.67E-12	1.00E-11	34.33	3.93	1.47	91.31	4.53E-12	1.10E-13	-4.33E-12	1.00
H_2O_2-treated Wet Perpendicular	5	3.03E-13	1.86E-11	1.58E-11	1.18	12.84	565.52	1.51	3.29E-14	1.04E-11	-1.01E-11	1.00
	50	5.88E-13	1.04E-11	1.63E-11	32.52	3.30	1.51	254.90	6.94E-12	6.39E-14	-6.42E-12	1.00

Supplementary Table 11: Fitting parameters, time, spring and damper constants for creep curve of the tests conducted with method 2. Fitting with a spring, a damper and two Kelvin-Voigt bodies (model 3) with ramp time of 60 s and load of 5 mN.

Sample	R_{Tip} [µm]	B	D_1	D_2	c_v [ ]	τ_1 [s]	τ_2 [s]	ρ_1 [s]	ρ_2 [s]	C_1	C_2	C_0	R^2
HAP Dry	5	1.78E-13	1.78E-13	9.48E-14	7.47E-14	-1.92 E-17	101.76	8.52	1.36	161.89	6.96E-14	4.62E-16	0.96
	50	1.22E-13	7.72E-15	1.14E-13	-1.98E-16	2.30	148.60	4.63 E+12	1.30	1.67E-27	8.75E-14	2.66E-14	0.99
HAP Wet	5	1.71E-11	1.67E-11	2.77E-13	-1.38E-14	924.78	13.97	1.03	16.84	1.62E-11	1.65E-14	1.66E-11	0.99 (failed)
	50	1.64E-13	1.15E-13	4.76E-14	1.36E-16	39.11	3.39	3.03	1.87E+08	3.79E-14	2.55E-22	1.69E-13	1.00
Untreated Dry Parallel	5	7.74E-13	4.86E-13	2.78E-13	-6.82E-16	44.70	2.99	2.11	2.51E+07	2.31E-13	1.11E-20	7.53E-13	0.99
	50	7.61E-13	4.76E-13	2.79E-13	9.18E-17	41.94	6.57	2.78	7928.05	1.71E-13	3.52E-17	7.65E-13	1.00
Untreated Wet Parallel	5	2.25E-12	7.93E-13	1.39E-12	-2.54E-16	4.65	55.58	3.09 E+04	1.80	2.56E-17	7.71E-13	1.47E-12	1.00
	50	9.29E-13	5.99E-13	3.20E-13	1.71E-16	45.93	6.84	2.52	5277.46	2.37E-13	6.06E-17	9.36E-13	1.00
Untreated Dry Perpendicular	5	6.06E-13	2.93E-13	2.99E-13	-7.55E-16	71.86	8.93	1.56	122.95	1.87E-13	2.43E-15	5.81E-13	0.98
	50	6.56E-13	4.11E-13	2.40E-13	-8.71E-17	50.94	6.61	2.28	7505.11	1.80E-13	3.20E-17	6.52E-13	1.00
Untreated Wet Perpendicular	5	2.74E-12	5.97E-13	2.14E-12	1.96E-15	2.39	33.47	3.07 E+09	2.79	1.94E-22	7.68E-13	2.03E-12	1.00
	50	8.69E-13	2.83E-13	5.78E-13	2.32E-16	6.14	42.86	16534.00	2.72	1.71E-17	2.13E-13	6.64E-13	1.00
KOH-treated Dry Parallel	5	1.11E-11	1.07E-11	4.16E-13	-1.49E-14	490.49	6.22	1.06	1601.07	1.00E-11	2.60E-16	1.07E-11	1.00 (failed)
	50	5.74E-13	3.76E-13	1.95E-13	2.88E-16	29.97	6.17	4.48	15575.86	8.39E-14	1.25E-17	5.85E-13	1.00
KOH-treated Wet Parallel	5	1.98E-12	1.18E-12	7.35E-13	-5.06E-16	40.92	4.17	2.27	122937.07	5.21E-13	5.98E-18	1.96E-12	1.00
	50	8.12E-13	5.10E-13	3.00E-13	2.63E-16	37.91	5.23	3.15	117645.42	1.62E-13	2.55E-18	8.22E-13	1.00
KOH-treated Dry Perpendicular	5	8.57E-12	4.15E-13	8.10E-12	-9.58E-15	10.22	618.49	60.19	1.05	6.89E-15	7.72E-12	5.65E-13	0.99 (failed)
	50	7.09E-13	1.82E-13	5.38E-13	-1.33E-16	4.08	37.19	5.20 E+06	3.23	3.50E-20	1.67E-13	5.38E-13	1.00

KOH-treated Wet Perpendicular	5	1.28E-12	8.67E-13	4.30E-13	1.04E-15	14.31	1.62	15.56	3.63E+14	5.57E-14	1.18E-27	1.31E-12	0.99
	50	8.04E-13	2.79E-13	5.25E-13	1.96E-16	5.19	37.68	1.30 E+05	3.18	2.15E-18	1.65E-13	6.46E-13	1.00
H_2O_2-treated Dry Parallel	5	5.29E-13	2.70E-13	2.55E-13	8.77E-16	3.37	21.52	3.09 E+06	5.47	8.72E-20	4.66E-14	5.09E-13	0.99
	50	5.26E-13	3.45E-13	1.80E-13	1.60E-17	44.30	6.16	2.62	16009.18	1.31E-13	1.13E-17	5.26E-13	1.00
H_2O_2-treated Wet Parallel	5	8.50E-13	2.80E-13	5.82E-13	1.20E-15	1.59	17.99	6.42 E+14	8.12	4.35E-28	7.17E-14	8.14E-13	0.99
	50	6.63E-13	4.35E-13	2.23E-13	-3.00E-16	55.82	6.49	2.11	9074.32	2.06E-13	2.46E-17	6.52E-13	1.00
H_2O_2-treated Dry Perpendicular	5	8.61E-13	5.60E-13	2.98E-13	1.12E-15	37.81	3.45	2.45	2.09E+06	2.28E-13	1.43E-19	8.95E-13	1.00
	50	7.35E-13	5.02E-13	2.25E-13	-9.34E-16	90.58	9.18	1.56	433.25	3.23E-13	5.20E-16	7.00E-13	1.00
H_2O_2-treated Wet Perpendicular	5	1.51E-11	8.53E-13	1.41E-11	-1.39E-14	10.68	782.85	48.76	1.04	1.75E-14	1.36E-11	1.09E-12	0.99 (failed)
	50	5.53E-13	1.91E-13	3.53E-13	6.98E-17	6.38	43.76	10845.75	2.66	1.77E-17	1.33E-13	4.22E-13	1.00

Supplementary Table 12: Fitting parameters, time, spring and damper constants for backcreep curve of the tests conducted with method 2. Fitting with a spring, a damper and two Kelvin-Voigt bodies (model 3) with ramp time of 10 s and load of 0.1 mN.

Sample	R_{Tip} [µm]	B	D_1	D_2	c_v [ ]	τ_1 [s]	τ_2 [s]	ρ_1 [s]	ρ_2 [s]	C_1	C_2	C_0	R^2
HAP Dry	5	n.a.	n.a.	n.a.	n.a.	n.a.	n.a.	n.a.	n.a.	n.a.	n.a.	n.a.	n.a.
	50	n.a.	n.a.	n.a.	n.a.	n.a.	n.a.	n.a.	n.a.	n.a.	n.a.	n.a.	n.a.
HAP Wet	5	-6.98E-15	-5.77E-13	1.70E-12	-2.81E-15	0.88	0.88	7407.84	7387.90	-7.79E-17	2.30E-16	-2.12E-14	0.98
	50	7.53E-13	1.15E-12	1.69E-12	3.34E-15	1.96	27.52	0.01	2.21	1.80E-10	7.67E-13	2.77E-14	1.00
Untreated Dry Parallel	5	-5.77E-13	1.27E-11	7.57E-12	-3.82E-15	1.82	32.40	44.64	1.17	2.84E-13	6.46E-12	-7.06E-12	0.99
	50	1.77E-12	1.12E-11	1.41E-11	8.97E-15	21.92	2.54	1.23	0.01	9.12E-12	1.31E-09	-1.30E-09	1.00
Untreated Wet Parallel	5	1.74E-12	2.35E-11	1.53E-11	1.12E-14	1.12	12.86	871.47	1.51	2.70E-14	1.01E-11	-8.31E-12	1.00
	50	2.13E-12	2.36E-11	1.96E-11	1.07E-14	2.37	24.64	0.01	1.65	2.50E-09	1.18E-11	-9.56E-12	1.00
Untreated Dry Perpendicular	5	3.34E-13	6.32E-12	5.93E-12	2.06E-15	1.52	15.16	110.15	1.42	5.74E-14	4.19E-12	-3.85E-12	0.99
	50	1.38E-12	1.33E-11	1.05E-11	5.66E-15	2.93	28.04	0.01	2.32	9.10E-10	4.54E-12	-3.09E-12	1.00
Untreated Wet Perpendicular	5	3.25E-12	3.00E-11	2.38E-11	2.32E-14	1.17	12.06	584.14	1.56	5.14E-14	1.53E-11	-1.19E-11	0.99
	50	2.08E-12	1.93E-11	1.49E-11	1.08E-14	2.20	21.57	0.01	1.18	2.37E-09	1.26E-11	-1.04E-11	1.00
KOH-treated Dry Parallel	5	5.95E-13	9.24E-12	4.68E-12	2.13E-14	0.82	6.78	16241.25	2.29	5.69E-16	2.05E-12	-1.35E-12	1.00
	50	4.52E-14	6.79E-12	6.29E-12	2.29E-16	1.63	14.97	0.00	0.49	1.55E-09	1.28E-11	-1.28E-11	1.00
KOH-treated Wet Parallel	5	1.57E-13	1.57E-11	2.31E-11	6.06E-16	21.88	1.93	1.27	34.12	1.24E-11	6.78E-13	-5.17E-13	1.00
	50	2.19E-12	1.53E-11	2.01E-11	9.80E-15	24.53	2.29	1.64	0.01	9.36E-12	2.28E-09	-2.27E-09	1.00
KOH-treated Dry Perpendicular	5	5.23E-13	7.30E-12	7.34E-12	7.60E-15	9.99	1.03	1.72	1726.83	4.24E-12	4.25E-15	5.57E-13	1.00
	50	3.48E-12	9.42E-12	9.57E-12	1.36E-14	17.17	1.99	0.68	0.01	1.39E-11	1.45E-09	-1.44E-09	1.00

KOH-treated Wet Perpendicular	5	1.98E-12	1.43E-11	2.70E-11	1.02E-14	20.47	1.85	1.29	41.03	1.11E-11	6.58E-13	1.37E-12	0.99
	50	2.06E-12	2.12E-11	1.46E-11	1.02E-14	2.24	21.68	0.01	1.20	2.52E-09	1.22E-11	-1.00E-11	1.00
H_2O_2-treated Dry Parallel	5	6.38E-14	1.04E-11	5.93E-12	1.02E-16	1.17	18.80	601.42	1.32	1.72E-14	4.49E-12	-4.43E-12	1.00
	50	4.40E-13	9.42E-12	8.35E-12	1.94E-15	2.81	23.53	0.01	1.47	7.06E-10	5.67E-12	-5.21E-12	1.00
H_2O_2-treated Wet Parallel	5	3.73E-13	1.81E-11	1.38E-11	-4.62E-15	1.53	31.03	103.78	1.18	1.74E-13	1.17E-11	-1.14E-11	0.99
	50	1.25E-12	1.17E-11	1.66E-11	6.34E-15	22.10	2.20	1.26	0.01	9.34E-12	2.05E-09	-2.05E-09	1.00
H_2O_2-treated Dry Perpendicular	5	-1.17E-14	6.06E-12	6.92E-12	-6.63E-17	0.92	5.36	4982.64	2.93	1.22E-15	2.36E-12	-2.38E-12	1.00
	50	1.45E-12	8.16E-12	8.38E-12	6.75E-15	19.30	2.29	0.90	0.01	9.08E-12	9.50E-10	-9.48E-10	1.00
H_2O_2-treated Wet Perpendicular	5	1.67E-12	1.72E-11	1.66E-11	1.89E-14	0.91	9.80	5119.91	1.74	3.37E-15	9.53E-12	-7.76E-12	1.00
	50	1.91E-12	1.49E-11	1.14E-11	7.97E-15	2.51	22.05	0.01	1.25	1.41E-09	9.11E-12	-7.10E-12	1.00

Supplementary Table 13: Fitting parameters, time, spring and damper constants for creep curve of the tests conducted with method 3. Fitting with a spring and one Kelvin-Voigt body (model 3) with a load of 5 mN and a ramp time of 5 mN divided by the respective load rate.

Sample	Load Rate [mN/s]	B	D_1	τ_1 [s]	ρ_1 [s]	C_1	C_0	R^2
Untreated Dry Parallel	0.05	3.25E-13	3.31E-13	21.92	20.77	1.59E-14	3.09E-13	0.98
	0.5	4.45E-13	3.75E-13	17.42	1.35	2.78E-13	1.67E-13	0.97
	1.5	4.61E-13	3.96E-13	12.85	1.14	3.47E-13	1.14E-13	0.97
	5	6.28E-13	5.33E-13	16.05	1.03	5.17E-13	1.12E-13	0.99
	10	4.49E-13	3.81E-13	12.12	1.02	3.73E-13	7.57E-14	0.97
Untreated Wet Parallel	0.05	3.53E-13	3.68E-13	18.10	45.19	8.15E-15	3.44E-13	0.99
	0.5	8.58E-13	6.86E-13	18.09	1.34	5.14E-13	3.44E-13	0.98
	1.5	1.40E-12	9.90E-13	19.37	1.09	9.07E-13	4.88E-13	0.97
	5	1.54E-12	1.02E-12	16.21	1.03	9.90E-13	5.46E-13	0.97
	10	1.43E-12	9.38E-13	14.03	1.02	9.21E-13	5.08E-13	0.97
KOH-treated Dry Parallel	0.05	2.50E-13	2.64E-13	16.83	63.88	4.13E-15	2.46E-13	0.98
	0.5	4.90E-13	4.25E-13	19.60	1.30	3.26E-13	1.65E-13	0.98
	1.5	6.04E-13	5.30E-13	16.03	1.11	4.77E-13	1.27E-13	0.99
	5	7.38E-13	6.03E-13	24.09	1.02	5.91E-13	1.47E-13	0.98
	10	6.09E-13	5.01E-13	18.79	1.01	4.94E-13	1.15E-13	0.98
KOH-treated Wet Parallel	0.05	4.54E-13	4.48E-13	24.22	14.81	3.03E-14	4.23E-13	0.99
	0.5	9.06E-13	7.62E-13	14.03	1.46	5.22E-13	3.83E-13	0.99
	1.5	9.39E-13	6.82E-13	19.57	1.09	6.26E-13	3.14E-13	0.98
	5	2.04E-12	1.38E-12	15.02	1.03	1.34E-12	7.06E-13	0.97
	10	2.14E-12	1.43E-12	15.76	1.02	1.40E-12	7.38E-13	0.97
H_2O_2-treated Dry Parallel	0.05	2.25E-13	2.31E-13	18.94	37.00	6.24E-15	2.19E-13	0.99
	0.5	3.53E-13	3.34E-13	11.97	1.56	2.13E-13	1.39E-13	0.99
	1.5	4.72E-13	3.93E-13	13.41	1.14	3.46E-13	1.26E-13	0.98
	5	5.48E-13	4.34E-13	19.47	1.03	4.23E-13	1.25E-13	0.98
	10	5.33E-13	4.17E-13	16.43	1.02	4.10E-13	1.22E-13	0.97
H_2O_2-treated Wet Parallel	0.05	4.63E-13	4.81E-13	20.94	24.63	1.95E-14	4.44E-13	0.99
	0.5	1.12E-12	9.07E-13	17.69	1.34	6.75E-13	4.46E-13	0.98
	1.5	1.33E-12	9.74E-13	16.07	1.11	8.76E-13	4.58E-13	0.98
	5	1.33E-12	8.93E-13	15.07	1.03	8.64E-13	4.68E-13	0.97
	10	1.34E-12	9.49E-13	10.87	1.02	9.27E-13	4.12E-13	0.98